Dissertation zur Erlangung des Doktorgrades
der Fakultät für Chemie und Pharmazie
der Ludwig-Maximilians-Universität München

A Systematic Experimental and Analytical Approach to Sr–(Si,P)–(O,N) Networks

Marwin Cosmo Dialer
aus
Walnut Creek, USA

2024

Erklärung

Diese Dissertation wurde im Sinne von §7 der Promotionsordnung vom 28. November 2011 von Herrn Prof. Dr. Wolfgang Schnick betreut.

Eidesstattliche Versicherung

Diese Dissertation wurde eigenständig und ohne unerlaubte Hilfsmittel erarbeitet

München, den 14.05.2024

_____

Marwin Cosmo Dialer

Dissertation eingereicht am:	28.03.2024
1. Gutachter:	Prof. Dr. Wolfgang Schnick
2. Gutachter:	Prof. Dr. Henning Höppe
Mündliche Prüfung am:	08.05.2024

To Sophia and the Family.

“Once we stop trying to validate our worth,
we become free to create without limits.”

Danksagung

Diese Doktorarbeit war auf wissenschaftlicher und persönlicher Ebene eine große Herausforderung, die ich ohne die Hilfe vieler herausragender Menschen nicht bewältigt hätte.

An vorderster Stelle möchte ich Prof. Dr. Wolfgang Schnick, meinem Doktorvater, meine Dankbarkeit aussprechen. Ich war als Absolvent einer fremden Universität nicht nur ein unbeschriebenes Blatt, sondern auch ein gewisses Wagnis. Umso mehr danke ich ihm für sein Vertrauen und die Chance, die er mir gegeben hat. Herr Schnick hat mir in seiner Arbeitsgruppe zudem ein Umfeld geboten, in dem ich sowohl als Wissenschaftler als auch als Mensch wachsen konnte. Ich habe in dieser Zeit ein tiefes Verständnis für Selbstwirksamkeit und Eigenverantwortung entwickelt, welches mein Leben nachhaltig positiv verändert, mehr vielleicht noch als es ein Doktortitel vermag. Für seine Förderung und vieles mehr gebührt ihm mein aufrichtiger Dank.

Danken möchte ich auch der Rosa-Luxemburg-Stiftung und dem Bundesministerium für Bildung und Forschung, deren Stipendium mein Promotionsvorhaben wesentlich bereichert und erleichtert hat.

Mein besonderer Dank gilt auch der Universität Augsburg und ihren Dozenten, bei denen ich eine vielseitige und zugewandte Ausbildung genießen durfte. Hervorheben möchte ich Prof. Dr. Henning Höppe, meinen Bachelorbetreuer, und PD Dr. Georg Eickerling, meinen Masterbetreuer, für ihren unermüdlichen Einsatz für meine akademische Ausbildung. Beide haben mich mehrfach über die eigenen Interessen hinweg gefördert, was ich ihnen nicht vergesse.

Zusätzlich danke ich Prof. Dr. Henning Höppe für die Übernahme des Zweitgutachtens meiner Dissertation und Prof. Dr. Dirk Johrendt, Prof. Dr. Silvija Markic, Prof. Dr. Thomas Klapötke und Prof. Dr. Hans-Christian Böttcher für die freundliche Bereitschaft, meinem Prüfungsausschuss beizuwohnen.

PD Dr. Constantin Hoch und Dr. Thomas Bräuniger danke ich für die exzellente fachliche Unterstützung im Rahmen nicht ausschließlich sinnvoller Fragen.

Christian Minke, Dr. Peter Mayer und Sandra Albrecht sei für ihre Messungen und Bemühungen herzlich gedankt, aus meinen Proben doch ein bisschen Sinn zu extrahieren.

Den wissenschaftlichen Beitrag, den meine Kollegen zu dieser Doktorarbeit beigetragen haben, kann man nicht überschätzen. Ich möchte mich von ganzem Herzen bei Monika

Pointner für ihre STEM Messungen bedanken. Diese Messungen waren nach drei Jahren Promotion ein alles verändernder Hoffnungsschimmer und die Grundlage dieser Dissertation. Reinhard Pritzl hat mich menschlich und wissenschaftlich durch diese Promotion getragen. Er wird das bestreiten, aber vieles, was ich über Chemie weiß, habe ich in seinem Windschatten gelernt. Seine Inspiration und sein chemisches Verständnis haben diese Dissertation maßgeblich mitgeformt. Kristian Witthaut ist zu danken für seine wohl einzigartige Begeisterung für fremde Themen und seinen Beitrag durch Überlegungen und Berechnungen. Für viele unzählige schöne Momente in Kaffeeküchen vor Aufzügen oder beim Mittagessen möchte ich mich ganz besonders bei Georg Krach, Amalina Buda, Dr. Stefanie Schneider, Sebastian Ambach, Dr. Tobias Giftthaler, Mirjam Zipkat, Dr. Stefan Rudel, Florian Engelsberger, Thaddäus Koller, Jennifer Steinadler und Brathanh Chau bedanken. Dieser Dank gilt auch unseren benachbarten Arbeitskreisen Hoch, Johrendt, Lotsch und Kloß für die angenehme Atmosphäre.

Ich danke Olga Lorenz, Wolfgang Wünschheim und Dr. Dieter Rau für die freundliche Unterstützung in allen organisatorischen, EDV- und sicherheitsrelevanten Bereichen.

Ich danke meinem Bruder Dr. Clemens Dialer für den Zuspruch und das Mitgefühl in harten Phasen meiner Promotion. Ich danke ihm auch für seine chemische Pionierarbeit schon seit meiner Facharbeit, die hergestellten Kontakte und die Türen, die sich mir dadurch geöffnet haben.

Mein Freundeskreis war mir stets ein sehr willkommener Rückzugsort, der mich daran erinnert hat, dass niemand außerhalb meiner Blase sich für Chemie interessiert. Ich halte das für gesund und weiß sie alle sehr zu schätzen. Besonders hervorheben möchte ich Dr. Tobias Schmid und il dottore, Sebastian Greppmair, denen ich für ihre offenen Ohren und Teilhabe an dieser Zeit danke.

Meiner Familie verdanke ich alles. Sie haben mich Denken und Fühlen gelehrt und nicht zu knapp an mich geglaubt, wenn ich es nicht getan habe. Ich danke meinen Eltern Lilith und Christian, und meinen Geschwistern Lennart, Corinne und Clemens. In meinen Augen sind sie einzigartig.

Den letzten und größten Dank verdient meine Freundin Dr. Sophia Wandelt. Auch unter Berücksichtigung dieser Dissertation ist unsere Beziehung mit Sicherheit das beste Ergebnis meiner Promotion. Ihre tägliche Unterstützung war und ist eine unschätzbare Bereicherung.

Table of Contents

List of Abbreviations

AE	Alkaline Earth
BN	Boron Nitride
BVS	Bond Valence Sums
CC	Counter Cation
CHARDI	Charge Distribution
CN	Coordination Number
CR	Cation Ratio
DFT	Density Functional Theory
DOS	Density of States
ECBVD	Ewald/CHARDI/BVS/Volumes/Distances
ECoN	Effective Coordination Number
EDX	Energy Dispersive X-ray Spectroscopy
EN	Electronegativity
FDU	Fundamental Disorder Unit
GoF	Goodness of Fit
HAADF	High-Angle Annular Dark Field
ICP-OES	Inductively Coupled Plasma Optical Emission Spectroscopy
IR	Infrared Spectroscopy
LCC	Low-Cost Crystallographic Calculations
LIG	Ligands
NFC	Network Forming Cations
NMR	Nuclear Magnetic Resonance
NOE	Nuclear Overhauser Effect
Ox	Oxidation States
PLE	Photoluminescence Excitation
PL	Photoluminescence
PND	Powder Neutron Diffraction
PXRD	Powder X-ray Diffraction
SCXRD	Single-Crystal X-ray Diffraction
SEM	Scanning Electron Microscopy
SHG	Second Harmonic Generation
STEM	Scanning Transmission Electron Microscopy
WMD	Weighted Mean Distances

1 Introduction

Figure 1.1 Deconstruction of the title of the dissertation to reflect the structure of the introduction.

Solid-state chemistry has the reputation of being one of the most complex areas of chemistry. Although every scientist is inclined to say this about their own field of research, there are three good reasons to support this thesis: 1) The complexity of atomic interactions depends strongly on the number of participants, which is by far the highest in solids. 2) The prevailing anisotropy of solids complicates many traditional analytical methods to elucidate their structures and properties, such as nuclear magnetic resonance, infrared, or Raman spectroscopy. 3) The strength of atomic interactions in solids spans a huge range, which is why their syntheses often require extreme conditions, such as high temperatures, high pressures, or very long reaction times. An example of this is the different reactivity of P_3N_5 and Si_3N_4, which is discussed below. At this point, however, it is important to mention that complexity is not to be confused with quality but is rather an indication of how essential a systematic methodology is for investigations in solid-state chemistry. This is also reflected in the title of this dissertation “A Systematic Experimental and Analytical Approach to Sr–(Si,P)–(O,N) Networks”, which at the same time serves as the structure of this introductory section to answer the research questions of what, why and how (Figure 1.1).

The first two questions "what" and "why" are discussed in more detail in section 1.1, but the main objective of this dissertation was to explore the largely unknown compositional space of Sr–(Si,P)–(O,N) and to investigate and understand its structural and optical peculiarities. Section 1.1 also describes the inherent challenges of such compounds involving mixed

tetrahedral networks to motivate the following chapters. Section 1.2, which is devoted to the "Systematic Experimental Design", answers the third question of “how” the synthetic work was conducted and is aimed to be reproducible, transferrable, and scalable. Scalability in particular is often underestimated in the context of a dissertation. Section 1.3 treats the different analytical workflows available for the characterization of Sr–(Si,P)–(O,N) compounds, with a particular focus on methods to elucidate the ordering of (Si,P)–(O,N) networks. This will also highlight another core objective of this dissertation, namely the estimation and testing of different analytical designs to leave a clear guidance on how to elucidate mixed tetrahedral networks. Finally, section 1.4 explains how the various analytical workflows come together with the discovered Sr–(Si,P)–(O,N) compounds to develop a logical and comprehensible thread for the main part of this thesis.

1.1 Sr–(Si,P)–(O,N) Networks

The main topic of this dissertation is the exploration of Sr–(Si,P)–(O,N) compounds whose core features are anionic, tetrahedral (Si,P)–(O,N) networks. The notation used here, refers to Sr as the counter cation (*CC*), to (Si,P) as the network-forming cations (*NFC*), i.e. those that occupy the centers of the tetrahedra, and to (O,N) as the ligands (*LIG*) that occupy the corners of the tetrahedra. Tetrahedral networks, in general, have a long tradition, a huge structural variety and countless possible applications. The best-known class of compounds associated with them are silicates, which is also the reason why their derivatives are often called silicate analogous materials. Research into such compounds has significantly advanced many fields of science. This includes catalysis, where, e.g., zeolites that consist of a tetrahedral network provide unique catalytic diversity due to their ability to confine reactants within their molecular-sized voids, leading to selective reactivity and product formation.[1,2] These voids can also be used for ion exchange reactions or act as molecular sieves. Another field of application are energy storage materials, e.g., the cathode materials MFeSiO$_4$ (M = Li, Na) or LiFePO$_4$, as well as hydrogen storage materials MBH$_4$ (M = Li, Na).[3–6] However, the biggest impact probably is found in the development of state-of-the-art inorganic luminescent materials for optoelectronics, such as phosphor-converted light-emitting diodes (pcLEDs). Anionic tetrahedral networks with alkaline earth metals as counter cations have proven themselves to be excellent host structures for Eu^{2+} doping. Prominent and widely industrialized examples are $Sr_2Si_5N_8$:Eu^{2+}, β-*sialon*:Eu^{2+}, $CaAlSiN_3$:Eu^{2+}, $SrLiAl_3N_4$:Eu^{2+} and $SrLi_2Al_2O_2N_2$:Eu^{2+}.[7–11] Recent developments also show that phosphorus-based luminescent materials are excellent candidates to further improve our the emission profile in the red spectral range, e.g. Ca_2PN_3:Eu^{2+}.[12]

The question is therefore not whether research into tetrahedral networks is promising, but rather which modifications of such a network are useful and for which type of application they would be suitable. On the one hand, nitridosilicates and nitridophosphates have impressively demonstrated their suitability as inorganic phosphors. On the other hand, both classes already comprise the largest number of representatives in the field of ternary nitrides, so that their pairing suggests an even higher number of combinations. This is the reason, why this dissertation focuses on the mixed networks of both classes of compounds with respect to their

optical properties. This mixture has several exciting implications, such as greater structural diversity, better tunability of these optical properties due to the chemical similarity between Si^{4+} and P^{5+}, and the vast expansion of compositional space through simple combinatorics. The latter can be well illustrated by pseudo-ternary phase diagram of the cationic components Sr^{2+}, Si^{4+} and P^{5+}, where the anionic composition, i.e. O^{2-} and N^{3-}, is implied by the charge balance (Figure 1.2a). In this representation it is easy to see that the compositional space of pure Sr–Si–N or Sr–P–N compounds is limited to the colored red and blue edges while the compositional space of Sr–(Si,P)–(O,N) compounds extends over the entire region that is marked as beige. At the beginning of this dissertation, the only known compound of this space was $SrSiP_3N_7$ that was published in 2021, making this a rather young class of compounds.[13] Oxonitridosilicate phosphates on the other hand were completely unknown.

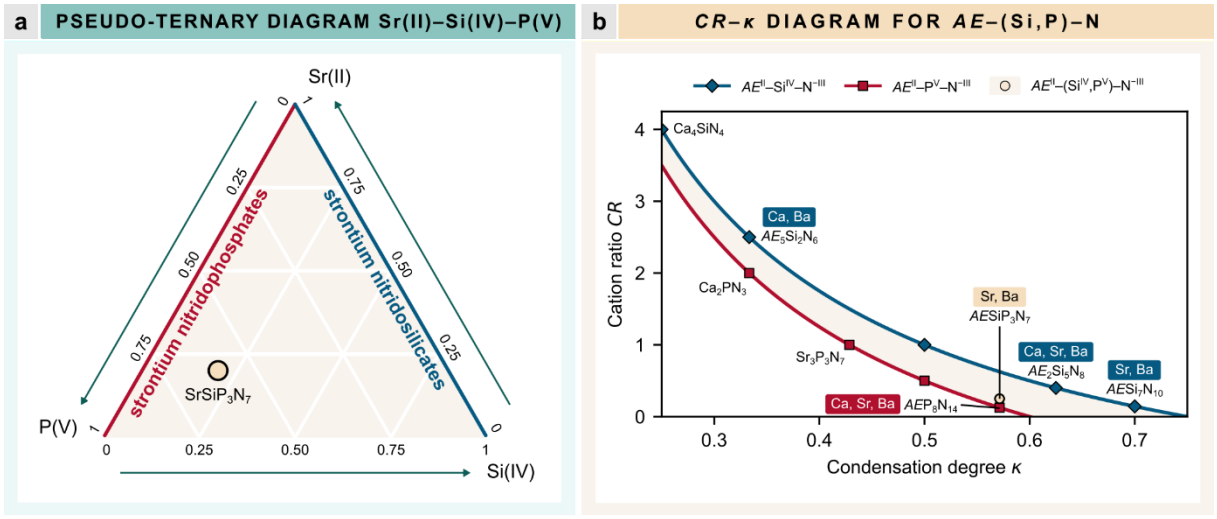

Figure 1.2 a) Pseudo-ternary Sr-Si-P diagram marking the only known representative $SrSiP_3N_7$. b) *CR*-κ diagram including all literature known *AE*–Si–N, *AE*–P–N, and *AE*–(Si,P)–N compounds (AE = Ca, Sr, Ba).

There is another representation of this combinatorial expansion, namely the *CR*–*κ* diagram (Figure 1.2b). This approach was developed during this dissertation in cooperation with Pritzl et al. and addresses frequently used metrics to classify such networks.[14] The first metric is the cation ratio *CR* which is defined as the ratio between counter cations (*CC*), here Sr^{2+}, and the network-forming cations (*NFC*), here Si^{4+} and P^{5+} (Equation 1). The second metric is the condensation degree *κ* which is defined as the ratio of the *NFC* and ligands, here O^{2-} and N^{3-} (Equation 2).

$$CR = \frac{N(CC)}{N(NFC)} \quad (1) \qquad \kappa = \frac{N(NFC)}{N(LIG)} \quad (2)$$

N: count, *NFC*: network forming cation, *LIG*: ligand, *CC*: counter cation

Considering only the cases in which the oxidation states of the ions involved are constant, *CR* and *κ* are linked via an analytical relationship, where $CR \propto 1/\kappa$ (Equation 3).

$$CR(\kappa) = -\frac{Ox(LIG)}{Ox(CC)} \cdot \frac{1}{\kappa} - \frac{Ox(NFC)}{Ox(CC)} \quad (3)$$

Ox: oxidation state

This means that all alkaline earth nitridosilicates (blue) and nitridophosphates (red) lie on a corresponding $1/\kappa$ curve, as shown in Figure 1.2b for all literature known compounds of these classes with Si(IV) and P(V). $SrSi_6N_8$, for example, would be excluded from this system due to Si–Si contacts that result in a formally reduced oxidation state of Si(III).[15] Again, nitridosilicate phosphates (beige) can occupy the entire area between the two curves, but this time in terms of their *CR* and *κ*. This is interesting in the context of luminescent materials, as the degree of condensation is often empirically correlated with the rigidity of a network. There are examples that a higher degree of linkage leads to a narrower emission profile when doping with Eu^{2+}.[16–18] Accordingly, it is important that the mixed (Si,P) networks provide a significantly larger space to synthesize highly condensed structures, which is equivalent to a *κ* greater than or equal to 0.5. However, the disadvantage of a larger compositional space is that it is easier to get lost in it without a strictly systematic experimental approach. Researchers must decide for themselves whether a serendipitous approach is more appropriate for them personally, but in this thesis a more rigorous framework is advocated, as explained in more detail in section 1.2.

In addition to the search for innovation and synthetic subtleties, this contribution also aims at a more holistic development: Since the completion of the periodic table, inorganic chemistry has developed from binary to ternary to multinary systems and continues to do so. On the one hand, this development is due to the fact that the field for new discoveries is becoming smaller and smaller with a practically complete periodic table and an intensively researched field of binary compounds. On the other hand, analytical methods are also becoming more precise, faster, and easier available, so that a large number of analytical methods that were a peculiarity decades ago are now standard methods of analysis. This enables the characterization of increasingly complex systems. Although multinary compounds hold great

potential, they also come with inherent challenges, particularly in terms of structure elucidation. This can be nicely explained on the example of strontium nitridosilicates Sr–Si–N and strontium oxonitridosilicate phosphates Sr–(Si,P)–(O,N). As mentioned above, these compound classes can be divided into counter cations, network-forming cations, and ligands. This division is based on the clearly distinguishable crystallographic behavior of these groups, i.e., *CC* can never occupy crystallographic *NFC* and *LIG* positions and vice versa, simply because of the ion sizes and charges. In Sr–Si–N compounds, each group has only one member, which means that in most cases - again, $SrSi_6N_8$ would be the exception - these structures can be elucidated by standard X-ray diffraction and chemical intuition, which is a great advantage.[15] In Sr–(Si,P)–(O,N), however, *NFC* and *LIG* both comprise two members, namely Si/P and O/N. Both pairings are neighbors in the periodic table with very similar X-ray scattering factors which is why they behave very similarly in crystal structures. This also means, standard X-ray diffraction is often ambiguous where at first glance it is not clear if Si and P occupy different crystallographic sites (substitutional order), the same sites (substitutional disorder), or a combination of both. The same is true for O and N. As a result, it is often necessary to use additional analytical methods that allow a better distinction between Si/P and O/N. There is no patent remedy for the question of which analytical methods are best suited for this. Therefore, another important focus of this work was to identify conceptually good analytical methods for the differentiation of chemically similar substituents on the examples of Si and P. Promising different analytical approaches are discussed in section 1.3.

1.2 Systematic Experimental Design for Sr–(Si,P)–(O,N) Networks

1.2.1 General Approach

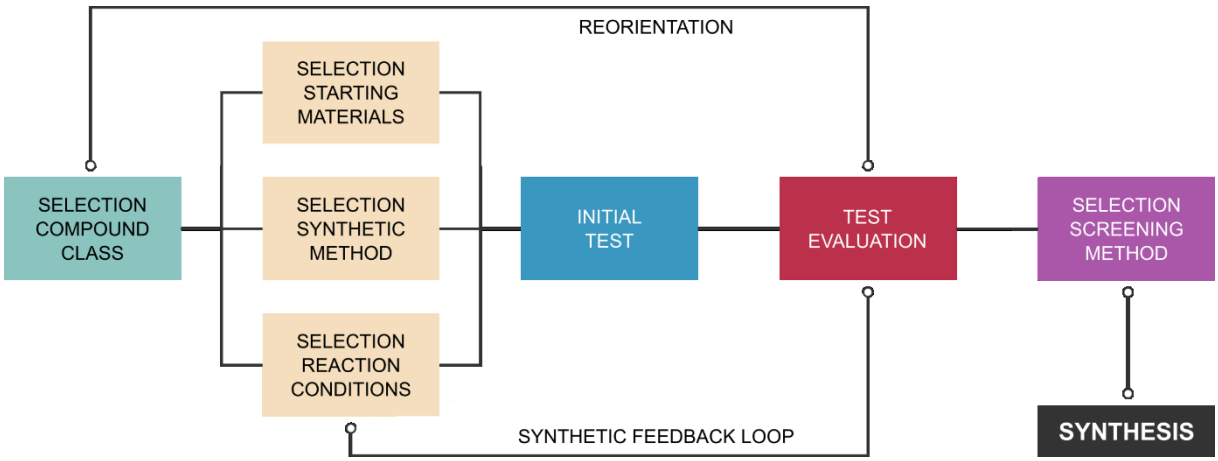

Figure 1.3 Illustration of the general approach to create an experimental design.

A good experimental approach involves several iterative steps and should not be confused with an overly direct or efficient process. In fact, there is a whole branch of science that deals with efficient and sophisticated experimental designs, also known as Design of Experiments (DOE), although the level of sophistication will be limited in this dissertation. It must also be mentioned that researchers tend to over-rationalize their decisions in hindsight, whereas many decisions at the time were based on intuition and availability. Nevertheless, it is possible to structure the experimental design process so that it is comprehensible, reproducible, and transferable to other researchers, as illustrated in Figure 1.3.

The decision on the compound class is usually dominated by broader motives, such as the search for certain properties, structural peculiarities, or simply serendipitous interest. Once this decision has been made, literature research is an indispensable tool for narrowing down the number of preliminary experiments required. Important questions are: What are suitable starting materials? Are there transferable systems in the literature? What were the synthesis conditions for comparable compounds? In the best case, this already limits the highly parametric field of reaction temperature, pressure, time, crucible material and method. In any case, however, it is necessary to create a feedback loop in which the initial test and the test

evaluation are carried out. A simple example of this would be to collect powder X-ray diffraction data of the sample before and after the test to evaluate whether the starting materials have reacted. If the result is unsatisfactory, the feedback loop adjusts the synthetic decisions until success is achieved or reverts to "selecting a new compound class". A good "initial test" for multinary compounds is often to be found in well-ground stoichiometric quantities of the starting materials, e.g. Sr:Si:P = 1:1:1. The reason for this is that it makes the separation into binary and ternary thermodynamic sinks more difficult, as significantly more diffusion is required. If the reactivities of the starting materials differ greatly, it may also be worthwhile to further reduce the proportion of the most inert participant or to add activating species such as fluxes or mineralizers. Once suitable synthetic settings are found, the next step is to select or create a suitable screening pattern that reduces the parametric fields to those of interest to the research. It is tempting to make the patterns very flexible in order to draw very general conclusions, but this is often impractical and risks being overwhelming. One or two parameters of interest are often sufficient. Examples could be: 1) Investigation of the temperature and pressure dependence of a fixed stoichiometry, method, and reaction time, e.g. in the study of phase transitions. 2) Investigation of luminescence properties related to doping or even co-doping of Eu^{2+}/Ce^{3+} on a given host structure with fixed reaction conditions and methods. 3) Investigation of pseudo-ternary phase diagrams by screening different stoichiometries with fixed reaction conditions and methods. The latter is also the screening method chosen for this dissertation, as explained in the following subsection.

1.2.2 Experimental Design

1.2.2.1 Selection of the Compound Class

This experimental design was originally developed only for the investigation of Sr–(Si,P)–N networks. However, experience has shown that the complete exclusion of oxygen in a multianvil press is often impractical. Typical sources of oxygen are hydrolysis products of the starting materials, oxidized crucible materials or simply the humidity in the laboratory. It is also known that the pyrophyllite parts in the assembly can contain a lot of H_2O, which can lead to high fugacities of water. To complicate matters further, Si and P are not only considered very oxophilic, but also form a rather iconic isolobal relationship, namely Si–O/P–N. Both facilitate the incorporation of oxygen into such networks in addition to the well-known chemical

similarity of O and N. Therefore, the original target was extended from Sr–(Si,P)–N to Sr–(Si,P)–(O,N), which should contain as much nitrogen as possible, i.e. n(N)>>n(O).

1.2.2.2 Selection of the Starting Materials

The literature search revealed that the pure alkaline earth nitridosilicates and nitridophosphates from the literature were valuable references, as was the only strontium nitridosilicate phosphate $SrSiP_3N_7$.[12,13,19,20] They provided a list of commonly used starting materials (Figure 1.4a):

For Sr^{2+}: SrN, SrN_2, Sr_2N, Sr_4N_3, "Sr_3N_2", or $Sr(N_3)_2$, although "Sr_3N_2" is only a commercialized heterogeneous mixture of different Sr–N species.

For Eu^{2+}: Eu_2O_3, $EuCl_2$, EuF_3, or EuN, where Eu^{3+} species are reduced to Eu^{2+} during the syntheses due to the reducing atmosphere created in the presence of nitrides or ammonia.

For Si^{4+}: Crystalline or amorphous Si_3N_4.

For P^{5+}: Semi-crystalline α-P_3N_5 or red P.

The choice after several preliminary experiments fell on $Sr(N_3)_2$ (available, nitrogen-rich, and reactive), EuN (no additional anions), amorphous Si_3N_4 (available and reactive), and P_3N_5 (available and reactive). Oxygen-containing starting materials are not listed here, as they only were used for optimization syntheses, as discussed in subsection 1.2.3.

1.2.2.3 Selection of the Synthetic Method

Another result from the literature research was that the pressures required for the synthesis of the individual classes differ considerably. While alkaline earth nitridophosphates often require tens of thousands, sometimes even hundreds of thousands of atmospheres (10000 atm ≈ 1 GPa), comparable nitridosilicates can easily be synthesized under ambient conditions and rarely under thousands of atmospheres. This discrepancy is due to the different reactivity of the respective binary nitrides P_3N_5 and Si_3N_4. At ambient pressures, the former decomposes already at 850 °C into PN and N_2, while the latter is stable up to 1900 °C. The aim was therefore to equalize the reactivity ranges of both nitrides. A common method based on Le Chatelier's principle is to apply pressure and push back the thermal decomposition of P_3N_5. Initial tests were carried out in a high-frequency furnace (1 atm) as a low-pressure reference, a hot isostatic press (2500 atm) for medium pressures and a large-volume multianvil press

(30000 atm) for high pressures in the temperature range of 1200–1400 °C, whereby only the latter delivered satisfactory results, so that it was selected as the synthesis method of choice. Although the multianvil press generates very high pressures (2–14 GPa) and temperatures (<1700 °C), this is only possible at the expense of sample volume and high throughput (Figure 1.4b). This approach has been discussed extensively in the literature and there are some excellent sources referenced here.[21–26]

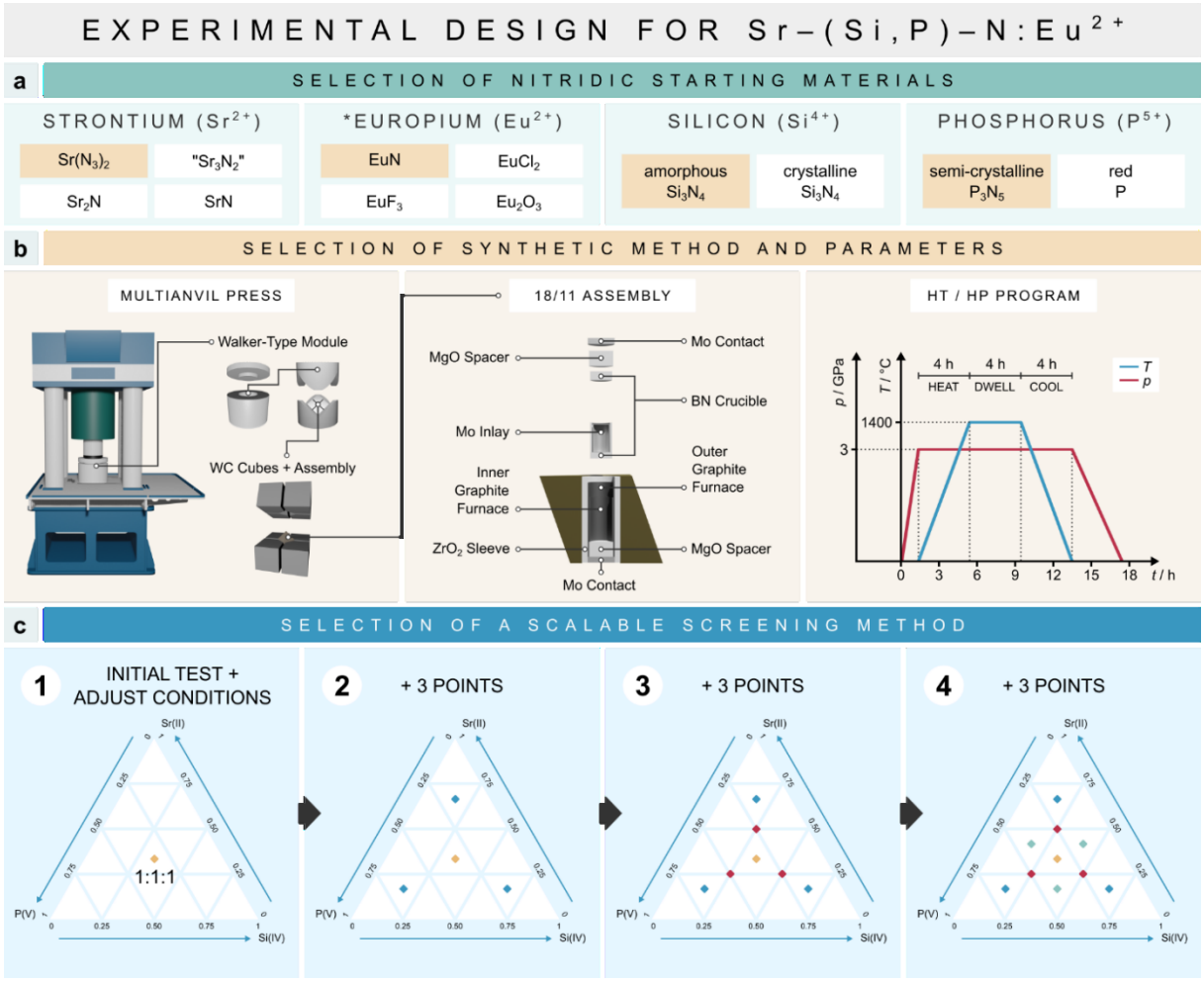

Figure 1.4 a) Illustration of the most frequently used starting materials for nitridosilicates and nitridophosphates (* Eu^{2+} is only used at doping levels of 1–3 mol%). b) Illustration of the synthetic setup and reaction conditions of the experimental design. c) Illustration of the pseudo-ternary screening method and its scalability.

1.2.2.4 Selection of the Synthetic Conditions

As already mentioned, the first tests were carried out at 1200–1400 °C and 3 GPa. This can only be considered an educated guess, and since the reaction results were good from the beginning, no intensive tests were performed for better conditions. The heating, dwell and cooling times were set to four hours each to allow sufficient time for diffusion and to support thermodynamically driven reactions.

1.2.2.5 Selection of the Screening Method

The choice of multianvil press has some important practical implications for the screening method, as a synthesis cycle typically takes one day due to device-specific limitations in pressure increase and decrease. Therefore, the main limiting factor for this method was the availability of the device with respect to research colleagues. Considering these factors, the screening method of choice was the equidistant scanning of the pseudo-ternary Sr–Si–P phase diagram at a constant temperature program, pressure and starting materials. In this method the large parametric field is reduced to the elementary Sr:Si:P ratios of the experiments. Although this may seem drastic at first glance, the reasoning is very simple: in this way, the screening method became highly scalable and could be expanded step by step until the criteria regarding scope and relevance for this dissertation were met (Figure 1.4c). After the initial test (yellow), the first screening iteration comprised three experiments (blue), which were successively extended by three further experiments (red and green), so that a total of ten points were achieved in the end. To ensure reliability, each experiment was reproduced at least once. This approach is primarily aimed at the discovery of new host structures and is well suited for combination with a single-particle approach. Phase-pure syntheses are not always necessary and may only be addressed by optimization experiments when needed, as explained in the next subsection.

1.2.3 Optimization Experiments

The optimization experiments are particularly important if subsequent analytical methods depend on phase-purity and sample size. Typical examples are nuclear magnetic resonance and vibrational spectroscopy, as well as powder diffraction or bulk elemental analyses. To optimize an experiment efficiently, it is essential to have some knowledge about the structure and composition of the target phase. How to obtain this knowledge is discussed in section 1.3. Once the target is identified, the procedure is similar to the overall screening method, yet in a smaller scale (Figure 1.5). The first experiment would surely involve unchanged reaction conditions and merely adapted stoichiometries (yellow), while smaller screening of the compositional vicinity might be a good idea to increase the phase fraction and maybe understand reaction dynamics (blue). Only if this fails, one should enter a new feedback loop, where starting materials and reaction conditions are altered, sometimes even the synthetic

method. In any case, it is good practice to change ideally one and not more than two parameters at the same time. Otherwise, the interpretation of the results might become tedious and ambiguous. Although having optimized reactions is in most cases beneficial for one's own research, it is not inherently necessary. There are many analytical methods that work well on single-particles and yield sufficient information. Here, the researcher must weigh up the effort and return.

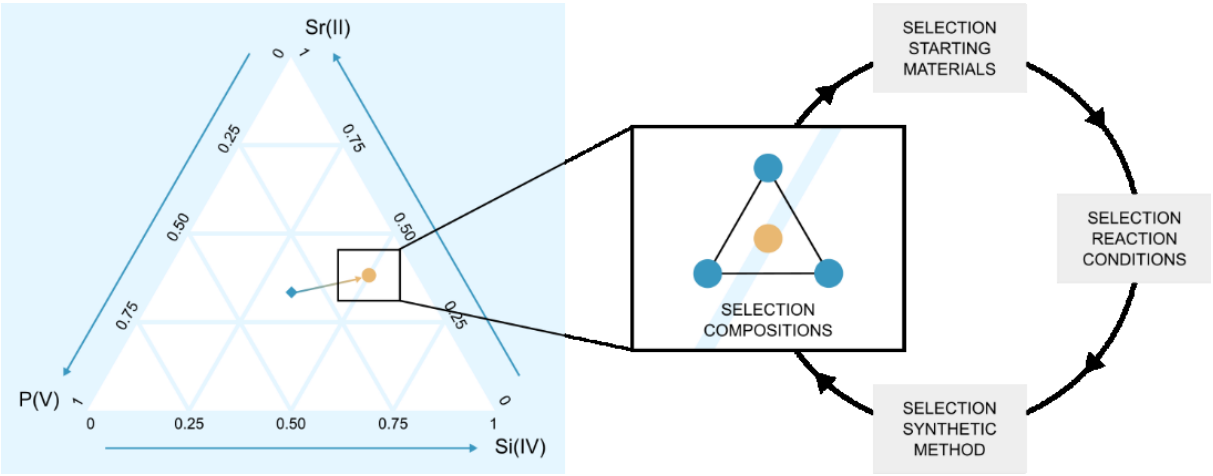

Figure 1.5 Illustration of the optimization process for a phase-pure bulk sample.

1.3 Systematic Analytical Design

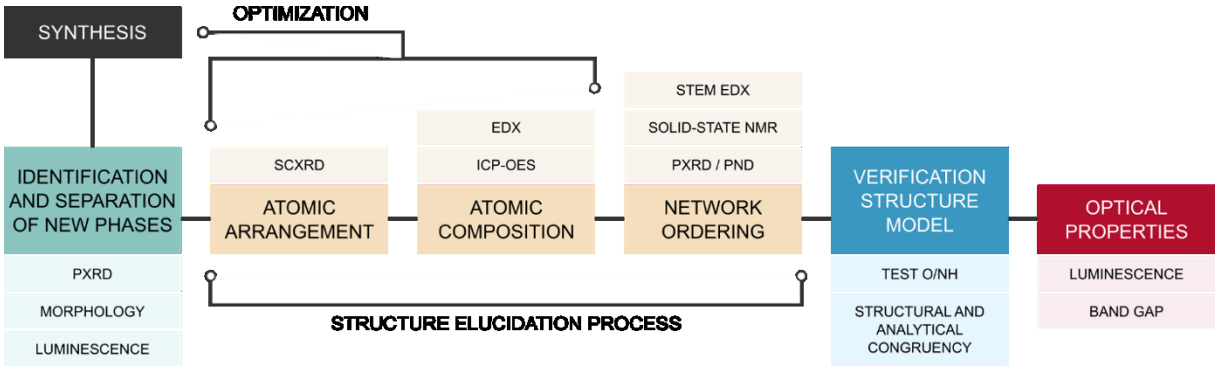

Figure 1.6 General structure of the analytical workflows that were used in the main part of this dissertation.

The analytical landscape in inorganic chemistry is very diverse, but sometimes also confusing. It is important to identify well-suited methods and workflows for the respective problems in one's own research. The aim of this dissertation was to explore important steps of the structure elucidation process of mixed tetrahedral networks and to investigate the available analytical methods for compatibility in order to solve the problem of differentiation between chemically similar atoms. The steps are illustrated in Figure 1.6.

1.3.1 Identification of New Phases

After synthesis, the first important decision is whether new interesting host structures have formed. With increasing experience, a first visual inspection under the microscope with focus on morphology and luminescence behavior can already give hints on interesting and less interesting samples. Powder X-ray diffraction (PXRD) can often help to objectify this assessment by comparing the diffractogram with diffraction patterns known from the literature. If these comparisons do not result in a (full) match, it makes sense to proceed to the next step.

1.3.2 Atomic Arrangement

Single crystal X-ray diffraction (SCXRD) is a high-quality method for determining the unit cell parameters and atomic positions in solids when they crystallize sufficiently well. Although SCXRD often does not provide reliable information about the network order in mixed tetrahedral networks, it is very useful to extract the relative ratios of the chemically distinct crystallographic positions based on their multiplicities, i.e. the *CC*:*NFC*:*LIG* ratios. The reason

for the ambiguity in terms of the occupations in the network, can be found in relatively low X-ray contrasts of Si/P and O/N, but also in the limited resolution of the measurements.[27] Single crystals of the Sr–(Si,P)–(O,N) compounds were of good but not excellent quality, making the collection of high-quality high-resolution SCXRD data impractical. Nevertheless, this process yielded the preliminary sum formula of the form $Sr_x(Si,P)_y(O,N)_z$, where *x, y, z* are the summed Wyckoff multiplicities of the respective species.

1.3.3 Atomic Composition

This preliminary sum formula is then combined with results from elemental analyses to obtain the empirical sum formula that already contains the approximately correct elemental ratios. This is particularly important if the following analytical methods require bulk samples, e.g. nuclear magnetic resonance spectroscopy (NMR) or powder neutron diffraction (PND), so that optimization experiments could be performed (cf. subsection 1.2.3). Two methods were available to investigate the elemental composition, namely energy dispersive X-ray spectroscopy (EDX) for individual particles and inductively coupled plasma optical emission spectroscopy (ICP-OES) for bulk samples. Both EDX and ICP-OES provide reliable results for Sr, Si and P, while O and N can only be determined qualitatively with EDX and not at all with ICP-OES. Therefore, O and N were usually determined taking into account the charge equilibrium and crystallographic considerations, e.g. bond distances or the binding situation of the anions.

1.3.4 Network Ordering

Analyzing the network order of Sr–(Si,P)–(O,N) compounds was one of the core objectives of this dissertation and at the same time a major challenge. Since it was not possible to reliably distinguish Si and P with SCXRD due to the low X-ray contrast at the given resolution, additional analytical methods were needed to complement the structural results. These methods were chosen to utilize other intrinsic properties of Si and P, such as the characteristic emission of X-rays in atomic-resolution scanning transmission electron microscopy (STEM) EDX mappings, the nuclear magnetic resonance frequencies in ^{31}P and ^{29}Si solid-state MAS NMR, as well as the high-resolution X-ray contrast in PXRD and the neutron scattering lengths in PND. Each of these methods provided reliable results on network order and are discussed in detail in the respective main chapter. Once the network order was known, the final structural model was refined using the SCXRD data.

1.3.5 Verification of the Structure Model

The verification and corroboration of the structure model is important in the context of structural consistency and checking for well-known pitfalls. There are many alkaline earth (oxo, imido)nitridosilicates and (oxo, imido)nitridophosphates available to evaluate and compare bonding situations, connectivity patterns and structural relationships. Typical methods for this include Ewald energies, charge distributions (CHARDI), bond valence sums (BVS), as well as polyhedral volumes and interatomic distances, which can be summarized under the generic term “low-cost crystallographic calculations” (LCC). For a detailed introduction into these calculations refer to chapter 2 and 3. From experience, it is also essential to address the incorporation of protonic hydrogen in (oxo)nitridosilicate phosphates due to the isolobal relationships between Si–O, Si–(NH), and P–N. Good tests for N–H functionality are found in cross-polarized $^{31}P\{^{1}H\}$ NMR experiments as well as vibrational spectroscopy, such as Fourier-transformed infrared (FTIR) and Raman spectroscopy.

1.3.6 Optical Properties

In most cases, materials chemists are not only interested in the structure of the material itself, but also in the properties associated with it, although this dissertation focuses mainly on the structural aspects. For Sr–(Si,P)–(O,N) networks, this refers to their ability to act as a host structure for Eu^{2+} doping and the corresponding luminescence properties upon irradiation with ultraviolet light. The parameters of interest were here the emission maxima and half-width, as well as their decomposition in the contributions of the individual activator environments. The former were measured by photoluminescence (PL) and photoluminescence excitation (PLE) spectroscopy on single particles. The latter was investigated by performing Pekarian-type fits that helped in deconvolution of the PL spectra.

1.4 Scope of This Dissertation

This chapter is intended to explain the logical thread of the main part of this dissertation. The core principle of each main chapter is to present one or more newly discovered Sr–(Si,P)–(O,N) networks and their luminescence properties on the one hand and to test new analytical workflows for their characterization for both single-particles and bulk samples on the other hand. For better visualization, all discovered compounds are presented in a pseudo-ternary Sr–(Si,P)–(O,N) map in which they are grouped with respect to the chapter in which they appear in Figure 1.7. The analytical differences between each main chapter are highlighted in Figure 1.8. The following section discusses the criteria used to group the compounds and analytical methods.

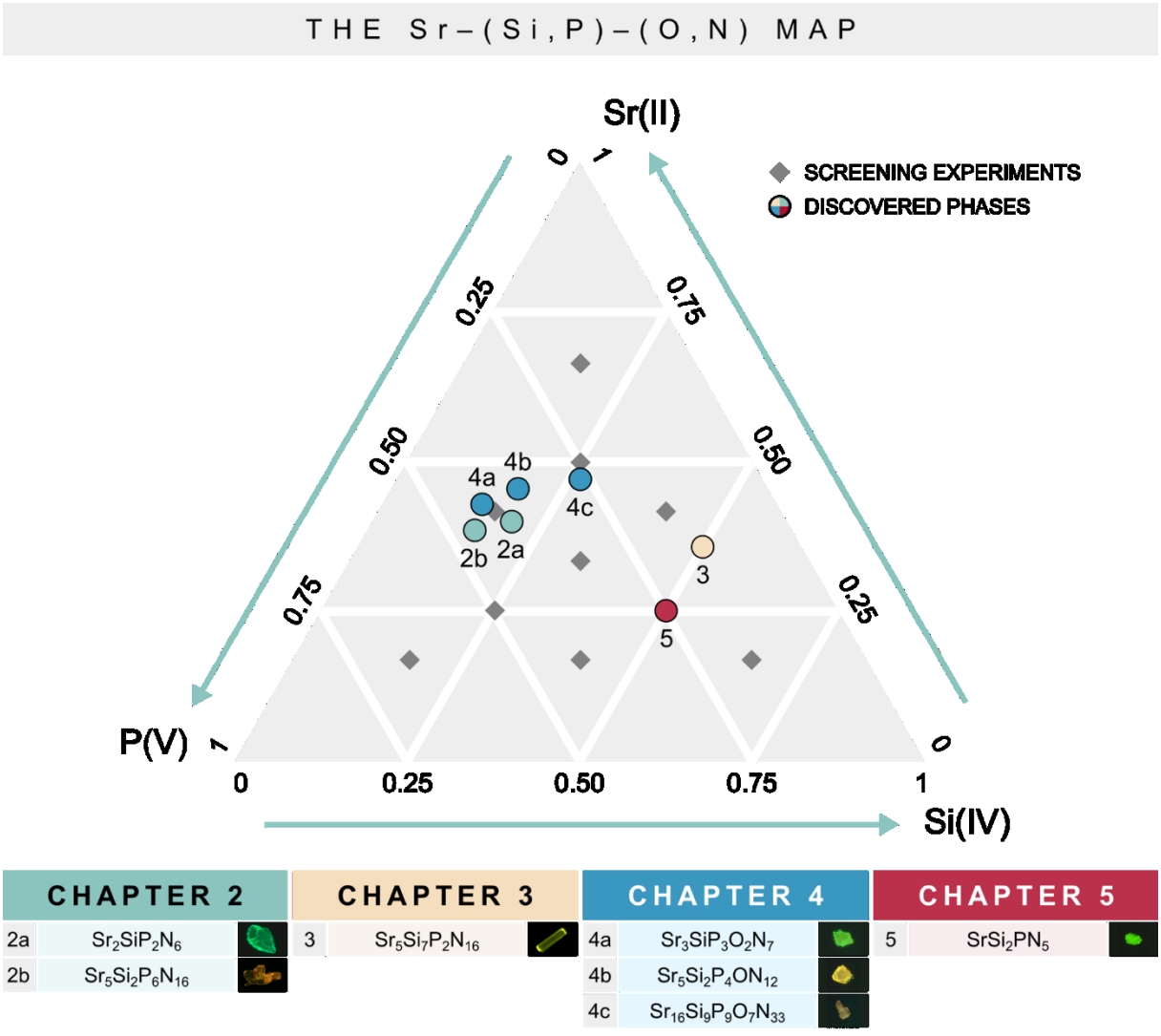

Figure 1.7 Graphical preview of the discovered Sr–(Si,P)–(O,N) compounds in the pseudo-ternary diagram. All compounds are grouped with respect to their chapters where they appear.

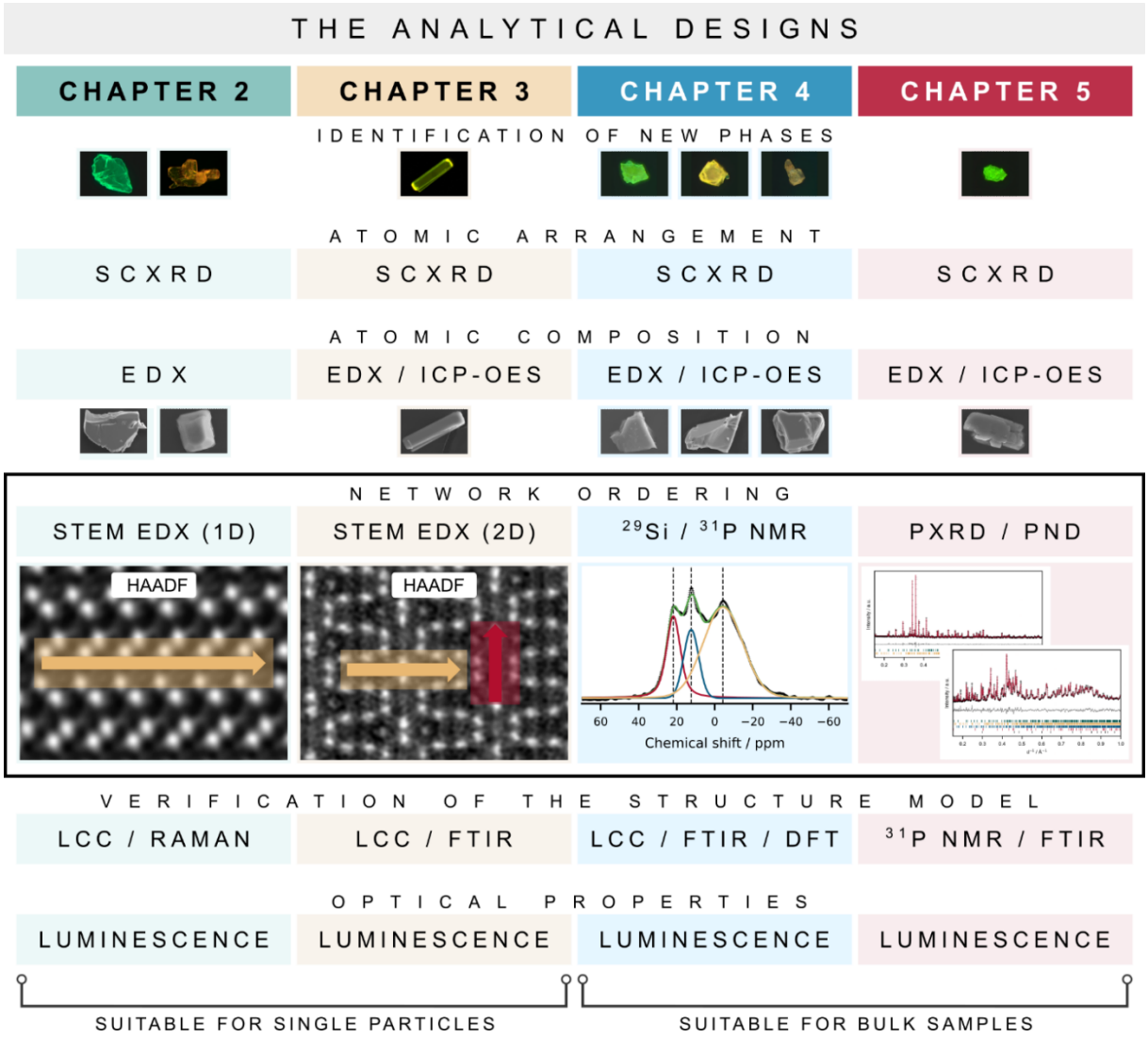

Figure 1.8 Comparison of all analytical workflows used throughout this dissertation based on the chapter where they were used.

CHAPTER 2

Order and Disorder in Mixed (Si,P)–N Networks $Sr_2SiP_2N_6:Eu^{2+}$ and $Sr_5Si_2P_6N_{16}:Eu^{2+}$

Essence: *The First Ordered and Disordered AE–(Si,P)–N Networks*

Chapter 2 introduces with $Sr_2SiP_2N_6$ (2a) the first ordered and with $Sr_5Si_2P_6N_{16}$ (2b) the first disordered Sr–(Si,P)–N network. It highlights achievements and addresses limitations of STEM EDX maps, the method chosen by Eisenburger et al. to investigate the network ordering in *AE*SiP_3N_7 and proposes low-cost crystallographic calculations as a useful supporting analytical method.[13] The different luminescence properties after doping with Eu^{2+} are discussed in detail, focusing on the contributions of the individual activator sites.

CHAPTER 3

(Dis)Order and Luminescence in Silicon-Rich (Si,P)–N Network $Sr_5Si_7P_2N_{16}:Eu^{2+}$

Essence: *The First Silicon-Rich (Si,P)–N Network with Unique Substitional Order and Positional Disorder*

Chapter 3 presents $Sr_5Si_7P_2N_{16}$ (3), the first silicon-rich (Si,P)–N network that comprises an unprecedented mixture of substitutional order and positional disorder, which refers to the phenomenon that atoms do not occupy well-defined crystallographic sites but occur proportionally in multiple positions. The network was investigated by two perpendicular STEM-EDX line scans and supported by LCC. The bright yellow Eu^{2+}-luminescence could be attributed to two distinct activator site contributions, which were quantified by Pekarian-type fitting curves.

CHAPTER 4

The Fundamental Disorder Unit in (Si,P)–(O,N) Networks

Essence: *The First Oxonitridosilicate Phosphates Characterized by a Common Disordered Building Unit*

Chapter 4 discusses the first representatives of oxonitridosilicate phosphates, namely $Sr_3SiP_3O_2N_7$ (4a), $Sr_5Si_2P_4ON_{12}$ (4b), and $Sr_{16}Si_9P_9O_7N_{33}$ (4c). All three comprise a similar disordered building unit which is coined as the “fundamental disorder unit”. The network was investigated by a sophisticated combination of ^{31}P and cross-polarized $^{31}P\{^1H\}$ NMR, which presented itself as a valuable and more accessible alternative to STEM EDX to characterize the (Si,P)–(O,N) networks. This chapter also introduces the first NMR benchmark values for the half-widths of ordered and disordered ^{31}P signals.

CHAPTER 5

The Super-Tunable $LaSi_3N_5$ Structure Type: Insights into the Structure and Luminescence of $SrSi_2PN_5:Eu^{2+}$

Essence: *Introduction of PXRD and PND as analytical tools for the network ordering and exploration of isolobal network tuning to alter luminescence properties.*

Chapter 5 introduces $SrSi_2PN_5$, which crystallizes in the same structure type as a well-known class of compounds, also known as $LaSi_3N_5$-analogous materials. The comparatively simple structure of this compound is a perfect candidate for extending the analytical possibilities for

network order determination with powder X-ray and neutron diffraction. Additionally, $SrSi_2PN_5:Eu^{2+}$ and its analogues demonstrate an exciting approach to slightly modify luminescence properties by isolobal network tuning.

CHAPTER 6

Conclusions and Outlook

Finally, Chapter 6 draws final conclusions from the systematic experimental and analytical approach. It focuses on what can be learned from the pseudo-ternary Sr–(Si,P)–(O,N) diagram and how these findings can be used for future research. It summarizes the optical properties of Sr–(Si,P)–(O,N) networks and gives an outlook on future mixed-tetrahedral compounds and their syntheses.

1.5 References

(1) Gounder, R.; Iglesia, E. The Catalytic Diversity of Zeolites: Confinement and Solvation Effects within Voids of Molecular Dimensions. *Chem. Comm.* **2013**, *49* (34), 3491–3509. https://doi.org/10.1039/C3CC40731D.

(2) Venuto, P. B.; Landis, P. S. Organic Catalysis over Crystalline Aluminosilicates. *Advances in Catalysis* **1968**, *18* (C), 259–371. https://doi.org/10.1016/S0360-0564(08)60430-7.

(3) Yang, J.; Zheng, J.; Kang, X.; Teng, G.; Hu, L.; Tan, R.; Wang, K.; Song, X.; Xu, M.; Mu, S.; Pan, F. Tuning Structural Stability and Lithium-Storage Properties by *d*-Orbital Hybridization Substitution in Full Tetrahedron Li_2FeSiO_4 Nanocrystal. *Nano Energy* **2016**, *20*, 117–125. https://doi.org/10.1016/J.NANOEN.2015.12.004.

(4) Li, S.; Guo, J.; Ye, Z.; Zhao, X.; Wu, S.; Mi, J. X.; Wang, C. Z.; Gong, Z.; McDonald, M. J.; Zhu, Z.; Ho, K. M.; Yang, Y. Zero-Strain Na_2FeSiO_4 as Novel Cathode Material for Sodium-Ion Batteries. *ACS Appl. Mater. Interfaces* **2016**, *8* (27), 17233–17238. https://doi.org/10.1021/ACSAMI.6B03969/ASSET/IMAGES/LARGE/AM-2016-039694_0005.JPEG.

(5) Delmas, C.; Maccario, M.; Croguennec, L.; Le Cras, F.; Weill, F. Lithium Deintercalation in $LiFePO_4$ Nanoparticles via a Domino-Cascade Model. *Nat. Mat.* **2008**, *7* (8), 665–671. https://doi.org/10.1038/nmat2230.

(6) Barron, A.; Ignatiev, A.; Chen, X.; Wu, N.; Lu, Z.; Stanley, M.; Blackburn, J. L.; Svedruzic, D.; McDonald, T. J.; Kim, Y.-H.; King, P. W.; Heben, M. J.; Wang, P.; Kang, X. Hydrogen-Rich Boron-Containing Materials for Hydrogen Storage. *Dalt. Trans.* **2008**, No. 40, 5400–5413. https://doi.org/10.1039/B807162D.

(7) Schlieper, T.; Milius, W.; Schnick, W. Nitrido-Silicate. II [1]. Hochtemperatur-Synthesen Und Kristallstrukturen von $Sr_2Si_5N_8$ Und $Ba_2Si_5N_8$. *Z. Anorg. Allg. Chem.* **1995**, *621* (8), 1380–1384. https://doi.org/10.1002/zaac.19956210817.

(8) Xie, R.-J.; Hirosaki, N.; Li, H.-L.; Li, Y. Q.; Mitomo, M. Synthesis and Photoluminescence Properties of β-Sialon:Eu^{2+} ($Si_{6-z}Al_zO_zN_{8-z}$:Eu^{2+}): A Promising Green Oxynitride Phosphor for White Light-Emitting Diodes. *J. Electrochem. Soc.* **2007**, *154* (10), J314. https://doi.org/10.1149/1.2768289.

(9) Uheda, K.; Hirosaki, N.; Yamamoto, Y.; Naito, A.; Nakajima, T.; Yamamoto, H. Luminescence Properties of a Red Phosphor, $CaAlSiN_3$:Eu^{2+}, for White Light-Emitting Diodes. *Electrochem. Solid-State Lett.* **2006**, *9* (4), H22. https://doi.org/10.1149/1.2173192/XML.

(10) Pust, P.; Weiler, V.; Hecht, C.; Tücks, A.; Wochnik, A. S.; Henß, A.-K.; Wiechert, D.; Scheu, C.; Schmidt, P. J.; Schnick, W. Narrow-Band Red-Emitting $Sr[LiAl_3N_4]$:Eu^{2+} as a next-Generation LED-Phosphor Material. *Nat. Mater.* **2014**, *13* (9), 891–896. https://doi.org/10.1038/nmat4012.

(11) Hoerder, G. J.; Seibald, M.; Baumann, D.; Schröder, T.; Peschke, S.; Schmid, P. C.; Tyborski, T.; Pust, P.; Stoll, I.; Bergler, M.; Patzig, C.; Reißaus, S.; Krause, M.; Berthold,

L.; Höche, T.; Johrendt, D.; Huppertz, H. $Sr[Li_2Al_2O_2N_2]:Eu^{2+}$—A High Performance Red Phosphor to Brighten the Future. *Nat. Commun.* **2019**, *10* (1), 1824. https://doi.org/10.1038/s41467-019-09632-w.

(12) Wendl, S.; Mardazad, S.; Strobel, P.; Schmidt, P. J.; Schnick, W. HIP to Be Square: Simplifying Nitridophosphate Synthesis in a Hot Isostatic Press. *Angew. Chem. Int. Ed.* **2020**, *59*, 18240. https://doi.org/10.1002/ANGE.202008570.

(13) Eisenburger, L.; Oeckler, O.; Schnick, W. High-Pressure High-Temperature Synthesis of Mixed Nitridosilicatephosphates and Luminescence of $AESiP_3N_7:Eu^{2+}$ (*AE*=Sr, Ba). *Chem. Eur. J.* **2021**, *27* (13), 4461–4465. https://doi.org/10.1002/chem.202005495.

(14) Dialer, M.; Pointner, M. M.; Wandelt, S. L.; Strobel, P.; Schmidt, P. J.; Bayarjargal, L.; Winkler, B.; Schnick, W. Order and Disorder in Mixed (Si, P)–N Networks $Sr_2SiP_2N_6:Eu^{2+}$ and $Sr_5Si_2P_6N_{16}:Eu^{2+}$. *Adv. Opt. Mater.* **2023**, 2302668. https://doi.org/10.1002/adom.202302668.

(15) Stadler, F.; Oeckler, O.; Senker, J.; Höppe, H. A.; Kroll, P.; Schnick, W. $SrSi_6N_8$—A Reduced Nitridosilicate with a Si–Si Bond. *Angew. Chem. Int. Ed.* **2005**, *44* (4), 567–570. https://doi.org/10.1002/ANIE.200461633.

(16) Zhao, M.; Zhou, Y.; Molokeev, M. S.; Zhang, Q.; Liu, Q.; Xia, Z.; Zhao, M.; Liu, Q. L.; Xia, Z. G.; Zhou, Y. Y.; Zhang, Q. Y. Discovery of New Narrow-Band Phosphors with the UCr_4C_4-Related Type Structure by Alkali Cation Effect. *Adv. Opt. Mater.* **2019**, *7* (6), 1801631. https://doi.org/10.1002/ADOM.201801631.

(17) Wagatha, P.; Weiler, V.; Schmidt, P. J.; Schnick, W. Tailoring Emission Characteristics: Narrow-Band Red Luminescence from SLA to $CaBa[Li_2Al_6N_8]:Eu^{2+}$. *Chem. Mater.* **2018**, *30* (21), 7885–7891. https://doi.org/10.1021/ACS.CHEMMATER.8B03485/SUPPL_FILE/CM8B03485_SI_001.CIF.

(18) Takeda, T.; Hirosaki, N.; Funahshi, S.; Xie, R. J. Narrow-Band Green-Emitting Phosphor $Ba_2LiSi_7AlN_{12}:Eu^{2+}$ with High Thermal Stability Discovered by a Single Particle Diagnosis Approach. *Chem. Mater.* **2015**, *27* (17), 5892–5898. https://doi.org/10.1021/ACS.CHEMMATER.5B01464/SUPPL_FILE/CM5B01464_SI_002.CIF.

(19) Zeuner, M.; Pagano, S.; Schnick, W. Nitridosilicates and Oxonitridosilicates: From Ceramic Materials to Structural and Functional Diversity. *Angew. Chem. Int. Ed.* **2011**, *50* (34), 7754–7775. https://doi.org/10.1002/anie.201005755.

(20) Kloß, S. D.; Schnick, W. Nitridophosphates: A Success Story of Nitride Synthesis. *Angew. Chem. Int. Ed.* **2019**, *58* (24), 7933–7944.

(21) Walker, D.; Carpenter, M. A.; Hitch, C. M. Some Simplifications to Multianvil Devices for High Pressure Experiments. *Am. Mineral.* **1990**, *75*, 1020–1028.

(22) Rubie, D. C. Characterising the Sample Environment in Multianvil High-Pressure Experiments. *Phase Transitions* **1999**, *68* (3), 431–451. https://doi.org/10.1080/01411599908224526.

(23) Huppertz, H. Multianvil High-Pressure / High-Temperature Synthesis in Solid State Chemistry. *Z. Kristallogr. Cryst. Mater.* **2004**, *219* (6), 330–338. https://doi.org/10.1524/zkri.219.6.330.34633.

(24) Bertschler, E.; Niklaus, R.; Schnick, W. $Li_{12}P_3N_9$ with Non-Condensed $[P_3N_9]^{12-}$-Rings and Its High-Pressure Polymorph Li_4PN_3 with Infinite Chains of PN_4-Tetrahedra. *Chem. Eur. J.* **2017**, *23* (40), 9592–9599. https://doi.org/10.1002/chem.201700979.

(25) Mallmann, M.; Wendl, S.; Strobel, P.; Schmidt, P. J.; Schnick, W. $Sr_3P_3N_7$: Complementary Approach by Ammonothermal and High-Pressure Syntheses. *Chem. Eur. J.* **2020**, *26* (28), 6257–6263. https://doi.org/10.1002/chem.202000297.

(26) Marchuk, A.; Neudert, L.; Oeckler, O.; Schnick, W. $CaMg_2P_6O_3N_{10}$ – A Quinary Oxonitridophosphate with an Unprecedented Tetrahedra Network Structure Type. *Eur. J. Inorg. Chem.* **2014**, *2014* (21), 3427–3434. https://doi.org/10.1002/ejic.201402302.

(27) Brown, P. J.; Fox, A. G.; Maslen, E. N.; O'Keefe, M. A.; Willis, B. T. M. Intensity of Diffracted Intensities. In *International Tables for Crystallography Volume C: Mathematical, physical and chemical tables*; Prince, E., Ed.; Springer Netherlands: Dordrecht, 2004; p 554. https://doi.org/10.1107/97809553602060000600.

2

Order and Disorder in Mixed (Si,P)–N Networks

$Sr_2SiP_2N_6:Eu^{2+}$ and $Sr_5Si_2P_6N_{16}:Eu^{2+}$

Marwin Dialer, Monika M. Pointner, Sophia L. Wandelt, Philipp Strobel, Peter J. Schmidt, Lkhamsuren Bayarjargal, Björn Winkler, Wolfgang Schnick

ADVANCED OPTICAL MATERIALS, WILEY-VCH

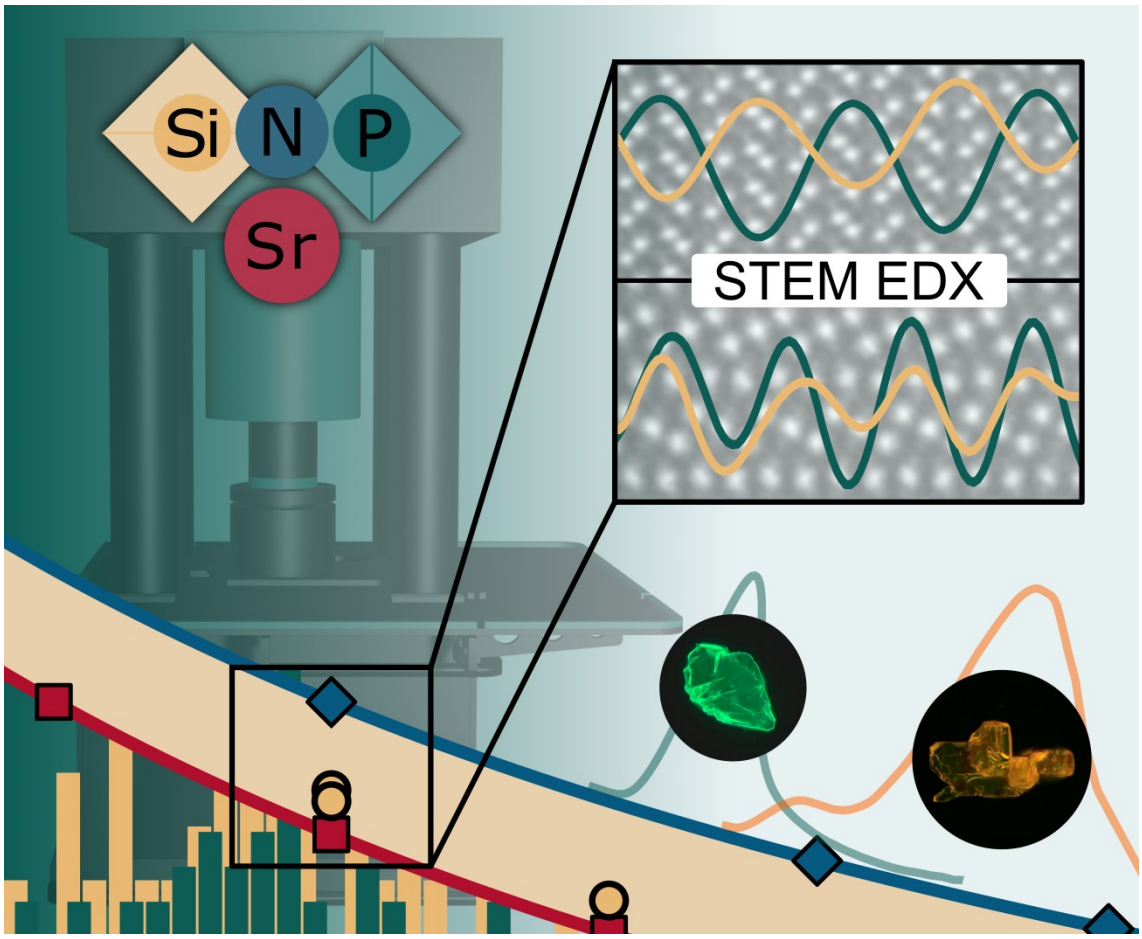

Reprinted (adapted) with permission from

Adv. Opt. Mater., **2023**, 2302668. https://doi.org/10.1002/adom.202302668.

ABSTRACT: In the field of nitride phosphors, which are crucial for phosphor-converted light-emitting diodes, mixed tetrahedral networks hold a significant position. With respect to the wide range of compositions, the largely unexplored (Si,P)–N networks are investigated as potential host structures. In this work, two highly condensed structures, namely $Sr_2SiP_2N_6$ and $Sr_5Si_2P_6N_{16}$ are reported to address the challenges that arise from the similarities of the network-forming cations Si^{4+} and P^{5+} in terms of charge, ionic radius, and atomic scattering factor, a multistep workflow is employed to elucidate their structure. Using single-crystal X-ray diffraction, energy-dispersive X-ray spectroscopy (EDX), atomic-resolution scanning transmission electron microscopy (STEM)-EDX maps, and straightforward crystallographic calculations, it is found that $Sr_2SiP_2N_6$ is the first ordered, and $Sr_5Si_2P_6N_{16}$ the first disordered, anionic tetrahedral (Si,P)–N network. After doping with Eu^{2+}, $Sr_2SiP_2N_6$:Eu^{2+} shows narrow cyan emission (λ_{max} = 506 nm, *fwhm* = 60 nm/2311 cm^{-1}), while for $Sr_5Si_2P_6N_{16}$:Eu^{2+} a broad emission with three maxima at 534, 662, and 745 nm upon irradiation with ultraviolet light is observed. An assignment of Sr sites as probable positions for Eu^{2+} and their relation to the emission bands of $Sr_5Si_2P_6N_{16}$:Eu^{2+} is discussed.

2.1 Introduction

Highly condensed (oxo-)nitride networks are known for their exceptional luminescence properties when doped with Eu^{2+} and convince with high quantum efficiency, low thermal quenching, as well as chemical and thermal stability.[1,2] These properties make them an essential element in commercially available phosphors used in phosphor-converted light-emitting diodes (pcLEDs). Prominent examples of such materials are β-sialon:Eu^{2+}, (Ca,Sr)[$AlSiN_3$]:Eu^{2+}, Sr[$LiAl_3N_4$]:Eu^{2+}, and Sr[$Li_2Al_2N_2O_2$]:Eu^{2+}, which all share a common feature, the presence of a mixed tetrahedral network.[3–6] In the development of novel host structures, multiple network-forming cations (*NFC*) offer significant advantages. First, by introduction of highly reactive compounds like Li_3N or Mg_3N_2, refractory inert binary nitrides can be activated, as has been shown for aluminum nitride or silicon nitride.[7–9] Second, it is possible to increase the condensation degree κ (Equation 1) and thus decrease the ratio between counter cations and *NFCs*, defined as the cation ratio *CR* (Equation 2). This is evident in the example of nitridosilicates, where κ_{max} is limited to a value of ¾ corresponding to pure Si_3N_4 (κ = 0.75). By adding Li_3N (κ = 3) or Mg_3N_2 (κ = 1.5) we can achieve higher values for the degree of condensation, as demonstrated for Sr[$Li_2Si_2N_4$]:Eu^{2+} and Sr[Mg_3SiN_4]:Eu^{2+} (κ = 1).[10,11] This is advantageous for achieving narrow emission bands which correlates with the condensation degree and thus the rigidity of a network. However, the main advantage of mixed networks is their wide range of compositions. This diversity is crucial, as significant

changes in luminescence properties often require a complete redesign of the host structure. This led us to investigate mixed (Si,P)–N networks, as the compound classes *AE*–Si–N and *AE*–P–N (*AE* = Ca, Sr, Ba) have the most representatives among ternary nitrides. This variety suggests that their combination yields numerous compounds with new structures and luminescent properties worth investigating. This can be illustrated by plotting the cation ratio *CR*, as defined by Pritzl et al., against the condensation degree κ for known compounds (Figure 2.1).[12]

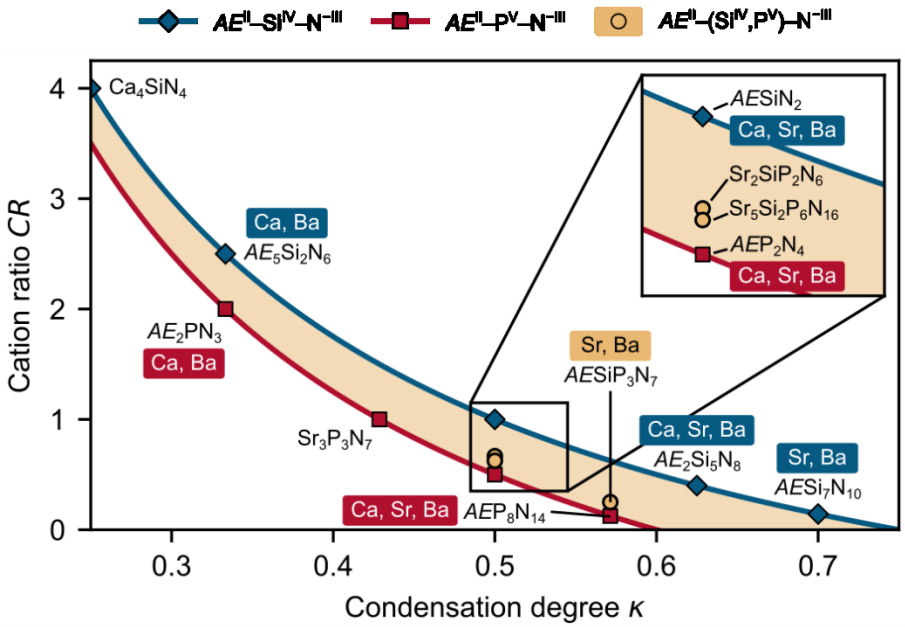

Figure 2.1 Graphical representation of the cation ratio *CR* versus the condensation degree κ for the ternary compound classes *AE*–Si–N (blue) and *AE*–P–N (red), as well as for quaternary *AE*–(Si,P)–N (beige) as the region between both curves (*AE* = Ca, Sr, Ba). All literature known compounds, including the new compounds $Sr_2SiP_2N_6$ and $Sr_5Si_2P_6N_{16}$ are marked as symbols. For a full list refer to Table 7.2. The expanded view in the inset shows all compounds with κ = 0.5, differing in *CR*.

$$\kappa = \frac{N(NFC)}{N(LIG)} \qquad (1) \qquad\qquad CR = \frac{N(CC)}{N(NFC)} \qquad (2)$$

where *N* is the count, *NFC* is the network-forming cation (Si,P), *LIG* is the ligand (N), and *CC* is the counter cation (Ca, Sr, Ba).

Mathematical transformations reveal the analytical relationship between the two parameters with respect to the oxidation states (*Ox*):

$$CR(\kappa) = -\frac{Ox(LIG)}{Ox(CC)} \cdot \frac{1}{\kappa} - \frac{Ox(NFC)}{Ox(CC)} \qquad (3)$$

More details about the mathematical derivation can be found in the section 7.2. While all ternary nitrides align with respective hyperbolic curves (blue and red), quaternary *AE*–(Si,P)–N can span the full region (beige) between both curves. For the latter, *Ox*(*NFC*) depends on the percentage composition of (Si,P) that is *CR*(κ) can vary between the edge cases *Ox*(Si) = 4 and *Ox*(P) = 5. To date, this compositional space remains largely unexplored, with only one representative, namely *AE*SiP_3N_7 (*AE* = Sr, Ba).[13] The challenging synthesis, either requiring NH_4F assisted high-pressure high-temperature conditions or molecular precursors, explains this uncharted territory. The crystallochemical similarities of Si^{4+} and P^{5+}, in terms of charge, ionic radius, and atomic scattering factor, complicate structure elucidation.[14,15] This is also the reason why Eisenburger et al. employed scanning transmission electron microscopy (STEM) to determine the partially ordered nature of their network. There are other related (Si,P)–N compounds, such as the disordered wurtzite type $SiPN_3$, or SiP_2N_4NH and *AE*$Si_3P_4N_{10}(NH)_2$ (*AE* = Mg, Ca, Sr), where Si occupies octahedra and P tetrahedra.[16–18] However, there are no reports of ordered and disordered (Si,P)–N networks in which Si and P form an anionic, tetrahedral network. Consequently, we introduce $Sr_2SiP_2N_6$ as the first ordered and $Sr_5Si_2P_6N_{16}$ as the first disordered representatives of anionic (Si,P)–N networks in this study, respectively.

2.2 Results and Discussion

2.2.1 Synthesis

Both compounds $Sr_2SiP_2N_6$ and $Sr_5Si_2P_6N_{16}$ were prepared via the azide route at 3 GPa and 1400 °C in a multianvil press starting from $Sr(N_3)_2$, amorphous Si_3N_4, and α-P_3N_5. For luminescence experiments, we added 1–3 mol.% EuN with respect to Sr^{2+}. Due to their similar compositions, the products typically occur as microcrystalline powder mixtures, distinguishable by their crystal shape and luminescence (Figure 7.1 and Figure 7.2). The products, like many highly condensed nitrides ($\kappa \geq 0.5$), are stable toward moisture and air.

2.2.2 Structure Elucidation

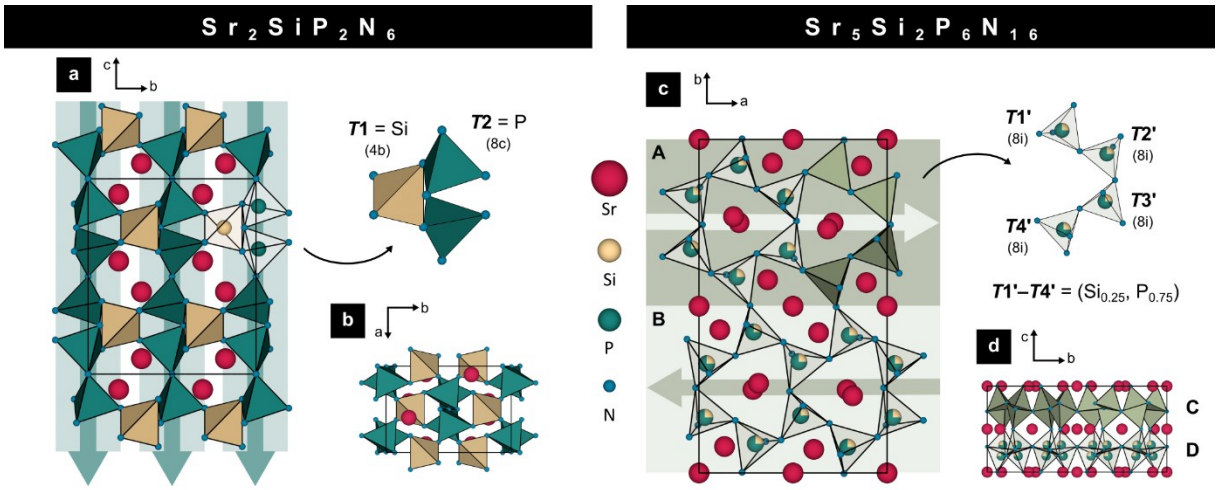

Figure 2.2 Crystal structure of $Sr_2SiP_2N_6$ in a) [100] and b) [001] showing an ordered tetrahedral network of P (*T*2, green) single chains which are cross-linked by Si (*T*1, yellow) tetrahedra. The crystal structure of $Sr_5Si_2P_6N_{16}$ in c) [001] shows alternating double-chains along [010] in ABAB sequence. The tetrahedra *T*1'–*T*4' are occupied by ($Si_{0.25}$,$P_{0.75}$) building a disordered network. In d) the ABAB layers are stacked along [001] in CDCD sequence with D being the inverse of C.

The similarities between Si and P make the structure elucidation a multistep process when both occupy the same sites in the crystal. Therefore, it is difficult to determine the network based on single-crystal X-ray diffraction data alone. The same applies to O and N as ligands. Even though we did not include oxygen, potential contamination by diffusion in a multianvil press needs to be considered. We followed a four-step workflow: 1) Determination of a preliminary structure model from single-crystal X-ray data of the form $Sr_x(Si,P)_y(N,O)_z$. 2) Determination of the chemical composition by measuring EDX on flat single-crystal surfaces. 3) Determination of tetrahedral occupancies by STEM-EDX. 4) Finalization of the structure

model by implementing occupational results from steps (2) and (3). $Sr_2SiP_2N_6$ crystallizes in the structure type of $K_2ZnSi_2O_6$ in the non-centrosymmetric space group $C222_1$ (no. 20) with a = 6.0849(1), b = 8.8203(2), c = 10.2500(2) Å, and Flack parameter x = −0.017(6).[19,20] Further crystallographic data are given in Table 7.3–Table 7.5. We confirmed the absence of centrosymmetry by measuring the second harmonic generation (SHG) intensities on a powder sample with grain sizes below 30 µm. The value of 31(11) mV is comparable to that of quartz with 24(4) mV (< 5 µm). The preliminary empirical formula from single-crystal X-ray data was $Sr_2(Si,P)_3(N,O)_6$. Single-crystal EDX measurements, averaged over ten points, gave a composition of Sr 18(1), Si 11(1), P 18(1), N 51(1), and O 3(1) at%, corresponding to a refined empirical formula $Sr_2Si_{1+x}P_{2-x}N_{6-x}O_x$ ($x \approx 0.1$). Given the isoelectronic relationship between Si–O and P–N, we consider oxygen impurities to this extent to be entropy-driven and hardly avoidable in a multianvil press, justifying the idealized sum formula of $Sr_2SiP_2N_6$. The structure itself consists of a highly condensed network of Q^4 tetrahedra with condensation degree κ = 0.5 (Figure 2.2). $T2$ tetrahedra (green) form single chains along [001], with all chains being cross-linked by $T1$ tetrahedra (yellow). The Sr^{2+} ions occupy a single crystallographic site with (6+3)-fold coordination through N^{3-} which can be described as a distorted tricapped trigonal prism (Johnson body 51) with a volume of V = 42.4 Å^3.[21] To determine the occupancy of $T1$ and $T2$ sites, we used scanning transmission electron microscopy on an atomic scale. In the first step, we oriented the crystal along a crystallographic axis in which we could study the tetrahedral Wyckoff positions separately, for $Sr_2SiP_2N_6$ this was the direction [100]. In the second step, we chose an area scan to measure a two-dimensional EDX map as highlighted in yellow in Figure 2.3. By integration over the EDX signal, we obtained a sinusoid where each maximum indicates the presence of the corresponding element at that position. For $Sr_2SiP_2N_6$, the signals of Si and P oscillate out of phase, which means that Si is only present when P is not and vice versa. It was possible to assign the tetrahedral positions $T1$ = Si^{4+} and $T2$ = P^{5+} and refine a final structure model, where $Sr_2SiP_2N_6$ comprises the first ordered (Si,P)–N network. We were able to corroborate the structure model by Raman spectroscopy, where the simulated spectrum shows very good agreement with the experimental spectrum (Figure 7.8). For the second compound $Sr_5Si_2P_6N_{16}$, the same workflow was chosen. Single-crystal X-ray diffraction data yielded a preliminary formula $Sr_5(Si,P)_8(N,O)_{16}$ and, in combination with EDX measurements, an experimental sum formula of $Sr_5Si_{2+x}P_{6-x}N_{16-x}O_x$ with $x \approx 0.7$ (Sr 18(1), Si 10(1), P 19(1), N 48(1), and O 4(1) at%). It crystallizes in the centrosymmetric space group

Pbam (no. 55) with lattice parameters a = 9.9136(2), b = 17.5676(3), and c = 8.39680(10) Å.[20] Further crystallographic data are given in Table 7.3, Table 7.6, and Table 7.7. In agreement with Liebau's classification of silicates, the fundamental building block of this network is best described as an unbranched double chain along [100] comprising four distinct tetrahedral positions *T*1'–*T*4' (Figure 2.2).[22] These double chains alternate along [010] in A–B–A–B sequence. The layers repeat along [001] in C–D–C– D sequence, forming a complex three-dimensional network of Q^4 tetrahedra with condensation degree κ = 0.5, analogous to $Sr_2SiP_2N_6$. Unlike in $Sr_2SiP_2N_6$, the Sr^{2+} ions in $Sr_5Si_2P_6N_{16}$ occupy not one but six crystallographic sites, which differ considerably in terms of coordination and polyhedral volume (*CN* = 6–13, *V* = 18.3–68.5 Å^3). Coordination polyhedra were determined using the Charge Distribution method.[23] Tetrahedral occupancies were further investigated for this network using atomic resolution STEM-EDX. In the case of $Sr_5Si_2P_6N_{16}$, the available viewing direction [101] did not match an ideal viewing direction, e.g., [001]. That means, we examined the tetrahedral sites in doublets of *T*1'+*T*4' and *T*2'+*T*3' rather than individually. This can be attributed to both the sample, e.g., preferred crystal orientations and textures, and constraints of the setup, e.g., limited rotational degrees of freedom. We measured two separate STEM-EDX area scans for both doublets, highlighted in yellow (*T*2'+*T*3') and red (*T*1'+*T*4') in Figure 2.3.

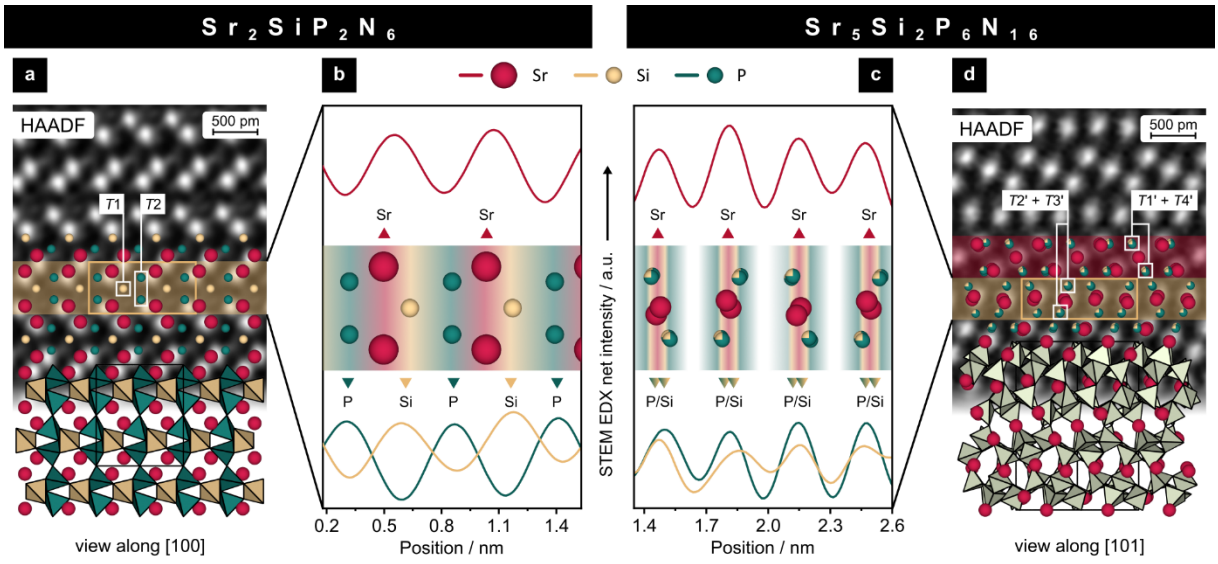

Figure 2.3 STEM high-angle annular dark-field (HAADF) images with structure overlay of a) $Sr_2SiP_2N_6$ and d) $Sr_5Si_2P_6N_{16}$. STEM-EDX area scans are highlighted in yellow. For the area scan highlighted in red, please refer to Figure 7.3. The integrated EDX signals of the area scans show out of phase oscillation of the Si (yellow) and P (green) signals for b) $Sr_2SiP_2N_6$ and in-phase oscillation for c) $Sr_5Si_2P_6N_{16}$, indicating an ordered network for $Sr_2SiP_2N_6$ and ruling out an ordered network for $Sr_5Si_2P_6N_{16}$. The Sr (red) EDX signal serves as a position reference.

They show in-phase EDX signals for Si and P in both cases, suggesting that the (Si,P)–N network is not ordered. This becomes clear when we consider the Si:P ratio of 1:3 in $Sr_5Si_2P_6N_{16}$ and the four available tetrahedral sites. Only one doublet would show a Si signal regardless of the ordering variant. Only an undetected superstructure would show similar signals, for which there is no evidence on the precession images (Figure 7.9). Nevertheless, the absence of order is not proof of disorder in a network. Eisenburger et al. recently reported a highly condensed (Si,P)–N network with partial order in $AESiP_3N_7$ (*AE* = Sr, Ba), where *T*1* is fully occupied by P and *T*2* by $(Si_{0.5},P_{0.5})$.[13] Based on our STEM-EDX data, it is not possible to distinguish the disordered from the partially ordered network since the EDX signal of Si and P can only be evaluated qualitatively.

2.2.3 Low-Cost Crystallographic Calculations

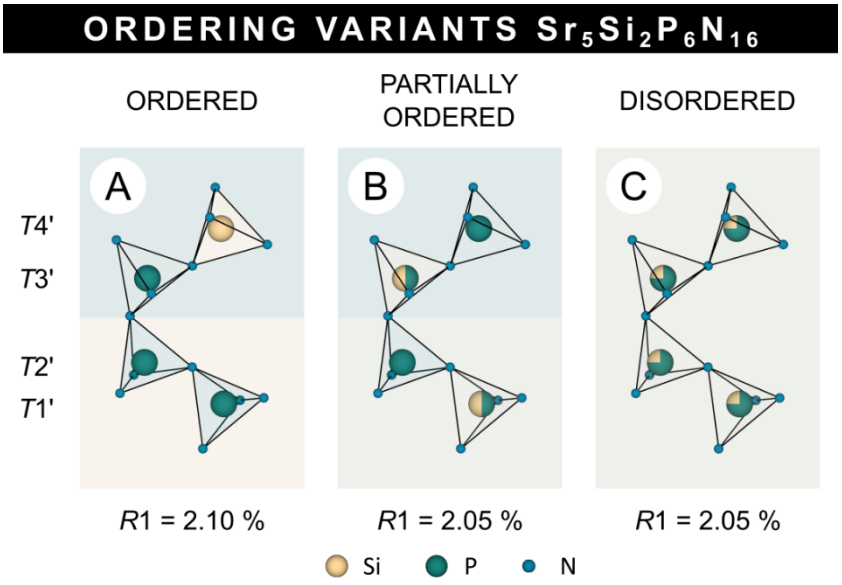

Figure 2.4 Figure 2.5 Ordering variants of $Sr_5Si_2P_6N_{16}$ with A) full ordering, B) partial ordering, and C) disordering of all tetrahedral sites *T*1'–*T*4'. The refinements yield very similar R1 values for all cases.

To determine the tetrahedral occupancies of $Sr_5Si_2P_6N_{16}$, we analyzed the ordered (A), partially ordered (B), and disordered (C) network variants () by low-cost crystallographic calculations. After refining each variant based on the single-crystal X-ray data, we calculated the Ewald site energies, charge distributions (CHARDI), bond valence sums (BVS), polyhedral volumes, and distances of all crystallographic (Si,P)–N sites.[24–30] Since there were insufficient reference data for mixed (Si,P)–N networks, the idea was that we could calculate expected values from

literature data of pure Si–N and P–N networks, proportional to their percentage composition. As an example, the volume of a ($Si_{0.25}$,$P_{0.75}$)–N_4 tetrahedron is calculated as:

$$\langle V\rangle((Si_{0.25}, P_{0.75})-N_4) = 0.25 \cdot \overline{V}(Si-N_4) + 0.75 \cdot \overline{V}(P-N_4) \qquad (4)$$

where ⟨V⟩ is the expected volume and $\overline{V}$ is the average volume calculated from literature.

The expected values can be used to calculate the percentage deviation of the different ordering variants for each method. In this way, the variant with the lowest mean percentage deviation is the most probable. This approach is based on several assumptions: 1) All structure models used are of sufficiently good quality, since all methods depend strongly on interatomic distances. 2) All networks are predominantly ionic, justifying the use of point charge concepts such as Ewald summation and CHARDI. 3) Our (Si,P)–N networks can be described as a combination of Si–N and P–N networks and, therefore, allow for the definition of expected values. 4) The differences in charge, size, and atomic scattering factor of Si^{4+} and P^{5+} lead to significant structural changes observable by single-crystal X-ray diffraction. Based on these assumptions, an appropriate group of literature compounds was selected. A full list is found in Table 7.1. The results of all methods and ordering variants of $Sr_5Si_2P_6N_{16}$ are shown in Figure 2.6. The disordered variant (C) showed the lowest mean deviation *D* of 1.0 %, followed by the partially ordered variant (B) with 3.3 % and the ordered variant (A) with 5.2 %. This is consistent with the results from STEM-EDX, where (A) has already been excluded. The deviations from both (B) and (C) are within the range of literature compounds, but *D*(B) more than triples compared to *D*(C) despite comparatively small changes in the tetrahedral composition. Furthermore, not only does the mean deviation increase from (C) to (B), but all individual methods show the same trend. Although partial ordering was observed in *AE*SiP_3N_7 (*AE* = Sr, Ba), most compounds exhibit either ordered or disordered networks, supporting the need to consider partial ordering without overestimating its probability. Based on our data, we claim, that $Sr_5Si_2P_6N_{16}$ is the first anionic, disordered (Si,P)–N network. For completeness, we also analyzed plausible ordering variants of the other compound $Sr_2SiP_2N_6$ by crystallographic calculations. Here, the ordered variant showed the smallest mean deviation of 1.1 %, while the partially ordered variant (*D* = 8.5 %) and disordered variant (*D* = 5.5 %) were considerably less congruent (Figure 7.10 and Figure 7.11). This is in line with our STEM-EDX experiment that has already confirmed the ordered nature of the (Si,P)–N network in $Sr_2SiP_2N_6$.

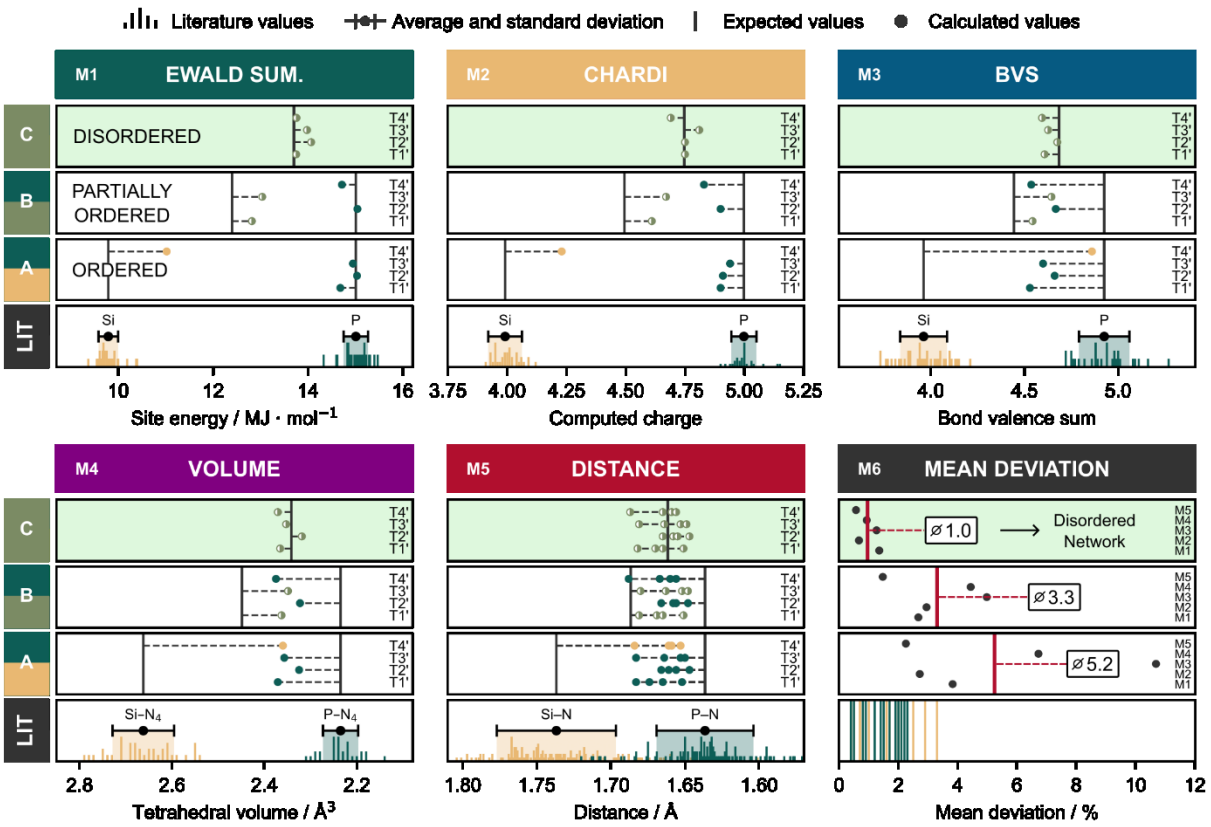

Figure 2.6 Comparison of all ordering variants (A)–(C) of $Sr_5Si_2P_6N_{16}$ by low-cost crystallographic calculations that is Ewald site energies, CHARDI, BVS, tetrahedral volumes, and distances. For each method, we considered the occupation of all tetrahedral positions T1'–T4' separately, with Si (yellow), P (green), and mixed (Si,P) (olive green). The ordering variant with the lowest mean percentage deviation from the expected values that were calculated from literature (LIT) gives the most probable solution. LIT values are given in relative frequency.

2.2.4 Luminescence

After doping with Eu^{2+}, $Sr_2SiP_2N_6:Eu^{2+}$ and $Sr_5Si_2P_6N_{16}:Eu^{2+}$, show cyan and orange luminescence upon irradiation with ultraviolet light, respectively. We measured the photoluminescence (PL) and photoluminescence excitation spectra (PLE, Figure 2.7a) on individual particles (Figure 2.8). $Sr_2SiP_2N_6:Eu^{2+}$ emits in the cyan region with a maximum at 506 nm (*M*1) and a full width at half-maximum *fwhm* = 60 nm/2311 cm^{-1}. The narrow emission is consistent with only one Sr site available for doping by Eu^{2+}. In contrast, we observe a broad emission in the PL spectrum of $Sr_5Si_2P_6N_{16}:Eu^{2+}$ starting at ≈500 nm and extending over the entire spectral range with three maxima at 534 (*M*2), 662 (*M*3, *fwhm* = 110 nm/2501 cm^{-1}), and 745 nm (*M*4). This indicates multiple distinct activator environments and is consistent with the six chemically different Sr sites in $Sr_5Si_2P_6N_{16}:Eu^{2+}$. In principle, all sites are suitable for Eu^{2+}-doping with respect to their volume V = 18.3–68.5 $Å^3$.[4,31] Reliable assignment of Sr sites to emission bands is possible only with theoretical calculations of the

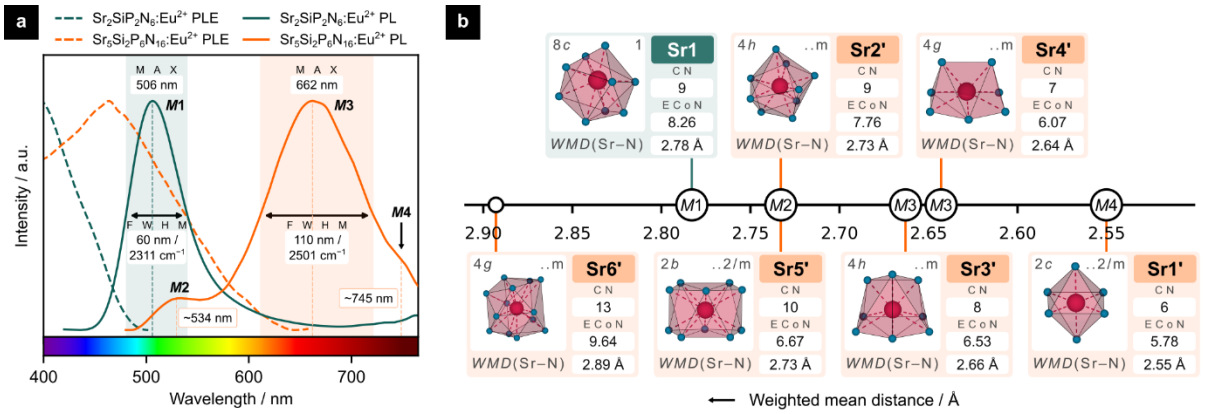

Figure 2.7 a) Photoluminescence excitation (PLE, dashed) and photoluminescence (PL, solid) spectra of $Sr_2SiP_2N_6:Eu^{2+}$ (green) and $Sr_5Si_2P_6N_{16}:Eu^{2+}$ (orange). $Sr_2SiP_2N_6:Eu^{2+}$ shows an emission maximum (*M*1) at 506 nm. $Sr_5Si_2P_6N_{16}:Eu^{2+}$ has three emission bands at 534 (*M*2), 662 (*M*3), and 745 nm (*M*4). We smoothed the data with a Gaussian filter (σ = 2). Unfiltered spectra are provided in Figure 7.12. b) Comparison of the coordination environment of possible activator sites with respect to their weighted mean Sr–N distances (*WMD*).

crystal fields and excited states of Eu^{2+} ($4f^6 5d^1$).[32] Nevertheless, a comparison of the Sr sites in terms of their weighted mean Sr–N distances (*WMD*(Sr–N)), effective coordination numbers (*ECoN*), and site symmetries can contribute to a better understanding of such a spectrum.[23,26] We expect that the smaller *WMD*(Sr–N) or the higher *ECoN*, the larger the Stokes shift, which is due to the stronger splitting of the ligand field. In contrast, the higher the site symmetry, the smaller the Stokes shift, because higher symmetry means fewer degrees of freedom for structural relaxation. With this in mind, we divided Sr1'–Sr6' into four groups to assign them to maxima *M*2–*M*4: 1) Sr6' does not contribute to any of the visible maxima. We argue that due to the largest weighted mean distance *WMD*(Sr6'–N) = 2.89 Å and *ECoN* = 9.64 its emission should be expected in the blue region. Therefore, its absence can be explained by the chosen excitation wavelength (λ_{exc} = 460 nm), which is too large. 2) Sr2' and Sr5' were assigned to maximum *M*2 because they have significantly larger environments (*WMD*(Sr2'–N) = *WMD*(Sr5'– N) = 2.73 Å, *ECoN*(Sr2') = 7.76, *ECoN*(Sr5') = 6.67) than Sr3' and Sr4' (*WMD*(Sr3'–N) = 2.66, *WMD*(Sr4'–N) = 2.64 Å, *ECoN*(Sr3') = 6.53, *ECoN*(Sr4') = 6.07). We expect additional splitting of *M*2 despite the identical weighted mean distances since Sr5' has a lower effective coordination number and higher symmetry than Sr2', two factors that will reduce the Stokes shift. However, due to the low intensity of *M*2, which we attribute to reabsorption effects and poor excitation at 460 nm, no further conclusions were drawn from the spectrum. 3) The gradual slope of *M*3 suggests a superposition of several similar emission maxima. This fits well with Sr3' and Sr4' which have similar *WMD* and *ECoN* values (*WMD*(Sr3'–N) = 2.66, *WMD*(Sr4'–N) = 2.64 *Å*, *ECoN*(Sr3') = 6.53, *ECoN*(Sr4') = 6.07) as well as the same site symmetry. 4) Sr1'

has the smallest coordination environment with *WMD*(Sr1'–N)=2.55 and *ECoN* =5.78, significantly smaller than those of Sr3' and Sr4'. Despite the higher site symmetry of 2/m, we expect for Sr1' the strongest Stokes shift that yields *M*4.

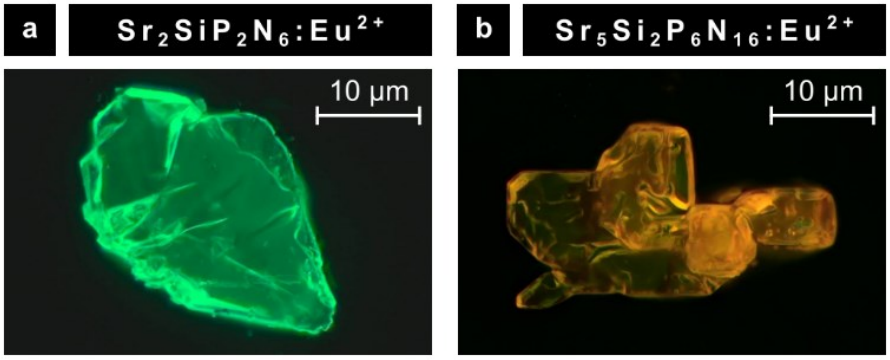

Figure 2.8 Luminescence micrographs of individual particles of a) $Sr_2SiP_2N_6:Eu^{2+}$ and b) $Sr_5Si_2P_6N_{16}:Eu^{2+}$, excited at 395 nm.

2.3 Conclusion

We successfully synthesized two novel strontium nitridosilicate phosphates, namely $Sr_2SiP_2N_6$ and $Sr_5Si_2P_6N_{16}$, via the azide route at 3 GPa and 1400 °C in a multianvil press. Using a four-step workflow adapted to mixed tetrahedral networks, we identified the structure of $Sr_2SiP_2N_6$, which reveals an unprecedented ordered (Si,P)–N network. The second compound, $Sr_5Si_2P_6N_{16}$, presented more challenges. Combining STEM-EDX data with low-cost crystallographic calculations provided evidence for a disordered (Si,P)–N network, which is the first of its kind to be reported. We introduced the dopant Eu^{2+} into both compounds to investigate their luminescence properties. $Sr_2SiP_2N_6:Eu^{2+}$ shows a narrow emission in the cyan region at 506 nm (*fwhm* = 60 nm/2311 cm^{-1}), consistent with the structure having only one Sr site available for Eu^{2+} doping. $Sr_5Si_2P_6N_{16}:Eu^{2+}$ shows a broad emission with three maxima at 534, 662, and 745 nm, where we suggested an assignment of Sr sites to the emission bands. In summary, our research represents a significant advance in the understanding of mixed (Si,P)–N networks, as we have been able to demonstrate their variability in two examples. Despite the same condensation degree and very similar stoichiometries, both compounds exhibit fundamentally different structures and luminescence properties, ranging from cyan to orange. Future investigations should further explore the compositional space of mixed networks with similar network-forming cations, e.g., (Si,P), (Al,Si), or (Mg,Si), especially with respect to their luminescence properties.

2.4 Acknowledgements

The authors gratefully thank Christian Minke (Department of Chemistry, LMU Munich) for the EDX measurements and SEM images. Massimo Nespolo (CRM, Université de Lorraine) and Corrado Cuocci (Institute of Crystallography, CNR) deserve thanks for their support with the CHARDI-2015 and EXPO2014 programs. M.D. also thanks the Bundesministerium für Bildung und Forschung (BMBF) for financial support. Open access funding enabled and organized by Projekt DEAL.

2.5 References

(1) Li, S.; Xie, R.-J.; Takeda, T.; Hirosaki, N. Critical Review—Narrow-Band Nitride Phosphors for Wide Color-Gamut White LED Backlighting. *ECS J. Solid State Sci. Technol.* **2017**, *7* (1), R3064. https://doi.org/10.1149/2.0051801JSS.

(2) Xie, R.-J.; Hirosaki, N. Silicon-Based Oxynitride and Nitride Phosphors for White LEDs—A Review. *Sci. Technol. Adv. Mater.* **2007**, *8* (7–8), 588. https://doi.org/10.1016/j.stam.2007.08.005.

(3) Xie, R.-J.; Hirosaki, N.; Li, H.-L.; Li, Y. Q.; Mitomo, M. Synthesis and Photoluminescence Properties of β-Sialon:Eu^{2+} ($Si_{6-z}Al_zO_zN_{8-z}$:Eu^{2+}): A Promising Green Oxynitride Phosphor for White Light-Emitting Diodes. *J. Electrochem. Soc.* **2007**, *154* (10), J314. https://doi.org/10.1149/1.2768289.

(4) Uheda, K.; Hirosaki, N.; Yamamoto, Y.; Naito, A.; Nakajima, T.; Yamamoto, H. Luminescence Properties of a Red Phosphor, $CaAlSiN_3$:Eu^{2+}, for White Light-Emitting Diodes. *Electrochem. Solid-State Lett.* **2006**, *9* (4), H22. https://doi.org/10.1149/1.2173192/XML.

(5) Pust, P.; Weiler, V.; Hecht, C.; Tücks, A.; Wochnik, A. S.; Henß, A.-K.; Wiechert, D.; Scheu, C.; Schmidt, P. J.; Schnick, W. Narrow-Band Red-Emitting $Sr[LiAl_3N_4]$:Eu^{2+} as a next-Generation LED-Phosphor Material. *Nat. Mater.* **2014**, *13* (9), 891–896. https://doi.org/10.1038/nmat4012.

(6) Hoerder, G. J.; Seibald, M.; Baumann, D.; Schröder, T.; Peschke, S.; Schmid, P. C.; Tyborski, T.; Pust, P.; Stoll, I.; Bergler, M.; Patzig, C.; Reißaus, S.; Krause, M.; Berthold, L.; Höche, T.; Johrendt, D.; Huppertz, H. $Sr[Li_2Al_2O_2N_2]$:Eu^{2+}—A High Performance Red Phosphor to Brighten the Future. *Nat. Commun.* **2019**, *10* (1), 1824. https://doi.org/10.1038/s41467-019-09632-w.

(7) Pust, P.; Pagano, S.; Schnick, W. $Ca[LiAlN_2]$: A Quaternary Nitridoaluminate. *Eur. J. Inorg. Chem.* **2013**, *7* (7), 1157. https://doi.org/10.1002/ejic.201201283.

(8) Wagatha, P.; Weiler, V.; Schmidt, P. J.; Schnick, W. Tunable Red Luminescence in Nitridomagnesoaluminates α-$Sr_2[MgAl_5N_7]$:Eu^{2+}, β-$Sr_2[MgAl_5N_7]$:Eu^{2+}, and

$Sr_8[LiMg_2Al_{21}N_{28}]:Eu^{2+}$. *Chem. Mater.* **2018**, *30* (5), 1755. https://doi.org/10.1021/acs.chemmater.8b00106.

(9) Pust, P.; Wochnik, A. S.; Baumann, E.; Schmidt, P. J.; Wiechert, D.; Scheu, C.; Schnick, W. $Ca[LiAl_3N_4]:Eu^{2+}$-A Narrow-Band Red-Emitting Nitridolithoaluminate. *Chem. Mater.* **2014**, *26* (11), 3544. https://doi.org/10.1021/CM501162N/SUPPL_FILE/CM501162N_SI_001.CIF.

(10) Wu, Q.; Li, Y.; Wang, C.; Luo, J. $Li_2SrSi_2N_4:Eu^{2+}$: Electronic Structure and Luminescence of a Red Phosphor. *J. Lumin.* **2018**, *201*, 485. https://doi.org/10.1016/J.JLUMIN.2018.05.038.

(11) Schmiechen, S.; Schneider, H.; Wagatha, P.; Hecht, C.; Schmidt, P. J.; Schnick, W. Toward New Phosphors for Application in Illumination-Grade White Pc-LEDs: The Nitridomagnesosilicates $Ca[Mg_3SiN_4]:Ce^{3+}$, $Sr[Mg_3SiN_4]:Eu^{2+}$, and $Eu[Mg_3SiN_4]$. *Chem. Mater.* **2014**, *26* (8), 2712–2719. https://doi.org/10.1021/cm500610v.

(12) Pritzl, R. M.; Prinz, N.; Strobel, P.; Schmidt, P. J.; Johrendt, D.; Schnick, W. From Framework to Layers Driven by Pressure – The Monophyllo-Oxonitridophosphate β-$MgSrP_3N_5O_2$ and Comparison to Its α-Polymorph. *Chem. Eur. J.* **2023**, *29* (41), e202301218. https://doi.org/10.1002/chem.202301218.

(13) Eisenburger, L.; Oeckler, O.; Schnick, W. High-Pressure High-Temperature Synthesis of Mixed Nitridosilicatephosphates and Luminescence of $AESiP_3N_7:Eu^{2+}$ (*AE*=Sr, Ba). *Chem. Eur. J.* **2021**, *27* (13), 4461–4465. https://doi.org/10.1002/chem.202005495.

(14) Shannon, R. D. Revised Effective Ionic Radii and Systematic Studies of Interatomie Distances in Halides and Chaleogenides. *Acta Crystallogr. Sect. A* **1976**, *32*, 751.

(15) Brown, P. J.; Fox, A. G.; Maslen, E. N.; O'Keefe, M. A.; Willis, B. T. M. Intensity of Diffracted Intensities. In *International Tables for Crystallography Volume C: Mathematical, physical and chemical tables*; Prince, E., Ed.; Springer Netherlands: Dordrecht, 2004; p 554. https://doi.org/10.1107/97809553602060000600.

(16) Baldus, H. P.; Schnick, W.; Lücke, J.; Wannagat, U.; Bogedain, G. Silicon Phosphorus Nitride, the First Ternary Compound in the Silicon-Phosphorus-Nitrogen System. *Chem. Mater.* **1993**, *5* (6), 845–850. https://doi.org/https://doi.org/10.1021/cm00030a021.

(17) Vogel, S.; Buda, A. T.; Schnick, W. Rivalry under Pressure: The Coexistence of Ambient-Pressure Motifs and Close-Packing in Silicon Phosphorus Nitride Imide SiP_2N_4NH. *Angew. Chem. Int. Ed.* **2019**, *58* (11), 3398. https://doi.org/10.1002/ANIE.201813789.

(18) Eisenburger, L.; Strobel, P.; Schmidt, P. J.; Bräuniger, T.; Wright, J.; Bright, E. L.; Giacobbe, C.; Oeckler, O.; Schnick, W. Nitridic Analogs of Micas $AESi_3P_4N_{10}(NH)_2$ (*AE*=Mg, $Mg_{0.94}Ca_{0.06}$, Ca, Sr). *Angew. Chem. Int. Ed.* **2022**, *61* (4), e202114902. https://doi.org/10.1002/anie.202114902.

(19) Hogrefe, A. R.; Czank, M. Synthetic Dipotassium Zinc Disilicate. *Acta Crystallogr.* **1995**, *51* (9), 1728. https://doi.org/10.1107/S0108270195003052.

(20) Deposition Numbers and contain the supplementary crystallographic data for this paper. These data are provided free of charge by the joint Cambridge Crystallographic Data Centre and Fachinformationszentrum Karlsruhe Access Structures service.

(21) Johnson, N. W. Convex Polyhedra with Regular Faces. *Can. J. Math.* **1966**, *18*, 169. https://doi.org/10.4153/CJM-1966-021-8.

(22) Liebau, F. Bemerkungen Zur Systematik Der Kristallstrukturen von Silikaten Mit Hochkondensierten Anionen. *Z. Phys. Chem.* **1956**, *206O* (1), 73–92. https://doi.org/10.1515/ZPCH-1956-20607.

(23) Hoppe, R. Effective Coordination Numbers (ECoN) and Mean Fictive Ionic Radii (MEFIR). *Z. Kristallogr. Cryst. Mater.* **1979**, *150* (1–4), 23–52. https://doi.org/10.1524/zkri.1979.150.14.23.

(24) Toukmaji, A. Y.; Board, J. A. Ewald Summation Techniques in Perspective: A Survey. *Comput. Phys. Commun.* **1996**, *95*, 73–92.

(25) Nespolo, M. Charge Distribution as a Tool to Investigate Structural Details. IV. A New Route to Heteroligand Polyhedra. *Acta Crystallogr. Sect. B* **2016**, *72* (1), 51–66. https://doi.org/10.1107/S2052520615019472.

(26) Nespolo, M.; Guillot, B. *CHARDI2015*: Charge Distribution Analysis of Non-Molecular Structures. *J. Appl. Crystallogr.* **2016**, *49* (1), 317–321. https://doi.org/10.1107/S1600576715024814.

(27) Altomare, A.; Cuocci, C.; Giacovazzo, C.; Moliterni, A.; Rizzi, R.; Corriero, N.; Falcicchio, A. *EXPO2013*: A Kit of Tools for Phasing Crystal Structures from Powder Data. *J. Appl. Crystallogr.* **2013**, *46* (4), 1231–1235. https://doi.org/10.1107/S0021889813013113.

(28) Momma, K.; Izumi, F. *VESTA 3* for Three-Dimensional Visualization of Crystal, Volumetric and Morphology Data. *J. Appl. Crystallogr.* **2011**, *44* (6), 1272–1276. https://doi.org/10.1107/S0021889811038970.

(29) Link, L.; Niewa, R. *Polynator* : A Tool to Identify and Quantitatively Evaluate Polyhedra and Other Shapes in Crystal Structures. *J. Appl. Crystallogr.* **2023**, *56* (6), 1855–1864. https://doi.org/10.1107/S1600576723008476.

(30) Ong, S. P.; Richards, W. D.; Jain, A.; Hautier, G.; Kocher, M.; Cholia, S.; Gunter, D.; Chevrier, V. L.; Persson, K. A.; Ceder, G. Python Materials Genomics (Pymatgen): A Robust, Open-Source Python Library for Materials Analysis. *Comput. Mater. Sci.* **2013**, *68*, 314–319. https://doi.org/10.1016/j.commatsci.2012.10.028.

(31) Anoop, G.; Lee, D. W.; Suh, D. W.; Wu, S. L.; Ok, K. M.; Yoo, J. S. Solid-State Synthesis, Structure, Second-Harmonic Generation, and Luminescent Properties of Noncentrosymmetric $BaSi_7N_{10}$:Eu^{2+} Phosphors. *J. Mater. Chem. C* **2013**, *1* (31), 4705–4712. https://doi.org/10.1039/c3tc30716f.

(32) Shafei, R.; Maganas, D.; Strobel, P. J.; Schmidt, P. J.; Schnick, W.; Neese, F. Electronic and Optical Properties of Eu^{2+} -Activated Narrow-Band Phosphors for Phosphor-Converted Light-Emitting Diode Applications: Insights from a Theoretical Spectroscopy Perspective. *J. Am. Chem. Soc.* **2022**, *144* (18), 8038–8053. https://doi.org/10.1021/jacs.2c00218.

3

(Dis)Order and Luminescence in Silicon-Rich (Si,P)–N Network $Sr_5Si_7P_2N_{16}:Eu^{2+}$

Marwin Dialer, Monika M. Pointner, Philipp Strobel, Peter J. Schmidt, Wolfgang Schnick

INORGANIC CHEMISTRY, ACS

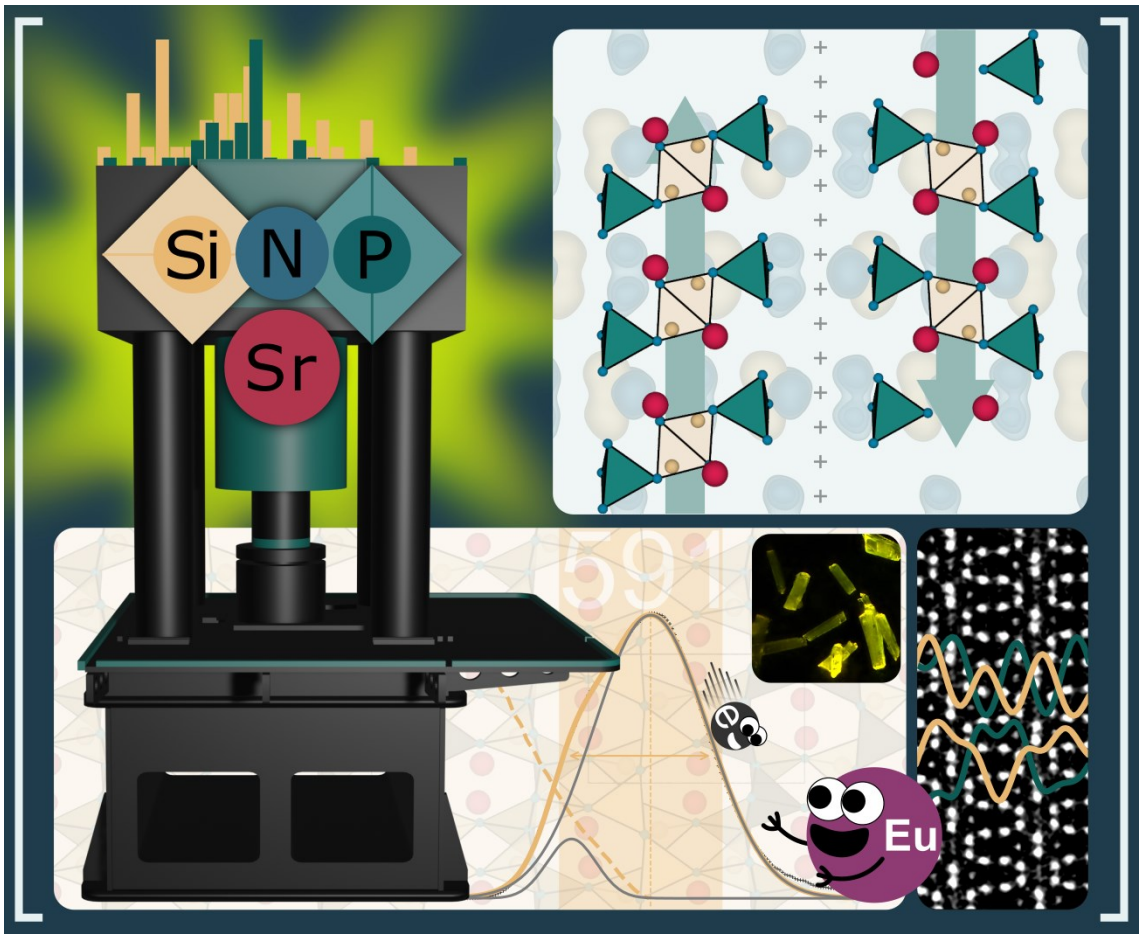

Reprinted (adapted) with permission from

Inorg. Chem. 2024, *63,* 1480−1487. https://doi.org/10.1021/acs.inorgchem.3c04109.

ABSTRACT: In this work, we present the synthesis, characterization, and optical properties of $Sr_5Si_7P_2N_{16}:Eu^{2+}$, the first tetrahedral (Si,P)−N network in which Si occupies more than 50% of the tetrahedra. While past studies have shown progress with anionic (Si,P)−N networks, the potential of silicon-rich compounds remains untapped. The synthesized compound $Sr_5Si_7P_2N_{16}$ exhibits a unique mixture of substitutional order and positional disorder within its network. The analytical challenges posed by the similarities between Si^{4+} and P^{5+}, along with the network's disorder, were overcome by combining single-crystal X-ray diffraction and scanning transmission electron microscopy EDX mapping. Low-cost crystallographic calculations provided additional insights into the identification of tetrahedral occupations in mixed networks. Luminescence investigations on $Sr_5Si_7P_2N_{16}:Eu^{2+}$ revealed yellow emission, adding to the known blue, green, and orange emission maxima of Sr−(Si,P)−N networks, highlighting the variability of such compounds.

3.1 Introduction

In the diverse world of materials chemistry, every new compound and every structural complication solved represent another step toward realizing the potential that materials offer for our technological and scientific progress. This is not just about innovation, but also about understanding. Despite the recent discoveries in the compositional space of *AE*–(Si,P)–N (*AE* = Sr, Ba), silicon-rich tetrahedral (Si,P)–N networks remain unavailable. In this context, "silicon-rich" means that more than 50 % of the tetrahedra are occupied by Si. At 33 %, $Sr_2SiP_2N_6$ has the highest silicon content to date, while the networks of $Sr_5Si_2P_6N_{16}$ and $AESiP_3N_7$ (*AE* = Sr, Ba) are even lower at 25 %.[1,2] If we extend the analysis to related compound classes, such as imido or neutral nitridosilicate phosphates, we obtain 33 % in SiP_2N_4NH, 43 % in $AESi_3P_4N_{10}(NH)_2$ (*AE* = Mg, Ca, Sr), and a maximum of 50 % in $SiPN_3$.[3–5] For comparison, in other known mixed tetrahedral compounds of the form *AE*–(*T*,Si)–N (*AE* = Ca, Sr, Ba; *T* = Li, Be, Mg, Al), Si dominates more than 80 % of the networks (Table 8.1). This is already an indication that silicon-rich (Si,P)–N networks are likely to exist. Yet, the synthesis of such compounds can be complicated. On the one hand, there is the problem of ternary segregation due to thermodynamic sinks, where $Sr_2Si_5N_8$ is a recurring side phase.[6] On the other hand, silicon is very oxophilic as a network forming cation, i.e., isolobal substitution of P–N by Si–O sometimes leads to little or no incorporation of phosphorus into the network once traces of oxygen are present. In addition, P_3N_5 already decomposes under ambient conditions at about 850 °C, while nitridosilicates often require temperatures above 1100 °C.[6–9] High-pressure chemistry in a multianvil press is a well-known remedy for this, as it prevents the decomposition and

evaporation of P_3N_5 before Si_3N_4 is activated.[10] In terms of oxygen exclusion and crucible inertness, we have previously reported that transition metal inlays, e.g., molybdenum, have performed well.[1] In the pursuit of scientific progress, it is also critical to constantly review and challenge the robustness of our analytical methods. Techniques such as scanning transmission electron microscopy (STEM), energy dispersive X-ray spectroscopy (EDX) on flat single crystal surfaces, and simple crystallographic concepts as Ewald site energies, charge distributions (CHARDI), bond valence sums (BVS), or polyhedral volumes and interatomic distances allow us not only to elucidate the structures, but also to test and confirm these methods on new compound classes such as Sr–(Si,P)–N.[11–14] These efforts ensure the continued reliability of these tools and strengthen their credibility in our research context. In this work, we present $Sr_5Si_7P_2N_{16}$, the first silicon-rich (Si,P)–N network comprising unusual and unprecedented structural motifs. We have addressed analytical challenges by using both sophisticated tools such as atomic-scale STEM-EDX maps and commonly available tools such as low-cost crystallographic calculations. While the main focus of this work was on the structural characterization of $Sr_5Si_7P_2N_{16}$, we were also interested in its optical properties after doping with Eu^{2+}, as the closely related compound classes of nitridosilicates and nitridophosphates are known to be excellent phosphors.[15,16] To this end, we measured the photoluminescence excitation (PLE) and the photoluminescence (PL) spectra on a single particle. A Pekarian-type fit of the PL spectrum allowed us to identify the different emission bands for which we propose a reasonable assignment to the activator environments.

3.2 Results and Discussion

3.2.1 Synthesis and Structure Determination

We synthesized $Sr_5Si_7P_2N_{16}$ in a multianvil press by a high-pressure high-temperature reaction at 3 GPa and 1400 °C according to Equation 1.

$$15\ Sr(N_3)_2 + 7\ Si_3N_4 + 2\ P_3N_5 \longrightarrow 3\ Sr_5Si_7P_2N_{16} + 40\ N_2 \qquad (1)$$

The reaction yielded a crystalline, colorless powder that is stable to moisture and air. Within the detection limit of PXRD, this synthesis leads to a phase-pure bulk sample (Figure 8.1 and Table 8.2). Microscopic examination of the product revealed that the crystals have predominantly acicular morphology (Figure 8.2) and are 10–20 µm in length. $Sr_5Si_7P_2N_{16}$ crystallizes in the orthorhombic space group *Pnma* (no. 62) in a new structure type with lattice parameters of a = 5.6751(2), b = 28.0387(10), and c = 9.5295(4) Å. Further crystallographic information is provided in Table 8.3–Table 8.5.[17] A preliminary structural model was refined based on single-crystal X-ray diffraction (SCXRD) data with a reduced sum formula of $Sr_5(Si,P)_9(N,O)_{16}$. To determine the elemental composition, we employed energy dispersive X-ray (EDX) spectroscopy on a single crystal (8 points), and inductively coupled plasma optical emission spectroscopy (ICP-OES) on the bulk sample. EDX analysis revealed a normalized composition of Sr 5.0(4), Si 7.4(4), P 2.5(4), N 13.2(6), and O 1.3(6), which is in good agreement with the ICP-OES results for the cations Sr 5.0(1), Si 6.7(1), and P 1.9(1), yielding the idealized empirical formula $Sr_5Si_7P_2N_{16}$. The presence of oxygen in the EDX measurement can be the result of the isolobal relationship between Si–O and P–N, as well as surface hydrolysis. To account for oxygen incorporation, a more general formula is written as $Sr_5Si_{7+x}P_{2-x}N_{16-x}O_x$ where x is estimated to be significantly less than 1. The presence of protonic hydrogen was excluded by infrared spectroscopy due to the absence of N–H vibrations (Figure 8.3). This makes $Sr_5Si_7P_2N_{16}$ the first silicon-rich (Si,P)–N network, i.e., Si occupies the majority of the network's tetrahedra.

3.2.2 Structure Description

The crystal structure comprises a three-dimensional, anionic network of $[SiN_4]$- and $[PN_4]$-tetrahedra with Sr^{2+} ions in its voids. The degree of condensation of $\kappa \approx 0.56$ is close to that of P_3N_5 (κ = 0.6). The network itself can be described by dividing it into nominal layers in the order

A–B–A'–B', where A' and B' are the inverse of A and B (Figure 3.1). According to Liebau's classification of silicates, layer A consists of condensed *zweier* single chains along the *a*-axis, with their tetrahedra alternating up or down along the *c*-axis.[18,19] In this way, they form two *zweier* layers of *sechser* rings exclusively occupied by Si^{4+} (Si2/Si3) as network forming cations (*NFC*).

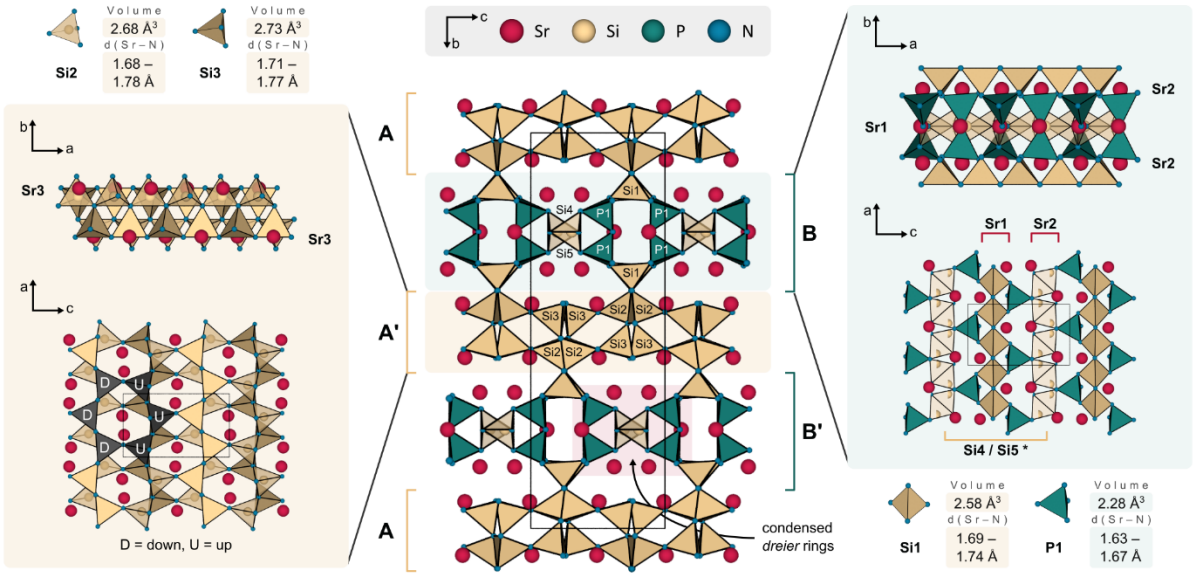

Figure 3.1 Graphical illustration of the crystal structure of $Sr_5Si_7P_2N_{16}$ along [100] (middle). Due to its layered structure in the ABA'B' sequence, layers A' (left, beige) and B (right, green) are shown as examples in additional viewing directions [001] and [010]. The structure motif of edge-sharing *dreier* rings is highlighted in red. Tetrahedral volumes and distances of Si1–Si3 and P1 are given in the top left and bottom right. (*) Additional data on Si4 and Si5 are given in Figure 3.2b.

The center of each *sechser* ring is occupied by Sr3. Layer B features an unprecedented and complex structural motif, namely two edge-sharing (Si,P)–N *dreier* rings. Si4 and Si5 occupy the bridging, edge-sharing tetrahedra, also referred to as a "bowtie unit" as reported in $BaSi_7N_{10}$, for example.[20] The remaining tetrahedra are centered with P1. To connect these motifs and also the layers with each other, $(Si1)N_4$ *einer* single chains serve as backbones. Layer B, however, is even more complex as the bowtie units show disorder. This means that the *dreier* rings can be connected either ascending or descending along the *a*-axis (Figure 3.2a). Such split positions sometimes occur as a result of incorrectly introduced symmetry elements or operations. Therefore, we examined the difference Fourier map of a new structure refinement that was integrated, absorption corrected, and refined in *P*1 symmetry (Figure 3.2b). Again, the residual electron density corroborates the same disordered model. Undetected superstructures were ruled out by evaluating the precession images due to the

absence of corresponding reflections (Figure 8.6). Refinement of the occupancies of Si4 and Si5 yields 0.49 and 0.47, respectively, indicating that there is no significant preference between ascending and descending connectivity within the estimated error. We argue that a reasonable theory for the occurrence of disorder can be found in the small tetrahedral volumes of $(Si4)N_4$ and $(Si5)N_4$, which are roughly 2.4 $Å^3$ each. Comparable compounds with Si-centered bowtie units have larger volumes of 2.5–2.9 $Å^3$, as in $BaSi_7N_{10}$, $Ca_3LiSi_2N_5$ and $AE_3Li_4Si_2N_6$ (*AE* = Ca, Sr).[20–22] Hence, each bowtie unit exerts a certain strain on the network, which must be relieved by skipping a connection (Figure 3.2a). This would then serve as a switch that toggles the connection of the *dreier* rings from ascending to descending and vice versa, resulting in a disordered model. This mechanism would also work for P-centered bowtie units, which have been reported in several compounds, e.g., α-P_3N_5, α'-P_3N_5, and BP_3N_6.[23–25] In this case, compression rather than stretching would occur due to the smaller average tetrahedral volumes of about 2.1–2.2 $Å^3$.[23–26] This brings us to the question of how we know whether the tetrahedra are occupied by Si^{4+} or P^{5+} in the first place.

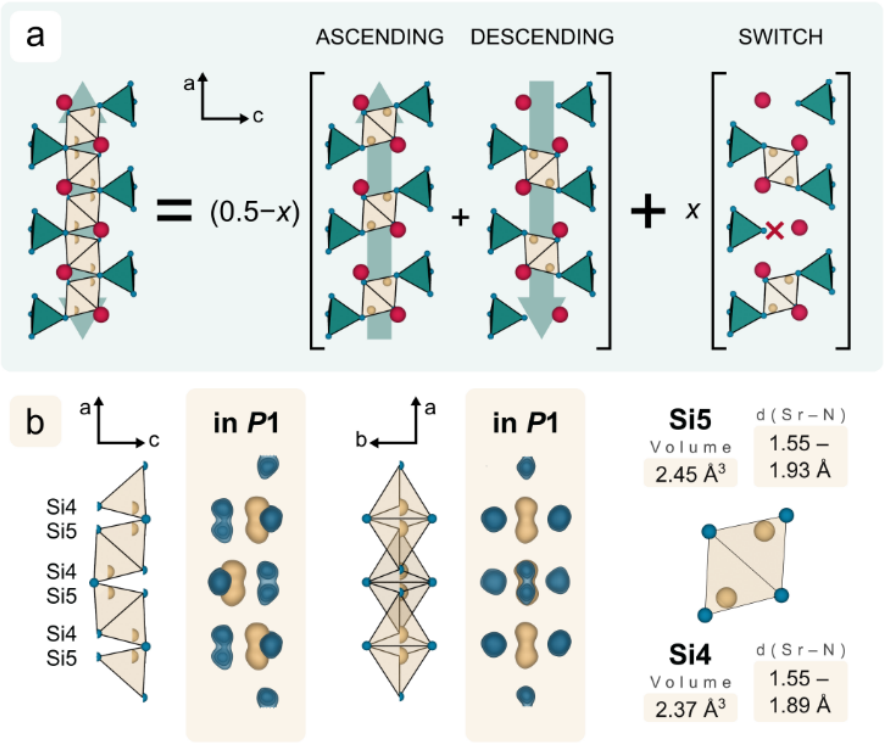

Figure 3.2 (a) Mathematical illustration of the disorder of the bowties with equal contribution of ascending and descending connectivity, and a proposed switch. (b) Difference Fourier maps of the disordered bowties refined in *P*1 symmetry that corroborate the proposed disordered model.

3.2.3 STEM-EDX and ECBVD Calculations

Up to this point, we have taken the tetrahedral occupancies of our network as given, which they are not. Due to crystallochemical similarities between Si^{4+} and P^{5+}, both cations can occupy the same tetrahedral sites in a structure. Therefore, we investigated the crystal structure using STEM-EDX maps with atomic resolution. In this way, each crystallographic site can be evaluated individually in terms of its elemental composition. For $Sr_5Si_7P_2N_{16}$, we analyzed STEM-EDX maps combined with STEM high-angle annular dark-field (HAADF) images, both along the zone axis [100]. Two independent STEM-EDX area scans were chosen to cover all sites of interest, highlighted as yellow and red in Figure 3.3a. From the integrated EDX signals, we obtained sinusoids where each peak indicates the presence of Si or P at that location. In both area scans, the curves of Si and P oscillate out of phase, confirming that there is no mixing present in this compound, not even in the disordered bowtie unit (Si4/Si5). This observation suggests that in this compound it is energetically more favorable to compress Si–N bonds than to elongate P–N bonds in bowtie units. This leads to a rather unusual result: $Sr_5Si_7P_2N_{16}$ comprises the first ordered disordered (Si,P)–N network. To understand this, it is important to clarify that we distinguish two types of disorder in (Si,P)–N networks: (1) substitutional disorder, where Si^{4+} and P^{5+} statistically occupy the same sites as in $Sr_5Si_2P_6N_{16}$,[1] and (2) positional disorder, where atoms do not occupy a well-defined position but instead can be found in multiple positions, e.g., Si4 and Si5 in $Sr_5Si_7P_2N_{16}$. In this compound, both are present. To further corroborate our results and in service of consistency, we evaluated the tetrahedral sites in terms of their Ewald site energy, charge distribution (CHARDI), bond valence sum (BVS), and tetrahedral volumes and distances, with respect to literature values (Figure 3b). As an evaluation criterion for each method, we define the mean percentage deviation, which is calculated from the values for Si and P of the compound and the expected literature values. However, to increase reliability, we not only evaluate the individual methods, but average over all mean percentage deviations to get the total mean deviation $\overline{D}$. For literature known nitridosilicates and nitridophosphates, we then obtain total mean deviations of 0.3–3.2 %, which we define as typical for such compounds. Further details on this approach can be found in our previous work.[1] In $Sr_5Si_7P_2N_{16}$, the total mean deviation of P1 as well as of Si1–Si3 is with $\overline{D}$ = 1.9 % in good agreement with what we expect and corroborates the substitutional order of these crystallographic sites. The disordered nature of

the bowtie units makes interatomic distances of Si4–N and Si5–N unreliable and thus an evaluation that depends heavily on the accuracy of crystallographic positions not very meaningful. However, for the sake of completeness, a full evaluation including Si4 and Si5 ($\overline{D}$ = 3.1 %) can be found in Figure 8.7. With all this information, we are able to fully understand the connectivity and occupancy of the anionic (Si,P)–N network. Still, we have paid little attention to its counterpart, the cationic coordination environments of Sr1–Sr3, which are essential and will therefore be part of the following investigation of luminescence upon doping with Eu^{2+}.

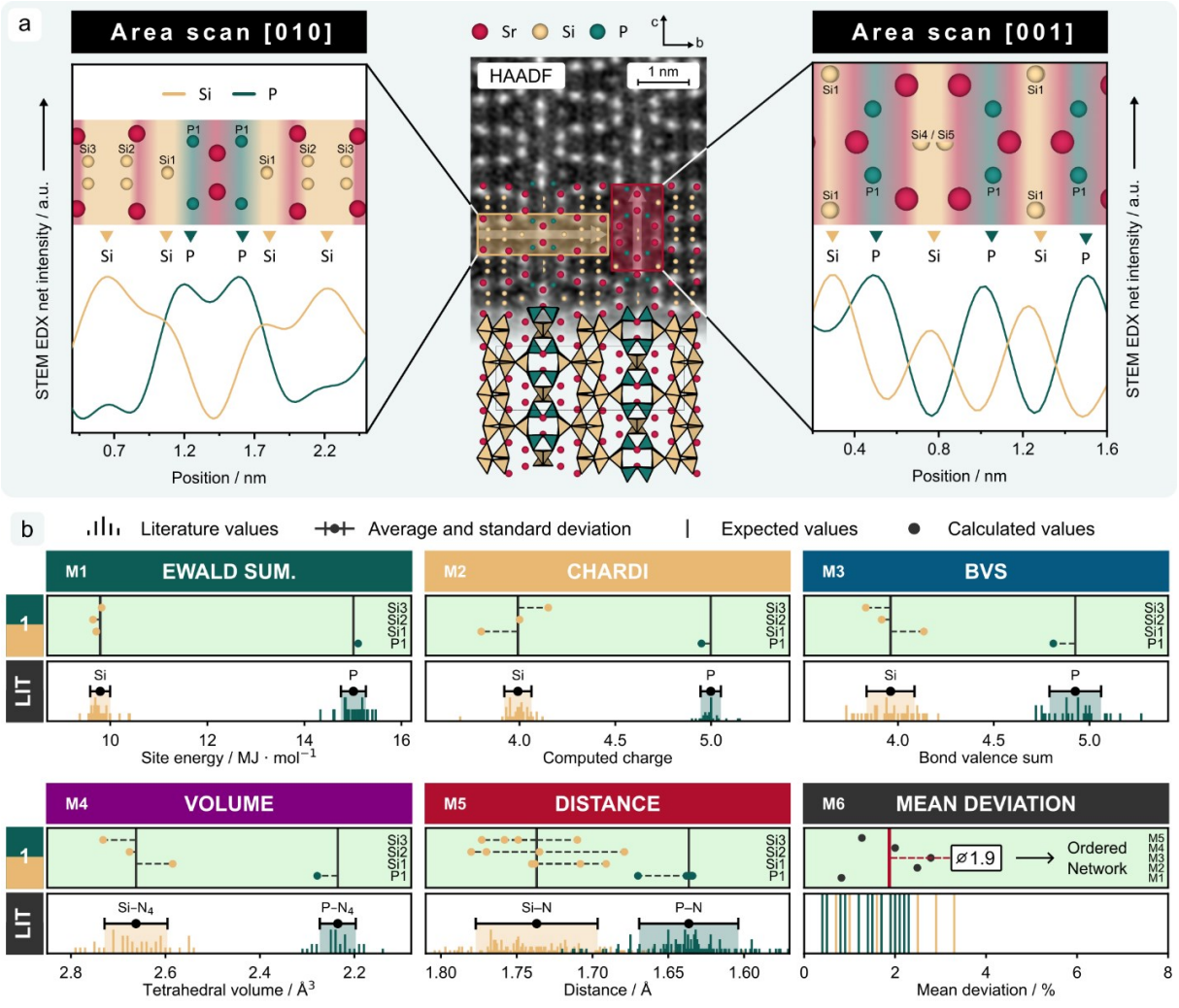

Figure 3.3 (a) STEM-EDX area scans of $Sr_5Si_7P_2N_{16}$ along [010] (yellow) and [001] (red), showing out of phase oscillation. Si and P show a substitutional order. Further information is given in Figure 8.4and Figure 8.5. (b) Comparison of Ewald site energies, CHARDI, BVS, and tetrahedral volumes and distances (ECBVD) of $Sr_5Si_7P_2N_{16}$ with literature values. The calculation of the total mean deviation is within the typical range of nitridosilicates and nitridophosphates. Si4 and Si5 are excluded due to their disorder. Literature values (LIT) are given in relative frequency.

3.2.4 Luminescence

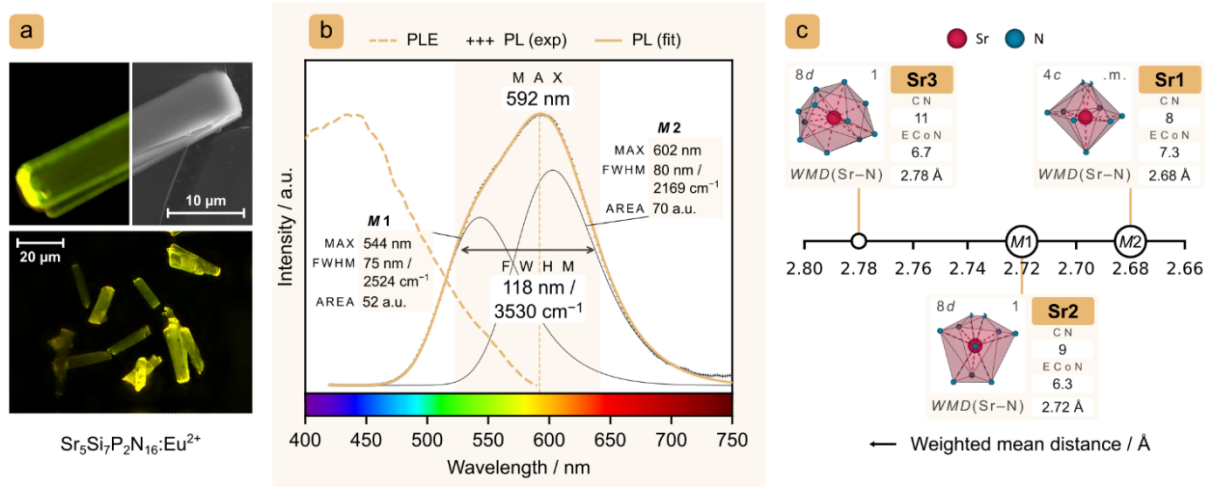

Figure 3.4 (a) SEM and luminescence images of $Sr_5Si_7P_2N_{16}:Eu^{2+}$ showing the acicular shape of the crystals. (b) PLE (610 nm) and PL (400 nm) spectrum of $Sr_5Si_7P_2N_{16}:Eu^{2+}$. The PL spectrum was fitted with Pekar curves with two maxima at 544 (*M*1) and 602 nm (*M*2). (c) Coordination environments of activator sites Sr1–Sr3 ordered by their weighted mean distances from Sr–N. Sr1 and Sr2 were assigned to maxima *M*2 and *M*1, respectively.

For our luminescence experiments, we doped $Sr_5Si_7P_2N_{16}$ with 1 mol% Eu^{2+}, yielding acicular crystals with bright yellow fluorescence (Figure 3.4a). To investigate the optical properties, we measured the PLE and the PL spectra (Figure 3.4b). The experimental PL data were fitted by a combination of two Pekarian-type functions to account for asymmetry of the emission bands caused by the Stokes shift.[27] In the service of reproducibility and portability, we provide a working Python example for Pekarian-type fits in section 8.3.8. The final fit has a maximum at 592 nm with a full width at half-maximum of *fwhm* = 118 nm / 3530 cm^{-1}. In general, this broad emission is consistent with multiple activator sites Sr1–Sr3 and the disordered ligands N9 and N10 in the chemical environments of Sr1 and Sr2. However, by applying simple concepts as the weighted mean distance (*WMD*), effective coordination number (*ECoN*), and site symmetry, we can gain deeper insights into the optical behavior of $Sr_5Si_7P_2N_{16}:Eu^{2+}$ (Figure 4c).[28] As a rule of thumb, we know that the smaller the *WMD* and the larger the *ECoN* are, the larger the Stokes shift is due to stronger ligand field splitting. On the other hand, a higher site symmetry reduces the Stokes shift due to a smaller number of degrees of freedom for relaxation of the excited Eu^{2+} ($4f^6 5d^1$) states.[29] The deconvolution of the fitted curve shows a contribution from two different maxima, *M*1 at 544 nm and *M*2 at 602 nm. Both emissions differ significantly in their Stokes shift, justifying the use of our simplified approach to assign emission bands to the Sr1–Sr3 activator sites. Since there are only two maxima instead of three, we can assume that one Sr site does not contribute to the observed luminescence. We

think that Sr3 is the most likely candidate because the combination of *WMD* = 2.78 Å and *ECoN* = 6.7 suggests the smallest Stokes shift. Its complete absence may be the result of improper excitation at λ_{exc} = 400 nm, complete reabsorption by Sr1 and Sr2, or both. We have neglected the possibility of selective doping of the sites, since all have polyhedral volumes typical of Eu^{2+} doping (V_{Sr} = 33.5–59.4 $Å^3$).[30,31] By the same reasoning, Sr1 is expected to exhibit the largest Stokes shift, having the smallest *WMD* = 2.68 Å and highest *ECoN* = 7.3. The slightly higher site symmetry of .*m*. at the Sr1 site will not change the order compared to Sr2. Therefore, we assigned Sr2 to *M*1 and Sr1 to *M*2. From their multiplicities (Sr1: 4*c* and Sr2: 8*d*), we would expect an intensity ratio of 1:2, while the integrated areas show that it is actually 1.35:1. This can be attributed to reabsorption effects, since the PLE spectrum still shows considerable excitation at the maximum *M*1 (544 nm). Finally, we concede that a definite assignment of activator sites to emission bands is only possible by high-level theoretical calculations of the ligand field splittings and excited states of Eu^{2+} ($4f^6 5d^1$).[29]

3.3 Conclusion

In summary, the successful synthesis and characterization of $Sr_5Si_7P_2N_{16}$ have brought to light a compound with remarkable structural properties, exhibiting an unprecedented (Si,P)–N network with both substitutional order and positional disorder. Following $Sr_2SiP_2N_6$, $Sr_5Si_2P_6N_{16}$, and $AESiP_3N_7$ (AE = Sr,Ba), $Sr_5Si_7P_2N_{16}$ is the first silicon-rich representative of anionic, tetrahedral (Si,P)–N networks with a condensation degree of $\kappa \approx 0.56$ close to that of P_3N_5 ($\kappa = 0.6$). While the crystallochemical similarities between Si^{4+} and P^{5+} as well as the disorder of the bowtie units presented an analytical challenge, advanced techniques such as STEM-EDX mapping were able to effectively elucidate the elemental occupancies within the structure. We were also able to show that low-cost crystallographic calculations reliably confirm these results if the corresponding sites show no positional disorder. This can greatly simplify the structure elucidation of materials with mixed networks, as the availability of STEM analysis to researchers is often limited. Moreover, we have provided a reasonable explanation for the disorder of the bowtie units. Luminescence studies of $Sr_5Si_7P_2N_{16}:Eu^{2+}$ offered valuable insight into the optical behavior of the compound. Analysis of the activator sites in terms of their weighted mean distances, effective coordination numbers, and site symmetries allowed us to propose a reasonable assignment of Sr sites to emission bands. With its bright yellow luminescence, $Sr_5Si_7P_2N_{16}:Eu^{2+}$ demonstrates the variability of emission maxima in (Si,P)–N networks, ranging from blue ($BaSiP_3N_7:Eu^{2+}$) to green ($Sr_2SiP_2N_6:Eu^{2+}$) to orange ($Sr_5Si_2P_6N_{16}:Eu^{2+}$). In essence, this study has shown that Sr–(Si,P)–N compounds are not limited to phosphorus-rich networks and include unusual structure motifs worth investigating. Future research on $Sr_5Si_7P_2N_{16}:Eu^{2+}$ should focus on the introduction of other counter cations, e.g. Ca or Ba, to investigate whether disorder persists or disappears and how they affect the luminescence properties.

3.4 Acknowledgements

The authors express their gratitude to Christian Minke (Department of Chemistry, LMU Munich) for conducting the EDX measurements and producing SEM images. We thank Massimo Nespolo (CRM, Université de Lorraine) and Corrado Cuocci (Institute of Crystallography, CNR) for their support with the CHARDI-2015 and EXPO2014 programs. M.D. would additionally like to thank the Bundesministerium für Bildung und Forschung (BMBF) for its financial support and Sophia L. Wandelt and Reinhard M. Pritzl for their excellent conceptual and scientific support.

3.5 References

(1) Dialer, M.; Pointner, M. M.; Wandelt, S. L.; Strobel, P.; Schmidt, P. J.; Bayarjargal, L.; Winkler, B.; Schnick, W. Order and Disorder in Mixed (Si, P)–N Networks $Sr_2SiP_2N_6:Eu^{2+}$ and $Sr_5Si_2P_6N_{16}:Eu^{2+}$. *Adv. Opt. Mater.* **2023**, 2302668. https://doi.org/10.1002/adom.202302668.

(2) Eisenburger, L.; Oeckler, O.; Schnick, W. High-Pressure High-Temperature Synthesis of Mixed Nitridosilicatephosphates and Luminescence of $AESiP_3N_7:Eu^{2+}$ (*AE*=Sr, Ba). *Chem. Eur. J.* **2021**, *27* (13), 4461–4465. https://doi.org/10.1002/chem.202005495.

(3) Vogel, S.; Buda, A. T.; Schnick, W. Rivalry under Pressure: The Coexistence of Ambient-Pressure Motifs and Close-Packing in Silicon Phosphorus Nitride Imide SiP_2N_4NH. *Angew. Chem. Int. Ed.* **2019**, *58* (11), 3398. https://doi.org/10.1002/ANIE.201813789.

(4) Eisenburger, L.; Strobel, P.; Schmidt, P. J.; Bräuniger, T.; Wright, J.; Bright, E. L.; Giacobbe, C.; Oeckler, O.; Schnick, W. Nitridic Analogs of Micas $AESi_3P_4N_{10}(NH)_2$ (*AE*=Mg, $Mg_{0.94}Ca_{0.06}$, Ca, Sr). *Angew. Chem. Int. Ed.* **2022**, *61* (4), e202114902. https://doi.org/10.1002/anie.202114902.

(5) Baldus, H. P.; Schnick, W.; Lücke, J.; Wannagat, U.; Bogedain, G. Silicon Phosphorus Nitride, the First Ternary Compound in the Silicon-Phosphorus-Nitrogen System. *Chem. Mater.* **1993**, *5* (6), 845–850. https://doi.org/https://doi.org/10.1021/cm00030a021.

(6) Schlieper, T.; Milius, W.; Schnick, W. Nitrido-Silicate. II [1]. Hochtemperatur-Synthesen Und Kristallstrukturen von $Sr_2Si_5N_8$ Und $Ba_2Si_5N_8$. *Z. Anorg. Allg. Chem.* **1995**, *621* (8), 1380–1384. https://doi.org/10.1002/zaac.19956210817.

(7) Schnick, W. Solid-State Chemistry with Nonmetal Nitrides. *Angew. Chem. Int. Ed.* **1993**, *32* (6), 806–818. https://doi.org/10.1002/anie.199308061.

(8) Gál, Z. A.; Mallinson, P. M.; Orchard, H. J.; Clarke, S. J. Synthesis and Structure of Alkaline Earth Silicon Nitrides: $BaSiN_2$, $SrSiN_2$, and $CaSiN_2$. *Inorg. Chem.* **2004**, *43* (13), 3998–4006. https://doi.org/10.1021/ic049901p.

(9) Pilet, G.; Höppe, H. A.; Schnick, W.; Esmaeilzadeh, S. Crystal Structure and Mechanical Properties of $SrSi_7N_{10}$. *Solid State Sci.* **2005**, *7* (4), 391–396. https://doi.org/10.1016/j.solidstatesciences.2005.01.011.

(10) Kloß, S. D.; Schnick, W. Nitridophosphates: A Success Story of Nitride Synthesis. *Angew. Chem. Int. Ed.* **2019**, *58* (24), 7933–7944.

(11) Toukmaji, A. Y.; Board, J. A. Ewald Summation Techniques in Perspective: A Survey. *Comput. Phys. Commun.* **1996**, *95*, 73–92.

(12) Nespolo, M. Charge Distribution as a Tool to Investigate Structural Details. IV. A New Route to Heteroligand Polyhedra. *Acta Crystallogr. Sect. B* **2016**, *72* (1), 51–66. https://doi.org/10.1107/S2052520615019472.

(13) Nespolo, M.; Guillot, B. *CHARDI2015*: Charge Distribution Analysis of Non-Molecular Structures. *J. Appl. Crystallogr.* **2016**, *49* (1), 317–321. https://doi.org/10.1107/S1600576715024814.

(14) Altomare, A.; Cuocci, C.; Giacovazzo, C.; Moliterni, A.; Rizzi, R.; Corriero, N.; Falcicchio, A. *EXPO2013*: A Kit of Tools for Phasing Crystal Structures from Powder Data. *J. Appl. Crystallogr.* **2013**, *46* (4), 1231–1235. https://doi.org/10.1107/S0021889813013113.

(15) Xie, R.-J.; Hirosaki, N. Silicon-Based Oxynitride and Nitride Phosphors for White LEDs—A Review. *Sci. Technol. Adv. Mater.* **2007**, *8* (7–8), 588. https://doi.org/10.1016/j.stam.2007.08.005.

(16) Wendl, S.; Mardazad, S.; Strobel, P.; Schmidt, P. J.; Schnick, W. HIP to Be Square: Simplifying Nitridophosphate Synthesis in a Hot Isostatic Press. *Angew. Chem. Int. Ed.* **2020**, *59*, 18240. https://doi.org/10.1002/ANGE.202008570.

(17) Deposition Number 2301099 Contains the Supplementary Crystallographic Data for This Paper. These Data Are Provided Free of Charge by the Joint Cambridge Crystallographic Data Centre and Fachinformationszentrum Karlsruhe Access Structures Service. **2023**.

(18) Liebau, F. Bemerkungen Zur Systematik Der Kristallstrukturen von Silikaten Mit Hochkondensierten Anionen. *Z. Phys. Chem.* **1956**, *206O* (1), 73–92. https://doi.org/10.1515/ZPCH-1956-20607.

(19) Liebau, F. *Structural Chemistry of Silicates*, 1st ed.; Springer Berlin Heidelberg: Berlin, Heidelberg, 1985. https://doi.org/10.1007/978-3-642-50076-3.

(20) Huppertz, H.; Schnick, W. Edge-sharing SiN_4 Tetrahedra in the Highly Condensed Nitridosilicate $BaSi_7N_{10}$. *Chem. Eur. J.* **1997**, *3* (2), 249–252. https://doi.org/10.1002/chem.19970030213.

(21) Lupart, S.; Schnick, W. $LiCa_3Si_2N_5$ – A Lithium Nitridosilicate with a $[Si_2N_5]^{7-}$ Double-Chain. *Z. Anorg. Allg. Chem.* **2012**, *638* (12–13), 2015–2019. https://doi.org/10.1002/zaac.201200106.

(22) Pagano, S.; Lupart, S.; Schmiechen, S.; Schnick, W. $Li_4Ca_3Si_2N_6$ and $Li_4Sr_3Si_2N_6$ – Quaternary Lithium Nitridosilicates with Isolated $[Si_2N_6]^{10-}$ Ions. *Z. Anorg. Allg. Chem.* **2010**, *636* (11), 1907–1909. https://doi.org/10.1002/zaac.201000163.

(23) Horstmann, S.; Irran, E.; Schnick, W. Synthesis and Crystal Structure of Phosphorus(V) Nitride α-P_3N_5. *Angew. Chem. Int. Ed.* **1997**, *36* (17), 1873–1875. https://doi.org/10.1002/anie.199718731.

(24) Laniel, D.; Trybel, F.; Néri, A.; Yin, Y.; Aslandukov, A.; Fedotenko, T.; Khandarkhaeva, S.; Tasnádi, F.; Chariton, S.; Giacobbe, C.; Bright, E. L.; Hanfland, M.; Prakapenka, V.; Schnick, W.; Abrikosov, I. A.; Dubrovinsky, L.; Dubrovinskaia, N. Revealing Phosphorus Nitrides up to the Megabar Regime: Synthesis of A′-P_3N_5, Δ-P_3N_5 and PN_2. *Chem. Eur. J.* **2022**, *28* (62), e202201998. https://doi.org/10.1002/chem.202201998.

(25) Vogel, S.; Buda, A. T.; Schnick, W. United in Nitride: The Highly Condensed Boron Phosphorus Nitride BP_3N_6. *Angew. Chem. Int. Ed.* **2018**, *57* (40), 13202–13205. https://doi.org/10.1002/anie.201808111.

(26) Horstmann, S.; Irran, E.; Schnick, W. Synthese, Kristallstruktur Und Eigenschaften von Phosphor(V)-Nitridimid HP_4N_7. *Z. Anorg. Allg. Chem.* **1998**, *624*, 221–227.

(27) de Jong, M.; Seijo, L.; Meijerink, A.; Rabouw, F. T. Resolving the Ambiguity in the Relation between Stokes Shift and Huang–Rhys Parameter. *Phys. Chem. Chem. Phys.* **2015**, *17* (26), 16959–16969. https://doi.org/10.1039/C5CP02093J.

(28) Hoppe, R. Effective Coordination Numbers (ECoN) and Mean Fictive Ionic Radii (MEFIR). *Z. Kristallogr. Cryst. Mater.* **1979**, *150* (1–4), 23–52. https://doi.org/10.1524/zkri.1979.150.14.23.

(29) Shafei, R.; Maganas, D.; Strobel, P. J.; Schmidt, P. J.; Schnick, W.; Neese, F. Electronic and Optical Properties of Eu^{2+} -Activated Narrow-Band Phosphors for Phosphor-Converted Light-Emitting Diode Applications: Insights from a Theoretical Spectroscopy Perspective. *J. Am. Chem. Soc.* **2022**, *144* (18), 8038–8053. https://doi.org/10.1021/jacs.2c00218.

(30) Uheda, K.; Hirosaki, N.; Yamamoto, Y.; Naito, A.; Nakajima, T.; Yamamoto, H. Luminescence Properties of a Red Phosphor, $CaAlSiN_3$:Eu^{2+}, for White Light-Emitting Diodes. *Electrochem. Solid-State Lett.* **2006**, *9* (4), H22. https://doi.org/10.1149/1.2173192/XML.

(31) Anoop, G.; Lee, D. W.; Suh, D. W.; Wu, S. L.; Ok, K. M.; Yoo, J. S. Solid-State Synthesis, Structure, Second-Harmonic Generation, and Luminescent Properties of Noncentrosymmetric $BaSi_7N_{10}$:Eu^{2+} Phosphors. *J. Mater. Chem. C* **2013**, *1* (31), 4705–4712. https://doi.org/10.1039/c3tc30716f.

4

The Fundamental Disorder Unit in (Si,P)–(O,N) Networks

Marwin Dialer, Kristian Witthaut, Thomas Bräuniger, Peter J. Schmidt, Wolfgang Schnick

ANGEWANDTE CHEMIE INTERNATIONAL EDITION, WILEY-VCH

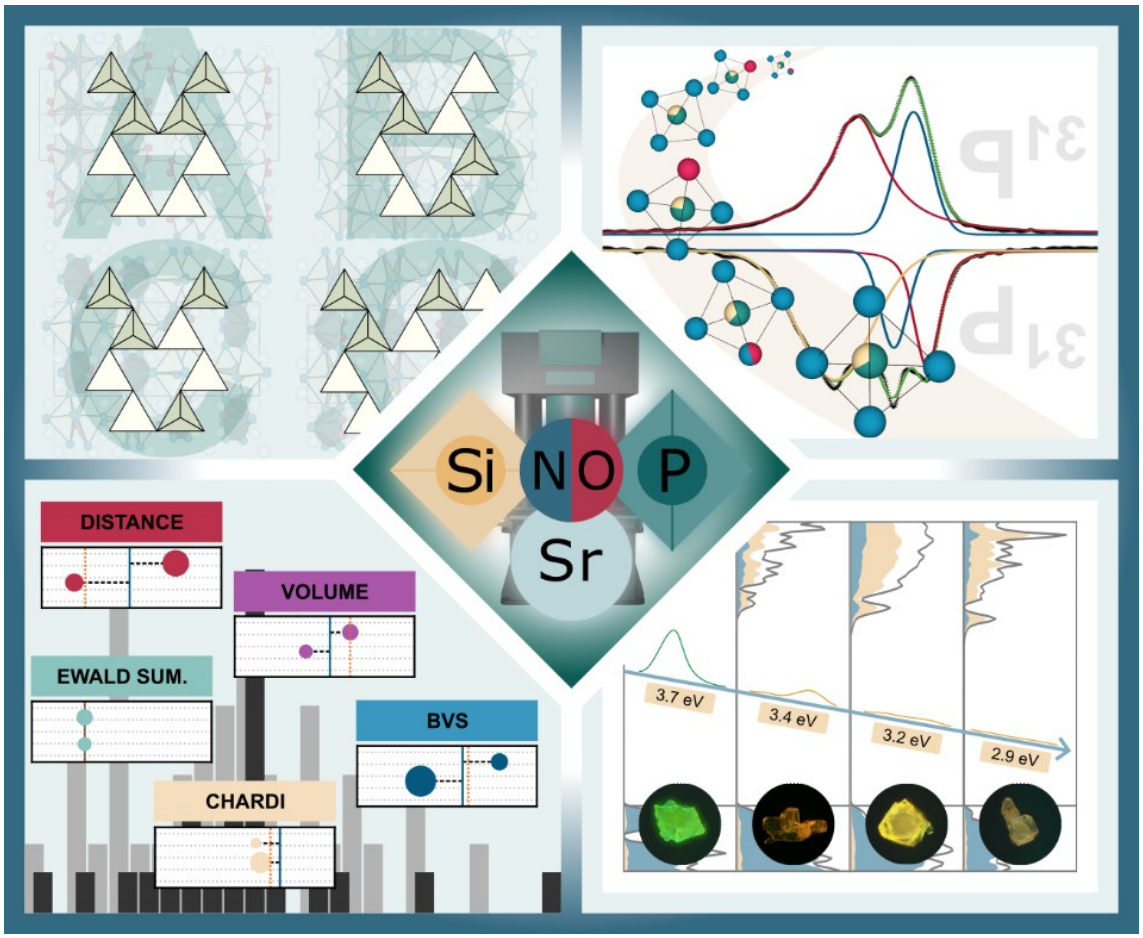

Reprinted (adapted) with permission from

Angew. Chem. Int. Ed. **2024**, e202401419. 10.1002/anie.202401419.

ABSTRACT: This study presents the synthesis and characterization of oxonitridosilicate phosphates $Sr_3SiP_3O_2N_7$, $Sr_5Si_2P_4ON_{12}$, and $Sr_{16}Si_9P_9O_7N_{33}$ as the first of their kind. These compounds were synthesized under high-temperature (1400 °C) and high-pressure (3 GPa) conditions. A unique structural feature is their common fundamental building unit, a *vierer* single chain of $(Si,P)(O,N)_4$ tetrahedra. All tetrahedra comprise substitutional disorder which is why we refer to it as the fundamental disorder unit (FDU). We classified four different FDU motifs, revealing systematic bonding patterns. Including literature known $Sr_5Si_2P_6N_{16}$, three of the four patterns were found in the presented compounds. Common techniques like single-crystal X-ray diffraction (SCXRD), elemental analyses, and ^{31}P nuclear magnetic resonance (NMR) spectroscopy were utilized for structural analysis. Additionally, low-cost crystallographic calculations (LCC) provided insights into the structure of $Sr_{16}Si_9P_9O_7N_{33}$ where NMR data were unavailable due to the lack of bulk samples. The optical properties of these compounds, when doped with Eu^{2+}, were investigated using photoluminescence excitation (PLE), photoluminescence (PL) measurements, and density functional theory (DFT) calculations. Factors influencing the emission properties, including thermal quenching mechanisms, were discussed. This research reveals the new class of oxonitridosilicate phosphates with unique systematic structural features that offer potential for theoretical studies of luminescence and band gap tuning in insulators.

4.1 Introduction

The learning process is significantly improved when new information is linked to existing knowledge. This approach is particularly beneficial in scientific research, where parallels are often drawn with known compounds to better understand newly discovered materials. In our case, we want to use the well-established compound class of alkaline earth and rare earth metal SiAlONs (silicon aluminum oxonitrides) to introduce the new class of alkaline earth oxonitridosilicate phosphates, or rather SiPONs. Their striking similarities serve not only as motivation to investigate such compounds in view of the diverse applications of SiAlONs, but also to facilitate the understanding of their rather complex structures.[1,2] SiAlONs are generally characterized by a tetrahedral network spanned by Al^{3+} and Si^{4+} as network-forming cations (NFC) and N^{3-} and O^{2-} as ligands. Although these networks can be neutral, we will only focus on anionic SiAlONs since the presented SiPONs include Sr^{2+} as a counter cation. The obvious difference between the two classes is that in SiAlONs the tetrahedra are occupied by Al^{3+}/Si^{4+} and in SiPONs by Si^{4+}/P^{5+} but the relationship of the pairings is the same, i.e., similar charges, ionic radii and isolobal behavior with respect to the ligands (Al–O/Si–N, Si–O/P–N). This already suggests that the nature and connectivity of the two networks should be correlated which is why we give a brief overview here. By nature, we refer to the substitutional ordering

and elemental composition of the network. There are examples of all ordering types with no obvious preference for SiAlONs, e.g., $Sr_{10}Sm_6Si_{30}Al_6O_7N_{54}$ (ordered), $BaSi_5AlO_2N_7$ (partially ordered), and $Pr_4Si_5AlO_7N_7$ (disordered), but there is a strong preference for silicon-rich compositions.[3–5] In fact, we know of only one example in which Al^{3+} occupies more than 50% of the tetrahedra, namely in $SrSiAl_2O_3N_2$.[6] This trend of mixed networks being dominated by the smaller NFC has already been mentioned in previous work.[7] The same was observed for pure nitridosilicate phosphates with $Sr_2SiP_2N_6$ (ordered), $SrSiP_3N_7$ (partially ordered), and $Sr_5Si_2P_6N_{16}$ (disordered), as well as $Sr_5Si_7P_2N_{16}$ being the only representative whose network is dominated by the larger NFC, here Si^{4+}.[7–9] The connectivity in SiAlONs known in the literature cannot easily be categorized into recurring patterns. Although most structures are composed of corner-sharing tetrahedra, their motifs range from three- to eight-membered rings, e.g., in $BaSi_5AlO_2N_7$, to distorted *vierer* single chains, e.g., in $Pr_4Si_5AlO_7N_7$, to even more complex structures.[4,5] All this could be understood as the absence of structural systematics, but the comparison of anionic SiAlONs with different counter cations can be rightly criticized. Especially since we will see below that Sr–(Si, P)–(O, N) compounds have a very close relationship which we refer to as the fundamental disorder unit (FDU). Given the many similarities, the question remains as to why SiPONs were not explored earlier. The answer to this is probably the more difficult synthesis, which requires high temperatures (>1400 °C) to activate the Si species, e.g., Si_3N_4 or SiO_2, and high pressures (>3 GPa) to avoid premature evaporation or decomposition of the Sr and P species, e.g., $Sr(N_3)_2$, P_3N_5 and P_4O_{10}. SiAlONs typically need significantly lower pressures (<150 MPa), which makes the synthesis easier successful outside a multianvil press. Furthermore, we have previously shown that the elucidation of the structure and in particular the network in (Si, P) compounds is a multi-step process that often utilizes high-level analytics, such as atomic-scale scanning transmission electron microscopy (STEM).[7,8] However, we are interested in making this workflow more accessible by extending the analytical scope to more common methods, such as NMR. In this contribution, we present $Sr_3SiP_3O_2N_7$, $Sr_5Si_2P_4ON_{12}$ and $Sr_{16}Si_9P_9O_7N_{33}$ as the first alkaline earth SiPONs. We analyzed their structures by a mixture of SCXRD, elemental analyses, NMR, and low-cost crystallographic calculations (LCC). To provide context and stimulate future research, we also investigated their optical properties upon doping with Eu^{2+}.

4.2 Results and Discussion

4.2.1 Synthesis

Stoichiometric amounts of $Sr(N_3)_2$, SrO, amorphous Si_3N_4, amorphous SiO_2, and α-P_3N_5 were used to synthesize the compounds $Sr_3SiP_3O_2N_7$ and $Sr_5Si_2P_4ON_{12}$ according to equations 1 and 2.

$$3\ Sr(N_3)_2 + 6\ SrO + Si_3N_4 + 3\ P_3N_5 \rightarrow 3\ Sr_3SiP_3O_2N_7 + 8\ N_2 \quad (1)$$

$$30\ Sr(N_3)_2 + 3\ Si_3N_4 + 3\ SiO_2 + 8\ P_3N_5 \rightarrow 6\ Sr_5Si_2P_4ON_{12} + 80\ N_2 \quad (2)$$

After thorough mixing in an agate mortar, the starting materials were transferred to a BN crucible with a Mo inlay and heated to 1400 °C under a pressure of 3 GPa using a multianvil press. For more details on the syntheses refer to the section 9.1.2. The syntheses of $Sr_3SiP_3O_2N_7$ and $Sr_5Si_2P_4ON_{12}$ resulted in colorless and microcrystalline powders with a phase fraction of the target phase higher than 90 wt% according to Rietveld refinements (Figure 9.1, Table 9.3). $Sr_{16}Si_9P_9O_7N_{33}$ appeared as a minor side phase of $Sr_5Si_2P_4ON_{12}$, while a direct synthesis was not successful.

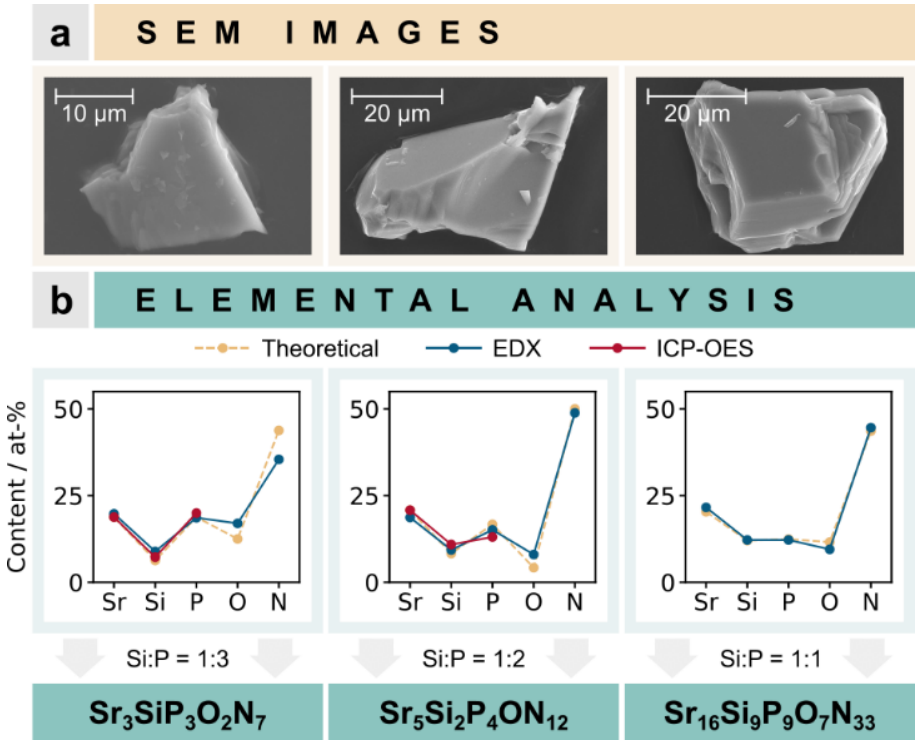

Figure 4.1 a) Scanning electron microscopy (SEM) images of $Sr_3SiP_3O_2N_7$, $Sr_5Si_2P_4ON_{12}$ and $Sr_{16}Si_9P_9O_7N_{33}$. b) Graphs of the EDX and ICP-OES results showing the percentage of each element on the y-axis and the respective elemental types on the x-axis.

4.2.2 Structure Elucidation Process

All compounds crystallize well enough to be studied by SCXRD (Figure 4.1a). In this way, we obtained preliminary structure models of the form $Sr_u(Si, P)_v(O, N)_w$ where *u*, *v*, and *w* are given by the number of sites and their multiplicities. The subdivision of the sites into Sr, (Si, P), and (O, N) sites is chemically unambiguous. This means that all atomic Sr positions can be determined solely based on X-ray diffraction due to the high X-ray contrast compared to Si, P, N and O.[10] In contrast, Si^{4+} and P^{5+} can occupy the same sites as network-forming cations with comparable charges and sizes. The same applies to the ligands N^{3-} and O^{2-}. The fundamental challenge with such networks is therefore to determine whether there is substitutional disorder of Si/P and O/N, i.e., whether a crystallographic site is occupied by more than one type of atom. The low X-ray contrast of Si/P and O/N make SCXRD an unsuitable method for this discrimination. Instead, we addressed these challenges with a complementary approach of elemental analysis, NMR spectroscopy, and LCC. In a first step, we determined the empirical sum formulas by measuring the Si:P ratio using energy-dispersive X-ray (EDX) and inductively coupled plasma optical emission spectroscopy (ICP-OES), if available (Figure 4.1b). The N:O ratio was extracted by enforcing charge neutrality. Considering these results and the isolobal relationship of Si–O and P–N, we obtain $Sr_3Si_{1+x}P_{3-x}O_{2+x}N_{7-x}$ (x≈0.2), $Sr_5Si_{2+x}P_{4-x}O_{1+x}N_{12-x}$ (x≈0.3–0.5), and $Sr_{16}Si_{9-x}P_{9+x}O_{7-x}N_{33+x}$ (x≈0.1). This makes them the first representatives of the oxonitridosilicate phosphates. In the interest of readability, we will only use idealized sum formulas in this contribution where x=0. In a second step, we performed solid-state NMR measurements on the bulk samples of $Sr_3SiP_3O_2N_7$ and $Sr_5Si_2P_4ON_{12}$ to investigate the substitutional ordering of the networks, while LCC provided information on the ordering of the ligands and of $Sr_{16}Si_9P_9O_7N_{33}$ as a whole, since NMR measurements were not possible on single particles. However, before we delve into the complexity of the structure elucidation process of disordered compounds, we believe it is beneficial to first understand the final structure models and then work our way back. To do this, it is also necessary to emphasize the similarities between the three compounds $Sr_3SiP_3O_2N_7$, $Sr_5Si_2P_4ON_{12}$, and $Sr_{16}Si_9P_9O_7N_{33}$.

4.2.3 The Fundamental Disorder Unit

All compounds share a common fundamental building unit, which according to Liebau can be described as a *vierer* single chain of $(Si,P)(O,N)_4$ tetrahedra with a regular tetrahedral orientation of down, down, up, up (Figure 4.2a).[11] The tetrahedra are subject to a flexible

statistical occupation of Si and P which can range from Si:P = 1:3 ($Sr_3SiP_3O_2N_7$) to Si:P = 1:2 ($Sr_5Si_2P_4ON_{12}$) to Si:P = 1:1 ($Sr_{16}Si_9P_9O_7N_{33}$). This supports the trend mentioned above that most mixed networks are dominated by the smaller NFC, here P^{5+}. In agreement with Pauling, the bridging ligands are occupied with N and the terminal ligands with O.[12–14] This structural unit is found in all disordered Sr–(Si, P)–(O, N) networks described in this work, which is why we refer to it as the fundamental disorder unit (FDU). In addition to the flexible compositions, the FDU also shows variable bonding patterns perpendicular to the chain. We illustrate this in Figure 4.2 a) Graphical illustration of the fundamental disorder unit showing the relative orientation of the tetrahedra and the possible compositions of central atoms as well as the ligands. b) Possible FDU motifs as double chains, whereby the second motif is either mirrored (m), translated (t) or both.b for motifs of double chains, including transformations such as mirroring and translation in the chain direction. We will see below that combinations A and C are sufficient to obtain a good understanding of the title compounds. For the sake of completeness, we also consider the literature known $Sr_5Si_2P_6N_{16}$ as an example of B.[8] Combination D is yet unknown and remains the subject of future research.

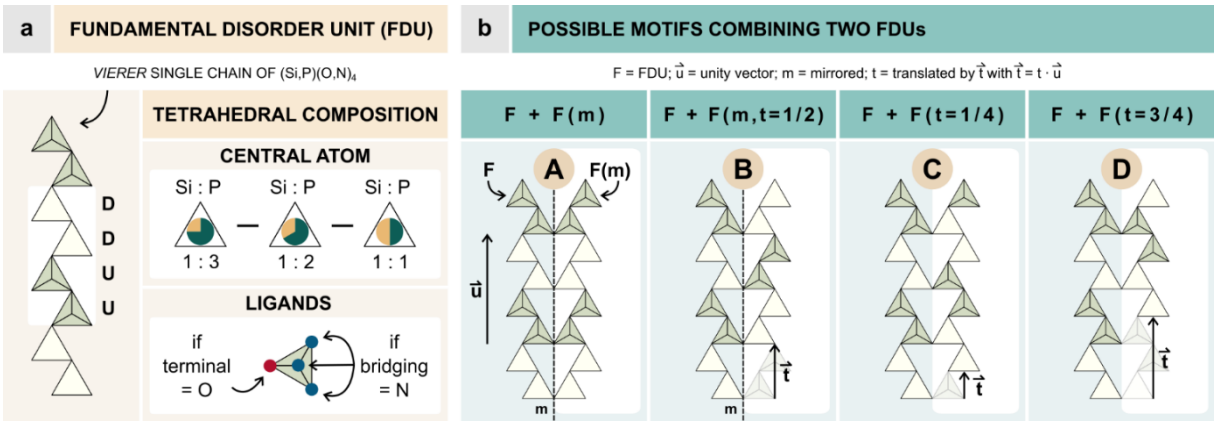

Figure 4.2 a) Graphical illustration of the fundamental disorder unit showing the relative orientation of the tetrahedra and the possible compositions of central atoms as well as the ligands. b) Possible FDU motifs as double chains, whereby the second motif is either mirrored (m), translated (t) or both.

4.2.4 Structure Description

Since our compounds crystallize in different space groups, they do not share the same reference coordinate system for the anionic (Si,P)–(O,N) networks. However, for a better comparison, we introduced a new one, in which *x* points in the chain direction of the FDU, *y* points in direction of neighboring FDUs and *z* points in the remaining direction perpendicular to *x* and *y* (Figure 4.3). The FDU motif in $Sr_3SiP_3O_2N_7$ is of type A and not connected along *y*.

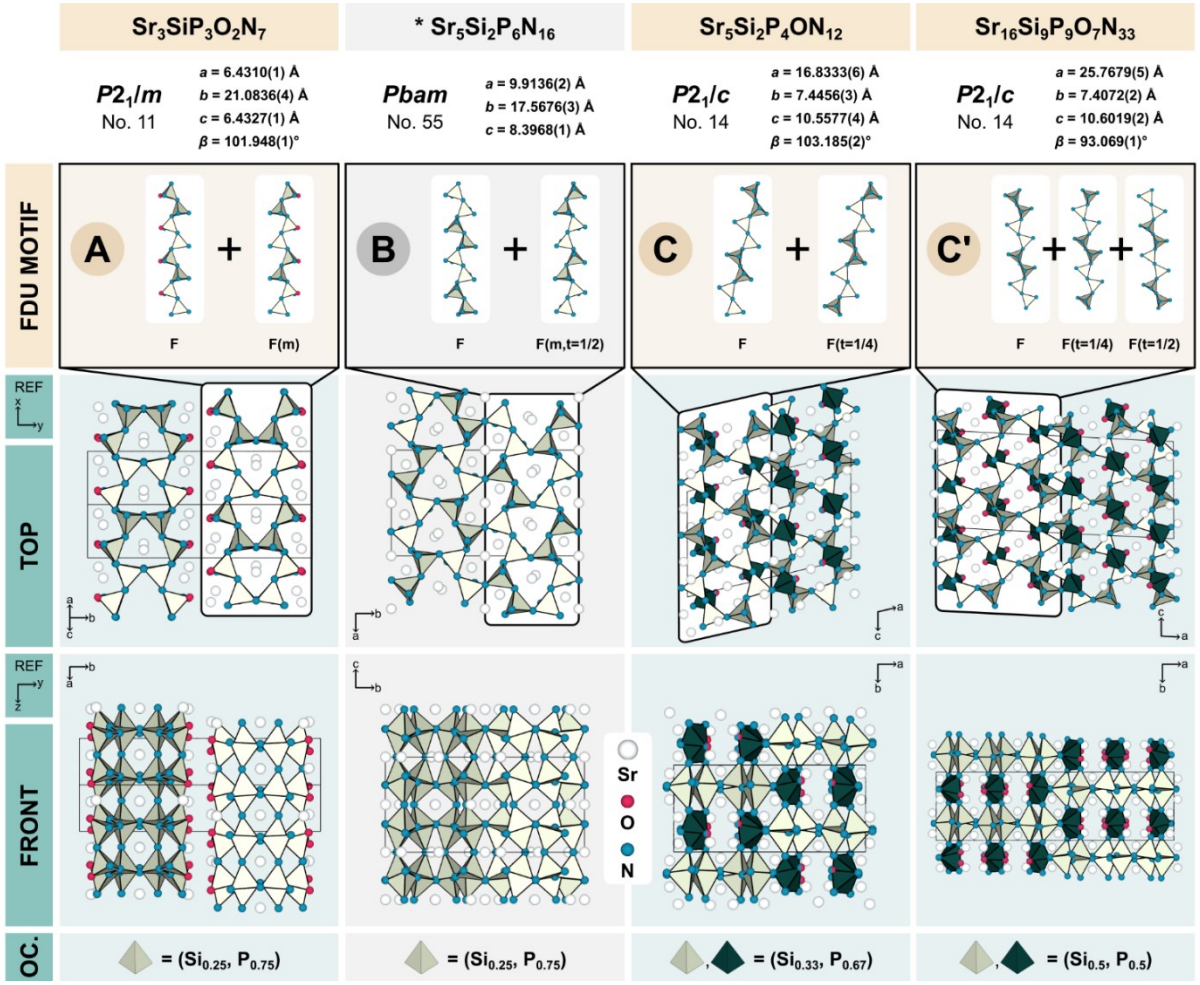

Figure 4.3 Crystal structures and parameters of $Sr_3SiP_3O_2N_7$, $Sr_5Si_2P_6N_{16}$ (*), $Sr_5Si_2P_4ON_{12}$, and $Sr_{16}Si_9P_9O_7N_{33}$. The FDU motifs were extracted for better visualization. Viewing directions were chosen to run along the reference coordinate system *z* (TOP) and *x* (FRONT). All tetrahedra in a compound exhibit the same occupation of central atoms. Color differentiation (light and dark green) was chosen to highlight different roles in the structure. Sr is white, N blue, and O red. (* from literature)

This leads to terminal ligands that are occupied by O. In *z*-direction, the double chains thus formed are fully condensed. As mentioned above, $Sr_5Si_2P_6N_{16}$ comprises the type B FDU motif, which is fully connected in *y* and *z* direction. This is also the reason why it is the only fully nitridic representative. It is noteworthy that although $Sr_3SiP_3O_2N_7$ and $Sr_5Si_2P_6N_{16}$ share the same Si:P ratio of 1:3, they exhibit different FDU motifs. This means that it is not the Si:P ratio that is decisive for the structure, but rather the reaction to the size of the tetrahedral gaps of the Sr–O/N lattice. In contrast, $Sr_5Si_2P_4ON_{12}$ and $Sr_{16}Si_9P_9O_7N_{33}$ differ significantly in their Si:P ratio of 1:2 and 1:1, respectively, but form quite similar FDU motifs, both of which can be assigned to type C. The difference is that the FDU motif in $Sr_5Si_2P_4ON_{12}$ is composed of two FDUs, while in $Sr_{16}Si_9P_9O_7N_{33}$ it is composed of three FDUs. These FDU motifs are not directly connected along *y* or *z* in either compound. The connection is established by a second motif,

which we call the linker moiety. For better differentiation, they are marked dark green in Figure 4.3. The linker tetrahedra have the same mixed occupancy of the central atoms as the tetrahedra in the FDUs. The difference is that they contain terminal ligands with a substitutional disorder of N and O. The N content on these sites is 50% for $Sr_5Si_2P_4ON_{12}$ and 12.5% for $Sr_{16}Si_9P_9O_7N_{33}$. For more crystallographic information refer to Table 9.4–Table 9.7. All crystallographic information files (CIF) are provided free of charge.[15] With this in mind, we want to take a step back and prove the substitutional disorder in our networks by NMR measurements and low-cost crystallographic calculations.

4.2.5 Nuclear Magnetic Resonance Spectroscopy

In SiPONs, only the two spin-1/2 nuclides ^{29}Si and ^{31}P are reasonably well suited for NMR spectroscopy. The only magnetically active isotope of oxygen is ^{17}O with a very low natural abundance of about 0.4%, which makes NMR impossible without isotope enrichment. 99.6% of natural nitrogen consists of the nuclide ^{14}N with spin-1, which means that it has a quadrupole moment. This makes the recording and interpretation of a ^{14}N NMR signal only possible in a highly symmetric environment, which does not exist in SiPONs or SiAlONs.[16] In contrast, ^{31}P has a natural abundance of 100%, a high Larmor frequency and acceptable relaxation times in the range of hundreds of seconds in the investigated compounds. The NMR of ^{29}Si poses a greater challenge, as the nuclide has a natural abundance of only about 5%, a comparatively low Larmor frequency and very long relaxation times (>3000 s) in our compounds. This situation can be improved by isotopic enrichment of ^{29}Si, very long measurement times or large sample quantities. The latter two options were attempted for $Sr_3SiP_3O_2N_7$, but the resulting ^{29}Si NMR spectrum was of significantly lower quality than the ^{31}P spectra (Figure 9.6). Since the ^{29}Si and ^{31}P NMR results are complementary, we focused on the latter. As shown in Figure 4.4a for $Sr_3SiP_3O_2N_7$ and Figure 4.4b for $Sr_5Si_2P_4ON_{12}$, we measured ^{31}P NMR both directly and in a cross-polarized experiment with ^{1}H. The fact that the $^{31}P\{^{1}H\}$ spectra show signals should be surprising at this point, considering the hydrogen-free empirical sum formulas. However, the reason for this is a well-known phenomenon: the isolobal relationship between an oxide anion O^{2-} and an imide group $(NH)^{2-}$. Two prominent examples of this can be found in literature with the pairings PON/P(NH)N and $Si_2ON_2/Si_2(NH)N_2$.[17–20] $(NH)^{2-}$ can also be incorporated into the structure through the isolobal relationship of Si–(NH) and P–N, which becomes clear when we extend the previous example

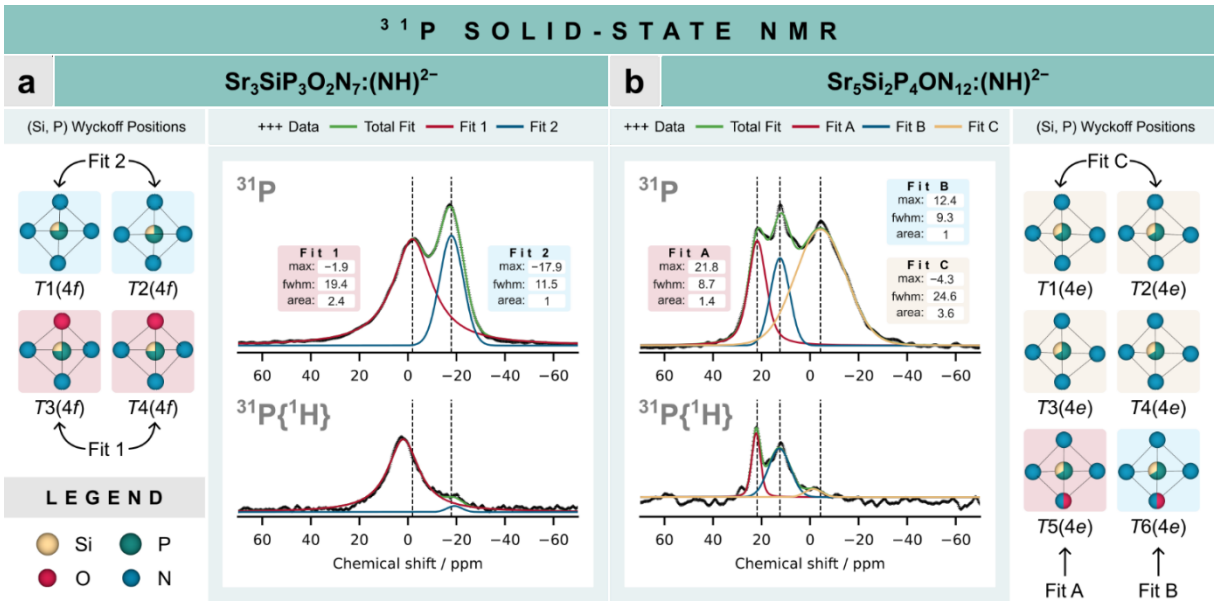

Figure 4.4 ^{31}P and $^{31}P\{^1H\}$ solid- state NMR spectra of (a) $Sr_3SiP_3O_2N_7:NH^{2-}$ and (b) $Sr_5Si_2P_4ON_{12}:NH^{2-}$. The curves were fitted with a combination of two or three Voigt curves. Each fit was assigned to the according Wyckoff positions, shown as red, blue, or yellow background. Their multiplicities are specified in brackets. Maxima and full widths at half-maximum (*fwhm*) are given in ppm, areas in arbitrary units. Measurements were conducted at room temperature and 20 kHz.

to Si_2ON_2/$Si_2(NH)N_2$/$SiPN_3$.[21] This raises the question of whether our empirical formulas were correct to begin with or whether H should be included. The answer is that the formulas are correct as they are. On the one hand, IR spectra of $Sr_3SiP_3O_2N_7$ and $Sr_5Si_2P_4ON_{12}$ show no significant change in transmission observed in the 3300–3600 cm^{-1} range, which is typically associated with N–H stretching vibrations (Figure 9.2). On the other hand, the signals of the $^{31}P\{^1H\}$ spectra are very weak, considering that the cross-polarized experiments comprised 324 scans and the direct measurements only eight. On this basis, we propose that the incorporation of $(NH)^{2-}$ is best viewed as a low-percentage doping, written as $Sr_3SiP_3O_2N_7:(NH)^{2-}$. Possible hydrogen sources are traces of hydrolysis products of SrO or SiO_2, as well as residual imide groups in amorphous Si_3N_4. The reason we devote so much space to this doping is that it was very helpful for the interpretation of our NMR spectra as we will see below. For $Sr_3SiP_3O_2N_7$, we found two broad peaks at –1.9 and –17.9 ppm with full widths at half maximum (*fwhm*) of 19.4 and 11.5 ppm, respectively (Figure 4.4a). This indicates two types of environments in our structure, namely (Si, P)N_4 (*T*1, *T*2) and (Si, P)ON_3 (*T*3, *T*4) tetrahedra. Which of both environments belong to which peak can be deduced from the $^{31}P\{^1H\}$ spectrum, which also shows two peaks in the same region. In our case the much stronger left peak corresponds to the (Si, P)ON_3 environment, based on the assumption that

the exchange of the terminal P–O/P–(NH) is much more likely than the bridging P–N–P/P–(NH)–Si due to the chemical similarity of O^{2-} and $(NH)^{2-}$. Nevertheless, both mechanisms appear. Therefore, *T*1/*T*2 were assigned to fit 2 and *T*3/*T*4 to fit 1. For the order in the network, we argue that the widths of our signals with half-widths greater than 11 ppm are reliable indications for the mixed occupancy of the central atoms Si and P, since irregular second coordination environments, as occur in substitutional disorder, lead to a significant broadening of the signals via a chemical shift distribution. To support this argument, we have measured ^{31}P NMR of previously published $Sr_2SiP_2N_6$ and $Sr_5Si_7P_2N_{16}$, two compounds that do not exhibit Si and P mixing.[7,8] In both cases, the signals are significantly narrower with a half-width of 6.2 and 6.3 ppm, respectively (Figure 9.7). As for the areas of fit 1 and fit 2, we would expect a ratio of 1:1 from the Wyckoff positions, but the result is approximately 2:1 in both the ^{31}P and ^{29}Si NMR spectra (Figure 9.6). Since this mismatch occurs in both cases, this rules out preferential occupation of Si and P. A more reasonable explanation is the Nuclear Overhauser Effect (NOE), in which the signals from Si and P nuclei closer to ^{1}H nuclei may be amplified due to dipole-dipole cross-relaxation under proton decoupling.[22]

In the case of $Sr_5Si_2P_4ON_{12}$ the ^{31}P and ^{31}P{^{1}H} spectra show three peaks at 21.8 (fit A), 12.4 (fit B), and –4.3 ppm (fit C). Following the same principle from before, we can divide the six potential crystallographic sites of P into two groups, namely four (Si, P)N_4 environments (*T*1–*T*4) and two (Si, P)$N_3(N_{0.5}O_{0.5})$ environments (*T*5, *T*6). *T*1–*T*4 belong to the FDU motif with quite similar chemical environments, which is consistent with the very broad signal at –4.3 ppm with *fwhm* = 24.6 ppm. In contrast, *T*5 and *T*6 form the linker tetrahedra whose neighborhoods are clearly different from *T*1–*T*4. This explains why we see two additional signals with half-widths of 8.7 and 9.3 ppm for fit A and fit B, respectively. Although both signals are narrower than fit C, they are still significantly wider than the reference signals at about 6 ppm, again indicating substitutional disorder. We propose that the upfield signal (fit B) is assigned to *T*6 due to stronger shielding, which can be inferred from the smaller tetrahedral volume (V(*T*6) = 2.27 Å^3) and smaller mean distance to O, N, and Sr (d(*T*6) = 2.43 Å) in the first and second coordination sphere compared to *T*5 (V(*T*5) = 2.30 Å^3, d(*T*5) = 2.46 Å). However, the differences are small, suggesting that theoretical chemical shift calculations are required to support this assignment. The area ratio of the fits of 1.4:1:3.6 agrees well with the theoretical ratio expected from the Wyckoff positions for *T*5:*T*6:*T*1–*T*4 = 1:1:4. Although NMR is a very sensitive method that

provides deep insights into our (Si, P)–(O, N) networks, there were still challenges that required complementary low-cost crystallographic calculations. One of them is the substitutional order of the ligands N and O, which has so far been taken as given without justification. Another is the overall substitutional order of both Si/P and O/N of the third compound $Sr_{16}Si_9P_9O_7N_{33}$, for which no NMR data were available due to the lack of a bulk sample.

4.2.6 Low-Cost Crystallographic Calculations

First, it is important to understand what kind of calculations were used and why. In previous work, we introduced “low-cost crystallographic calculations” as a generic term for widely used crystallographic concepts that require low computational resources compared to density functional theory (DFT) calculations.[7,8] In this work, we calculated (Si, P)–(O, N) bond lengths, (Si, P)(O, N)$_4$ tetrahedral volumes, as well as electrostatic potential energies (Ewald Summation), charge distributions (CHARDI), and bond valence sums (BVS) of Si^{4+} and P^{5+}.[23–28] On the one hand, we use the distributions of bond lengths and volumes in a compound to distinguish between N and O. If the distributions show a discrete clustering with a clear gap, it can be assumed in most cases that there are distinct O sites. In conjunction with Pauling's principle, according to which O^{2-} tends to occupy terminal positions, a reliable assignment of the ligands is possible.[12–14] On the other hand, the Ewald summation, CHARDI, and BVS are useful methods to evaluate the occupancy of the central atoms. However, the most important information we obtain from all methods is whether the overall atom assignment in our network is congruent. To evaluate the congruence, we need to define reference data from literature compounds for each method. In case of a pure nitridosilicate, this would be, for example, the mean Si–N bond length or the mean electrostatic potential energy of Si^{4+}. The main problem is that there is insufficient reference data for SiPONs, as Si and P need not only to be present in the reference, but also in the same ratio as in the sample. This can be remedied by calculating the corresponding expected values from pure nitridosilicates and nitridophosphates as the percentage composition as shown in equation 3 using the example of a ($Si_{0.5}$,$P_{0.5}$)–N bond length.

$$\langle d\rangle((Si_{0.5},P_{0.5})\text{–}N) = 0.5 \cdot \overline{d}(Si\text{–}N) + 0.5 \cdot \overline{d}(P\text{–}N) \quad (3)$$

$\langle d\rangle$: expected distance, $\overline{d}$: average distance calculated from literature

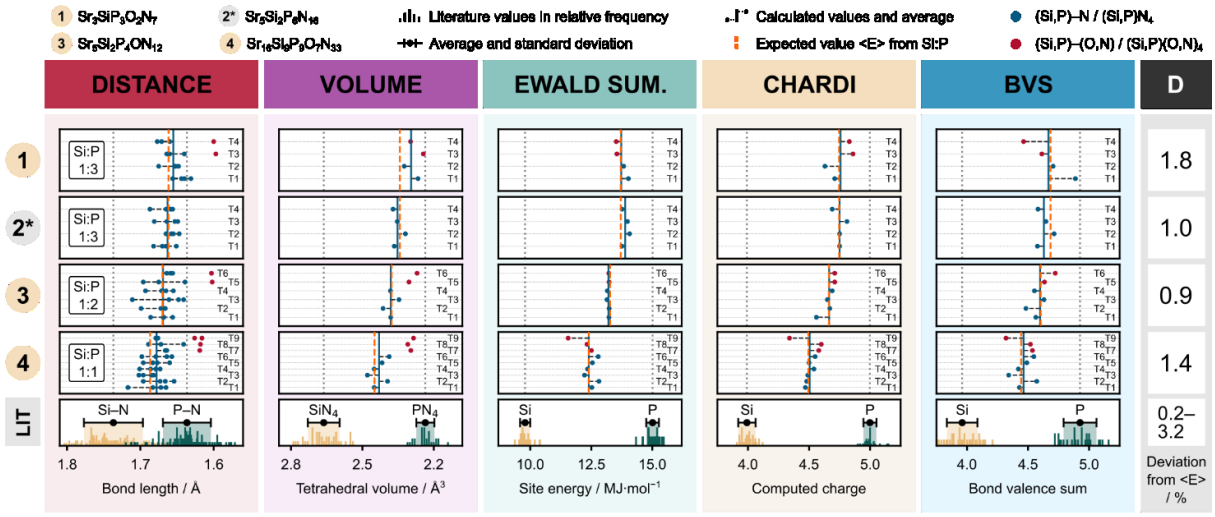

Figure 4.5 Graphical representation of the LCC results. Columns 1–5 show the respective methods, column 6 the total percentage deviation from expected values, rows 1–4 the compounds, and the bottom row the literature data (LIT) in relative frequency. The calculated values are marked as blue if only N is present in the first coordination sphere, otherwise red for O and N. Expected values are dashed orange lines. (Si, P)–(O, N) bond lengths and (Si, P)(O, N)$_4$ volumes were dismissed for the calculation of total deviations due to the lack of suitable reference data. (* from literature)

As a numerical measure of congruence, we used the total percentage deviation (D) of the sample data from these expected values. Typically, total deviations below 3% indicate a congruent model.[7] The comparison and evaluation of all five methods for the four compounds $Sr_3SiP_3O_2N_7$ (1), $Sr_5Si_2P_6N_{16}$ (2), $Sr_5Si_2P_4ON_{12}$ (3), and $Sr_{16}Si_9P_9O_7N_{33}$ (4), are shown in Figure 4.5, where columns 1–5 represent each method, column 6 the total percentage deviation, rows 1–4 the respective compounds and the bottom row the reference data of pure nitridosilicates and nitridophosphates. Each cell shows a stack of all (Si, P) Wyckoff positions with their calculated values, their overall average, and their expected value. From this we can draw several conclusions: First, for compounds (1), (3) and (4), we can see that the bond lengths exhibit clustering, with the bridging ligands N comprising the longer bond lengths (blue) and the terminal ligands (O, N) the shorter bond lengths (red). The proportion of N in the terminal ligands was calculated taking charge neutrality into account and yields 0, 50, and 12.5% for (1), (3), and (4), respectively. The clustering is also reflected in the tetrahedral volumes, however, with one exception. In $Sr_3SiP_3O_2N_7$ (1), the tetrahedral volumes of *T*1–*T*4 are approximately equal despite their different composition of (Si, P)N_4 and (Si, P)ON_3. This shows that the central atoms Si and P in this compound do not determine the structure, but only react to the Sr–O/N lattice. The bond lengths show that the central atoms move towards O as a ligand, but only at the cost of a proportional elongation of the other bonds. As a future

prospect, this behavior would generally be interesting for isolobal substitutions of the counter cations and ligands, e.g., the substitution of Sr–O by La–N would yield $SrLa_2SiP_3N_9$. Second, the calculated values of the Ewald summation, CHARDI, and BVS agree very well with what we expect. This would not be the case if we assumed a wrong substitutional order of our networks, as we have shown in previous work for $Sr_5Si_2P_6N_{16}$ (2).[8] Finally, according to our definition, all networks with total deviations of 0.9–1.8% are congruent. This completes the complex structure elucidation process of the $Sr_3SiP_3O_2N_7$, $Sr_5Si_2P_4ON_{12}$, and $Sr_{16}Si_9P_9O_7N_{33}$ compounds. Although the structural features of this new class of compounds were our main focus, we also wanted to take a closer look at their optical properties, as SiAlONs, nitridosilicates and nitridophosphates are known to exhibit excellent luminescence properties.[29,30] This was also with the ulterior motive of placing these compounds in a larger context regarding their applicability and suitability as model systems.

4.2.7 Optical Properties

In our research, the addition of 1 mol% Eu^{2+} to the starting materials is a standard procedure when alkaline earth metals are present. Apart from obvious reasons such as the search for new phosphor materials, this doping also serves as a useful indicator for the differentiation and separation of multiphase products. The suitability of Eu^{2+} as a dopant is not limited to its high sensitivity to its coordination environment, but also includes the fact that even low concentrations are sufficient at which no structure-altering effects normally occur. Without further analysis, the experienced eye can already gain valuable information from a purely visual inspection of the luminescence behavior of a compound. The most prominent example is the emission maxima but also the nature of the luminescence such as brightness and decay time or even absence can indicate structural features to look out for, as we will see below. In our work, we found that $Sr_3SiP_3O_2N_7$ (1) shows green emission at first glance, $Sr_5Si_2P_6N_{16}$ (2) shows orange emission, $Sr_5Si_2P_4ON_{12}$ (3) shows very weak yellow to orange emission, and $Sr_{16}Si_9P_9O_7N_{33}$ (4) shows no visible emission when irradiated with ultraviolet light. This is also reflected in the corresponding PLE and PL measurements shown in Figure 4.6a. Only under a luminescence microscope were we able to show that (4) also exhibits very weak orange emission. In a next step, we tried to attribute these brightness gradations to one of the following causes. First, luminescence can be quenched by N–H vibrations. As discussed above, we concluded that this is unlikely, as in this case $Sr_3SiP_3O_2N_7$ should be the most affected due

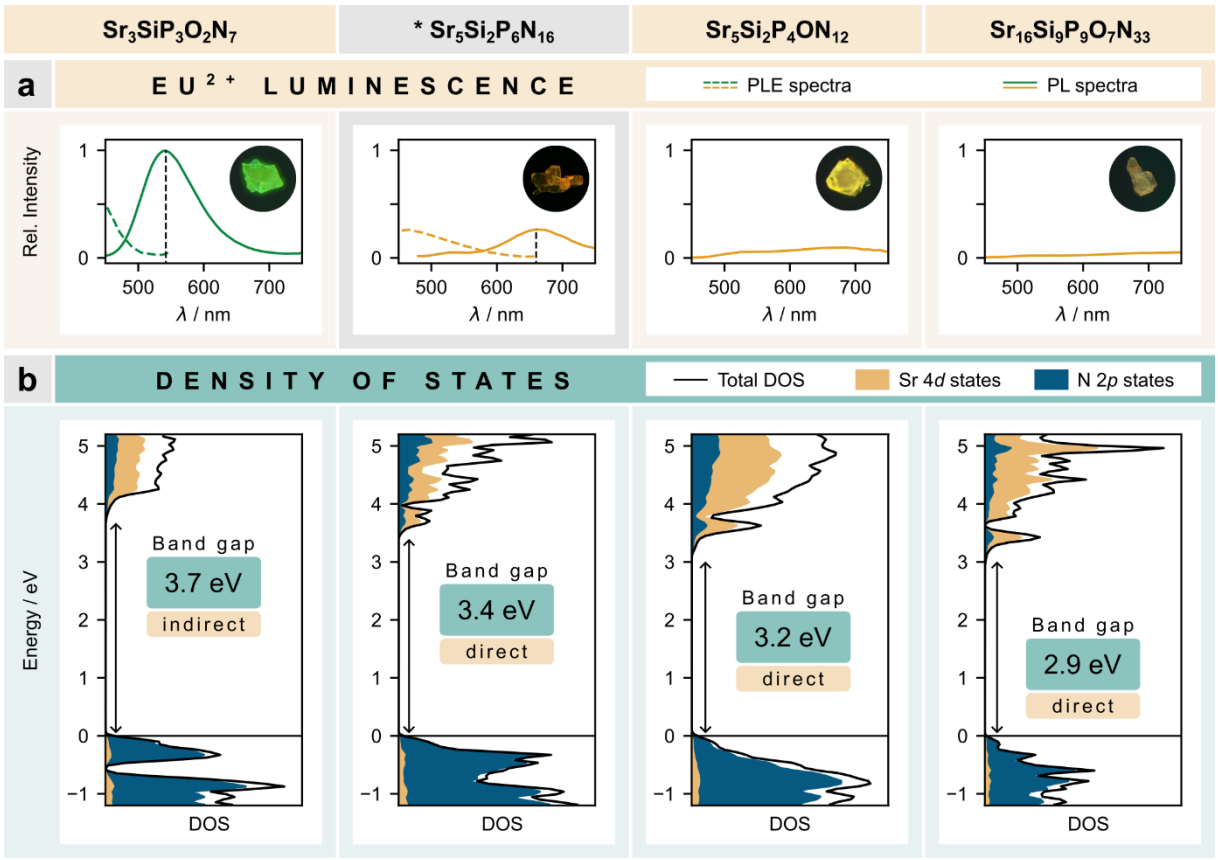

Figure 4.6 (a) PL and PLE spectra as well as (b) densities of states (DOS) of $Sr_3SiP_3O_2N_7$, $Sr_5Si_2P_6N_{16}$ (*), $Sr_5Si_2P_4ON_{12}$, and $Sr_{16}Si_9P_9O_7N_{33}$. Luminescence measurements were performed on single particles of comparable size at room temperature. Luminescence images were excited at 395 nm. (* PL/PLE from literature; electronic calculations original.)

to the highest amount of O/N–H. Second, we reduced the dopant concentration to less than 0.5 mol% to avoid potential concentration quenching, which resulted in no change. Third, we investigated the band gaps of all compounds to check whether photoionization as a thermal quenching mechanism is a reasonable explanation.[31] Since no bulk samples were available for (2) and (4), we decided to calculate all band gaps by periodic DFT calculations using the LMBJ functional.[32,33] This approach demonstrated to lead to band gaps that are in better agreement with experimental data than those calculated with traditional generalized gradient approximation (GGA) functionals such as PBE.[34] Nevertheless, absolute values should only give an idea about the magnitude of the gaps, while the relative differences are reliable. The resulting densities of states (DOS) were plotted in Figure 4.6b with the theoretical band gaps of 3.7, 3.4, 3.2, and 2.9 eV, respectively, for compounds (1)–(4). This stepwise gradation of band gaps can be interpreted as a form of band gap tuning in insulators. The main contributions to the valence band near the Fermi level come from N 2*p* and Sr 4*d* states. The

same is true for the conduction band with inverse ratios. $Sr_3SiP_3O_2N_7$ is the only compound with a predicted indirect band gap, while the others are direct. All valence band minima are found at the high-symmetry Γ-point (Figure 9.8–Figure 9.11). The decrease in band gaps agrees well with the decrease in luminescence which is why we believe that photoionization is a reasonable quenching mechanism. This could be supported by low-temperature measurements of the luminescence. However, we realize and hope that this can only be the beginning of more comprehensive studies of the electronic and optical properties of these compounds. Due to the high-pressure synthesis, their applicability is limited, nevertheless, their structural and optical relationships make them excellent model systems for theoretical calculations, such as those performed by Shafei et al. on $UCrC_4$-type phosphors.[35,36]

4.3 Conclusion

We successfully synthesized and characterized the new oxonitridosilicate phosphates $Sr_3SiP_3O_2N_7$, $Sr_5Si_2P_4ON_{12}$ and $Sr_{16}Si_9P_9O_7N_{33}$, which are the first representatives of this class. The synthesis was carried out under high-temperature and high-pressure conditions and led to a phase purity of the target compounds of over 90 % for the first two, which was confirmed by Rietveld refinements. The structures of these compounds share a common fundamental disorder unit (FDU) characterized by a single *vierer* chain of (Si, P)(O, N)$_4$ tetrahedra with substitutional disorder of the central atoms. We introduced a classification of FDU motifs and showed that $Sr_3SiP_3O_2N_7$, $Sr_5Si_2P_4ON_{12}$ and $Sr_{16}Si_9P_9O_7N_{33}$, as well as $Sr_5Si_2P_6N_{16}$ known from literature, comprise three of the four possible bonding patterns. The structure elucidation process included advanced techniques such as SCXRD, EDX and ICP-OES, ^{31}P and $^{31}P\{^1H\}$ NMR, as well as low-cost crystallographic calculations. Using these methods, we were able understand the composition of the networks in which central atoms and terminal ligands exhibit substitutional disorder of Si/P and O/N, respectively. In contrast, we found that bridging ligands are only occupied by N. Compared to previous work, where we often used STEM to verify occupancy in mixed (Si, P) networks, we were able to show that ^{31}P NMR spectroscopy is a viable alternative, especially when combined with $^{31}P\{^1H\}$ NMR. In this context, we also added new ^{31}P NMR data on literature known $Sr_2SiP_2N_6$ and $Sr_5Si_7P_2N_{16}$ as reference for ordered (Si, P) networks.[7,8] LCC were used to confirm our results and provide insight into $Sr_{16}Si_9P_9O_7N_{33}$ where no NMR data were available. As an impetus for future research, we briefly investigated the optical properties of the SiPONs when doped with Eu^{2+}. To this end, we performed PLE and PL measurements as well as DFT calculations to determine the densities of states and band gaps. The differences in emission properties were attributed to various factors, including potential N–H vibrations, concentration quenching and photoionization as a thermal quenching mechanism. The latter was identified as the most likely among them. In summary, this study presents the first three representatives of oxonitridosilicate phosphates, a new class of compounds remarkable for their versatility but also for the systematic nature of the FDU motifs. The unique structure-property relationships observed in these compounds make them exciting model systems for future studies, especially in the context of luminescence and quenching mechanisms as well as band gap tuning in insulators.

4.4 Acknowledgements

The authors express their gratitude to Christian Minke for providing the SEM images, EDX, and NMR measurements. Appreciation is also extended to Jennifer Steinadler for her assistance in interpreting the NMR spectra. Reinhard Pritzl and Sophia Wandelt are acknowledged for their engaging discussions and invaluable contributions to the concept and interpretation. (Department of Chemistry, LMU Munich) M.D. also thanks the Bundesministerium für Bildung und Forschung (BMBF) for financial support. Open Access funding enabled and organized by Projekt DEAL.

4.5 References

(1) Yamada, T.; Yamao, T.; Sakata, S. Development of SiAlON - From Mechanical to Optical Applications. *Key Eng. Mater.* **2007**, *352*, 173–178. https://doi.org/10.4028/WWW.SCIENTIFIC.NET/KEM.352.173.

(2) Xie, R. J. Development of Sialon Phosphors and Their Applications to Solid-State Lighting. *J. Ceram. Soc. Jpn.* **2020**, *128* (10), 710–717. https://doi.org/10.2109/JCERSJ2.20097.

(3) Lauterbach, R.; Schnick, W. High-Temperature Synthesis and Single-Crystal X-Ray Structure Determination of $Sr_{10}Sm_6Si_{30}Al_6O_7N_{54}$ — a Layered Sialon with an Ordered Distribution of Si, Al, O, and N. *Solid State Sci.* **2000**, *2* (4), 463–472. https://doi.org/10.1016/S1293-2558(00)00147-3.

(4) Esmaeilzadeh, S.; Grins, J.; Shen, Z.; Edén, M.; Thiaux, M. Study of Sialon S-Phases $M_2Al_xSi_{12-x}N_{16-x}O_{2+x}$, *M* = Ba and $Ba_{0.9}Eu_{0.1}$, by X-Ray Single Crystal Diffraction, X-Ray Powder Diffraction, and Solid-State Nuclear Magnetic Resonance. *Chem. Mater.* **2004**, *16* (11), 2113–2120. https://doi.org/10.1021/CM031129L/SUPPL_FILE/CM031129L.CIF.

(5) Lauterbach, R.; Schnick, W. Sm2Si3O3N4 Und Ln2Si2,5Al0,5O3,5N3,5 (Ln = Ce, Pr, Nd, Sm, Gd) – Neuer Synthetischer Zugang Zu N-haltigen Melilith-Phasen Und Deren Einkristall-Röntgenstrukturanalyse. *Z. Anorg. Allg. Chem.* **1999**, *625*, 429–434.

(6) Lauterbach, R.; Schnick, W. Synthese, Kristallstruktur Und Eigenschaften Eines Neuen Sialons - $SrSiAl_2O_3N_2$. *Z. Anorg. Allg. Chem* **1998**, *624*, 1154–1158. https://doi.org/10.1002/(SICI)1521-3749(199807)624:7%3C1154::AID-ZAAC1154%3E3.0.CO;2-P.

(7) Dialer, M.; Pointner, M. M.; Strobel, P.; Schmidt, P. J.; Schnick, W. (Dis)Order and Luminescence in Silicon-Rich (Si,P)–N Network $Sr_5Si_7P_2N_{16}:Eu^{2+}$. *Inorg. Chem.* **2024**, *63* (2), 1480–1487. https://doi.org/10.1021/acs.inorgchem.3c04109.

(8) Dialer, M.; Pointner, M. M.; Wandelt, S. L.; Strobel, P.; Schmidt, P. J.; Bayarjargal, L.; Winkler, B.; Schnick, W. Order and Disorder in Mixed (Si, P)–N Networks $Sr_2SiP_2N_6:Eu^{2+}$ and $Sr_5Si_2P_6N_{16}:Eu^{2+}$. *Adv. Opt. Mater.* **2023**, 2302668. https://doi.org/10.1002/adom.202302668.

(9) Eisenburger, L.; Oeckler, O.; Schnick, W. High-Pressure High-Temperature Synthesis of Mixed Nitridosilicatephosphates and Luminescence of *AE*$SiP_3N_7:Eu^{2+}$ (*AE*=Sr, Ba). *Chem. Eur. J.* **2021**, *27* (13), 4461–4465. https://doi.org/10.1002/chem.202005495.

(10) Brown, P. J.; Fox, A. G.; Maslen, E. N.; O'Keefe, M. A.; Willis, B. T. M. Intensity of Diffracted Intensities. In *International Tables for Crystallography Volume C: Mathematical, physical and chemical tables*; Prince, E., Ed.; Springer Netherlands: Dordrecht, 2004; p 554. https://doi.org/10.1107/97809553602060000600.

(11) Liebau, F. *Structural Chemistry of Silicates*, 1st ed.; Springer Berlin Heidelberg: Berlin, Heidelberg, 1985. https://doi.org/10.1007/978-3-642-50076-3.

(12) Fuertes, A. Prediction of Anion Distributions Using Pauling's Second Rule. *Inorg. Chem.* **2006**, *45* (24), 9640–9642. https://doi.org/10.1021/IC061640R/SUPPL_FILE/IC061640RSI20061106_122451.PDF.

(13) George, J.; Waroquiers, D.; Di Stefano, D.; Petretto, G.; Rignanese, G. M.; Hautier, G. The Limited Predictive Power of the Pauling Rules. *Angew. Chem. Int. Ed.* **2020**, *59* (19), 7569–7575. https://doi.org/10.1002/ANIE.202000829.

(14) Pauling, L. *The Nature of the Chemical Bond, An Introduction to Modern Structural Chemistry*, 3rd ed.; Cornell University Press: Ithaca, 1960.

(15) Deposition Numbers 2325125, 2325127, and 2325128 contain the supplementary crystallographic data for this paper. These data are provided free of charge by the joint Cambridge Crystallographic Data Centre and Fachinformationszentrum Karlsruhe Access Structures service.

(16) Bräuniger, T.; Kempgens, P.; Harris, R. K.; Howes, A. P.; Liddell, K.; Thompson, D. P. A Combined $^{14}N/^{27}Al$ Nuclear Magnetic Resonance and Powder X-Ray Diffraction Study of Impurity Phases in β-Sialon Ceramics. *Solid State Nucl. Magn. Reson.* **2003**, *23* (1–2), 62–76. https://doi.org/10.1016/S0926-2040(02)00016-4.

(17) Léger, J. M.; Haines, J.; Chateau, C.; Bocquillon, G.; Schmidt, M. W.; Hull, S.; Gorelli, F.; Lesauze, A.; Marchand, R. Phosphorus Oxynitride PON, a Silica Analogue: Structure and Compression of the Cristobalite-like Phase; P-T Phase Diagram. *Phys. Chem. Miner.* **2001**, *28* (6), 388–398. https://doi.org/10.1007/S002690100161/METRICS.

(18) Schnick, W.; Lücke, J. Darstellung, Kristallstruktur Und IR-Spektroskopische Untersuchung von Phosphor(V)-Nitrid-Imid, HPN_2. *Z. Anorg. Allg. Chem.* **1992**, *610* (4), 121–126. https://doi.org/10.1002/ZAAC.19926100120.

(19) Brosset, C.; Idrestedt, I. Crystal Structure of Silicon Oxynitride, Si_2N_2O. *Nature* **1964**, *201* (4925), 1211. https://doi.org/10.1038/2011211a0.

(20) Peters, D.; Jacobs, H. Ammonothermalsynthese von Kristallinem Siliciumnitridimid, Si_2N_2NH. *J. Less-Common Met.* **1989**, *146* (C), 241–249. https://doi.org/10.1016/0022-5088(89)90382-2.

(21) Baldus, H. P.; Schnick, W.; Lücke, J.; Wannagat, U.; Bogedain, G. Silicon Phosphorus Nitride, the First Ternary Compound in the Silicon-Phosphorus-Nitrogen System. *Chem. Mater.* **1993**, *5* (6), 845–850. https://doi.org/https://doi.org/10.1021/cm00030a021.

(22) Neuhaus, D. Nuclear Overhauser Effect. In *Encyclopedia Magnetic Resonance*; John Wiley & Sons, Ltd: Chichester, UK, 2011. https://doi.org/10.1002/9780470034590.emrstm0350.pub2.

(23) Link, L.; Niewa, R. *Polynator* : A Tool to Identify and Quantitatively Evaluate Polyhedra and Other Shapes in Crystal Structures. *J. Appl. Crystallogr.* **2023**, *56* (6), 1855–1864. https://doi.org/10.1107/S1600576723008476.

(24) Toukmaji, A. Y.; Board, J. A. Ewald Summation Techniques in Perspective: A Survey. *Comput. Phys. Commun.* **1996**, *95*, 73–92.

(25) Nespolo, M. Charge Distribution as a Tool to Investigate Structural Details. IV. A New Route to Heteroligand Polyhedra. *Acta Crystallogr. Sect. B* **2016**, *72* (1), 51–66. https://doi.org/10.1107/S2052520615019472.

(26) Nespolo, M.; Guillot, B. *CHARDI2015*: Charge Distribution Analysis of Non-Molecular Structures. *J. Appl. Crystallogr.* **2016**, *49* (1), 317–321. https://doi.org/10.1107/S1600576715024814.

(27) Altomare, A.; Cuocci, C.; Giacovazzo, C.; Moliterni, A.; Rizzi, R.; Corriero, N.; Falcicchio, A. *EXPO2013*: A Kit of Tools for Phasing Crystal Structures from Powder Data. *J. Appl. Crystallogr.* **2013**, *46* (4), 1231–1235. https://doi.org/10.1107/S0021889813013113.

(28) Momma, K.; Izumi, F. *VESTA 3* for Three-Dimensional Visualization of Crystal, Volumetric and Morphology Data. *J. Appl. Crystallogr.* **2011**, *44* (6), 1272–1276. https://doi.org/10.1107/S0021889811038970.

(29) Fang, M. H.; Bao, Z.; Huang, W. T.; Liu, R. S. Evolutionary Generation of Phosphor Materials and Their Progress in Future Applications for Light-Emitting Diodes. *Chem. Rev.* **2022**, *122* (13), 11474–11513. https://doi.org/10.1021/ACS.CHEMREV.1C00952/ASSET/IMAGES/LARGE/CR1C00952_0041.JPEG.

(30) Hariyani, S.; Sójka, M.; Setlur, A.; Brgoch, J. A Guide to Comprehensive Phosphor Discovery for Solid-State Lighting. *Nat. Rev. Mater.* **2023**, *8* (11), 759–775. https://doi.org/10.1038/s41578-023-00605-6.

(31) Dorenbos, P. Thermal Quenching of Lanthanide Luminescence via Charge Transfer States in Inorganic Materials. *J. Mater. Chem. C* **2023**, *11* (24), 8129–8145. https://doi.org/10.1039/D2TC04439K.

(32) Rauch, T.; Marques, M. A. L.; Botti, S. Local Modified Becke-Johnson Exchange-Correlation Potential for Interfaces, Surfaces, and Two-Dimensional Materials. *J. Chem. Theory Comput.* **2020**, *16* (4), 2654–2660. https://doi.org/10.1021/ACS.JCTC.9B01147/SUPPL_FILE/CT9B01147_SI_001.PDF.

(33) Rauch, T.; Marques, M. A. L.; Botti, S. Accurate Electronic Band Gaps of Two-Dimensional Materials from the Local Modified Becke-Johnson Potential. *Phys. Rev. B* **2020**, *101* (24), 245163. https://doi.org/10.1103/PhysRevB.101.245163.

(34) Perdew, J. P.; Burke, K.; Ernzerhof, M. Generalized Gradient Approximation Made Simple. *Phys. Rev. Lett.* **1996**, *77* (18), 3865–3868. https://doi.org/10.1103/PhysRevLett.77.3865.

(35) Shafei, R.; Maganas, D.; Strobel, P. J.; Schmidt, P. J.; Schnick, W.; Neese, F. Electronic and Optical Properties of Eu^{2+} -Activated Narrow-Band Phosphors for Phosphor-Converted Light-Emitting Diode Applications: Insights from a Theoretical Spectroscopy Perspective. *J. Am. Chem. Soc.* **2022**, *144* (18), 8038–8053. https://doi.org/10.1021/jacs.2c00218.

(36) Shafei, R.; Strobel, P. J.; Schmidt, P. J.; Maganas, D.; Schnick, W.; Neese, F. A Theoretical Spectroscopy Study of the Photoluminescent Properties of Narrow Band Eu^{2+}-Doped Phosphors Containing Multiple Candidate Doping Centers. Prediction of an Unprecedented Narrow Band Red Phosphor. *Phys. Chem. Chem. Phys.* **2024**, 26(7), 6277–6291. https://doi.org/10.1039/D3CP06039J.

5

Super-Tunable $LaSi_3N_5$ Structure Type: Insights into the Structure and Luminescence of $SrSi_2PN_5:Eu^{2+}$

Marwin Dialer, Reinhard M. Pritzl, Sophia L. Wandelt, Dmitry Khalyavin, Peter J. Schmidt, Wolfgang Schnick

CHEMISTRY OF MATERIALS, ACS

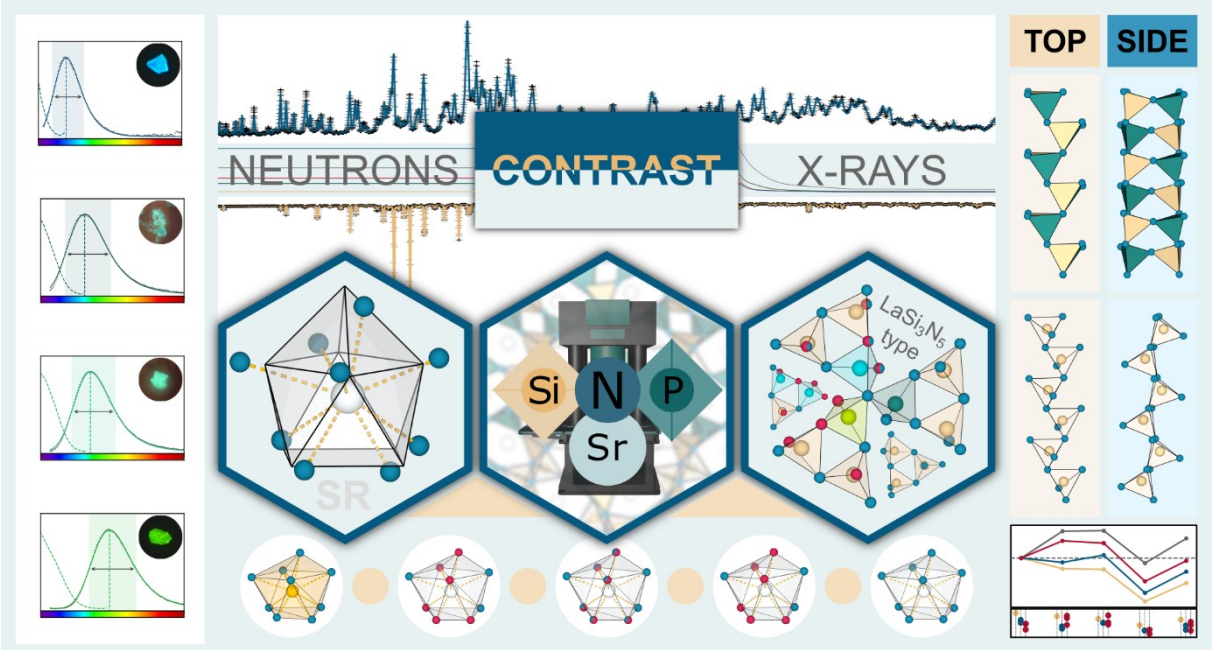

Reprinted (adapted) with permission from

Chem. Mater. **2024**, *36*, 3933–3940.

ABSTRACT: In this study, the structural and luminescence properties of $SrSi_2PN_5:Eu^{2+}$ and its analogues within the $LaSi_3N_5$ structure type are investigated by using a variety of analytical techniques including X-ray diffraction (XRD), ^{31}P solid-state NMR, and powder neutron diffraction. We are exploring the challenges of chemical similarity and low X-ray contrast between the key elements to extend our analytical capabilities by powder neutron diffraction (PND) for (Si,P)–N networks. In principle, PND shows greater differences in scattering contrasts for O/N and Si/P, although it does not surpass standard powder XRD in elemental discrimination of Si/P within the network. The Eu^{2+} doping of $SrSi_2PN_5$ demonstrates the potential for tunable optical applications within the group of $LaSi_3N_5$ analogous materials. Our results contribute to the understanding of the structural diversity and luminescence mechanisms of nitridosilicate phosphates and emphasize the importance of a comprehensive analytical approach in materials science, with implications for the future development of optoelectronic devices.

5.1 Introduction

The simple truth in materials chemistry is that one must interact with new materials in order to characterize them. The question, however, is how. When one is interested in the atomic arrangement of materials, there are generally two approaches, namely interaction with the electron clouds or nuclei of the atoms. The first method that comes to mind for the interaction with the electron cloud in crystalline materials is X-ray diffraction (XRD), which is available for both single crystals and powder samples. This method is very powerful to study the atomic positions, the interatomic distances, the angles, and even the elemental compositions if the X-ray contrast is sufficiently high for the present elements. However, we are particularly interested in materials for which this is not the case. Not necessarily because of the analytical challenge but because of the tunability of these compounds, which is based on the chemical similarity of the components. This chemical similarity is often associated with similar size and electron density, which reduces the X-ray contrast, but makes it possible to occupy the same crystallographic sites. Prominent examples of this are the pairings O^{2-} and N^{3-} as well as the network-forming cations Si^{4+} and P^{5+}.[1,2] It is no coincidence that these elements make up the main component of the compound presented in this contribution, namely $SrSi_2PN_5$, a new strontium nitridosilicate phosphate. Since the investigation and differentiation of these elements by X-ray diffraction are often considered insufficient, it must be complemented by other analytical methods. In a previous work, we have already proposed different approaches to distinguish Si^{4+} and P^{5+}, e.g. by exploiting their characteristic X-ray emissions in scanning transmission electron microscopy in combination with energy-dispersive X-ray spectroscopy at

atomic resolution, better known as scanning transmission electron microscopy energy-dispersive X-ray (STEM-EDX) maps.[3,4] However, their discrimination is not limited to the interaction with their electron clouds, as we have shown by studying the ^{31}P solid-state NMR spectra of disordered oxonitridosilicate phosphates (SiPONs), $Sr_3SiP_3O_2N_7$ and $Sr_5Si_2P_4ON_{12}$.[2] While these methods provide reliable results, in this work, we were interested in further extending the analytical capabilities for this class of compounds by powder neutron diffraction (PND) and adding another method that interacts with the nuclei. Not as a proof of principle, but due to the fact that we expected better scattering contrasts for Si^{4+}/P^{5+} and O^{2-}/N^{3-} when using neutrons compared to X-rays. The correct physical quantification of this can be found in the atomic form factors for X-rays and the coherent scattering lengths (b_c) for neutrons, as illustrated in Figure 5.1a and Figure 5.1b.[5,6] The neutron contrast of about 3.5 fm for O and N is known to be well suited for their discrimination, while the contrast of about 1 fm for Si and P is comparatively low even with neutrons, confirming the need to test the suitability of this method for Si and P discrimination. However, the interest in $SrSi_2PN_5$ is not only limited to the analytical challenge but also extends to the exciting tunability of optical properties with respect to the related compounds $SrSiAl_2O_3N_2$, $SrSi_2AlO_2N_3$, and $SrSi_2BeO_3N_2$, upon doping with Eu^{2+}.[7–9] All compounds are connected via the isolobal principle and share a common structure type, namely, that of $LaSi_3N_5$, which is itself already a prominent luminescent material when doped with Ce^{3+}.[10,11] Due to the single crystallographic activator site in this structure type and the variable composition, this group offers a promising and comparatively simple approach to understand compositional aspects of the change in the luminescence properties.

5.2 Results and Discussion

5.2.1 Synthesis

$SrSi_2PN_5$ was synthesized in a multianvil press at 1400 °C and a pressure of 3 GPa. As starting materials, we utilized stoichiometric amounts of $Sr(N_3)_2$, amorphous Si_3N_4 and semi-crystalline α-P_3N_5 (Equation 1).

$$3\ Sr(N_3)_2 + 2\ Si_3N_4 + P_3N_5 \rightarrow 3SrSi_2PN_5 + 8\ N_2 \qquad (1)$$

The reaction results in a microcrystalline, colorless powder that is inert to moisture and air (Figure 1c). When doped with Eu^{2+} using EuN, the powder exhibits pale green color and shows green luminescence upon radiation with ultraviolet light.

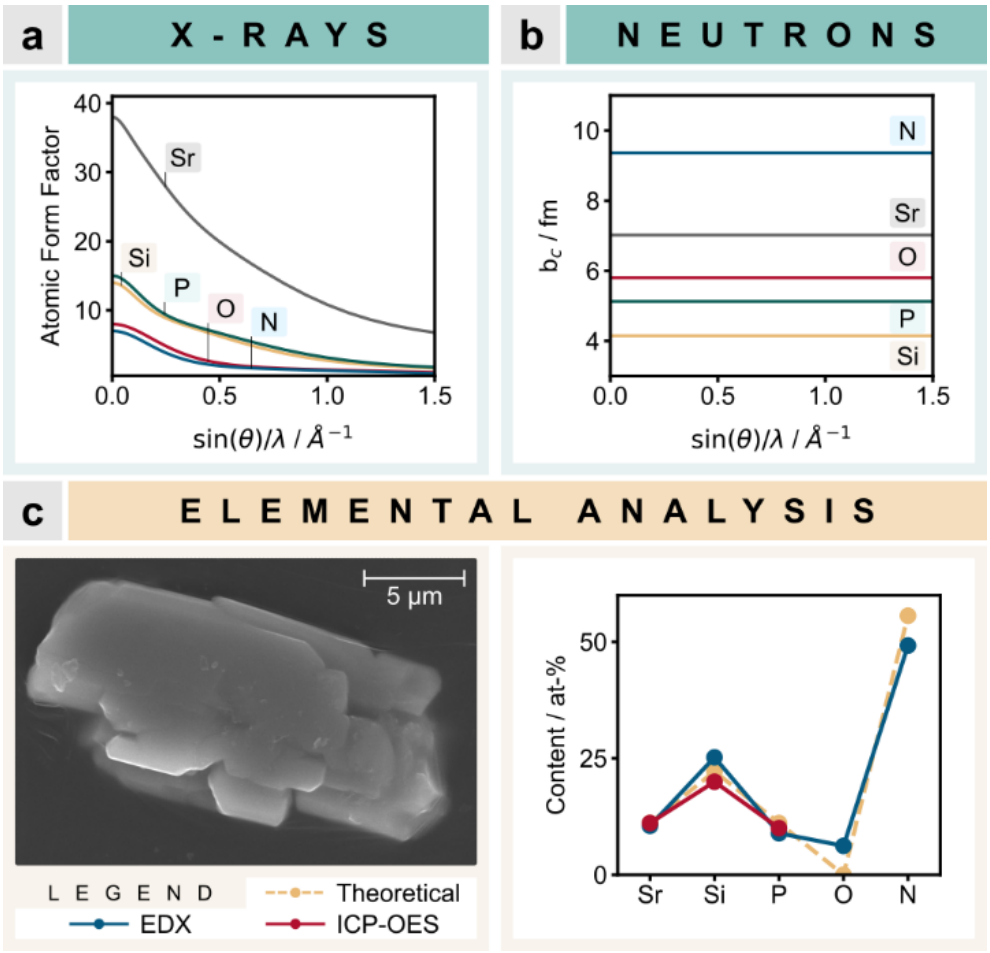

Figure 5.1 (a) Atomic form factors and (b) coherent scattering lengths of Sr, Si, P, O, and N atoms. The atomic form factors show very weak contrasts of Si/P and O/N, while the coherent scattering lengths show significantly better contrast. (c) Scanning electron microscopy (SEM) image of $SrSi_2PN_5$ and comparison of the results for energy-dispersive X-ray spectroscopy and inductively coupled plasma optical emission spectroscopy (ICP-OES). More details are given in Figure 10.1 and Table 10.1.

5.2.2 Structure Elucidation Process

As mentioned above, the structure elucidation process of $SrSi_2PN_5$ addressed challenges typical of (Si,P)–N networks, which arise from the limited X-ray contrast of Si/P and O/N/(NH), leading to ambiguous ordering variants of the network. Consideration of O^{2-} as well as $(NH)^{2-}$ during this process is good practice even when it is not intentionally added due to the isolobal relationship between Si–O, Si–(NH), and P–N. Typical sources of trace amounts of O and H are adsorbed H_2O or hydrolysis products in the starting materials. As a first step, we collected single-crystal XRD data, which yielded the preliminary structural model $Sr(Si,P)_3(O,N)_5$. In combination with elemental analyses, we obtained the empirical sum formula of $SrSi_{2+x}P_{1-x}N_{5-x}O_x$ ($x \approx 0.1$) (Figure 5.1c). Since EDX is not suitable for light elements, the O/N content was deduced from charge neutrality and later confirmed by powder neutron diffraction. For the sake of readability, only the idealized sum formula $SrSi_2PN_5$ is used in this contribution. The incorporation of significant amounts of hydrogen was excluded by infrared spectroscopy and cross-polarized $^{31}P\{^1H\}$ NMR measurements. In both cases, the corresponding signals were absent or negligible (Figure 10.3 and Figure 10.4). To understand the basis on which we determined the order of the present (Si,P)–N network, it is beneficial to first understand the final structure model and then work backward.

5.2.3 Structure Description

$SrSi_2PN_5$ crystallizes in the structure type of $LaSi_3N_5$ in space group $P2_12_12_1$ (no. 19) with lattice parameters a = 4.84640(10), b = 7.7480(3), and c = 11.4066(3) Å. Further crystallographic data are listed in Table 10.3 and Table 10.4. The structure comprises an ordered, anionic, tetrahedral network of SiN_4 and PN_4 tetrahedra with a single crystallographic site for the Sr^{2+} counter ion in its vacancies (Figure 5.2a). The network can be described by two structural motifs *A* and *B* extending along *a* (Figure 5.2b). According to Liebau's classification of silicates, motif *A* corresponds to a *zweier* double chain in which each individual single chain consists of alternating PN_4 (P1) and SiN_4 (Si2) tetrahedra with the same orientation.[12] In contrast, motif *B* forms a *zweier* single chain of only SiN_4 (Si3) tetrahedra with alternating up and down orientation. The connectivity pattern of both motifs consists of an *A*-*B*-*A*-*B* sequence along *b* leading to a formal layer *C*. This layer *C* is in turn connected along *c* in a *C*-*D*-*C*-*D* sequence. The relationship between *C* and *D* is a 2_1-screw axis, as shown in Figure 5.2a. This is not surprising given the $P2_12_12_1$ space group. The Sr^{2+} environment can be described as a distorted

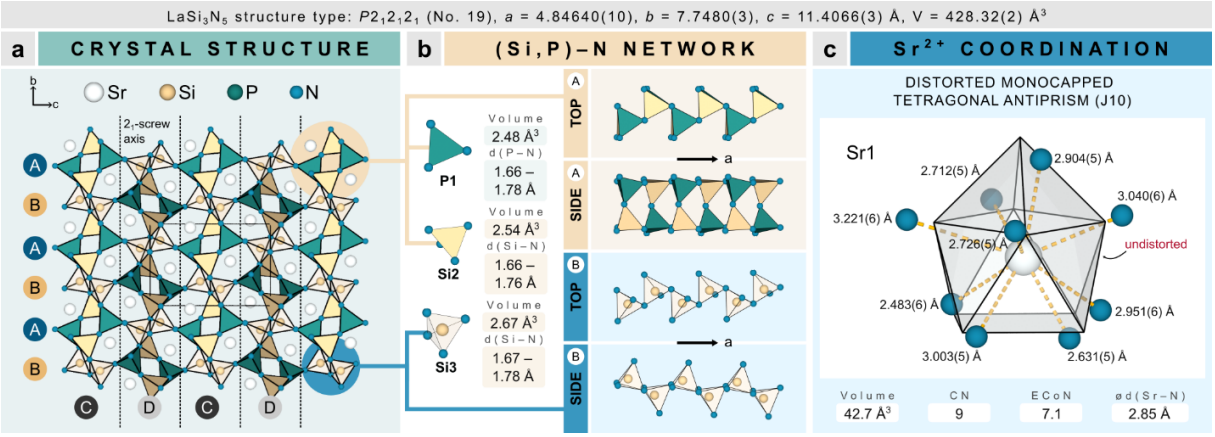

Figure 5.2 (a) Crystal structure of $SrSi_2PN_5$ along *a*. (b) Polyhedral description of the (Si,P)–N tetrahedra and illustration of the structural motifs *A* and *B*. (c) Depiction of the real and idealized Sr^{2+} environment as given by the program Polynator by Link et al..[14]

monocapped tetragonal antiprism corresponding to the Johnson body #10 (Figure 5.2c).[13,14] Here, Sr^{2+} is coordinated by nine N^{3-} ligands with an effective coordination number (*ECoN*) of 7.1 and a mean interatomic Sr–N distance of 2.85 Å. A more detailed classification of this structure with regard to its $LaSi_3N_5$ analogues is given below. Before that, it is necessary to prove the ordering of this network.

5.2.4 Powder X-ray and Neutron Diffraction

The determination of the ordering in the (Si,P)–N network involves an initial check of the possible ordering variants. In $SrSi_2PN_5$, there are three possible crystallographic sites available for two Si and one P resulting in three potential ordering variants, since the two Si species are combinatorially indistinguishable. Theoretically, there is also a fourth combination in which all tetrahedra have a mixed occupancy of ($Si_{0.67}$,$P_{0.33}$), but we were able to rule out this possibility by prior ^{31}P NMR spectroscopy (Figure 5.3). The ^{31}P spectrum shows a single narrow signal at -7.9 ppm with a half-width of 3.8 ppm, which indicates the ordered nature of our network, as has been discussed in previous work.[2] The weak additional peaks match well with those of the previously published minor side phase $Sr_3SiP_3O_2N_7$:$(NH)^{2-}$. Therefore, each variant is named after the position of P in $SrSi_2PN_5$, namely P1–P3 (Figure 5.4a). To evaluate the performance of powder neutron diffraction as a method for distinguishing Si and P, we compared it with standard powder X-ray diffraction. For both methods, we generated Rietveld refinements of all three ordering variants, of which the best fits are shown in Figure 5.4b and Figure 5.4c. For a better comparison, both diffraction patterns are plotted against 1/*d*, where *d* is the lattice

spacing. Conventional plots in 2ϑ for X-rays and *d* for time-of-flight neutron data, the refinements for P2 and P3, and the corresponding diffraction data are included in Figure 10.5 and Figure 10.6, Table 10.6 and Table 10.7. As quality factors to determine the best fit, we chose R_{Bragg} to assess the quality of the fit with respect to our target phase $SrSi_2PN_5$ and the goodness of fit (GoF) to assess the overall fit. The results show that for both PXRD and PND, the P1 variant clearly provides the best values, with relative deviations from R_{Bragg} of more than 10 % for P2 and P3 (Figure 5.4d). The same trend can be observed for the GoF, but in a much weaker form. It must be said that the quality of the two measurements and samples is certainly not identical, but comparable. Various low-percentage secondary phases in Figure 5.4c imply that the quality of the neutron sample in terms of phase fractions is significantly worse than that of the X-ray sample. However, the occurrence of these minor phases is better explained by the sensitivity of neutrons to the minor light-element phases. Finally, both PXRD and PND can provide reliable results of similar quality for order discrimination in the (Si,P)–N network. Considering the usual additional effort for neutron measurements, we cannot see any advantage for the discrimination of Si and P here. The exception is certainly the investigation of the O/N distribution. In our case, all ligands were confirmed as N by the neutron refinement. With all structural doubts removed, we want to discuss the structural relationship between the $LaSi_3N_5$ analogous compounds.

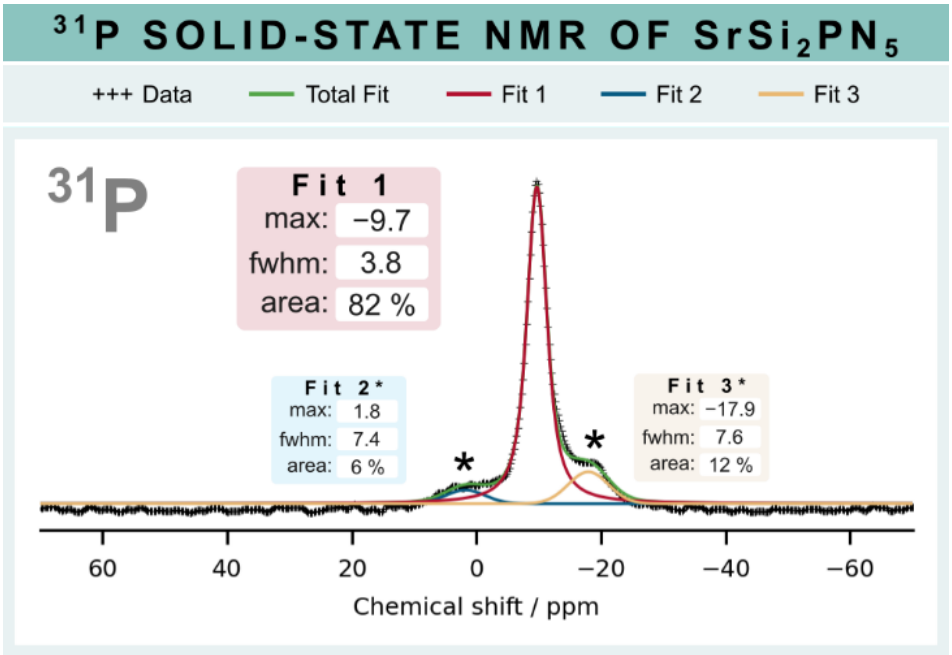

Figure 5.3 ^{31}P NMR spectrum of $SrSi_2PN_5$ with a signal at –9.7 ppm and a half-width of 3.8 ppm, which confirms the ordered nature of the (Si,P)–N network. Signals of the minor phase are marked by (*) and can be attributed to $Sr_3SiP_3O_2N_7$:$(NH)^{2-}$.[2]

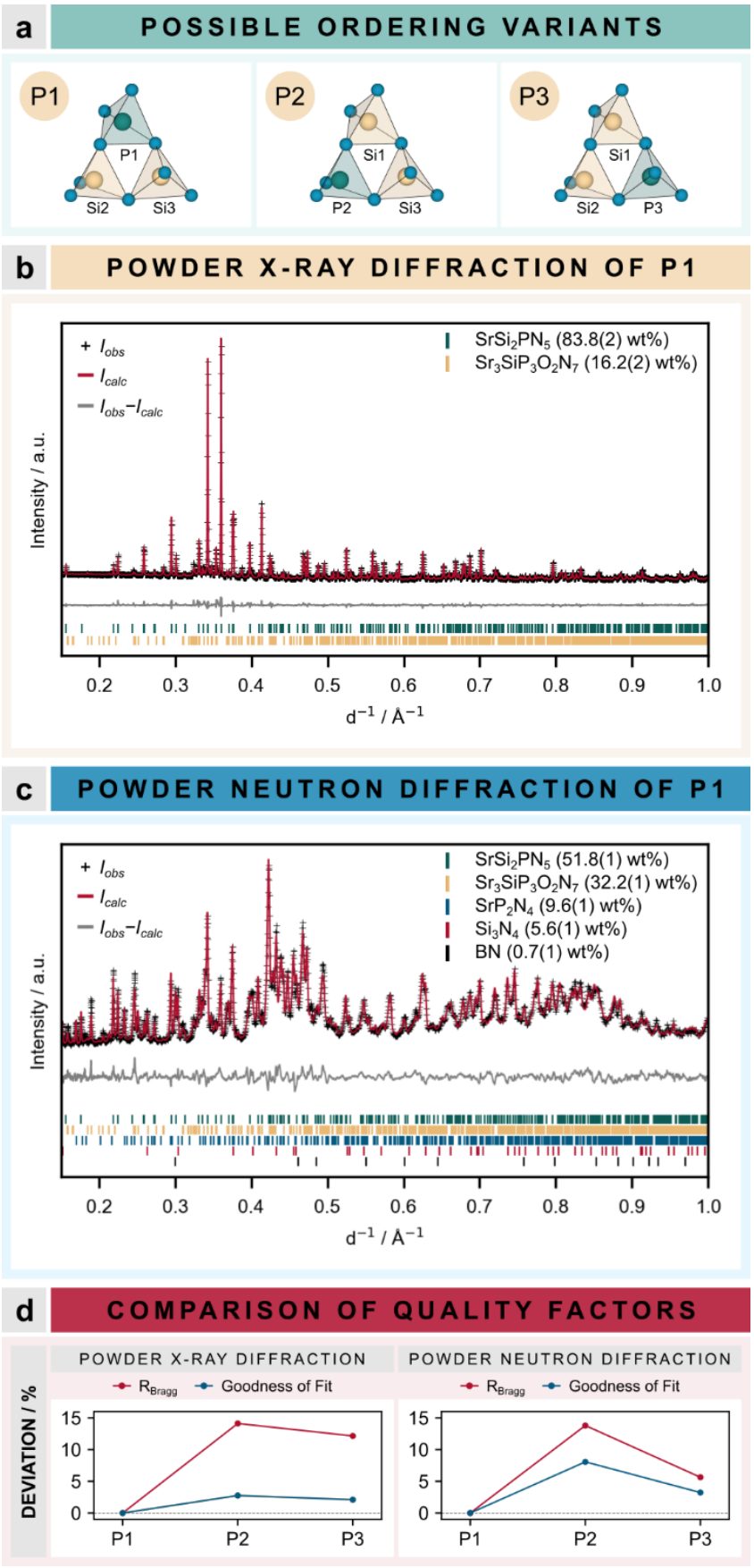

Figure 5.4 (a) Possible ordering variants of the (Si,P)–N network in $SrSi_2PN_5$. The Rietveld refinements of the best ordering variant based on (b) powder X-ray diffraction (Cu-$K_{\alpha 1}$ radiation) and (c) powder neutron diffraction (2ϑ = 90°). (d) Percentage deviation of the quality factors of the refinements.

5.2.5 $LaSi_3N_5$ Analogous Compounds

Table 5.1 Shannon Ionic Radii at Given Coordination Numbers (CN) and Allred-Rochow Electronegativities (EN) of N, O, Be, Al, Si, P, Sr, and La.[15,16]

Element	CN	Ionic Radius (Charge) / Å	EN
N	4	1.46 (−3)	3.1
O	4	1.38 (−2)	3.5
Be	4	0.27 (+2)	1.5
Al	4	0.39 (+3)	1.5
Si	4	0.26 (+4)	1.7
P	4	0.17 (+5)	2.1
Sr	9	1.31 (+2)	1.0
La	9	1.22 (+3)	1.1

The appeal of $LaSi_3N_5$ analogous compounds is primarily due to their rich compositional space, which has kept researchers engaged for over 40 years. The compounds are $LaSi_3N_5$, $SrSiAl_2O_3N_2$, $SrSi_2AlO_2N_3$, $SrSi_2BeO_3N_2$, and $SrSi_2PN_5$.[7–10] No structure model has been published for $SrSi_2AlO_2N_3$, so we collected single-crystal data and refined a reasonable structure model (Table 10.3 and Table 10.5). Elemental analysis clearly distinguishes the compound from its counterpart $SrSiAl_2O_3N_2$, but it is likely that both are better described as edge cases of a solid solution series of the form $SrSi_{2-x}Al_{1+x}O_{2+x}N_{3-x}$ (x = 0–1) (Figure 10.2, Table 10.2). The diversity of these networks is reminiscent of the well-established and studied $UCrC_4$ structure type with prominent representatives, such as $SrLiAl_3N_4:Eu^{2+}$ or $RbNa_2K(Li_3SiO_4)_4:Eu^{2+}$, which are used in white light-emitting diodes.[17,18] In addition, the single-crystallographic activator site in the $LaSi_3N_5$ structure type increases the attractiveness of such compounds, since, on the one hand, simple training models are required for theoretical calculations of the luminescence properties and, on the other hand, inhomogeneous broadening due to various emission centers is avoided. Structurally, the compounds differ in terms of their tetrahedral occupancies and activator sites, as shown in Figure 5.5a. $LaSi_3N_5$ is the only variant in which the counterion is La^{3+} and the network forming cations are exclusively Si^{4+}. In $SrSi_2BeO_3N_2$, $SrSi_2AlO_2N_3$, and $SrSi_2PN_5$, Sr^{2+} becomes the counterion and Si1 is substituted by either Be^{2+}, Al^{3+}, or P^{5+}. In $SrSiAl_2O_3N_2$, Al^{3+} also replaces Si2. In order to achieve charge balance of the

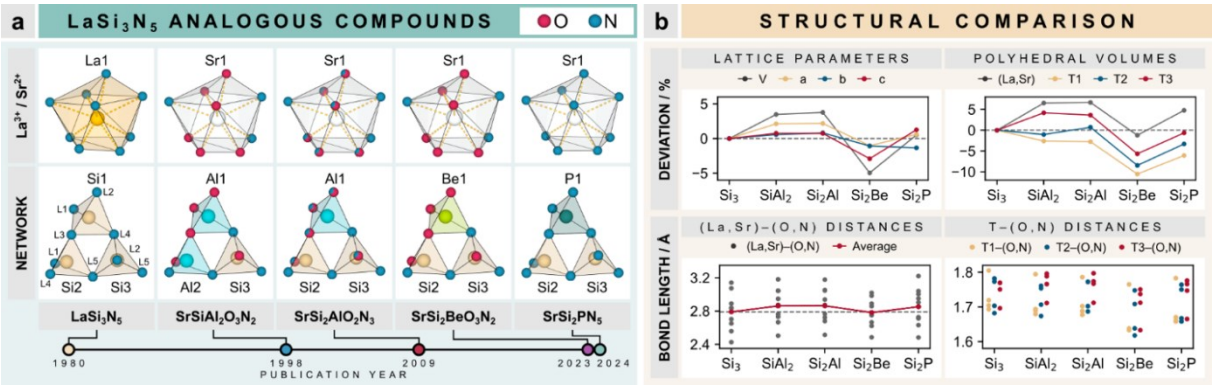

Figure 5.5 (a) Comparison of the $LaSi_3N_5$ analogous compounds with respect to their anionic network and countercation environment. (b) Quantitative comparison of the lattice parameters, polyhedral volumes, and interatomic distances of all analogs, which are named after their network's composition, e.g., Si_2P for $SrSi_2PN_5$.

resulting structures, O^{2-} proportionally replaces N^{3-} at the ligand positions L1–L3, while L4 and L5 remain N^{3-} in all variants. We attribute the interchangeability according to the isolobal principle to the chemical similarity of the ions involved, i.e. their similar ionic radii according to Shannon and their similar electronegativities according to Allred and Rochow (Table 1).[15,16] However, this explanation is only partially sufficient and raises the question of why such a diverse substitution is not observed more frequently in other structure types. One explanation is that the $LaSi_3N_5$ structure type is dominated by stabilization of the countercations, which gives the network greater freedom. This would also be supported by the fact that $BaSiAl_2O_3N_2$ is the only variant discovered so far that contains neither La^{3+} nor Sr^{2+}.[19] In addition to the qualitative assessments, we also wanted to take a look at the quantitative changes in these structures, as shown in Figure 5.5b.

To do so, we compared the lattice parameters, polyhedral volumes, as well as the (La,Sr)–(O,N) and *T*–(O,N) distances, where *T* = Be, Al, Si, P. In general, the observed changes are consistent with the change in ionic sizes, e.g., the introduction of Sr^{2+} increases volumes and distances compared to La^{3+}, while O^{2-} decreases them compared to N^{3-}. Nevertheless, there are some peculiarities that need to be pointed out. First, $SrSi_2BeO_3N_2$ shows a strong contraction of the whole structure compared to $LaSi_3N_5$ which means that the incorporation of 3/5 O^{2-} outweighs the exchange of La^{3+} by Sr^{2+}. Second, $SrSi_2PN_5$ is overall quite similar to $LaSi_3N_5$, which implies that the isolobal exchange of La^{3+}/Si^{4+} by Sr^{2+}/P^{5+} involves a good size balance. In fact, the sums of the ionic radii of these pairings both give 1.48 Å, although this is considered to be only an interesting coincidence. Third and finally, the bonding distribution in the tetrahedra *T*–(O,N) follows a particular pattern of short and long bonds. That is, *T*1 always consists of three short

bonds and one long bond, *T*2 consists of two short bonds and two long bonds, and *T*3 consists of only one short bond and three long bonds. When oxygen is present in the compounds, the ligands with shorter bonds are, as expected, the preferred crystallographic sites, but fully nitridic compounds exhibit the same distribution. This is a further indication that both the network-forming cations and the ligands are dominated by the countercations. As mentioned above, this rather tolerant behavior of the countercations toward their chemical environment makes them interesting candidates for doping with Eu^{2+}, which we discuss below.

5.2.6 Luminescence

To investigate the luminescence properties of the corresponding Sr compounds, all compounds were synthesized with a Eu^{2+} doping of less than 3 mol%. An exact specification of the doping is not possible at this point, as the syntheses were not phase pure. The synthesis of $La_{1-x}Si_3N_{5-x}O_x:Eu_x^{2+}$ with our means was not successful.[20] The photoluminescence (PL) emission and excitation (PLE) spectra were measured on single particles. The data for $SrSi_2BeO_3N_2:Eu^{2+}$ were taken from previous work.[9] To determine the maximum and half-width, all spectra were fitted with Pekarian type fit curves, as shown in Figure 5.6a.[21] The shape and width of the signals are in good agreement with a single activator site and also prove Eu^{2+} as the emitting species, i.e. a $5d \rightarrow 4f$ transition. Eu^{3+} is a line emitter with very narrow emissions around 600 nm, generally unaffected by the chemical environment and the underlying $4f \rightarrow 4f$ transitions. When irradiated with ultraviolet light (λ_{exc} = 400 nm), $SrSi_2BeO_3N_2:Eu^{2+}$ shows blue emission at 456 nm (full width at half-maximum (fwhm) = 66 nm / 3117 cm^{-1}), while $SrSiAl_2O_3N_2:Eu^{2+}$ and $SrSi_2AlO_2N_3:Eu^{2+}$ show cyan emission at 492 nm (fwhm = 95 nm / 3867 cm^{-1}) and 504 nm (fwhm = 92 nm / 3553 cm^{-1}), respectively. $SrSi_2PN_5:Eu^{2+}$ emits at 544 nm (fwhm = 99 nm / 3295 cm^{-1}) which is slightly shorter than the published value λ_{em} = 553 nm for $La_{1-x}Si_3N_{5-x}O_x:Eu_x^{2+}$.[22] This again underscores the similarity between the two as mentioned earlier. To evaluate the luminescence properties, it is common to take a closer look at the activator environment (Figure 5.6b). On the one hand, the red shift of the lowest-lying absorption band and emission from $SrSiAl_2O_3N_2:Eu^{2+}$ to $SrSi_2PN_5:Eu^{2+}$ can be well attributed to the increasing nitrogen content in the coordination sphere. This is due to the stronger nephelauxetic effect of N^{3-} compared to that of O^{2-}. Although the polyhedral volume and effective coordination number also decrease slightly and would cause a more pronounced Stokes shift, we consider this effect here to be negligible. On the other hand, $SrSi_2BeO_3N_2:Eu^{2+}$

behaves completely contrary to what would be expected on the basis of sole geometry arguments. Formally, the compositions of the first coordination sphere of Sr^{2+} in $SrSi_2BeO_3N_2$ and $SrSiAl_2O_3N_2$ are identical, differing only by the shorter interatomic distances of the former. However, these shorter distances should in principle lead to a significantly stronger ligand field splitting and thus to a red shift if the electron density of the ligands is comparable. What we observe is a strong blue shift of almost 40 nm, caused by a significantly smaller Stokes shift and emission bandwidth. This indicates that in this case our simple considerations of interatomic distances and compositions of the first coordination sphere are not sufficient to understand this luminescence behavior. In addition to the differences in the ligand electron density, the lattice dynamics, i.e. the electron-phonon coupling, could differ considerably in the host lattices under discussion. Since other Be containing Eu^{2+} phosphors like $SrLi_2Be_4O_6:Eu^{2+}$ show very narrow emission bands, a significantly lower average phonon frequency of the Eu^{2+} center in the $SrSi_2BeO_3N_2$ host lattice compared to $SrSi_{2-x}Al_{1+x}O_{2+x}N_{3-x}$ (x = 0–1) may explain the observed differences.[23] Future theoretical investigations of the respective excited states of Eu^{2+} in the studied host lattices should help to further improve our understanding of the observed luminescence properties.

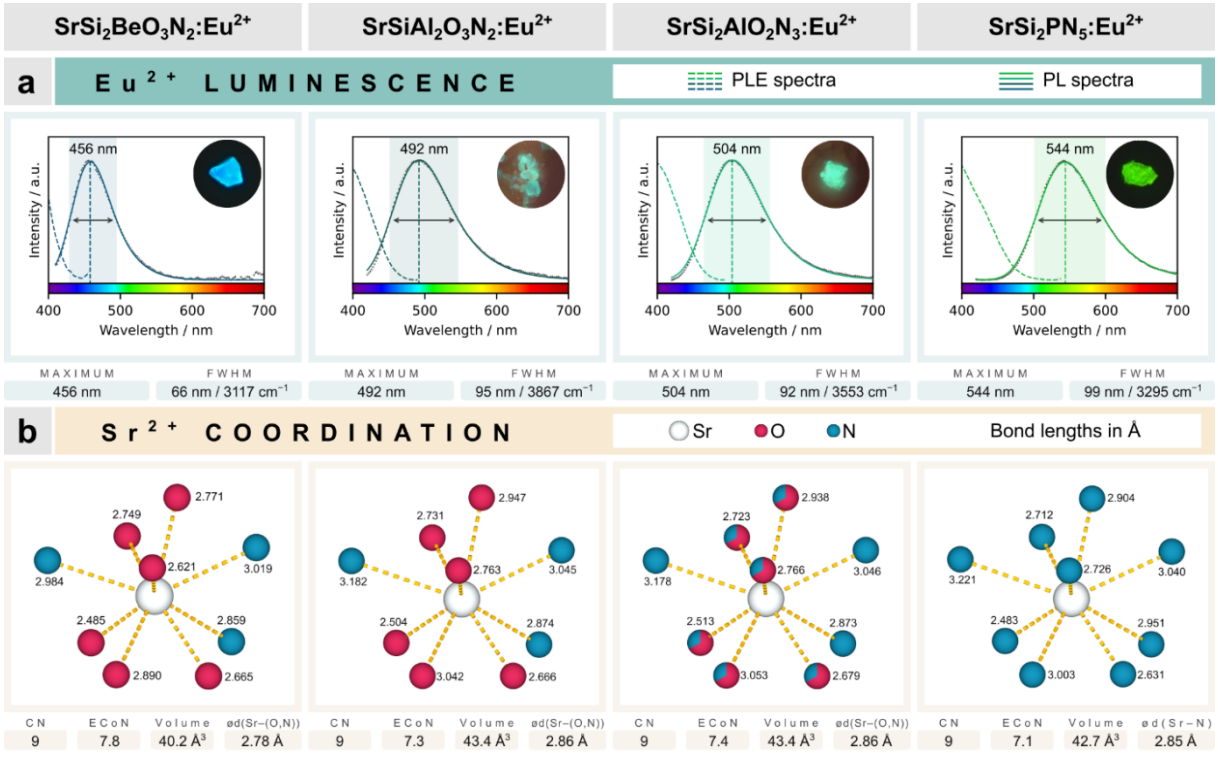

Figure 5.6 a) PL and PLE spectra of all Sr analogues of $LaSi_3N_5$ with luminescence microscopy images. b) Bond lengths and compositions of the first coordination sphere of the activator sites.

5.3 Conclusion

In summary, our study provides a comprehensive analysis of the structural and luminescence properties of $SrSi_2PN_5:Eu^{2+}$ and its related compounds with the $LaSi_3N_5$ structure type. By using a combination of analytical techniques, including single-crystal and powder X-ray diffraction, as well as ^{31}P solid-state NMR and powder neutron diffraction, we were able to elucidate its complex network. After $Sr_5Si_7P_2N_{16}$, $SrSi_2PN_5$ is the second silicon-rich, but this time fully ordered (Si,P)–N network.[4] The challenges posed by the chemical similarity and low X-ray contrast between the key elements were effectively addressed, highlighting the importance of methodological diversity in material characterization. Furthermore, the introduction of powder neutron diffraction into our analytical system underscored the nuanced differences in scattering contrasts for the critical elemental pairings Si/P and O/N, although the method did not outperform standard powder X-ray diffraction in discriminating Si and P within the network. Considering the usual additional effort for neutron measurements, we believe that powder X-ray diffraction is sufficient in most cases if the O/N is not to be determined additionally. The synthesis of $SrSi_2PN_5$ and its doping with Eu^{2+} to modulate the luminescence properties highlight the potential of the compound for tunable optical applications. The detailed investigation of the luminescence behavior of the doped $LaSi_3N_5$ type compounds provided insights into the impact of the nephelauxetic effect and ligand field splitting on the emission wavelengths, with $SrSi_2BeO_3N_2$ proving to be a strong outlier. This opens up possibilities for future theoretical and experimental investigations to further understand these phenomena. Our results contribute to a broader understanding of the structural diversity of nitridosilicate phosphates and their luminescence mechanisms and offer a promising perspective for the development of new materials with tailored optical properties. The study not only highlights the complexity of characterizing materials with similar elemental composition, but also illustrates the importance of a multilayered analytical approach to unveil the intricacies of materials science. Future studies could use this work to further explore the structural and optical properties of analog compounds and expand the potential applications of these materials in optoelectronic devices and beyond.

5.4 Acknowledgements

The authors thank Christian Minke for providing the SEM images, EDX, and NMR measurements, Sandra Albrecht for ICP-OES measurements, as well as Kristian Witthaut for his support and fruitful discussions (all at Department of Chemistry, LMU Munich). The authors gratefully acknowledge the ISIS Neutron and Muon Source for granting beamtime (proposal no. 2220086). Appreciation is also extended to Alexander Mutschke for his help with the refinement of the neutron data (Heinz Maier-Leibnitz Zentrum, TU Munich). M.D. is also grateful to the Bundesministerium für Bildung und Forschung (BMBF) for financial support.

5.5 References

(1) Eisenburger, L.; Oeckler, O.; Schnick, W. High-Pressure High-Temperature Synthesis of Mixed Nitridosilicatephosphates and Luminescence of *AE*SiP_3N_7:Eu^{2+} (*AE*=Sr, Ba). *Chem. Eur. J.* **2021**, *27* (13), 4461–4465. https://doi.org/10.1002/chem.202005495.

(2) Dialer, M.; Witthaut, K.; Bräuniger, T.; Schmidt, P. J.; Schnick, W. The Fundamental Disorder Unit in (Si, P)–(O, N) Networks. *Angew. Chem. Int. Ed.* **2024**, e202401419. https://doi.org/10.1002/ANIE.202401419.

(3) Dialer, M.; Pointner, M. M.; Wandelt, S. L.; Strobel, P.; Schmidt, P. J.; Bayarjargal, L.; Winkler, B.; Schnick, W. Order and Disorder in Mixed (Si, P)–N Networks $Sr_2SiP_2N_6$:Eu^{2+} and $Sr_5Si_2P_6N_{16}$:Eu^{2+}. *Adv. Opt. Mater.* **2023**, 2302668. https://doi.org/10.1002/adom.202302668.

(4) Dialer, M.; Pointner, M. M.; Strobel, P.; Schmidt, P. J.; Schnick, W. (Dis)Order and Luminescence in Silicon-Rich (Si,P)–N Network $Sr_5Si_7P_2N_{16}$:Eu^{2+}. *Inorg. Chem.* **2024**, *63* (2), 1480–1487. https://doi.org/10.1021/acs.inorgchem.3c04109.

(5) Brown, P. J.; Fox, A. G.; Maslen, E. N.; O'Keefe, M. A.; Willis, B. T. M. Intensity of Diffracted Intensities. In *International Tables for Crystallography Volume C: Mathematical, physical and chemical tables*; Prince, E., Ed.; Springer Netherlands: Dordrecht, 2004; p 554. https://doi.org/10.1107/97809553602060000600.

(6) Sears, V. F. Neutron Scattering Lengths and Cross Sections. *Neutron News* **1992**, *3* (3), 26–37. https://doi.org/10.1080/10448639208218770.

(7) Lauterbach, R.; Schnick, W. Synthese, Kristallstruktur Und Eigenschaften Eines Neuen Sialons - $SrSiAl_2O_3N_2$. *Z. Anorg. Allg. Chem* **1998**, *624*, 1154–1158. https://doi.org/10.1002/(SICI)1521-3749(199807)624:7%3C1154::AID-ZAAC1154%3E3.0.CO;2-P.

(8) Bachmann, V.; Meijerink, A.; Ronda, C. Luminescence Properties of $SrSi_2AlO_2N_3$ Doped with Divalent Rare-Earth Ions. *J. Lumin.* **2009**, *129* (11), 1341–1346. https://doi.org/10.1016/J.JLUMIN.2009.06.023.

(9) Giftthaler, T.; Dialer, M.; Strobel, P.; Schmidt, P. J.; Schnick, W. Blue Emitting $SrBe_{1-x}Si_{2+x}O_{3-2x}N_{2+2x}:Eu^{2+}$ (x ≈0.1). *Z. Anorg. Allg. Chem.* **2024**, *650* (2), e202300208. https://doi.org/10.1002/zaac.202300208.

(10) Inoue, Z.; Mitomo, M.; Ii, N. A Crystallographic Study of a New Compound of Lanthanum Silicon Nitride, $LaSi_3N_5$. *J. Mater. Sci.* **1980**, *15* (11), 2915–2920. https://doi.org/10.1007/BF00550562/METRICS.

(11) Suehiro, T.; Hirosaki, N.; Xie, R. J.; Sato, T. Blue-Emitting $LaSi_3N_5:Ce^{3+}$ Fine Powder Phosphor for UV-Converting White Light-Emitting Diodes. *Appl. Phys. Lett.* **2009**, *95* (5). https://doi.org/10.1063/1.3193549/338259.

(12) Liebau, F. *Structural Chemistry of Silicates*, 1st ed.; Springer Berlin Heidelberg: Berlin, Heidelberg, 1985. https://doi.org/10.1007/978-3-642-50076-3.

(13) Johnson, N. W. Convex Polyhedra with Regular Faces. *Can. J. Math.* **1966**, *18*, 169. https://doi.org/10.4153/CJM-1966-021-8.

(14) Link, L.; Niewa, R. *Polynator* : A Tool to Identify and Quantitatively Evaluate Polyhedra and Other Shapes in Crystal Structures. *J. Appl. Crystallogr.* **2023**, *56* (6), 1855–1864. https://doi.org/10.1107/S1600576723008476.

(15) Shannon, R. D. Revised Effective Ionic Radii and Systematic Studies of Interatomie Distances in Halides and Chaleogenides. *Acta Crystallogr. Sect. A* **1976**, *32*, 751.

(16) Ghosh, D. C.; Chakraborty, T.; Mandal, B. The Electronegativity Scale of Allred and Rochow: Revisited. *Theor. Chem. Acc.* **2009**, *124* (3–4), 295–301. https://doi.org/10.1007/S00214-009-0610-4/TABLES/3.

(17) Pust, P.; Weiler, V.; Hecht, C.; Tücks, A.; Wochnik, A. S.; Henß, A.-K.; Wiechert, D.; Scheu, C.; Schmidt, P. J.; Schnick, W. Narrow-Band Red-Emitting $Sr[LiAl_3N_4]:Eu^{2+}$ as a next-Generation LED-Phosphor Material. *Nat. Mater.* **2014**, *13* (9), 891–896. https://doi.org/10.1038/nmat4012.

(18) Zhao, M.; Zhou, Y.; Molokeev, M. S.; Zhang, Q.; Liu, Q.; Xia, Z.; Zhao, M.; Liu, Q. L.; Xia, Z. G.; Zhou, Y. Y.; Zhang, Q. Y. Discovery of New Narrow-Band Phosphors with the UCr_4C_4-Related Type Structure by Alkali Cation Effect. *Adv. Opt. Mater.* **2019**, *7* (6), 1801631. https://doi.org/10.1002/ADOM.201801631.

(19) Huang, W. Y.; Yoshimura, F.; Ueda, K.; Shimomura, Y.; Sheu, H. S.; Chan, T. S.; Chiang, C. Y.; Zhou, W.; Liu, R. S. Chemical Pressure Control for Photoluminescence of $MSiAl_2O_3N_2:Ce^{3+}/Eu^{2+}$ (M = Sr, Ba) Oxynitride Phosphors. *Chem. Mater.* **2014**, *26* (6), 2075–2085. https://doi.org/10.1021/CM404058J/ASSET/IMAGES/LARGE/CM-2013-04058J_0009.JPEG.

(20) Uheda, K.; Takizawa, H.; Endo, T.; Yamane, H.; Shimada, M.; Wang, C.-M.; Mitomo, M. Synthesis and Luminescent Property of Eu^{3+}-Doped $LaSi_3N_5$ Phosphor. *J. Lumin.* **2000**, *87–89*, 967–969. https://doi.org/10.1016/S0022-2313(99)00494-9.

(21) de Jong, M.; Seijo, L.; Meijerink, A.; Rabouw, F. T. Resolving the Ambiguity in the Relation between Stokes Shift and Huang–Rhys Parameter. *Phys. Chem. Chem. Phys.* **2015**, *17* (26), 16959–16969. https://doi.org/10.1039/C5CP02093J.

(22) Zhou, Y.; Yoshizawa, Y.; Hirao, K.; Lenčéš, Z.; Šajgalík, P. Combustion Synthesis of $LaSi_3N_5:Eu^{2+}$ Phosphor Powders. *J. Eur. Ceram. Soc* **2011**, *31* (1–2), 151–157. https://doi.org/10.1016/j.jeurceramsoc.2010.08.004.

(23) Strobel, P.; Maak, C.; Weiler, V.; Schmidt, P. J.; Schnick, W. Ultra-Narrow-Band Blue-Emitting Oxoberyllates $AELi_2[Be_4O_6]:Eu^{2+}$ (*AE*=Sr,Ba) Paving the Way to Efficient RGB Pc-LEDs. *Angew. Chem. Int. Ed.* **2018**, *57* (28), 8739–8743. https://doi.org/10.1002/anie.201804721.

6 Conclusion and Outlook

6.1 Evaluation of the Systematic Experimental and Analytical Approach

Systematic designs have a great impact on both a scientific and a personal level. They provide structure and a more general idea of success. For example, experiments in which the starting materials did not react are no longer classified as "failed", as they still contribute to a greater understanding. The experimental approach of this dissertation led to the discovery of seven new Sr–(Si,P)–(O,N) compounds, which is a success. This success was certainly supported by a number of helpful conditions, such as the structural diversity of this class, the sufficiently good crystallization and the striking luminescence properties, which greatly facilitated the separation of single crystals. However, the design itself proved to be reproducible, transferable, and scalable, which makes it a good candidate for many dissertations with certain limitations. Pseudo-ternary diagrams work well for compound classes with three cations with constant oxidation states, e.g. Sr(II):Si(IV):P(V), as the anions can often be derived from charge neutrality. However, for more than one anion, this calculation can already be ambiguous. For example, for Sr:Si:P = 2:1:2, there are at least two solutions if the number of anions is not known, such as $Sr_2SiP_2N_6$ or $Sr_2SiP_2O_3N_4$. Therefore, the Sr–(Si,P)–(O,N) map is mathematically underdetermined, which is acceptable, but should not be forgotten. Similarly, when there are two, four or more cations with a fixed oxidation state, the usefulness is limited as the representation becomes difficult. With two cations, e.g. in Sr(II)–Si(IV)–N(−III), all connections would be located on one of the edges. With four or more cations, it would be necessary to add another dimension or, for example, to perform color coding. Nevertheless, the research field of pseudo-ternary compounds is still rich, and this design is widely applicable.

For the analytical designs, the largest differences between them were the approach to test the network ordering. Nevertheless, this recapitalization also addresses the commonly used techniques. As mentioned earlier, the distinction of compounds in a sample by visual inspection is a huge benefit in a preparative sense. For this, Eu^{2+} doping was excellent due to

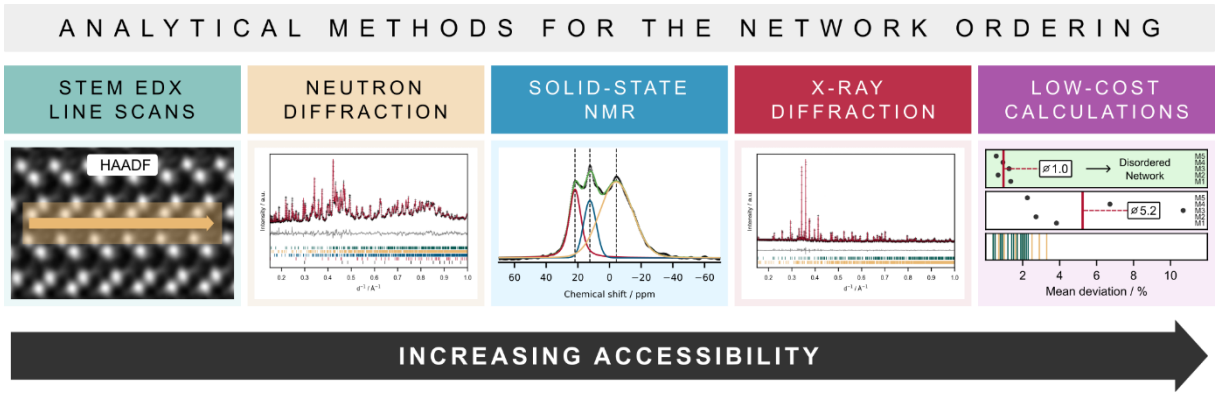

Figure 6.1 Illustration of the different analytical methods used for the determination of the network ordering. Their general accessibility increases from left to right, however, this order might differ under certain circumstances.

the high sensitivity towards its environment and the low concentrations needed to see a result. A problem is that it is not available for all compounds. In this context, it might be interesting for future research to exploit other materials properties, such as the body color (3*d* elements), the crystal shape (mineralizers), or magnetism (magnetic moieties). For the atomic arrangement, SCXRD was very reliable even though the network ordering was not deductible. The practical preparation of these single crystals for EDX measurements were sometimes tedious but measurements on flat surfaces gave the best results. Furthermore, ICP-OES was a helpful confirmation of the Sr:Si:P ratios even though O and N could not be determined. At this point, there is certainly room for improvement to find a good method to also quantify the anionic contributions. Although neutron diffraction is very suitable for distinguishing between O and N, the effort involved is often so high that easier accessible methods are preferred, accepting their intrinsic uncertainties. The network ordering posed the biggest challenge since the goal of this dissertation was not only to find methods that are capable of distinguishing Si and P but also to test different methods in the context of accessibility for a broad range of researchers (Figure 6.1). The most straightforward method was STEM-EDX mapping at atomic resolution. However, its high-quality and rather intuitive evaluation of line scans is accompanied by the need for highly trained personnel as well as high costs and maintenance of the according machinery. Solid-state NMR spectroscopy can be found in many research facilities but easily becomes very complicated to evaluate once the natural abundancy is low or quadrupolar interactions play a role for the nuclei of interest. Fortunately, for Sr–(Si,P)–(O,N) networks, ^{31}P is an ½ nucleus with natural abundancy of 100 %. The most accessible method described here is powder X-ray diffraction, which in our case was in no way inferior to

powder neutron diffraction. The low X-ray contrast of Si and P could be overcome by high-quality measurements. This also brings one to the very import part “supporting analytics” play in the whole process. Consistency over several analytical methods is probably still the best proof of a network ordering, which can be very well supported by low-cost crystallographic calculations or even density functional theory calculations. Throughout this dissertation, many analytical methods have been challenged and evaluated and at the end it is safe to say that all of them in combination with supporting analytics were able to determine the respective network orderings. Each method comes with their own strengths and weaknesses, enabling researchers to pick from a large pool of possibilities and further customize their own designs.

6.2 What to Learn From the Sr–(Si,P)–(O,N) Map

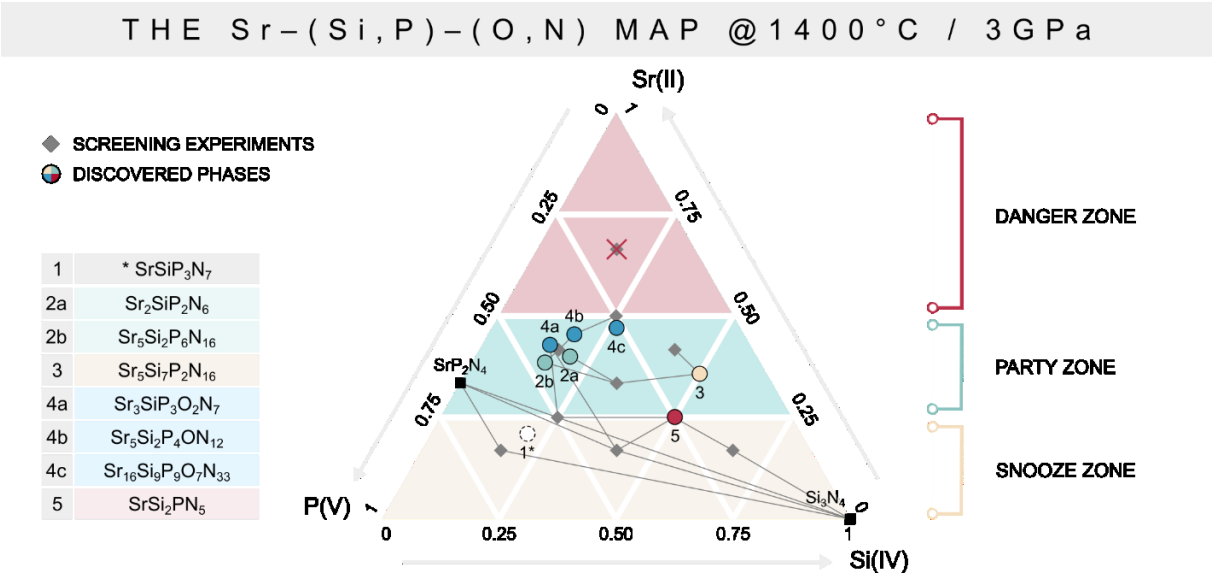

Figure 6.2 Pseudo-ternary Sr–(Si,P)–(O,N) diagram illustrating the relationship between screening experiments and discovered compounds. The diagram is divided into empirical reaction zones, called the danger, party, and snooze zone. * Synthesis at 1400 °C and 8 GPa as well as NH_4F as mineralizer.[7]

The equidistant screening of the pseudo-ternary Sr–(Si,P)–(O,N) diagram provided more information than the discovery of the seven new host materials. An important result is the assignment of the products to the corresponding screening experiments, shown as lines in Figure 6.2. This helps to understand certain reaction dynamics and to identify regions in the diagram with common patterns. This includes the so-called "danger zone" (red) at the upper end, which already indicates that one must be careful with the corresponding stoichiometries. The lack of reaction lines indicates that no new Sr–(Si,P)–(O,N) networks were found in this area. The reason for this lies in the nature of the predominant starting material here, namely $Sr(N_3)_2$. Its reactivity and high nitrogen content make it a very attractive Sr species, but it has the disadvantage that its decomposition also destabilizes the assembly. In other words: After $Sr(N_3)_2$ decomposed, the BN crucible and Mo inlay collapsed, exposing the starting materials to fragments of the BN crucible and graphite furnaces. The result was large amounts of $SrCN_2$ and $Sr_3(BN_2)_2$ in the sample, in addition to black crystals, which according to EDX consisted only of Sr and P. Therefore, reasonable adjustments for future research in this composition space could be to increase the pressure, even slower heating ramps to bring about a more controlled decomposition of $Sr(N_3)_2$, or the partial or complete replacement of $Sr(N_3)_2$ with Sr_2N or SrN. From a structural point of view, the danger zone should result in less condensed

(Si,P)–(O,N) networks (κ < 0.5) due to the high Sr content. Good results for such lowly condensed structures were obtained for other compounds, e.g. nitridophosphates, in the hot isostatic press and at temperatures below 1000 °C.[1] The bottom area is referred to as the "snooze zone" (yellow), which means that the reactivity of these compositions is very limited. Typical products are the thermodynamically very stable SrP_2N_4 and crystalline Si_3N_4.[2] This was surprising in that the only nitridosilicate phosphate published to date, namely $SrSiP_3N_7$, belongs to this zone and was not observed in any of these experiments. The putative reason for this is that in the synthesis of $SrSiP_3N_7$, NH_4F was used as an additional activator for Si_3N_4 as well as higher reaction pressures. This is also a good example of how this area could be further developed in the future. In contrast, the central region, also known as the "party zone" (green), is the region in which the selected conditions (1400 °C, 3 GPa) agree very well with the reactivity of the stoichiometric mixtures. All seven new compounds were synthesized in this range, with a clear preference for phosphorus-rich networks. This trend of the smaller *NFC* dominating many mixed tetrahedral networks has been mentioned previously.[3] It also shows that instead of NH_4F, the simple addition of reactive counter cation species can help to activate the inert Si_3N_4. Nevertheless, the imbalance between phosphorus-rich and silicon-rich networks could benefit from the addition of mineralizers.

6.3 Sr–(Si,P)–(O,N) Networks As Luminescent Materials

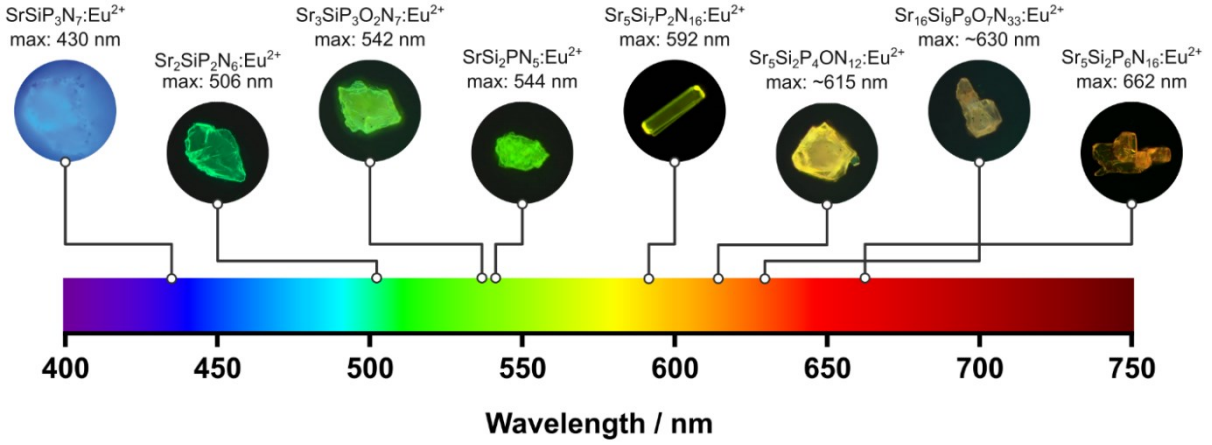

Figure 6.3 Illustration of the placement of the discovered compounds in the spectral range with corresponding emission maxima.

The versatility of the luminescence properties of this young class of compounds when doped with Eu^{2+} is impressive. The emission colors extend over a broad spectral range from blue to deep orange with both very narrow half-widths, e.g. 2300 cm^{-1} in $Sr_2SiP_2N_6:Eu^{2+}$, and very broad half-widths, e.g. 3300 cm^{-1} in $SrSi_2PN_5:Eu^{2+}$ (Figure 6.3). In addition, a clear focus was placed in this study on the investigation of the individual contribution of the activator sites to the emission profile. By leveraging accessible concepts of the CHARDI method such as effective coordination number (*ECoN*) and weighted mean Sr–N distances (*WMD*), it was possible to propose meaningful assignments of coordination environments to different emission bands for $Sr_2SiP_2N_6:Eu^{2+}$, $Sr_5Si_2P_6N_{16}:Eu^{2+}$ and $Sr_5Si_7P_2N_{16}:Eu^{2+}$.[4] However, these considerations were not limited to qualitative assessments, but were supplemented by the implementation of Pekarian-type fits, i.e. fitting curves adapted to the emission characteristics of Eu^{2+} in order to quantify the individual emission contributions. The same reasoning could in turn be used for single-band phosphors such as $SrSi_2PN_5:Eu^{2+}$ and its analogs to confirm that their emission profiles originate from only one activator site. This fitting procedure has been made publicly available in the cited reference and in section 12.4.2.[3] All this serves as a solid basis for more sophisticated investigations of luminescence properties in the future, as performed by Shafei

et al.[5,6] Since all compounds were synthesized in a multianvil press, there is no direct impact on the actual application in optoelectronics, but it is very important to estimate the value of such model systems. In times of machine learning and "big data", the generation of reliable and well-studied results is essential to provide the basis for forward-looking prediction algorithms.

6.4 Where I Would Go from Here

At some point, every researcher must answer to critical questions, such as “Why are you doing this?”, “What can we use this for?”, or “What is the impact of your research?”. Often enough, the honest answer is: “We are in the process of finding the reasons ourselves” and that is fine. In this dissertation, the final goal was and is to improve the general understanding of mixed tetrahedral networks, shed light on their structural subtleties and provide a clear idea of how they can be analyzed. But again, this goal has also evolved over the years. The most important takeaway is certainly that the most sophisticated tools are not always needed, even when it comes to highly complicated structures. Sometimes a combination of easily accessible tools such as powder X-ray diffraction and low-cost crystallographic calculations is sufficient or at least a good starting point.

As already mentioned, the research field of pseudo-ternary mixed tetrahedral networks is virtually endless. There is still much to explore and many surprising things to discover. Had this dissertation not ended at this point, the next steps would have been to investigate lowly condensed Sr–(Si,P)–(O,N) networks (danger zone) outside of a multianvil and preferably within a hot isostatic press. This step would make this class of compounds much more interesting for commercial applications. It goes without saying that typical substitutions of Sr by its homologues Ca and Ba are also a promising and basically unexplored field. The same applies to alkali or rare earth (Si,P)–(O,N) networks and their combinations. When it comes to the network itself, Si and P are not the only candidates, especially given the great success of $SrLiAl_3N_4:Eu^{2+}$ or $SrLi_2Al_2O_2N_2:Eu^{2+}$. Both *AE*–(Li,P)–(O,N) and *AE*–(Li,Si)–(O,N) networks have been sparsely studied and are likely to be synthesized at much lower pressures due to the highly reactive nature of Li_3N. It would not be surprising if they were to play a role in future optical applications.

However, for me personally, the best advice and outlook is not to get stuck on a particular compound class and to allow yourself to let go if there is little chance of success. The preparative work during this PhD involved over 500 experiments and the “unsuccessful” exploration of many classes of compounds. This contrasts with the number of experiments required to write this dissertation, namely less than 50. Research can be frustrating at times and sometimes all the time. Nonetheless, in retrospect, most of it seems worthwhile and there is great value in doing it, academically and personally. This dissertation would not have been possible without the support of many excellent people. Thank you and be careful with $Sr(N_3)_2$.

6.5 References

(1) Wendl, S.; Mardazad, S.; Strobel, P.; Schmidt, P. J.; Schnick, W. HIP to Be Square: Simplifying Nitridophosphate Synthesis in a Hot Isostatic Press. *Angew. Chem. Int. Ed.* **2020**, *59*, 18240. https://doi.org/10.1002/ANGE.202008570.

(2) Karau, F. W.; Seyfarth, L.; Oeckler, O.; Senker, J.; Landskron, K.; Schnick, W. The Stuffed Framework Structure of SrP_2N_4: Challenges to Synthesis and Crystal Structure Determination. *Chem. Eur. J.* **2007**, *13* (24), 6841–6852. https://doi.org/10.1002/CHEM.200700216.

(3) Dialer, M.; Pointner, M. M.; Strobel, P.; Schmidt, P. J.; Schnick, W. (Dis)Order and Luminescence in Silicon-Rich (Si,P)–N Network $Sr_5Si_7P_2N_{16}:Eu^{2+}$. *Inorg. Chem.* **2024**, *63* (2), 1480–1487. https://doi.org/10.1021/acs.inorgchem.3c04109.

(4) Hoppe, R. Effective Coordination Numbers (ECoN) and Mean Fictive Ionic Radii (MEFIR). *Z. Kristallogr. Cryst. Mater.* **1979**, *150* (1–4), 23–52. https://doi.org/10.1524/zkri.1979.150.14.23.

(5) Shafei, R.; Maganas, D.; Strobel, P. J.; Schmidt, P. J.; Schnick, W.; Neese, F. Electronic and Optical Properties of Eu^{2+} -Activated Narrow-Band Phosphors for Phosphor-Converted Light-Emitting Diode Applications: Insights from a Theoretical Spectroscopy Perspective. *J. Am. Chem. Soc.* **2022**, *144* (18), 8038–8053. https://doi.org/10.1021/jacs.2c00218.

(6) Shafei, R.; Strobel, P. J.; Schmidt, P. J.; Maganas, D.; Schnick, W.; Neese, F. A Theoretical Spectroscopy Study of the Photoluminescence Properties of Narrow Band Eu^{2+}-Doped Phosphors Containing Multiple Candidate Doping Centers. Prediction of an Unprecedented Narrow Band Red Phosphor. *Phys. Chem. Chem. Phys* **2024**, *26* (7), 6277–6291. https://doi.org/10.1039/D3CP06039J.

(7) Eisenburger, L.; Oeckler, O.; Schnick, W. High-Pressure High-Temperature Synthesis of Mixed Nitridosilicatephosphates and Luminescence of $AESiP_3N_7:Eu^{2+}$ (*AE*=Sr, Ba). *Chem. Eur. J.* **2021**, *27* (13), 4461–4465. https://doi.org/10.1002/chem.202005495.

7 Supporting Information

Chapter 2

7.1 Experimental Part

7.1.1 Preparation of starting materials

Partially crystalline α-P_3N_5 was synthesized by ammonolysis of P_4S_{10} as already described in literature.[1,2] $Sr(N_3)_2$ was prepared by reaction of $SrCO_3$ with aqueous HN_3 as described by Suhrmann et al., and more recently by Pritzl et al.[3,4] We used amorphous Si_3N_4 (UBE, SNA-00) as purchased. EuN was synthesized in a tungsten crucible by reacting 500 mg Eu metal (smart-elements, 99.99%) in a nitrogen atmosphere in a radiofrequency furnace (TIG 10/100; Hüttinger Elektronik Freiburg, Germany) at 1000 °C for 12 h.

7.1.2 High-pressure high-temperature synthesis

$Sr_2SiP_2N_6$ and $Sr_5Si_2P_6N_{16}$ were synthesized through high-pressure high-temperature methods, utilizing a 1000 t press with a modified Walker-type multianvil apparatus.[5–7] The synthesis involved 48.2 mg (0.28 mmol) $Sr(N_3)_2$, 15.3 mg (0.09 mmol) P_3N_5, and 6.6 mg (0.045 mmol) Si_3N_4. To prevent oxygen exposure and hydrolysis, the starting materials were handled in an Ar-filled glovebox (Unilab, MBraun, Garching; O_2 <1 ppm; H_2O <1 ppm). For the preparation of $Sr_2SiP_2N_6:Eu^{2+}$ and $Sr_5Si_2P_6N_{16}:Eu^{2+}$, we added 1–3 mol% EuN with respect to Sr^{2+}. The materials were thoroughly ground in an agate mortar before they were transferred to a boron nitride crucible with molybdenum inlay. Further information on the preparation and operation of the multianvil press can be found in the literature.[8–10] Reactions were conducted at 1400 °C and 3 GPa with heating, dwelling, and cooling times of each 6 h.

7.1.3 Single-crystal X-ray diffraction

A Bruker D8 VENTURE diffractometer with a rotating anode and Mo-Kα radiation (λ = 0.71073 Å) was employed to gather the diffraction data. The integration and absorption

correction were carried out using the APEX3 program package.[11–13] For structure solution and refinement, SHELXS and SHELXL were utilized with direct methods and the least-squares method.[14–16]

7.1.4 Scanning transmission electron microscopy

The samples were ground using absolute ethanol, and a resulting suspension drop was deposited onto a TEM grid coated with a lacey carbon film (Plano GmbH, Wetzlar, Germany). The grid was placed on a double-tilt low background holder and introduced into a Cs DCOR probe-corrected Titan Themis 300 TEM (FEI, USA). The TEM is equipped with a X-FEG source, a post-column filter (Enfinium ER-799), a US1000XP/FT camera system (Gatan, Germany), and a windowless, 4-quadrant Super-X EDX detector (FEI, USA). TEM images were captured using a 4k × 4k FEI Ceta CMOS camera. The microscope operated at a 300 kV accelerating voltage with a semiconvergence angle of 16.6 mrad, 50 µm aperture, and HAADF detector inner half angle of 33 mrad for a 245 mm camera length. Digital Micrograph was used for Fourier filtering of STEM images. The software Velox was used to obtain STEM images and atomic-resolution EDX maps.[17–20]

7.1.5 Scanning electron microscopy (SEM) and energy-dispersive X-ray spectroscopy (EDX)

The samples were positioned on conducting carbon foil and subsequently coated with carbon. EDX spectra were acquired using an FEI Helios Nanolab G3 Dual Beam UC (FEI, Hillsboro, OR, USA) equipped with an attached X-Max 80 SDD detector (Oxford Instruments, Abingdon, UK).

7.1.6 Selection and calculation of crystallographic reference data

As reference we selected a group of compounds compatible with $Sr_2SiP_2N_6$ and $Sr_5Si_2P_6N_{16}$. We defined compatibility as follows:

1) Structure model elucidation from single-crystal X-ray diffraction data.
2) Similar composition, i.e., $CC_xNFC_yLIG_z$ with *CC* = counter cation, *NFC* = network forming cation, *LIG* = Ligand. Possible *CC* = *A*(I), *AE*(II), *LN*(III), possible *NFC* = Li, Be, Mg, Al, Si, P, and possible *LIG* = N.
3) Condensation degree of $\kappa > 1/3$.
4) Compounds containing at least 50 % Si^{4+} or P^{5+} as network forming cations.

Obvious outliers were removed. A full alphabetical list of the literature compounds with all calculated values is given in Table S1.

Table 7.1 Literature values for Ewald site energies, charge distributions (CHARDI), bond valence sums (BVS), tetrahedral volumes, and tetrahedral distances.

Compound	ICSD code	Site	EWALD / MJ · mol^{-1}	CHARDI	BVS	Volume / Å^3	(Si, P)–N distances / Å	Citation
$Ba_2Si_5N_8$	401501	Si2	9.609	4.04	3.735	2.783	[1.692, 1.768, 1.78, 1.794]	21
		Si3	10.398	3.94	4.151	2.592	[1.709, 1.718, 1.718, 1.726]	
		Si4	9.692	4.07	3.76	2.769	[1.666, 1.788, 1.788, 1.791]	
		Si5	9.766	3.95	3.815	2.747	[1.674, 1.741, 1.797, 1.797]	
$BaCa_2P_6N_{12}$	415714	P2	15.193	4.99	5.155	2.179	[1.592, 1.595, 1.61, 1.684]	22
BaP_2N_4	153060	P2	15.147	4.99	4.972	2.221	[1.593, 1.632, 1.635, 1.669]	23
$BaSi_7N_{10}$	405772	Si1	9.796	3.95	4.049	2.545	[1.644, 1.752, 1.76, 1.764]	24
		Si2	9.671	3.95	3.936	2.571	[1.681, 1.747, 1.752, 1.774]	
		Si3	10	4.09	4.022	2.653	[1.646, 1.746, 1.75, 1.789]	
		Si4	9.855	4.05	3.858	2.695	[1.688, 1.764, 1.765, 1.767]	
		Si5	9.631	3.98	4.085	2.623	[1.705, 1.717, 1.731, 1.74]	
		Si6	9.549	3.97	4.052	2.633	[1.721, 1.723, 1.725, 1.737]	
		Si7	9.72	3.99	4.096	2.613	[1.692, 1.712, 1.735, 1.752]	
$BaSr_2P_6N_{12}$	415716	P2	14.826	5	4.753	2.302	[1.606, 1.621, 1.663, 1.712]	22
BeP_2N_4	40797	P1	15.047	5.03	4.885	2.252	[1.633, 1.633, 1.638, 1.648]	25
		P2	14.977	4.97	4.937	2.238	[1.622, 1.635, 1.637, 1.642]	
$BeSiN_2$	25704	Si1	9.367	4	3.725	2.786	[1.756, 1.756, 1.757, 1.76]	26
Ca_2PN_3	28375	P2	15.024	4.99	4.718	2.292	[1.625, 1.631, 1.675, 1.675]	27
$Ca_2Si_5N_8$	419318	Si2	9.599	4.02	3.884	2.715	[1.667, 1.765, 1.767, 1.78]	28
		Si3	9.653	3.99	3.834	2.737	[1.684, 1.764, 1.765, 1.782]	
		Si4	9.677	4.12	4.043	2.643	[1.679, 1.734, 1.746, 1.754]	
		Si5	9.607	3.99	3.839	2.71	[1.664, 1.765, 1.767, 1.804]	

		Si6	10.193	3.93	4.127	2.606	[1.695, 1.698, 1.732, 1.757]	
$CaLi_2N_4Si_2$	421548	Si3	9.788	4.01	3.967	2.657	[1.714, 1.723, 1.736, 1.766]	[29]
CaP_2N_4	425997	P10	15.136	4.94	5.005	2.205	[1.622, 1.631, 1.632, 1.659]	[30]
		P11	15.156	4.98	4.941	2.236	[1.633, 1.634, 1.636, 1.648]	
		P12	15.213	5.08	5.076	2.195	[1.627, 1.628, 1.63, 1.652]	
		P13	15.191	5.15	5.272	2.144	[1.626, 1.64, 1.642, 1.645]	
		P6	15.401	5.03	4.912	2.246	[1.622, 1.623, 1.633, 1.639]	
		P7	15.291	4.96	4.886	2.246	[1.615, 1.631, 1.64, 1.65]	
		P8	15.101	4.96	4.938	2.236	[1.596, 1.629, 1.635, 1.637]	
		P9	15.311	4.9	4.885	2.238	[1.531, 1.632, 1.645, 1.645]	
$Ce_2P_3N_7$	241681	P1	14.85	4.95	4.767	2.28	[1.644, 1.644, 1.651, 1.651]	[31]
		P2	14.865	5	4.795	2.251	[1.583, 1.66, 1.67, 1.675]	
$Cs_3P_6N_{11}$	51397	P2	14.601	5	4.976	2.23	[1.595, 1.613, 1.62, 1.707]	[32]
$EuBeSi_2N_4$	130185	Si2	9.924	3.69	3.964	2.673	[1.694, 1.749, 1.749, 1.749]	[33]
$Ho_2P_3N_7$	241683	P1	14.851	5.14	4.725	2.306	[1.65, 1.65, 1.65, 1.65]	[31]
		P2	14.898	4.92	4.856	2.223	[1.571, 1.637, 1.683, 1.683]	
$K_3P_6N_{11}$	50211	P2	14.61	5.01	5.091	2.201	[1.576, 1.599, 1.622, 1.708]	[34]
$Li_2SrSi_2N_4$	8336	Si3	9.889	4.01	4.001	2.636	[1.709, 1.728, 1.741, 1.747]	[29]
$Li_5Ce_5Si_4N_{12}$	421527	Si4	9.988	3.95	3.984	2.651	[1.709, 1.727, 1.746, 1.749]	[35]
		Si4	9.841	3.95	3.774	2.735	[1.74, 1.749, 1.758, 1.763]	
$LiNdP_4N_8$	429542	P2	15.092	5	4.976	2.22	[1.612, 1.623, 1.637, 1.655]	[36]
		P3	15.231	5	5.002	2.18	[1.624, 1.63, 1.632, 1.632]	
Mg_2PN_3	12986	P1	14.917	4.97	4.751	2.293	[1.616, 1.616, 1.675, 1.693]	[37]
$MgSiN_2$	90730	Si1	9.722	4	3.791	2.754	[1.732, 1.744, 1.761, 1.767]	[38]
$NaPN_2$	411818	P1	15.22	5	4.878	2.238	[1.639, 1.639, 1.639, 1.639]	[39]
$NaSi_2N_3$	72466	Si1	9.877	4.01	4.101	2.681	[1.601, 1.64, 1.836, 1.89]	[40]

$Pr_2P_3N_7$	241682	P1	14.829	4.97	4.759	2.281	[1.643, 1.643, 1.653, 1.653]	31
		P2	14.879	5	4.818	2.245	[1.577, 1.659, 1.669, 1.676]	
$Rb_3P_6N_{11}$	51396	P2	14.622	5	5.012	2.222	[1.59, 1.605, 1.618, 1.713]	32
$Sr_2Si_5N_8$	401500	Si2	9.657	4.04	3.887	2.715	[1.676, 1.751, 1.762, 1.786]	21
		Si3	10.376	3.93	4.214	2.551	[1.68, 1.718, 1.718, 1.733]	
		Si4	9.758	4.09	3.941	2.686	[1.653, 1.767, 1.767, 1.773]	
		Si5	9.759	3.96	3.887	2.707	[1.688, 1.748, 1.769, 1.769]	
$SrBeSi_2N_4$	130184	Si2	9.919	4	3.954	2.678	[1.695, 1.75, 1.75, 1.75]	33
$SrLi_2N_4Si_2$	421549	Si3	9.829	4.01	3.932	2.666	[1.721, 1.731, 1.735, 1.764]	29
SrP_8N_{14}	434260	P1	15.474	4.98	4.994	2.229	[1.595, 1.602, 1.616, 1.72]	41
		P2	14.331	5.04	5.11	2.191	[1.539, 1.579, 1.691, 1.704]	
$SrSi_7N_{10}$	154166	Si1	9.689	3.91	3.982	2.552	[1.66, 1.739, 1.745, 1.801]	42
		Si2	9.776	3.93	4.028	2.548	[1.66, 1.744, 1.759, 1.76]	
		Si3	9.87	4.06	3.883	2.685	[1.682, 1.763, 1.763, 1.767]	
		Si4	9.69	3.98	4.106	2.607	[1.696, 1.727, 1.729, 1.734]	
		Si5	9.908	4.06	3.938	2.684	[1.67, 1.742, 1.76, 1.786]	
		Si6	9.669	4.04	4.141	2.598	[1.697, 1.717, 1.724, 1.736]	
		Si7	9.566	4.02	4.074	2.618	[1.712, 1.721, 1.727, 1.737]	

7.1.7 Calculation of Ewald site energies

For the calculation of Ewald site energies, we used the *EwaldSummation* class of Python Materials Genomics (pymatgen) library.[43,44] In the following a reduced working code example:

```
from pymatgen.core.structure import Structure
from pymatgen.symmetry.analyzer import SpacegroupAnalyzer
from pymatgen.analysis.ewald import EwaldSummation
# Variables
oxidation_states = {'Sr': 2, 'Si': 4, 'P': 5, 'N': -3}
file_path = 'path_to_your_file.cif'
def calculate_ewald_site_energy(file_path, oxidation_states):
    # Create a structure from a cif file (always in P1)
    structure = Structure.from_file(file_path)
    # Add oxidation states to your structure
    structure.add_oxidation_state_by_element(oxidation_states)
    # Symmetrize structure
    symmetry_analyzer = SpacegroupAnalyzer(structure)
    symmetric_structure = symmetry_analyzer.get_symmetrized_structure()
    # Instantiate EwaldSummation object for symmetric_structure
    ewald = EwaldSummation(symmetric_structure)
    # Calculate site energies for all equivalent sites
    for n, equivalent_sites in enumerate(symmetric_structure.equivalent_sites):
        # Identify equivalent site
        element = equivalent_sites[0].species.elements[0].symbol
        site = f"{element}{n}"
        # Get correct index of equivalent_sites[0] in symmetric_structure.sites
        # get_site_energy() requires the index of the site in symmetric_structure.sites NOT
equivalent_sites
        index_in_sites = symmetric_structure.index(equivalent_sites[0])
        # Calculate site energy in MJ/mol
        site_energy = round(ewald.get_site_energy(
            index_in_sites) * (-96.485) / 1000, 3)
        print(f"{site}:       {site_energy}       MJ/mol")
calculate_ewald_site_energy(file_path, oxidation_states)
```

7.1.8 Calculation of the charge distribution (CHARDI)

CHARDI values were calculated using CHARDI2015 (Build 21) by Nespolo et al.[45,46]

7.1.9 Polyhedral volumes and distances

Tetrahedral volumes and distances of (Si,P)–N_4 were calculated with Polynator v1.3, a program distributed by Lukas Link and Prof. Dr. Rainer Niewa of the University of Stuttgart (https://www.iac.uni-stuttgart.de/forschung/akniewa/downloads/).[47] Polyhedral volumes and distances of Sr–N were calculated with VESTA v3.5.8.[48]

7.1.10 Bond valence sum (BVS) calculations

BVS calculations were performed with EXPO2014 v1.22.11.[49] We optimized the BVS parameters R_0 on the selected reference data (Table S1) as proposed by Brese and O'Keeffe, giving new parameters $R_0(Si^{4+}–N^{3-}) = 1.731$ and $R_0(P^{5+}–N^{3-}) = 1.712$.[50]

7.1.11 Luminescence measurements

Eu^{2+}-doped samples were subjected to luminescence spectroscopy using a HORIBA Fluoromax4 spectrofluorimeter system in combination with an Olympus BX51 microscope. PL and PLE spectra were recorded at room temperature with emission and excitation wavelengths of $\lambda_{emi}(Sr_2SiP_2N_6) = 522$ nm and $\lambda_{exc}(Sr_2SiP_2N_6) = 400$ nm, $\lambda_{emi}(Sr_5Si_2P_6N_{16}) = 660$ nm, and $\lambda_{exc}(Sr_5Si_2P_6N_{16}) = 460$ nm, covering a range from 400 to 800 nm with a step size of 2 nm.

7.1.12 Second harmonic generation (SHG) measurements

We performed second harmonic generation (SHG) measurements on a powder sample of $Sr_2SiP_2N_6$ using the Kurtz-Perry approach.[51] Quartz, corundum (Al_2O_3), and KDP (KH_2PO_4) served as reference. A Q-switched Nd:YAG laser with a wavelength of 1064 nm, pulse duration of 5-6 ns, and a repetition rate of 2 kHz was employed to generate the fundamental laser pulse. To separate the incident infrared light from the SHG light (532 nm), we used a harmonic separator, a short-pass filter, and an interference filter. The SHG signal was acquired from six different areas of the sample using a photomultiplier and an oscilloscope under ambient conditions in transmission geometry. For each position, 64 pulses were measured and averaged. The background signals occurring between the laser pulses were used to correct the measured intensities.

7.1.13 Raman spectroscopy

Raman measurements were carried out with a custom set-up in Frankfurt described in detail elsewhere.[52] We used an OXXIUS S.A. Laser-Boxx LMX532 laser (λ = 532 nm) and a (Princeton Instruments ACTON SpectraPro 2300i) spectrograph equipped with a Pixis256E CCD camera.

7.1.14 Density functional theory (DFT) calculations

Atomistic model calculations were carried out within the framework of DFT and the pseudopotential method using the CASTEP simulation package.[53,54] Norm-conserving pseudopotentials were generated “on the fly” using the parameters provided with the CASTEP distribution. These pseudopotentials have been extensively tested for accuracy and transferability.[55] The pseudopotentials were employed in conjunction with plane waves up to a kinetic energy cutoff of 1350 eV. The calculations were carried out with the PBE exchange-correlation functional.[56] Monkhorst-Pack grids were used for Brillouin zone integrations with a distance of <0.025 $Å^{-1}$ between grid points.[57] A dispersion correction according to Grimme et al. was used.[58] Convergence criteria included an energy change of < 5×10^{-6} eV/atom, a maximal force of < 0.008 eV/Å, and a maximal deviation of the stress tensor <0.02 GPa from the imposed stress tensor. Optical properties were computed as described by Refson et al.[59] Phonon frequencies were obtained from density functional perturbation theory (DFPT) calculations. Raman intensities and NLO properties were computed using DFPT with the ‘2n+1’ theorem approach and a scissor operator of 1.3 eV.[60] It should be stressed that all calculations were carried out in the athermal limit, i.e., the influence of temperature and zero-point motion were not taken into account.

7.2 Introduction

The cation ratio (*CR*) is defined according to Pritzl et al. as the ratio between the number (*N*) of the counter cations (*CC*) and network forming cations (NFC):

$$CR = \frac{N(CC)}{N(NFC)} \tag{1}$$

The condensation degree *κ* on the other hand as the ratio between the number of network forming cations (NFC) and ligands (LIG):

$$\kappa = \frac{N(NFC)}{N(LIG)} \tag{2}$$

By introducing the oxidation state (*Ox*) and enforcing charge neutrality, we get a third equation:

$$N(CC) \cdot Ox(CC) + N(NFC) \cdot Ox(NFC) + N(LIG) \cdot Ox(LIG) = 0 \tag{3}$$

Now to introduce *CR* and *κ*, we divide equation (3) by *N*(*NFC*):

$$\underbrace{\frac{N(CC)}{N(NFC)}}_{CR} \cdot Ox(CC) + Ox(NFC) + \underbrace{\frac{N(LIG)}{N(NFC)}}_{\kappa^{-1}} \cdot Ox(LIG) = 0 \tag{4}$$

After transforming we obtain the final equation *CR*(*κ*):

$$CR(\kappa) = -\frac{Ox(LIG)}{Ox(CC)} \cdot \frac{1}{\kappa} - \frac{Ox(NFC)}{Ox(CC)} \tag{5}$$

Table 7.2 Full list of literature known alkaline earth nitridosilicates, -phosphates, and -silicate phosphates with *AE* = Ca, Sr, Ba.

Compound Class	Compound	*AE*	*CR*	*κ*	Citation
AE–Si–N	Ca_4SiN_4	Ca	4	$^1/_4$	61
	$AE_5Si_2N_6$	Ca Ba	$^5/_2$	$^1/_3$	62 63
	$AESiN_2$	Ca Sr Ba	1	$^1/_2$	64
	$AE_2Si_5N_8$	Ca Sr Ba	$^2/_5$	$^5/_8$	28 21
	$AESi_7N_{10}$	Sr Ba	$^1/_7$	$^7/_{10}$	42 24
AE–P–N	Ca_2PN_3	Ca	2	$^1/_3$	27

	SrP_3N_7	Sr	$^1/_3$	$^3/_7$	[9]
	AEP_2N_4	Ca Sr Ba	$^1/_2$	$^1/_2$	[30]
	AEP_8N_{14}	Ca Sr Ba	$^1/_8$	$^4/_7$	[65]
AE–(Si,P)–N	$Sr_2SiP_2N_6$	Sr	$^2/_3$	$^1/_2$	This work
	$Sr_5Si_2P_6N_{16}$	Sr	$^5/_8$	$^1/_2$	This work
	$AESiP_3N_7$	Sr Ba	$^1/_4$	$^4/_7$	[2]

7.3 Results and Discussion

7.3.1 Crystallography

Table 7.3 Crystallographic data of $Sr_2SiP_2N_6$ and $Sr_5Si_2P_6N_{16}$ from single-crystal refinement. Standard deviations are given in parentheses.

Formula	$Sr_2SiP_2N_6$	$Sr_5Si_2P_6N_{16}$
Crystal system	orthorhombic	orthorhombic
Space group	$C222_1$ (no. 20)	*Pbam* (no. 55)
Lattice parameters / Å	a = 6.08490(10)	a = 9.9136(2)
	b = 8.8203(2)	b = 17.5676(3)
	c = 10.2500(2)	c = 8.39680(10)
Cell volume / Å^3	550.124(19)	1462.37(4)
Formula units / unit cell	4	4
Calculated X-ray density / g · cm^{-3}	4.218	4.107
Molar mass / g · mol^{-1}	349.34	904.22
μ / mm^{-1}	20.103	18.981
Temperature / K	297(2)	298(2)
Absorption correction	multi-scan	multi-scan
Radiation	Mo-Kα	Mo-Kα
F(000)	648	1680
ϑ range / °	7.952 ≤ ϑ ≤ 72.24	4.1120 ≤ ϑ ≤ 33.1479
Total no. of reflections	3219	21825
Independent reflections [$I \geq 2\sigma(I)$ / all]	812 / 849	1712 / 1927
R_{int} / R_σ	0.0663 / 0.0454	0.0397 / 0.0199
Refined parameters / restraints	52 / 0	147 / 0
Goodness of fit	1.119	1.116
R-values [$I \geq 2\sigma(I)$]	$R1$ = 0.0229, w$R2$ = 0.0533	$R1$ = 0.0205, w$R2$ = 0.0470
R-values (all data)	$R1$ = 0.0249, w$R2$ = 0.0540	$R1$ = 0.0261, w$R2$ = 0.0491
$\Delta\rho_{max}$, $\Delta\rho_{min}$ / e · Å^3	0.611, −0.981	0. 668, −0.655

Table 7.4 Wyckoff position, coordinates, equivalent thermal displacement parameters and occupancy of $Sr_2SiP_2N_6$ from single-crystal refinement. Standard deviations are given in parentheses.

Atom	Wyckoff	x	y	z	U_{eq}	S.O.F.
Sr1	8*c*	0.90288(8)	0.68203(5)	0.92122(4)	0.00826(13)	1
P1	8*c*	0.64719(18)	0.51550(13)	0.64086(12)	0.0038(2)	1
Si1	4*b*	0	0.3103(2)	3/4	0.0028(3)	1
N1	8*c*	0.6947(6)	0.6950(5)	0.6746(4)	0.0073(7)	1
N2	4*a*	0.9922(10)	0	0	0.0081(11)	1
N3	8*c*	0.6191(6)	0.9178(4)	0.8713(4)	0.0055(7)	1
N4	4*b*	0	0.9311(7)	3/4	0.0080(11)	1

Table 7.5 Anisotropic displacement parameters (U_{ij} / Å^2) of $Sr_2SiP_2N_6$ from single-crystal refinement. Standard deviations are given in parentheses.

Atom	U_{11}	U_{22}	U_{33}	U_{23}	U_{13}	U_{12}
Sr1	0.00835(19)	0.0081(2)	0.0083(2)	−0.00100(17)	−0.00230(17)	0.00421(19)
P1	0.0042(4)	0.0029(5)	0.0044(5)	−0.0004(4)	0.0000(4)	0.0004(4)
Si1	0.0035(6)	0.0016(8)	0.0035(7)	0.000	0.0005(6)	0.000

N1	0.0084(17)	0.0045(17)	0.0089(18)	−0.0007(14)	0.0015(14)	−0.0017(17)
N2	0.005(2)	0.013(3)	0.007(3)	0.000(2)	0.000	0.000
N3	0.0055(17)	0.0041(15)	0.0068(16)	0.0003(13)	−0.0001(14)	0.0005(15)
N4	0.012(2)	0.003(3)	0.009(3)	0.000	0.004(2)	0.000

Table 7.6 Wyckoff position, coordinates, equivalent thermal displacement parameters and occupancy of $Sr_5Si_2P_6N_{16}$ from single-crystal refinement. Standard deviations are given in parentheses.

Atom	Wyckoff	*x*	*y*	*z*	U_{eq}	S.O.F.
Sr1	2*c*	1/2	0	0	0.00683(11)	1
Sr2	4*h*	0.28705(4)	0.25039(2)	1/2	0.00908(9)	1
Sr3	4*h*	0.11039(4)	0.42916(2)	1/2	0.00943(9)	1
Sr4	4*g*	0.63556(4)	0.42078(2)	0	0.01156(10)	1
Sr5	2*b*	1/2	1/2	1/2	0.02229(16)	1
Sr6	4*g*	0.31656(4)	0.26873(3)	0	0.01809(11)	1
P1	8*i*	0.20024(7)	0.58744(4)	0.31506(9)	0.00605(15)	0.75
Si1	8*i*	0.20024(7)	0.58744(4)	0.31506(9)	0.00605(15)	0.25
P2	8*i*	0.53070(7)	0.33325(4)	0.31420(9)	0.00618(15)	0.75
Si2	8*i*	0.53070(7)	0.33325(4)	0.31420(9)	0.00618(15)	0.25
P3	8*i*	0.54084(7)	0.17245(4)	0.18650(9)	0.00598(15)	0.75
Si3	8*i*	0.54084(7)	0.17245(4)	0.18650(9)	0.00598(15)	0.25
P4	8*i*	0.29013(7)	0.42274(4)	0.18703(9)	0.00567(15)	0.75
Si4	8*i*	0.29013(7)	0.42274(4)	0.18703(9)	0.00567(15)	0.25
N1	8*i*	0.6926(3)	0.34229(14)	0.2649(3)	0.0108(5)	1
N2	4*g*	0.2524(4)	0.4446(2)	0	0.0100(7)	1
N3	8*i*	0.2710(3)	0.50174(14)	0.2942(3)	0.0095(5)	1
N4	8*i*	0.1932(3)	0.35157(14)	0.2585(3)	0.0087(5)	1
N5	4*g*	0.5539(4)	0.2016(2)	0	0.0087(7)	1
N6	8*i*	0.4358(3)	0.09892(15)	0.2013(3)	0.0140(6)	1
N7	4*h*	0.1449(4)	0.5944(2)	1/2	0.0101(7)	1
N8	8*i*	0.4480(2)	0.39219(15)	0.1949(3)	0.0104(5)	1
N9	8*i*	0.4819(3)	0.24428(14)	0.2921(3)	0.0110(5)	1
N10	4*h*	0.4943(4)	0.3571(2)	1/2	0.0133(8)	1

Table 7.7 Anisotropic displacement parameters (U_{ij} / Å^2) of $Sr_5Si_2P_6N_{16}$ from single-crystal refinement. Standard deviations are given in parentheses.

Atom	U_{11}	U_{22}	U_{33}	U_{23}	U_{13}	U_{12}
Sr1	0.0081(2)	0.0052(2)	0.0071(2)	0.000	0.000	0.0011(2)
Sr2	0.01102(19)	0.00706(18)	0.00916(19)	0.000	0.000	-0.00135(15)
Sr3	0.00920(19)	0.01127(19)	0.00782(19)	0.000	0.000	0.00190(15)
Sr4	0.0131(2)	0.0145(2)	0.0070(2)	0.000	0.000	-0.00624(16)
Sr5	0.0111(3)	0.0061(3)	0.0496(5)	0.000	0.000	0.0005(2)
Sr6	0.0113(2)	0.0184(2)	0.0245(3)	0.000	0.000	0.00753(17)
P1	0.0061(3)	0.0060(3)	0.0060(4)	-0.0005(3)	0.0000(3)	-0.0001(3)
Si1	0.0061(3)	0.0060(3)	0.0060(4)	-0.0005(3)	0.0000(3)	-0.0001(3)
P2	0.0065(3)	0.0055(3)	0.0065(4)	0.0002(3)	-0.0010(3)	-0.0002(3)
Si2	0.0065(3)	0.0055(3)	0.0065(4)	0.0002(3)	-0.0010(3)	-0.0002(3)
P3	0.0061(3)	0.0056(3)	0.0062(4)	-0.0001(3)	0.0006(3)	0.0007(3)
Si3	0.0061(3)	0.0056(3)	0.0062(4)	-0.0001(3)	0.0006(3)	0.0007(3)
P4	0.0054(3)	0.0058(3)	0.0058(4)	-0.0001(3)	0.0004(3)	0.0001(3)
Si4	0.0054(3)	0.0058(3)	0.0058(4)	-0.0001(3)	0.0004(3)	0.0001(3)
N1	0.0078(12)	0.0067(12)	0.0179(14)	0.0004(10)	-0.0042(10)	0.0003(10)
N2	0.0095(17)	0.0124(18)	0.0082(18)	0.000	0.000	0.0035(14)

N3	0.0116(12)	0.0076(12)	0.0095(12)	0.0006(10)	0.0011(10)	-0.0002(10)
N4	0.0101(12)	0.0090(12)	0.0069(13)	0.0006(10)	-0.0007(9)	-0.0022(10)
N5	0.0084(17)	0.0094(17)	0.0083(18)	0.000	0.000	0.0005(14)
N6	0.0171(14)	0.0097(13)	0.0151(14)	-0.0029(11)	0.0083(11)	-0.0020(11)
N7	0.0113(17)	0.0113(18)	0.0076(18)	0.000	0.000	0.0017(14)
N8	0.0081(12)	0.0142(13)	0.0090(13)	0.0019(11)	0.0009(10)	0.0020(10)
N9	0.0123(12)	0.0077(12)	0.0129(12)	-0.0045(10)	0.0058(10)	-0.0019(10)
N10	0.022(2)	0.0073(17)	0.0102(18)	0.000	0.000	-0.0025(15)

7.3.2 EDX measurements

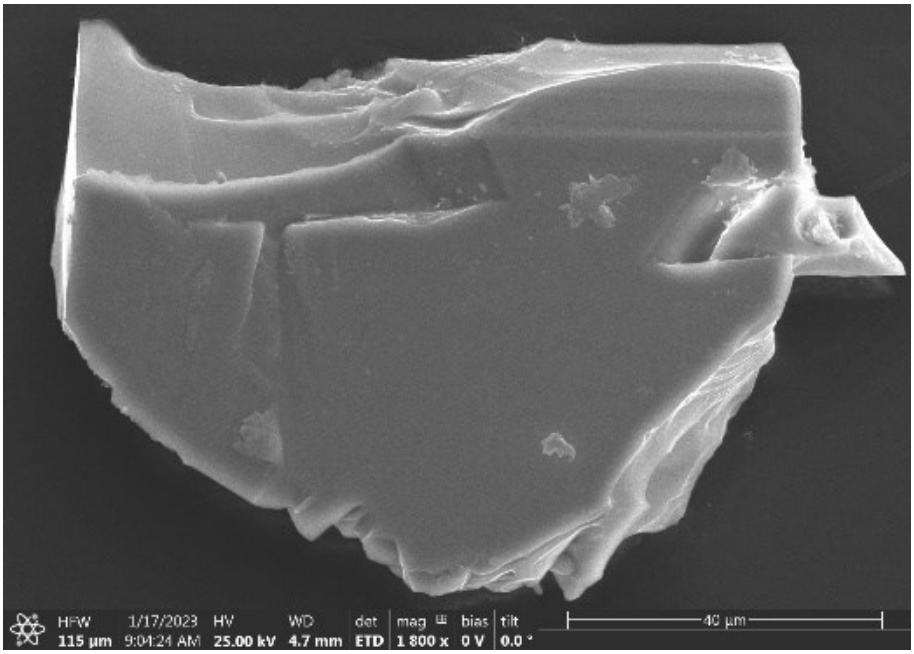

Figure 7.1 SEM image of a particle of $Sr_2SiP_2N_6$ on which EDX was measured.

Table 7.8 Results of EDX measurements on a single crystal of $Sr_2SiP_2N_6$.

Measurement	Sr	Si	P	N	O
1	18	11	18	50	3
2	18	11	18	49	3
3	18	11	19	50	2
4	18	11	17	52	2
5	18	11	17	52	3
6	18	11	18	50	3
7	18	11	18	51	2
8	18	11	18	51	2
9	18	11	18	51	3
10	18	11	18	51	2
Average	18(1)	11(1)	18(1)	51(1)	3(1)
Calculated	18	9	18	55	0

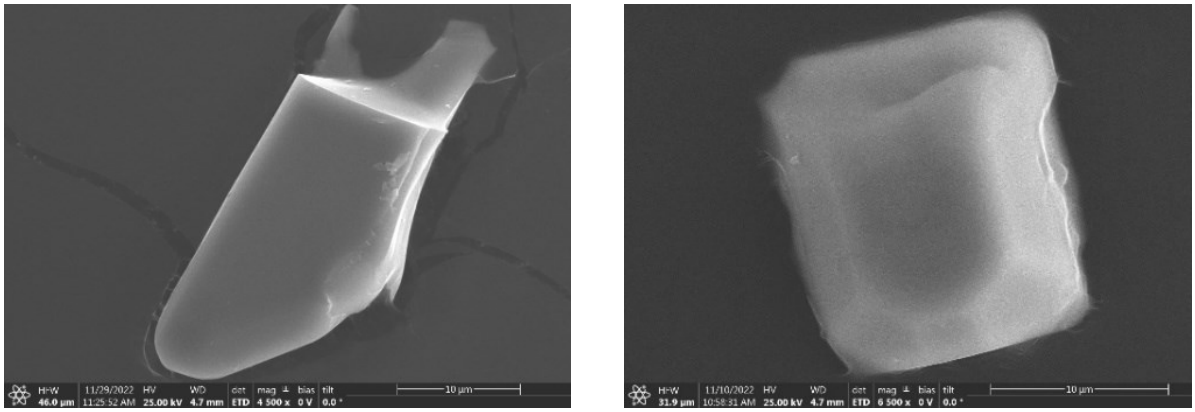

Figure 7.2 SEM images of two particles of $Sr_5Si_2P_6N_{16}$ on which EDX was measured.

Table 7.9 Results of EDX measurements on a single crystal of $Sr_5Si_2P_6N_{16}$.

Crystal	Measurement	Sr	Si	P	N	O
	1	18	11	19	45	6
	2	16	10	18	50	6
1	3	18	11	18	49	4
	4	19	11	19	46	4
	5	16	10	19	50	5
	1	20	11	20	45	4
	2	19	10	20	48	3
2	3	19	10	20	48	3
	4	19	10	20	48	3
	5	19	10	20	49	3
	Average	18(1)	10(1)	19(1)	48(2)	4(1)
	Calculated	17	7	21	55	0

7.3.3 STEM-EDX maps

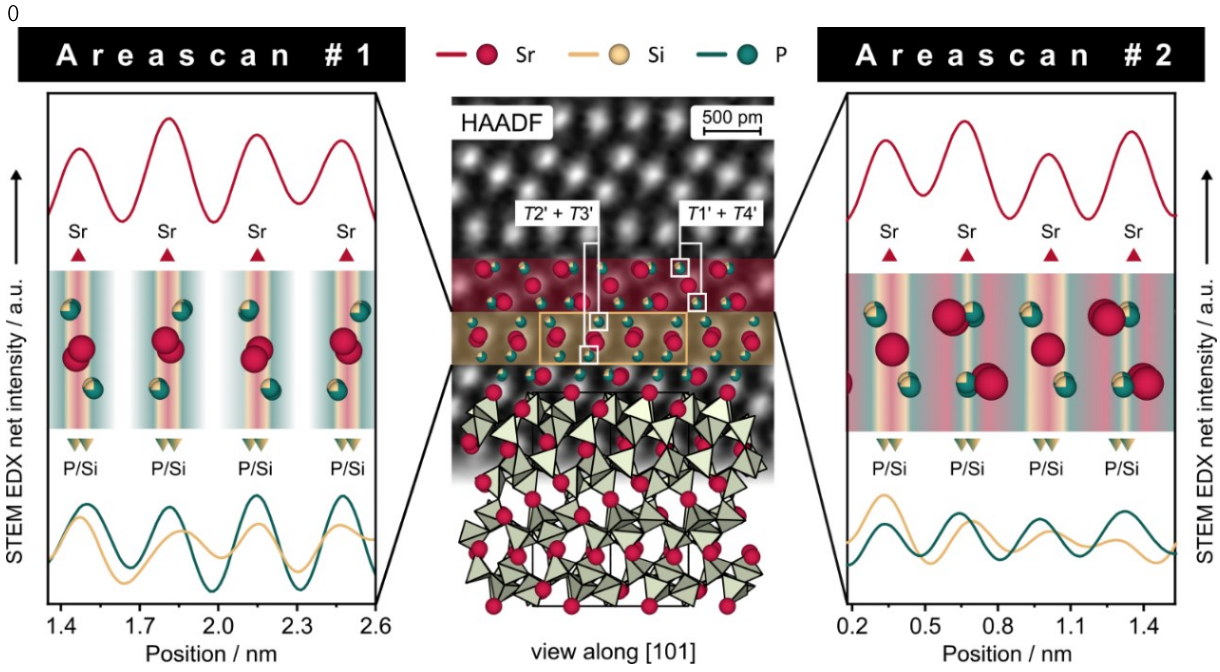

Figure 7.3 STEM high-angle annular dark-field (HAADF) images with structure overlay of $Sr_5Si_2P_6N_{16}$. STEM EDX area scans are highlighted in yellow and in red. The integrated EDX signals of the area scans show for both in-phase oscillation of the Si (yellow) and P (green) signals for $Sr_5Si_2P_6N_{16}$, ruling out an ordered network. The Sr (red) EDX signal serves as a position reference.

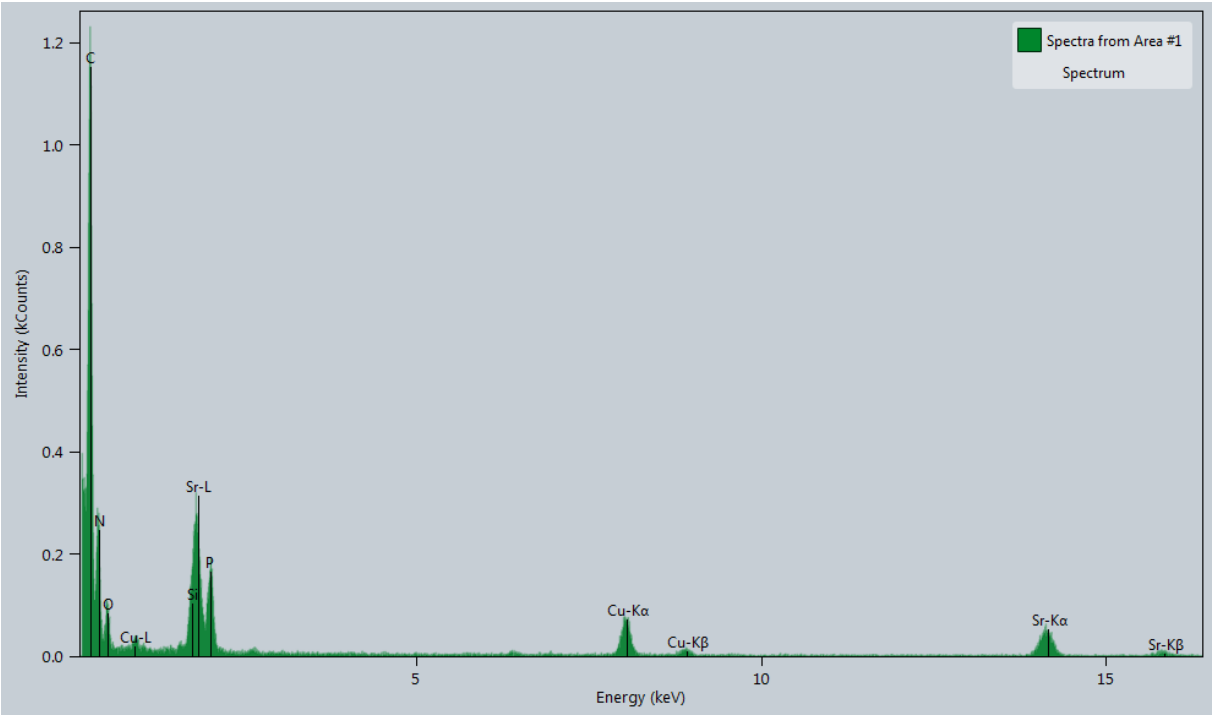

Figure 7.4 Raw EDX spectrum of the STEM EDX maps of $Sr_2SiP_2N_6$ where Cu and C originate from the TEM grid.

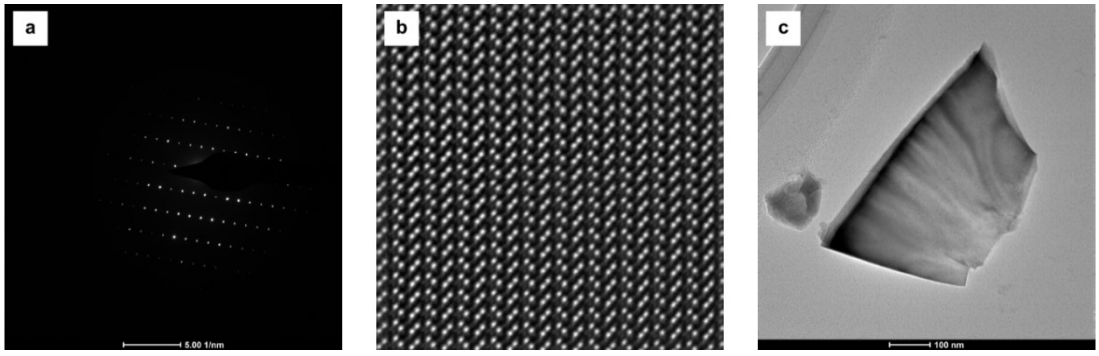

Figure 7.5 Graphical representations of (a) the zone axis, (b) the high-angle annular dark field (HAADF) image, and (c) a bright field image of the investigated crystallite of $Sr_2SiP_2N_6$.

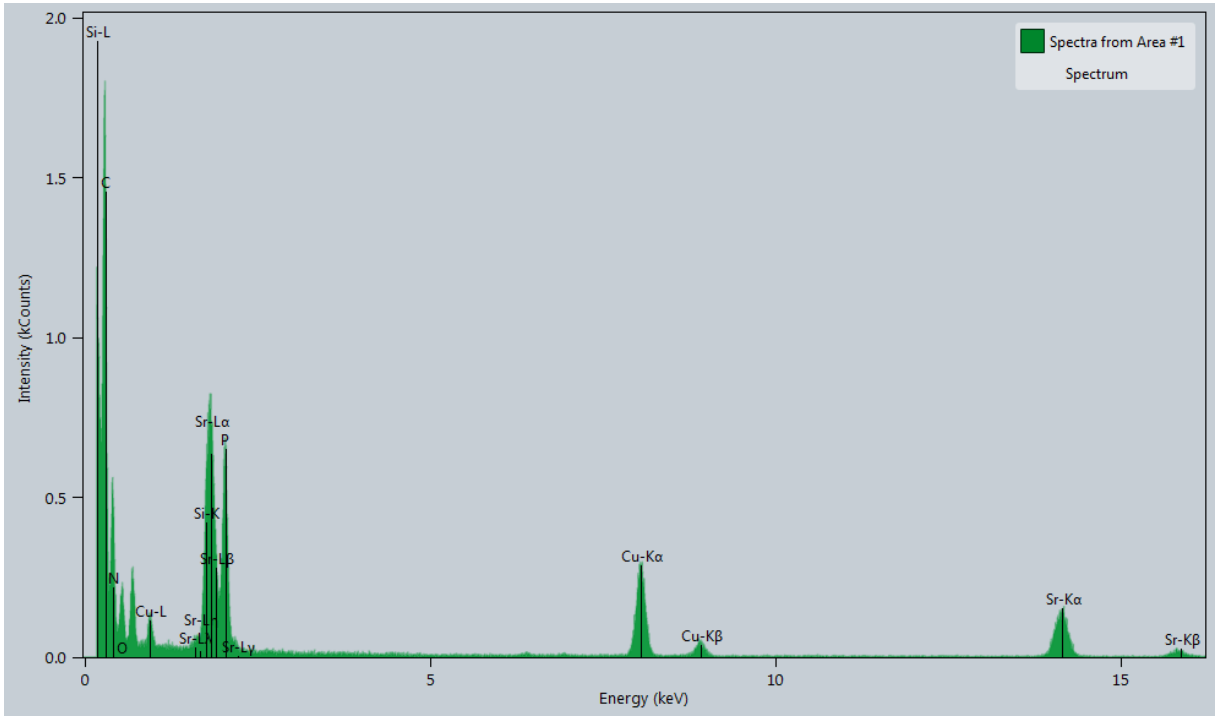

Figure 7.6 Raw EDX spectrum of the STEM EDX maps of $Sr_5Si_2P_6N_{16}$ where Cu and C originate from the TEM grid.

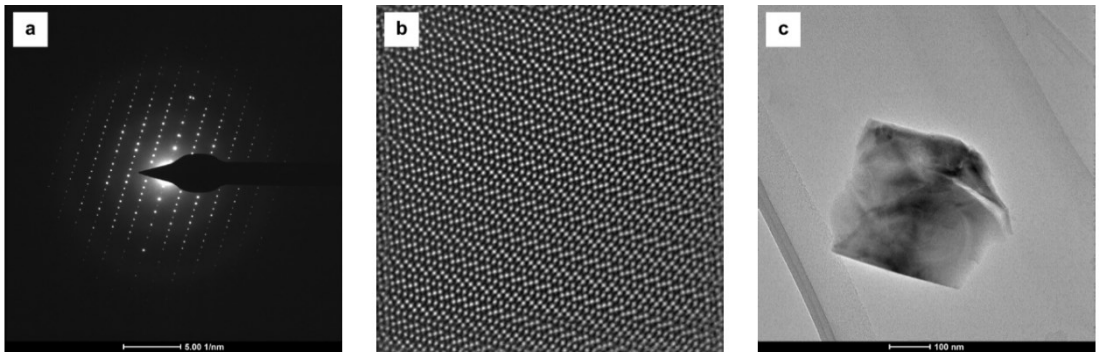

Figure 7.7 Graphical representations of (a) the zone axis, (b) the high-angle annular dark field (HAADF) image, and (c) a bright field image of the investigated crystallite of $Sr_5Si_2P_6N_{16}$.

7.3.4 SHG results of $Sr_2SiP_2N_6$

Table 7.10 Results of SHG measurements on powder samples of Quartz, KDP (KH_2PO_4), Al_2O_3 and $Sr_2SiP_2N_6$.

Samples	SHG intensities in mV
Quartz (<5μm)	24(4)
Quartz (5-25 μm)	174(25)
Quartz (25-50 μm)	344(100)
Al_2O_3 (9 μm)	0(1)
KDP (5-25 μm)	650(108)
KDP (25-50 μm)	2120(290)
$Sr_2SiP_2N_6$ (<30μm)	31(11)

The structure of $Sr_2SiP_2N_6$ has space group symmetry $C222_1$. The respective point group 222 has three nonzero coefficients d_{14}, d_{25} and d_{36}. Considering the Kleinman symmetry condition, there is one independent coefficient, namely $d_{14}=d_{25}=d_{36}$, contributing in the SHG intensity. We calculated the SHG tensor coefficient d_{14}= -1.48 pm/V for $Sr_2SiP_2N_6$ using DFT. According our calculation, the SHG tensor coefficient of $Sr_2SiP_2N_6$ is about 5-times as large as those of quartz. Quartz (SiO_2) has the SHG tensor coefficient of d_{11} = 0.3 pm/V and is not phase matchable. For comparison, KDP (KH_2PO_4) has a SHG tensor coefficient of d_{36} = 0.39 pm/V and is phase matchable. Therefore, its SHG signal is about three to six times stronger than that of quartz. The experiment shows that the SHG effect of $Sr_2SiP_2N_6$ is weak and comparable with quartz. Due the weak SHG signal and the calculated high SHG tensor coefficient, most probably $Sr_2SiP_2N_6$ is non-phase matchable. Additional measurements to determine the grain size dependence of SHG signals could provide information on the phase matching conditions. However, such measurements were beyond the scope of the present study.

7.3.5 Raman spectrum of $Sr_2SiP_2N_6$

Raman spectra obtained from DFPT-based calculations are generally in good agreement with the experimental data (Figure S8). The characteristic and strongest two Raman modes of $Sr_2SiP_2N_6$ can be observed at 544.5 and 680 cm^{-1}. The excellent agreement between the theoretical and experimental Raman spectra very strongly supports the underlying structural model with an ordered network.

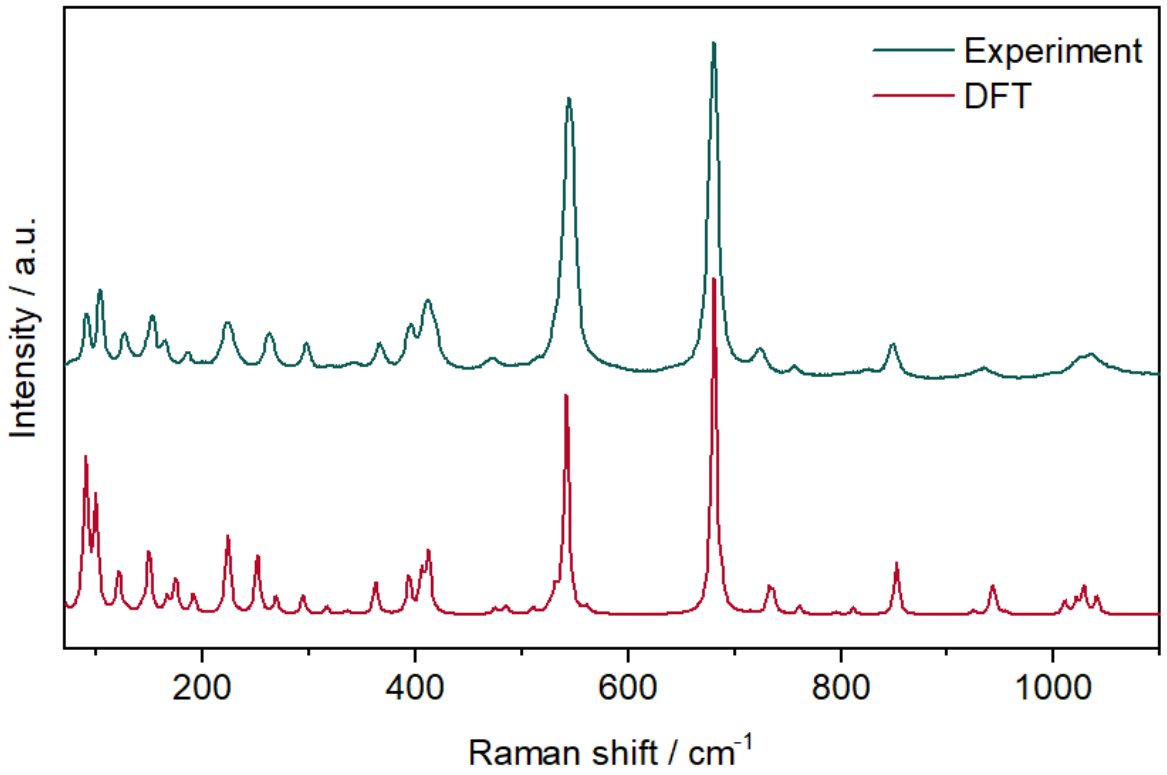

Figure 7.8 Comparison of Raman bands of experimental data (green) and DFT-calculated data (red) for $Sr_2SiP_2N_6$. The calculated data was scaled by a factor of 1.0441.

7.3.6 Precession images

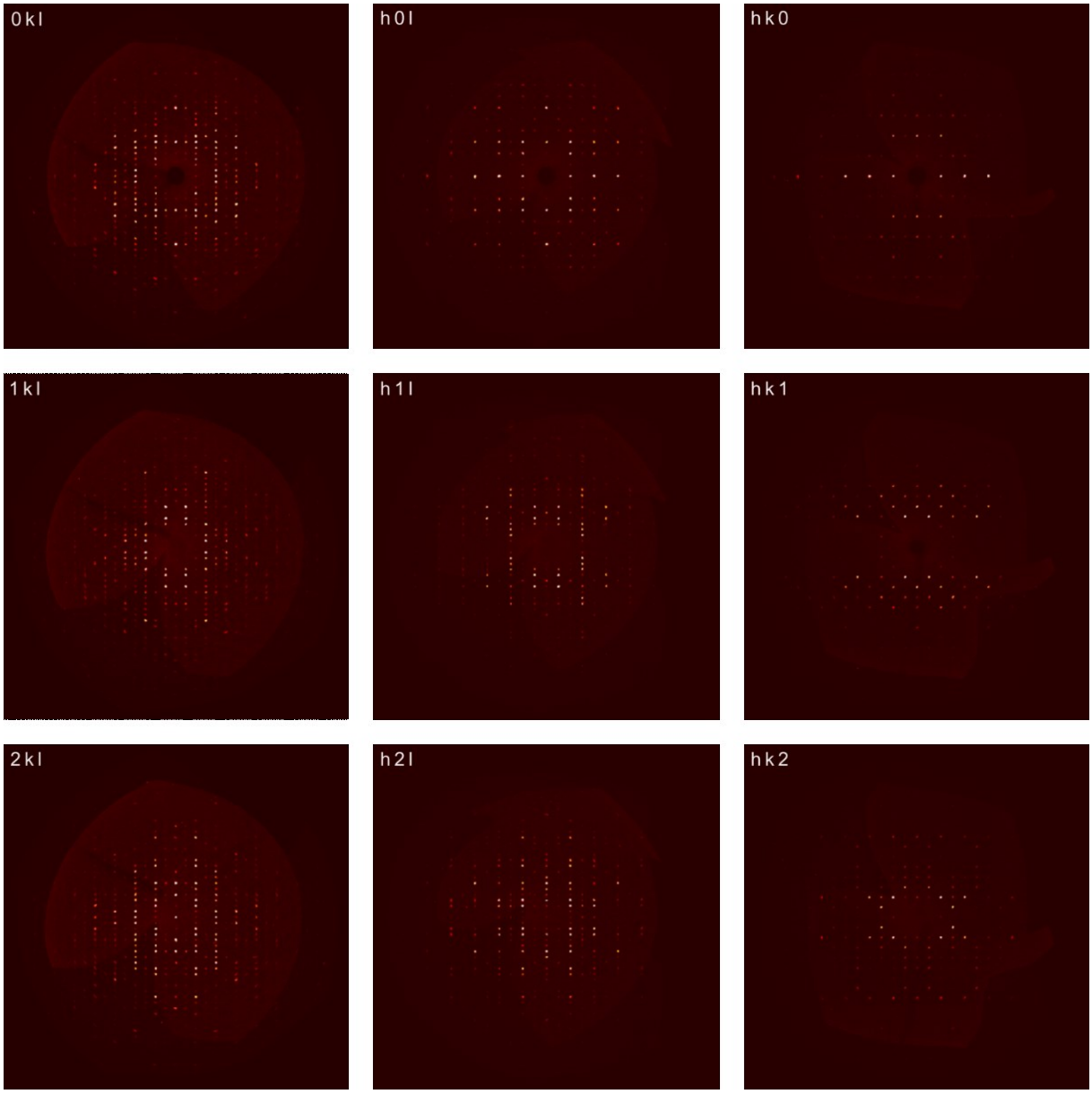

Figure 7.9 Precession images of $Sr_5Si_2P_6N_{16}$ where there are no superstructure reflections visible.

7.3.7 Crystallographic calculations

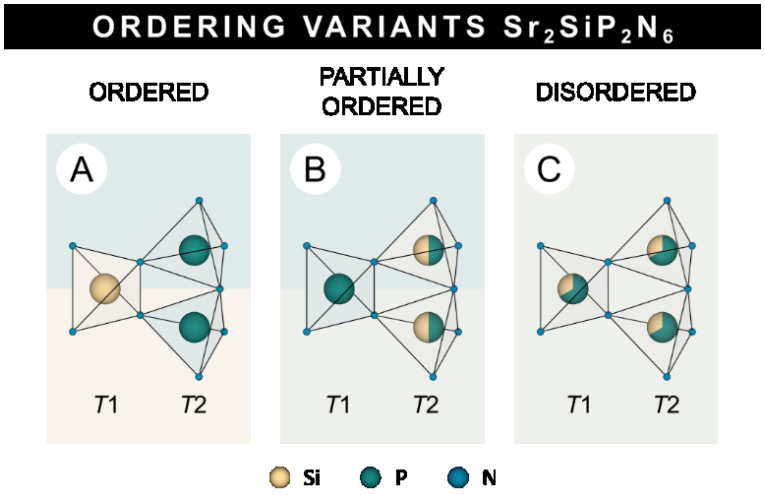

Figure 7.10 Ordering variants of $Sr_2SiP_2N_6$ with (A) full ordering, (B) partial ordering, and (C) disorder of tetrahedral sites *T*1 and *T*2.

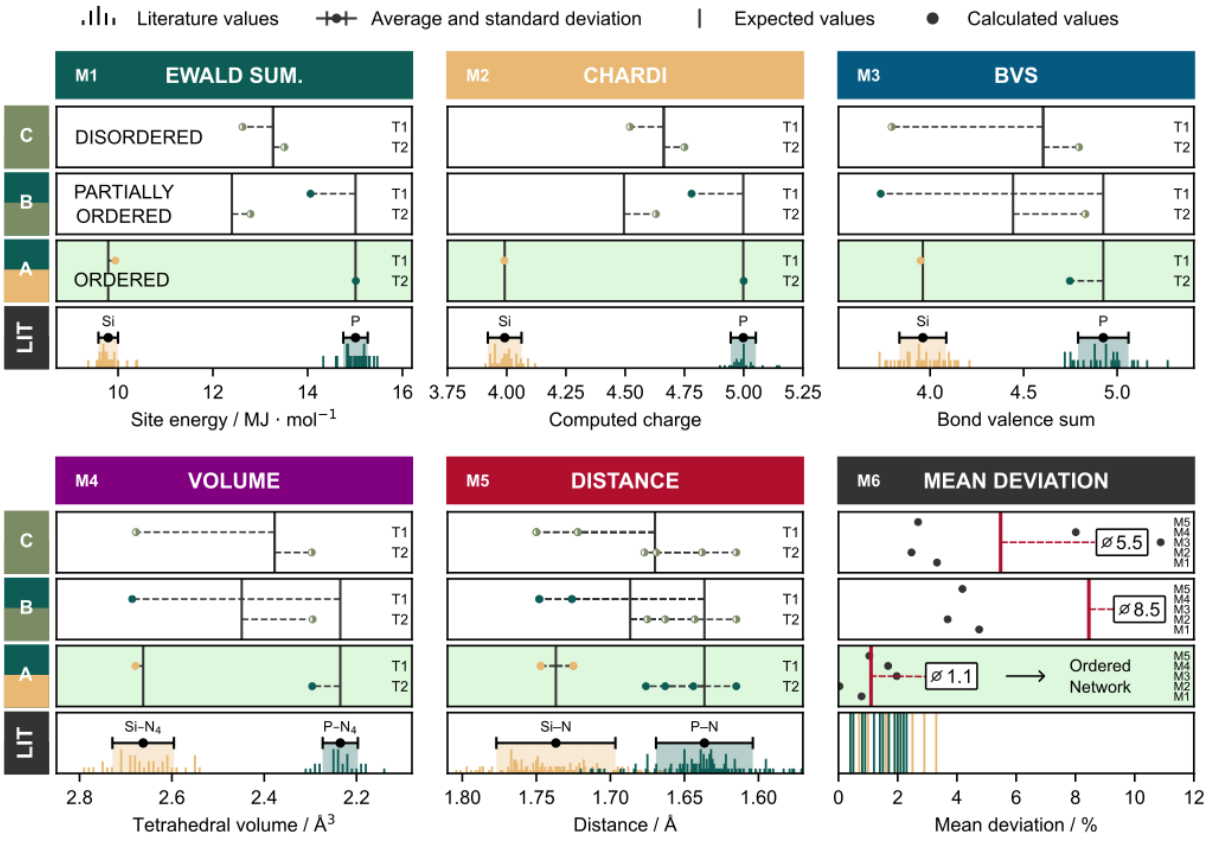

Figure 7.11 Comparison of all ordering variants (A)–(C) of $Sr_2SiP_2N_6$ by low-cost crystallographic calculations, i.e., Ewald site energies, CHARDI, BVS, tetrahedral volumes, and distances. For each method, we considered the occupation of all tetrahedral positions *T*1'–*T*4' separately, with Si (yellow), P (green), and mixed (Si, P) (olive green). The ordering variant with the lowest mean percentage deviation from the expected values that were calculated from literature (LIT) gives the most probable solution.

Table 7.11 Calculated values for $Sr_2SiP_2N_6$ for Ewald site energies, charge distributions (CHARDI), bond valence sums (BVS), tetrahedral volumes, and tetrahedral distances.

Ordering Variant	Site	OCC.	EWALD	CHARDI	BVS	Volume / Å^3	(Si, P)–N distances / Å	Mean deviation / %
1 (Ordered)	*T*1	Si	9.94	3.99	3.949	2.679	[1.725, 1.725, 1.747, 1.747]	1.1
	*T*2	P	15.016	5	4.747	2.296	[1.615, 1.644, 1.663, 1.676]	
2 (Partially ordered)	*T*1	P	14.06	4.78	3.736	2.686	[1.726, 1.726, 1.748, 1.748]	8.5
	*T*2	($Si_{0.5}$, $P_{0.5}$)	12.794	4.63	4.83	2.295	[1.615, 1.643, 1.663, 1.675]	
3 (Disordered)	*T*1	($Si_{0.33}$, $P_{0.67}$)	12.626	4.52	3.794	2.678	[1.722, 1.722, 1.75, 1.75]	5.5
	*T*2	($Si_{0.33}$, $P_{0.67}$)	13.509	4.75	4.796	2.297	[1.615, 1.638, 1.669, 1.677]	

Table 7.12 Calculated values of $Sr_5Si_2P_6N_{16}$ for Ewald site energies, charge distributions (CHARDI), bond valence sums (BVS), tetrahedral volumes, and tetrahedral distances.

Ordering Variant	Site	OCC.	EWALD	CHARDI	BVS	Volume / Å^3	(Si, P)–N distances / Å	Mean deviation / %
1 (Ordered)	*T*1’	P	14.684	4.9	4.529	2.371	[1.652, 1.665, 1.674, 1.683]	5.2
	*T*2’	P	15.035	4.91	4.661	2.325	[1.647, 1.656, 1.661, 1.666]	
	*T*3’	P	14.949	4.94	4.599	2.357	[1.65, 1.653, 1.664, 1.683]	
	*T*4’	Si	11.022	4.23	4.86	2.36	[1.653, 1.659, 1.661, 1.684]	
2 (Partially ordered)	*T*1’	($Si_{0.5}$, $P_{0.5}$)	12.819	4.61	4.543	2.363	[1.651, 1.665, 1.669, 1.681]	3.3
	*T*2’	P	15.044	4.9	4.667	2.323	[1.648, 1.656, 1.658, 1.666]	
	*T*3’	($Si_{0.5}$, $P_{0.5}$)	13.037	4.67	4.644	2.349	[1.648, 1.652, 1.663, 1.68]	
	*T*4’	P	14.717	4.83	4.536	2.375	[1.656, 1.66, 1.667, 1.688]	
3 (Disordered)	*T*1’	($Si_{0.25}$, $P_{0.75}$)	13.753	4.75	4.60725	2.366	[1.651, 1.665, 1.67, 1.682]	1.0
	*T*2’	($Si_{0.25}$, $P_{0.75}$)	14.069	4.75	4.675	2.319	[1.647, 1.655, 1.658, 1.665]	
	*T*3’	($Si_{0.25}$, $P_{0.75}$)	13.981	4.81	4.626	2.353	[1.649, 1.653, 1.664, 1.681]	
	*T*4’	($Si_{0.25}$, $P_{0.75}$)	13.759	4.69	4.59375	2.371	[1.656, 1.659, 1.665, 1.687]	

7.3.8 Luminescence

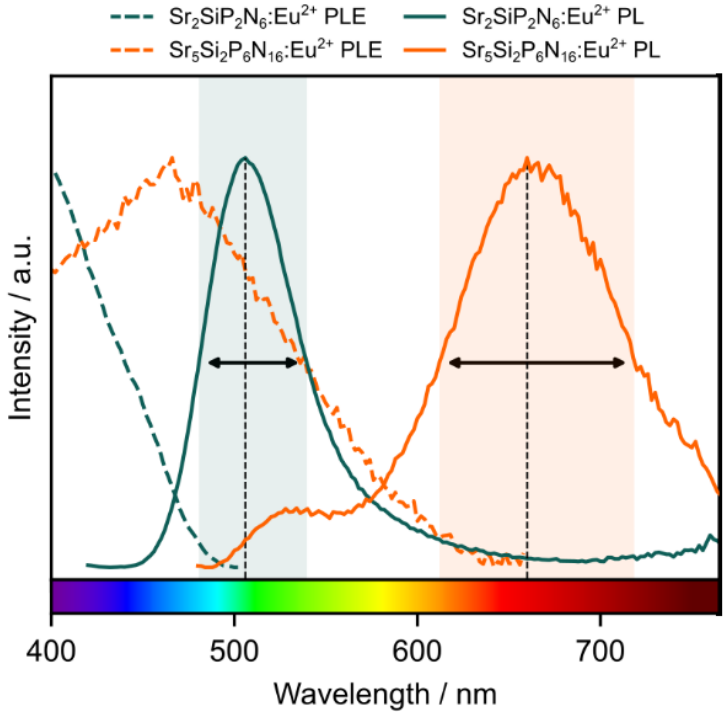

Figure 7.12 Unfiltered photoluminescence excitation (PLE, dashed) and photoluminescence (PL, solid) spectra of $Sr_2SiP_2N_6:Eu^{2+}$ (green) and $Sr_5Si_2P_6N_{16}:Eu^{2+}$ (orange).

7.4 References

(1) Stock, A.; Grüneberg, H. Über Den Phosphorstickstoff. *Ber. Dtsch. Chem. Ges.* **1907**, *40* (2), 2573–2578. https://doi.org/10.1002/cber.190704002184.

(2) Eisenburger, L.; Oeckler, O.; Schnick, W. High-Pressure High-Temperature Synthesis of Mixed Nitridosilicatephosphates and Luminescence of $AESiP_3N_7:Eu^{2+}$ (*AE*=Sr, Ba). *Chem. Eur. J.* **2021**, *27* (13), 4461–4465. https://doi.org/10.1002/chem.202005495.

(3) Suhrmann, R.; Clusius, K. Über Die Reindarstellung Der Alkalimetalle. *Z. Anorg. Allg. Chem.* **1926**, *152* (1), 52–58. https://doi.org/10.1002/zaac.19261520107.

(4) Pritzl, R. M.; Prinz, N.; Strobel, P.; Schmidt, P. J.; Johrendt, D.; Schnick, W. From Framework to Layers Driven by Pressure – The Monophyllo-Oxonitridophosphate β-$MgSrP_3N_5O_2$ and Comparison to Its α-Polymorph. *Chem. Eur. J.* **2023**, *29* (41), e202301218. https://doi.org/10.1002/chem.202301218.

(5) Walker, D.; Carpenter, M. A.; Hitch, C. M. Some Simplifications to Multianvil Devices for High Pressure Experiments. *Am. Mineral.* **1990**, *75*, 1020–1028.

(6) Rubie, D. C. Characterising the Sample Environment in Multianvil High-Pressure Experiments. *Phase Transitions* **1999**, *68* (3), 431–451. https://doi.org/10.1080/01411599908224526.

(7) Huppertz, H. Multianvil High-Pressure/High-Temperature Synthesis in Solid State Chemistry. *Z. Kristallogr. Cryst. Mater.* **2004**, *219* (6), 330–338. https://doi.org/10.1524/ZKRI.219.6.330.34633/MACHINEREADABLECITATION/RIS.

(8) Bertschler, E. M.; Niklaus, R.; Schnick, W. Li12P3N9 with Non-Condensed [P3N9]12−-Rings and Its High-Pressure Polymorph Li4PN3 with Infinite Chains of PN4-Tetrahedra. *Chem. Eur. J.* **2017**, *23* (40), 9592–9599. https://doi.org/10.1002/CHEM.201700979.

(9) Mallmann, M.; Wendl, S.; Strobel, P.; Schmidt, P. J.; Schnick, W. $Sr_3P_3N_7$: Complementary Approach by Ammonothermal and High-Pressure Syntheses. *Chem. Eur. J.* **2020**, *26* (28), 6257–6263. https://doi.org/10.1002/chem.202000297.

(10) Marchuk, A.; Neudert, L.; Oeckler, O.; Schnick, W. $CaMg_2P_6O_3N_{10}$ – A Quinary Oxonitridophosphate with an Unprecedented Tetrahedra Network Structure Type. *Eur. J. Inorg. Chem.* **2014**, *2014* (21), 3427–3434. https://doi.org/10.1002/ejic.201402302.

(11) Bruker-AXS, APEX3, Vers. 2016.5-0, Karlsruhe, Germany, 2016. **2016**.

(12) SAINT. SAINT, Data Integration Software, Madison, Wisconsin, USA. **1997**.

(13) Bruker-AXS. XPREP Reciprocal Space Exploration, Vers. 6.12, Karlsruhe. **2001**.

(14) Sheldrick, G. M. SHELXS-97 Program of the Solution of Crystal Structure, University of Göttingen, Göttingen. **1997**.

(15) Sheldrick, G. M. Crystal Structure Refinement with *SHELXL*. *Acta Crystallogr. C Struct. Chem.* **2015**, *71* (1), 3–8. https://doi.org/10.1107/S2053229614024218.

(16) Farrugia, L. J. *WinGX* and *ORTEP for Windows*: An Update. *J. Appl. Crystallogr.* **2012**, *45* (4), 849–854. https://doi.org/10.1107/S0021889812029111.

(17) Gatan, I.; DigitalMicrograph; Version 3.6.5; Pleasanton; California (USA). STEM EDX. **1999**.

(18) Lábár, J. L. Consistent Indexing of a (Set of) Single Crystal SAED Pattern(s) with the ProcessDiffraction Program. *Ultramicroscopy* **2005**, *103* (3), 237. https://doi.org/10.1016/J.ULTRAMIC.2004.12.004.

(19) Stadelmann, J. P.; jEMS software package; Version 3.60907U2011; Saas-Fee (Switzerland). JEMS Software. **2011**.

(20) Thermo Fisher Scientific; Velox; Waltham, Massachusetts (USA), **2021**.

(21) Schlieper, T.; Milius, W.; Schnick, W. Nitrido-Silicate. II [1]. Hochtemperatur-Synthesen Und Kristallstrukturen von $Sr_2Si_5N_8$ Und $Ba_2Si_5N_8$. *Z. Anorg. Allg. Chem.* **1995**, *621* (8), 1380–1384. https://doi.org/10.1002/zaac.19956210817.

(22) Karau, F.; Schnick, W. Hochdrucksynthese von $BaSr_2P_6N_{12}$ und $BaCa_2P_6N_{12}$ und Strukturvergleich der Reihe BaP_2N_4, $BaCa_2P_6N_{12}$ und $BaSr_2P_6N_{12}$. *Z. Anorg. Allg. Chem.* **2006**, *632* (2), 231. https://doi.org/10.1002/ZAAC.200500362.

(23) Karau, F. W.; Schnick, W. High-Pressure Synthesis and X-Ray Powder Structure Determination of the Nitridophosphate BaP_2N_4. *J. Solid State Chem.* **2005**, *178* (1), 135. https://doi.org/10.1016/J.JSSC.2004.10.034.

(24) Huppertz, H.; Schnick, W. Edge-Sharing SiN_4 Tetrahedra in the Highly Condensed Nitridosilicate $BaSi_7N_{10}$. *Chem. Eur. J.* **1997**, *3* (2), 249. https://doi.org/10.1002/CHEM.19970030213.

(25) Vogel, S.; Bykov, M.; Bykova, E.; Wendl, S.; Kloß, S. D.; Pakhomova, A.; Dubrovinskaia, N.; Dubrovinsky, L.; Schnick, W. Nitride Spinel: An Ultraincompressible High-Pressure Form of BeP_2N_4. *Angew. Chem. Int. Ed.* **2020**, *59* (7), 2730. https://doi.org/10.1002/ANIE.201910998.

(26) Eckerlin, P. Zur Kenntnis des Systems Be_3N_2 – Si_3N_4, IV. Die Kristallstruktur von BeSiN2. *Z. Anorg. Allg. Chem.* **1967**, *353* (5–6), 225. https://doi.org/10.1002/ZAAC.19673530502.

(27) Wendl, S.; Mardazad, S.; Strobel, P.; Schmidt, P. J.; Schnick, W. HIP to Be Square: Simplifying Nitridophosphate Synthesis in a Hot Isostatic Press. *Angew. Chem. Int. Ed.* **2020**, *59*, 18240. https://doi.org/10.1002/ANGE.202008570.

(28) Römer, S. R.; Braun, C.; Oeckler, O.; Schmidt, P. J.; Kroll, P.; Schnick, W. HP-$Ca_2Si_5N_8$—A New High-Pressure Nitridosilicate: Synthesis, Structure, Luminescence, and DFT Calculations. *Chem. Eur. J.* **2008**, *14* (26), 7892. https://doi.org/10.1002/CHEM.200800602.

(29) Zeuner, M.; Pagano, S.; Hug, S.; Pust, P.; Schmiechen, S.; Scheu, C.; Schnick, W. $Li_2CaSi_2N_4$ and $Li_2SrSi_2N_4$ – a Synthetic Approach to Three-Dimensional Lithium Nitridosilicates. *Eur. J. Inorg. Chem.* **2010**, *2010* (31), 4945. https://doi.org/10.1002/EJIC.201000671.

(30) Pucher, F. J.; Marchuk, A.; Schmidt, P. J.; Wiechert, D.; Schnick, W. Luminescent Nitridophosphates CaP_2N_4:Eu^{2+}, SrP_2N_4:Eu^{2+}, BaP_2N_4:Eu^{2+}, and $BaSr_2P_6N_{12}$:Eu^{2+}. *Chem. Eur. J.* **2015**, *21* (17), 6443. https://doi.org/10.1002/CHEM.201500047.

(31) Kloß, S. D.; Weidmann, N.; Niklaus, R.; Schnick, W. High-Pressure Synthesis of Melilite-Type Rare-Earth Nitridophosphates $RE_2P_3N_7$ and a $Ba_2Cu[Si_2O_7]$-Type Polymorph. *Inorg. Chem.* **2016**, *55* (18), 9400. https://doi.org/10.1021/ACS.INORGCHEM.6B01611/SUPPL_FILE/IC6B01611_SI_004.CIF.

(32) Landskron, K.; Schnick, W. $Rb_3P_6N_{11}$ and $Cs_3P_6N_{11}$—New Highly Condensed Nitridophosphates by High-Pressure High-Temperature Synthesis. *J. Solid State Chem.* **2001**, *156* (2), 390. https://doi.org/10.1006/JSSC.2000.9010.

(33) Strobel, P.; Weiler, V.; Schmidt, P. J.; Schnick, W. Sr[$BeSi_2N_4$]:Eu^{2+}/Ce^{3+} and Eu[$BeSi_2N_4$]: Nontypical Luminescence in Highly Condensed Nitridoberyllosilicates. *Chem. Eur. J.* **2018**, *24* (28), 7243. https://doi.org/10.1002/CHEM.201800912.

(34) Jacobs, H.; Nymwegen, R. Darstellung Und Kristallstruktur Eines Kaliumnitridophosphats, $K_3P_6N_{11}$. *Z. Anorg. Allg. Chem.* **1997**, *623* (1–6), 429. https://doi.org/10.1002/ZAAC.19976230168.

(35) Lupart, S.; Zeuner, M.; Pagano, S.; Schnick, W. Chain-Type Lithium Rare-Earth Nitridosilicates – $Li_5Ln_5Si_4N_{12}$ with *Ln* = La, Ce. *Eur. J. Inorg. Chem.* **2010**, *2010* (18), 2636. https://doi.org/10.1002/EJIC.201000245.

(36) Kloß, S. D.; Schnick, W. Rare-Earth-Metal Nitridophosphates through High-Pressure Metathesis. *Angew. Chem. Int. Ed.* **2015**, *54* (38), 11250. https://doi.org/10.1002/ANIE.201504844.

(37) Mallmann, M.; Maak, C.; Niklaus, R.; Schnick, W. Ammonothermal Synthesis, Optical Properties, and DFT Calculations of Mg_2PN_3 and Zn_2PN_3. *Chem. Eur. J.* **2018**, *24* (52), 13963. https://doi.org/10.1002/CHEM.201803293.

(38) Bruls, R. J.; Hintzen, H. T.; Metselaar, R.; Loong, C. K. Anisotropic Thermal Expansion of $MgSiN_2$ from 10 to 300 K as Measured by Neutron Diffraction. *J. Phys. Chem. Solids* **2000**, *61* (8), 1285. https://doi.org/10.1016/S0022-3697(99)00416-3.

(39) Landskron, K.; Schmid, S.; Schnick, W. Hochdruck-Synthese, Kristallstruktur und Eigenschaften von $NaPN_2$. *Z. Anorg. Allg. Chem.* **2001**, *627* (11), 2469. https://doi.org/10.1002/1521-3749.

(40) Jacobs, H.; Mengis, H. Preparation and Crystal Structure of a Sodium Silicon Nitride, $NaSi_2N_3$. *Eur. J. Solid State Inorg. Chem.* **1993**, *30*, 45.

(41) Wendl, S.; Schnick, W. $SrH_4P_6N_{12}$ and SrP_8N_{14}: Insights into the Condensation Mechanism of Nitridophosphates under High Pressure. *Chem. Eur. J.* **2018**, *24* (59), 15889. https://doi.org/10.1002/CHEM.201803125.

(42) Pilet, G.; Höppe, H. A.; Schnick, W.; Esmaeilzadeh, S. Crystal Structure and Mechanical Properties of $SrSi_7N_{10}$. *Solid State Sci.* **2005**, *7* (4), 391. https://doi.org/10.1016/J.SOLIDSTATESCIENCES.2005.01.011.

(43) Ong, S. P.; Richards, W. D.; Jain, A.; Hautier, G.; Kocher, M.; Cholia, S.; Gunter, D.; Chevrier, V. L.; Persson, K. A.; Ceder, G. Python Materials Genomics (Pymatgen): A Robust, Open-Source Python Library for Materials Analysis. *Comput. Mater. Sci.* **2013**, *68*, 314–319. https://doi.org/10.1016/j.commatsci.2012.10.028.

(44) Toukmaji, A. Y.; Board, J. A. Ewald Summation Techniques in Perspective: A Survey. *Comput. Phys. Commun.* **1996**, *95*, 73–92.

(45) Nespolo, M.; Guillot, B. *CHARDI2015*: Charge Distribution Analysis of Non-Molecular Structures. *J. Appl. Crystallogr.* **2016**, *49* (1), 317–321. https://doi.org/10.1107/S1600576715024814.

(46) Nespolo, M. Charge Distribution as a Tool to Investigate Structural Details. IV. A New Route to Heteroligand Polyhedra. *Acta Crystallogr. Sect. B* **2016**, *72* (1), 51–66. https://doi.org/10.1107/S2052520615019472.

(47) Link, L.; Niewa, R. *Polynator* : A Tool to Identify and Quantitatively Evaluate Polyhedra and Other Shapes in Crystal Structures. *J. Appl. Crystallogr.* **2023**, *56* (6), 1855–1864. https://doi.org/10.1107/S1600576723008476.

(48) Momma, K.; Izumi, F. *VESTA 3* for Three-Dimensional Visualization of Crystal, Volumetric and Morphology Data. *J. Appl. Crystallogr.* **2011**, *44* (6), 1272–1276. https://doi.org/10.1107/S0021889811038970.

(49) Altomare, A.; Cuocci, C.; Giacovazzo, C.; Moliterni, A.; Rizzi, R.; Corriero, N.; Falcicchio, A. *EXPO2013*: A Kit of Tools for Phasing Crystal Structures from Powder Data. *J. Appl. Crystallogr.* **2013**, *46* (4), 1231–1235. https://doi.org/10.1107/S0021889813013113.

(50) Brese, N. E.; O'Keeffe, M. Bond-Valence Parameters for Solids. *Acta Crystallogr. Sect. B* **1991**, *47*, 192.

(51) Kurtz, S. K.; Perry, T. T. A Powder Technique for the Evaluation of Nonlinear Optical Materials: A Powder Technique for the Evaluation of Nonlinear Optical Materials. *J. Appl. Phys.* **1968**, *39* (8), 3798. https://doi.org/10.1063/1.1656857.

(52) Bayarjargal, L.; Fruhner, C. J.; Schrodt, N.; Winkler, B. $CaCO_3$ Phase Diagram Studied with Raman Spectroscopy at Pressures up to 50 GPa and High Temperatures and DFT Modeling. *Phys. Earth Planet. Inter.* **2018**, *281*, 31. https://doi.org/10.1016/J.PEPI.2018.05.002.

(53) Hohenberg, P.; Kohn, W. Inhomogeneous Electron Gas. *Phys. Rev. B* **1964**, *136* (3B), B864. https://doi.org/10.1103/PHYSREV.136.B864/FIGURE/1/THUMB.

(54) Clark, S. J.; Segall, M. D.; Pickard, C. J.; Hasnip, P. J.; Probert, M. I. J.; Refson, K.; Payne, M. C. First Principles Methods Using CASTEP. *Z. Kristallogr. Cryst. Mater.* **2005**, *220* (5–6), 567. https://doi.org/10.1524/ZKRI.220.5.567.65075/MACHINEREADABLECITATION/RIS.

(55) Perdew, J. P.; Burke, K.; Ernzerhof, M. Generalized Gradient Approximation Made Simple. *Phys. Rev. Lett.* **1996**, *77* (18), 3865–3868. https://doi.org/10.1103/PhysRevLett.77.3865.

(56) Lejaeghere, K.; Bihlmayer, G.; Björkman, T.; Blaha, P.; Blügel, S.; Blum, V.; Caliste, D.; Castelli, I. E.; Clark, S. J.; Dal Corso, A.; De Gironcoli, S.; Deutsch, T.; Dewhurst, J. K.; Di Marco, I.; Draxl, C.; Dułak, M.; Eriksson, O.; Flores-Livas, J. A.; Garrity, K. F.; Genovese, L.; Giannozzi, P.; Giantomassi, M.; Goedecker, S.; Gonze, X.; Grånäs, O.; Gross, E. K. U.; Gulans, A.; Gygi, F.; Hamann, D. R.; Hasnip, P. J.; Holzwarth, N. A. W.; Iuşan, D.; Jochym, D. B.; Jollet, F.; Jones, D.; Kresse, G.; Koepernik, K.; Küçükbenli, E.; Kvashnin, Y. O.; Locht, I. L. M.; Lubeck, S.; Marsman, M.; Marzari, N.; Nitzsche, U.; Nordström, L.; Ozaki, T.; Paulatto, L.; Pickard, C. J.; Poelmans, W.; Probert, M. I. J.; Refson, K.; Richter, M.; Rignanese, G. M.; Saha, S.; Scheffler, M.; Schlipf, M.; Schwarz, K.; Sharma, S.; Tavazza, F.; Thunström, P.; Tkatchenko, A.; Torrent, M.; Vanderbilt, D.; Van Setten, M. J.; Van Speybroeck, V.; Wills, J. M.; Yates, J. R.; Zhang, G. X.; Cottenier, S. Reproducibility in Density Functional Theory Calculations of Solids. *Science* **2016**, *351* (6280).

(57) Monkhorst, H. J.; Pack, J. D. Special Points for Brillouin-Zone Integrations. *Phys. Rev. B* **1976**, *13* (12), 5188. https://doi.org/10.1103/PhysRevB.13.5188.

(58) Grimme, S.; Antony, J.; Ehrlich, S.; Krieg, H. A Consistent and Accurate Ab Initio Parametrization of Density Functional Dispersion Correction (DFT-D) for the 94 Elements H-Pu. *J. Chem. Phys.* **2010**, *132* (15).

(59) Refson, K.; Tulip, P. R.; Clark, S. J. Variational Density-Functional Perturbation Theory for Dielectrics and Lattice Dynamics. *Phys. Rev. B* **2006**, *73* (15), 155114. https://doi.org/10.1103/PHYSREVB.73.155114/FIGURES/7/MEDIUM.

(60) Miwa, K. Prediction of Raman Spectra with Ultrasoft Pseudopotentials. *Phys. Rev. B* **2011**, *84* (9), 094304. https://doi.org/10.1103/PHYSREVB.84.094304/FIGURES/2/MEDIUM.

(61) Yamane, H.; Morito, H. Synthesis and Crystal Structures of Ca_4SiN_4 and NEW POLYMORPH of $Ca_5Si_2N_6$. *Inorg. Chem.* **2013**, *52* (9), 5559. https://doi.org/10.1021/IC400522Z/SUPPL_FILE/IC400522Z_SI_003.CIF.

(62) Ottinger, F.; Nesper, R. Synthesis and Crystal Structure of the Nitridosilicates $Ca_5[Si_2N_6]$ and $Ca_7[NbSi_2N_9]$. *Z. Anorg. Allg. Chem.* **2005**, *631* (9), 1597. https://doi.org/10.1002/ZAAC.200500094.

(63) Yamane, H.; DiSalvo, F. J. Preparation and Crystal Structure of a New Barium Silicon Nitride, $Ba_5Si_2N_6$. *J. Alloys Compd.* **1996**, *240* (1–2), 33. https://doi.org/10.1016/0925-8388(96)02242-6.

(64) Gál, Z. A.; Mallinson, P. M.; Orchard, H. J.; Clarke, S. J. Synthesis and Structure of Alkaline Earth Silicon Nitrides: $BaSiN_2$, $SrSiN_2$, and $CaSiN_2$. *Inorg. Chem.* **2004**, *43* (13), 3998. https://doi.org/10.1021/IC049901P/SUPPL_FILE/IC049901PSI20040126_125250.CIF.

(65) Wendl, S.; Eisenburger, L.; Strobel, P.; Günther, D.; Wright, J. P.; Schmidt, P. J.; Oeckler, O.; Schnick, W. Nitridophosphate-Based Ultra-Narrow-Band Blue-Emitters: Luminescence Properties of $AEP_8N_{14}:Eu^{2+}$ (*AE*=Ca, Sr, Ba). *Chem. Eur. J.* **2020**, *26* (32), 7292. https://doi.org/10.1002/CHEM.202001129.

8 Supporting Information

Chapter 3

8.1 Experimental Part

8.1.1 Synthesis of Starting Materials

We synthesized semicrystalline P_3N_5 by reacting P_4S_{10} in a steady flow of ammonia at 850 °C, as described in the literature.[1,2] $Sr(N_3)_2$ was prepared from $SrCO_3$ with aqueous HN_3 in a cation exchange reaction as reported by Suhrmann et al., and again by Pritzl et al.[3,4] Amorphous Si_3N_4 (UBE, SNA-00) was commercially available. For doping we used europium(III) nitride that we synthesized from Eu metal (smart-elements, 99.99%) and dried N_2 gas in a radiofrequency furnace (TIG 10/100; Hüttinger Elektronik Freiburg, Germany) at 1000 °C for 2 h.

8.1.2 High-Pressure High-Temperature Synthesis

We prepared $Sr_5Si_7P_2N_{16}$ from 33.2 mg (0.19 mmol) of $Sr(N_3)_2$, 4.2 mg (0.03 mmol) of P_3N_5, and 12.7 mg (0.09 mmol) of Si_3N_4. For $Sr_5Si_7P_2N_{16}:Eu^{2+}$, we added 1 mol% EuN with respect to Sr^{2+}. Since the starting materials are sensitive to hydrolysis, we handled all materials in an Ar-filled glovebox (Unilab, MBraun, Garching; O_2 <1 ppm; H_2O <1 ppm) where the mixture was ground and filled into a boron nitride crucible with a molybdenum inlay. The reaction was carried out at 3 GPa and 1400 °C, for which we used a multianvil press with a Walker type module.[5–7] Heating, dwelling, and cooling times were all set to 240 min. Additional information on the synthesis in and operation of the multianvil press can be found in the literature.[8–10]

8.1.3 Powder X-ray Diffraction

Powder X-ray diffraction (PXRD) data were obtained using a STOE Stadi P diffractometer from STOE & Cie GmbH in Darmstadt. The setup consisted of a modified Debye-Scherrer configuration using Cu-$K_{\alpha1}$ radiation with a wavelength of 1.54060 Å. The system was equipped with a MYTHEN 1K stripe detector and a Ge(111) monochromator. For analysis, the powdered

samples were enclosed in a glass capillary from Hilgenberg, Malsfeld, with an outer diameter of 0.3 mm and positioned in the center of a rotating goniometer head. To verify $Sr_5Si_7P_2N_{16}$ as the major component of the prepared sample, the collected data were subjected to Rietveld refinement using TOPAS Academic software.[11,12] Throughout the refinement process, peak shapes were defined by using the fundamental parameter method. Possible preferred orientations of the crystallites were corrected using a fourth order spherical harmonic function. In addition, the background was determined using a shifted Chebyshev polynomial.[13,14]

8.1.4 Single-Crystal X-ray Diffraction

Diffraction data were collected using a Bruker D8 VENTURE diffractometer equipped with a rotating anode and using Mo-K_α radiation with a wavelength of 0.71073 Å. Data integration and absorption fits were performed using APEX4 software.[15–17] Both SHELXS and SHELXL were used to determine and refine the structure, using Direct Methods and the least-squares approach.[18–20]

8.1.5 Scanning Transmission Electron Microscopy

Ground samples were mixed with pure ethanol and one drop was placed on a TEM grid coated with a lacey carbon film (Plano GmbH, Wetzlar, Germany). This grid was placed on an analytical double-tilt holder (±30°) and then inserted into a Cs DCOR (Heidelberg, Germany) probe-corrected Titan Themis 300 TEM from FEI, USA. This STEM has an X-FEG source, a postcolumn filter called Enfinium ER-799 from Gatan, USA, a US1000XP camera from Gatan, USA, and a windowless 4-quadrant Super-X EDX detector from FEI, USA. TEM images were acquired using a 4k × 4k FEI Ceta CMOS camera. The device was operated at 300 kV, with specific settings like a 16.6 mrad semiconvergence angle, a 50 µm opening, and a HAADF detector inner semiangle of 33 mrad for a camera length of 245 mm. The program package Digital Micrograph was used to Fourier filter the STEM-HAADF image. Velox software was used to acquire the accompanying EDX maps.[21–24]

8.1.6 Scanning Electron Microscopy (SEM) and Energy-Dispersive X-ray Spectroscopy (EDX)

The specimens were placed on a conductive carbon film and then received a carbon overlay. EDX analysis was conducted with an FEI Helios Nanolab G3 Dual Beam UC from FEI, based in Hillsboro, OR, USA, which was outfitted with an X-Max 80 SDD detection system from Oxford Instruments in Abingdon, UK.

8.1.7 Inductively Coupled Plasma Optical Emission Spectroscopy

Measurements were made at a Varian Vista RL with a 40 MHz RF generator, and a VistaChip CCD detector.

8.1.8 Luminescence

Samples doped with Eu^{2+} were analyzed by using luminescence spectroscopy through a HORIBA Fluoromax4 system paired with an Olympus BX51 microscope. At room temperature, the PL and PLE spectra were measured. The emission and excitation wavelengths for $Sr_5Si_7P_2N_{16}:Eu^{2+}$ were set at 610 and 400 nm, respectively. The spectral range spanned from 400 to 800 nm, progressing in 2 nm increments.

8.1.9 Fourier-Transform Infrared Spectroscopy

The infrared spectra of the specimens were obtained by using a Bruker Alpha II FTIR device equipped with a diamond ATR component. All spectral data were captured inside a glovebox filled with argon, spanning a range from 450 to 4000 cm^{-1}.

8.1.10 Low-Cost Crystallographic Calculations

Ewald site energies were calculated with the *EwaldSummation* class of the Python Materials Genomics (pymatgen) library.[25,26] For charge distribution (CHARDI) and bond valence sum (BVS) calculations we used CHARDI2015 (Build 21) and EXPO2014 (v1.22.11), respectively.[27–29] To improve the quality of the BVS results, we used optimized R_0 parameters, as we reported earlier ($R_0(Si^{4+}–N^{3-})$ = 1.731 and $R_0(P^{5+}–N^{3-})$ = 1.712).[30] Volumes and distances were calculated with Polynator v1.3 and VESTA v3.5.8.[31,32] All values were compared to literature values by

calculating method-related and total mean deviations. For a full list of reference compounds, refer to our previous work.[30]

8.2 Introduction

Table 8.1 Mixed anionic tetrahedral networks of Si of the form AE–(T,Si)–N (AE = Ca, Sr, Ba; T = Li, Be, Mg, Al). 13 out of 16 networks, in other words, 81 % show a Si content larger than or equal to 50 %.

Compound	*AE*	Si content	Citation
AEMg_3SiN_4	Ba Sr Ca	25 %	[33] [34]
AE$AlSi_4N_7$	Ca Sr	80 %	[35] [36]
AE$Li_2Si_2N_4$	Ca Sr	50 %	[37]
AE$_3Li_4Si_2N_6$	Ca Sr	33 %	[38]
$Ba_2AlSi_5N_9$	Ba	83 %	[39]
$CaAlSiN_3$	Ca	50 %	[40]
Ca_4AlSiN_5	Ca	50 %	[41]
$Ca_5Al_2Si_2N_8$	Ca	50 %	[42]
$Ca_3LiSi_2N_5$	Ca	67 %	[43]
$SrBeSi_2N_4$	Sr	67 %	[44]
$Sr_8Mg_7Si_9N_{22}$	Sr	56 %	[45]

8.3 Results and Discussion

8.3.1 Powder X-Ray Diffraction

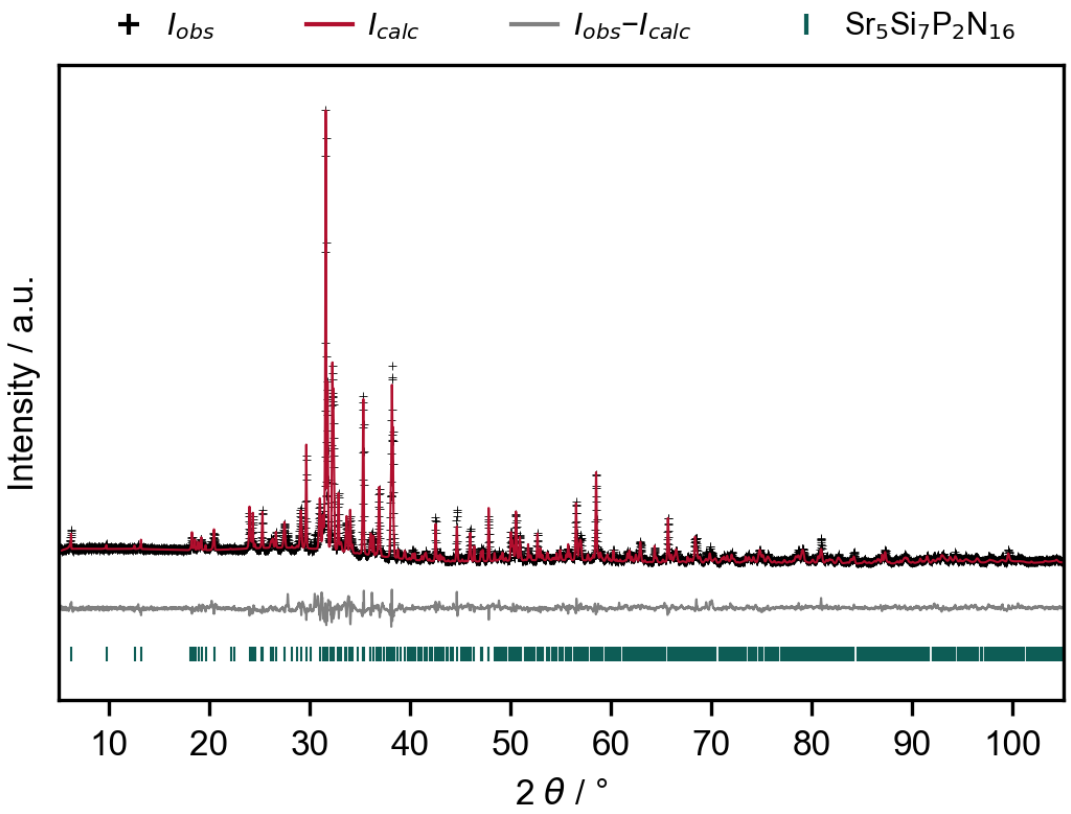

Figure 8.1 Plot of the Rietveld refinement based on powder X-ray diffraction data of the bulk sample of $Sr_5Si_7P_2N_{16}$.

Table 8.2 Crystallographic data of the Rietveld refinement based on powder XRD data of $Sr_5Si_7P_2N_{16}$. Standard deviations are given in parentheses.

Formula	$Sr_5Si_7P_2N_{16}$
Molar mass / g · mol^{-1}	920.83
Crystal system	Orthorhombic
Space group	*Pnma* (no. 62)
Lattice parameters / Å	a = 5.6828(2)
	b = 28.1117(1)
	c = 9.5277(3)
Cell volume / Å^3	1522.1(1)
Formula units / unit cell	4
X-ray density / g · cm^{-3}	4.018
Diffractometer	STOE Stadi P
Radiation	Cu-Kα_1 (λ = 1.54059 Å)
Monochromator	Ge(111)
Detector	Mythen1K
2ϑ range / °	5 ≤ 2ϑ ≤ 121

Data points	7740
Number of reflections	1190
Refined parameters	131
Background function	Shifted Chebyshev, 18 polynomials
R_p	0.0779
R_{wp}	0.1042
R_{exp}	0.0645
R_{Bragg}	0.0358
Goodness of fit	1.615

8.3.2 Crystallography

Table 8.3 Crystallographic data of $Sr_5Si_7P_2N_{16}$ from single-crystal refinement. Standard deviations are given in parentheses.

Formula	$Sr_5Si_7P_2N_{16}$
Crystal system	Orthorhombic
Space group	*Pnma* (no. 62)
Lattice parameters / Å	a = 5.67480(10) b = 28.0367(6) c = 9.5280(2)
Cell volume / Å^3	1515.93(5)
Formula units / unit cell	4
Calculated X-ray density / g · cm^{-3}	4.035
Molar mass / g · mol^{-1}	920.83
μ / mm^{-1}	18.287
Temperature / K	299(2)
Absorption correction	Multi-scan
Absorption details	TWINABS – Bruker AXS scaling for twinned crystals - Version 2012/1
Fraction (2nd domain)	0.0686
Radiation	Mo-Kα
F(000)	1720
ϑ range / °	8.43 ≤ ϑ ≤ 73.67
Total no. of reflections	70837
Independent reflections [$I \geq 2\sigma(I)$ / all]	1765 / 2165
R_σ	0.0395
Refined parameters / restraints	147 / 0
Goodness of fit	1.100
R-values [$I \geq 2\sigma(I)$]	$R1$ = 0.0431, w$R2$ = 0.0721
R-values (all data)	$R1$ = 0.0633, w$R2$ = 0.0786
$\Delta\rho_{max}$, $\Delta\rho_{min}$ / e · Å^3	1.531, −1.607

Table 8.4 Wyckoff position, coordinates, equivalent thermal displacement parameters and occupancy of $Sr_5Si_7P_2N_{16}$ from single-crystal refinement. Standard deviations are given in parentheses.

Atom	Wyckoff	*x*	*y*	*z*	U_{eq}	S.O.F.
Sr1	4*c*	0.61084(14)	1/4	0.12079(8)	0.01149(16)	1
Sr2	8d	0.13392(10)	0.34403(2)	0.62084(5)	0.01153(12)	1
Sr3	8d	-0.34972(10)	0.43229(2)	0.50867(5)	0.01707(14)	1
P1	8*d*	0.6178(3)	0.30468(5)	0.45730(14)	0.0086(3)	1
Si1	8*d*	0.3680(3)	0.36261(5)	0.24607(15)	0.0056(3)	1
Si2	8*d*	0.1358(3)	0.45503(5)	0.32544(13)	0.0037(3)	1
Si3	8*d*	0.1593(3)	0.45771(5)	0.67639(13)	0.0042(3)	1
Si4	4*c*	0.5195(10)	1/4	0.6942(6)	0.0196(8)	0.5
Si5	4*c*	0.6858(10)	1/4	0.6925(6)	0.0196(8)	0.5
N1	8*d*	0.1378(8)	0.51875(15)	0.7235(4)	0.0075(8)	1
N2	8*d*	0.1179(8)	0.39846(14)	0.2525(5)	0.0051(7)	1
N3	4*c*	0.6410(13)	1/4	0.3892(7)	0.0120(13)	1
N4	8*d*	-0.0980(8)	0.43103(14)	0.7401(5)	0.0068(8)	1
N5	8*d*	0.8515(9)	0.33534(18)	0.4139(5)	0.0136(10)	1
N6	8*d*	0.1923(9)	0.45357(19)	0.4984(5)	0.0133(10)	1
N7	8*d*	0.3788(9)	0.32874(18)	0.3928(5)	0.0146(10)	1
N8	8*d*	0.5981(12)	0.3020(2)	0.6286(5)	0.0287(14)	1
N9	4*c*	0.516(3)	1/4	0.8572(15)	0.020(2)	0.5
N10	4*c*	0.697(3)	1/4	0.8548(15)	0.020(2)	0.5

Table 8.5 Anisotropic displacement parameters (U_{ij} / Å^2) of $Sr_5Si_7P_2N_{16}$ from single-crystal refinement. Standard deviations are given in parentheses.

Atom	U_{11}	U_{22}	U_{33}	U_{23}	U_{13}	U_{12}
Sr1	0.0152(4)	0.0086(3)	0.0107(3)	0	-0.0012(3)	0
Sr2	0.0133(3)	0.0118(2)	0.0095(2)	-0.00126(18)	-0.0007(2)	0.0016(2)
Sr3	0.0086(2)	0.0365(3)	0.0061(2)	-0.0038(2)	-0.00029(19)	0.0034(2)
P1	0.0103(7)	0.0073(6)	0.0081(6)	0.0024(5)	-0.0003(5)	0.0004(5)
Si1	0.0052(7)	0.0036(6)	0.0079(6)	0.0003(5)	0.0011(5)	-0.0002(6)
Si2	0.0038(6)	0.0035(6)	0.0037(6)	-0.0007(5)	-0.0001(5)	-0.0002(5)
Si3	0.0054(7)	0.0033(6)	0.0041(6)	-0.0002(5)	-0.0004(5)	0.0006(5)
Si4	0.0264(19)	0.0083(14)	0.0241(15)	0	-0.0033(17)	0
Si5	0.0264(19)	0.0083(14)	0.0241(15)	0	-0.0033(17)	0
N1	0.006(2)	0.0070(19)	0.010(2)	-0.0006(16)	-0.0007(16)	-0.0001(17)
N2	0.006(2)	0.0044(17)	0.0045(16)	0.0007(17)	0.0010(15)	0.0007(18)
N3	0.018(4)	0.006(3)	0.012(3)	0	0.000(3)	0
N4	0.008(2)	0.0054(18)	0.0071(18)	-0.0011(17)	0.0009(15)	0.0020(17)
N5	0.009(2)	0.014(2)	0.018(2)	0.0104(19)	-0.0057(19)	-0.006(2)
N6	0.016(2)	0.022(3)	0.0025(18)	-0.0019(19)	-0.0020(17)	0.0096(19)
N7	0.009(2)	0.014(2)	0.021(2)	0.012(2)	0.000(2)	-0.0007(19)
N8	0.058(4)	0.018(3)	0.010(2)	-0.003(2)	0.002(3)	0.005(3)
N9	0.042(7)	0.007(4)	0.012(4)	0	0.005(6)	0
N10	0.042(7)	0.007(4)	0.012(4)	0	0.005(6)	0

8.3.3 EDX measurements

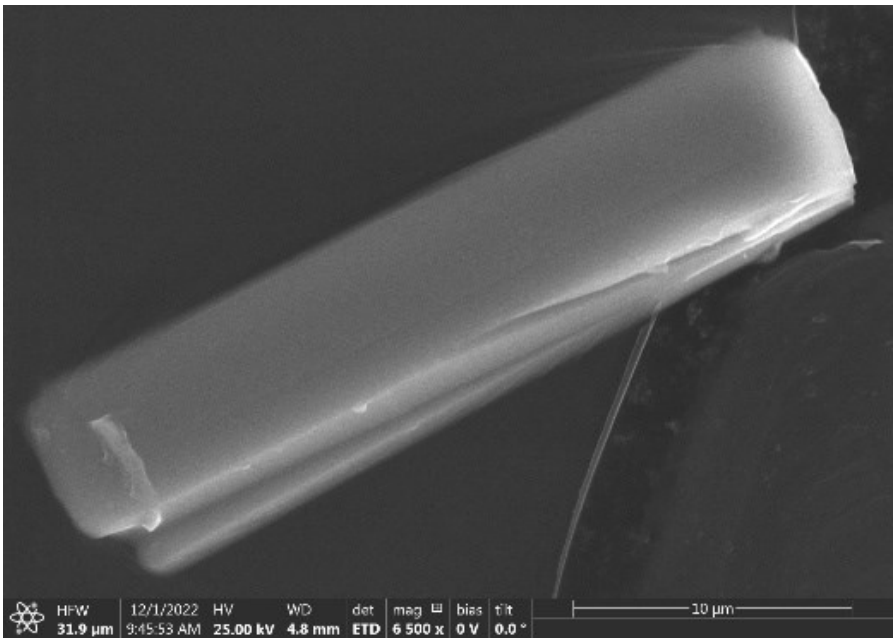

Figure 8.2 SEM image of a particle of $Sr_5Si_7P_2N_{16}$ on which EDX was measured.

Table 8.6 Results of EDX measurements on a single crystal of $Sr_5Si_7P_2N_{16}$.

Measurement	Sr	Si	P	N	O
1	16	25	8	46	5
2	17	25	9	45	3
3	17	25	8	45	4
4	17	26	9	43	5
5	17	25	8	47	3
6	17	25	9	43	5
7	17	25	8	45	4
8	17	26	9	44	4
Average	17(1)	25(1)	9(1)	45(2)	4(1)
Calculated	17	23	7	53	0

8.3.4 Infrared Spectroscopy

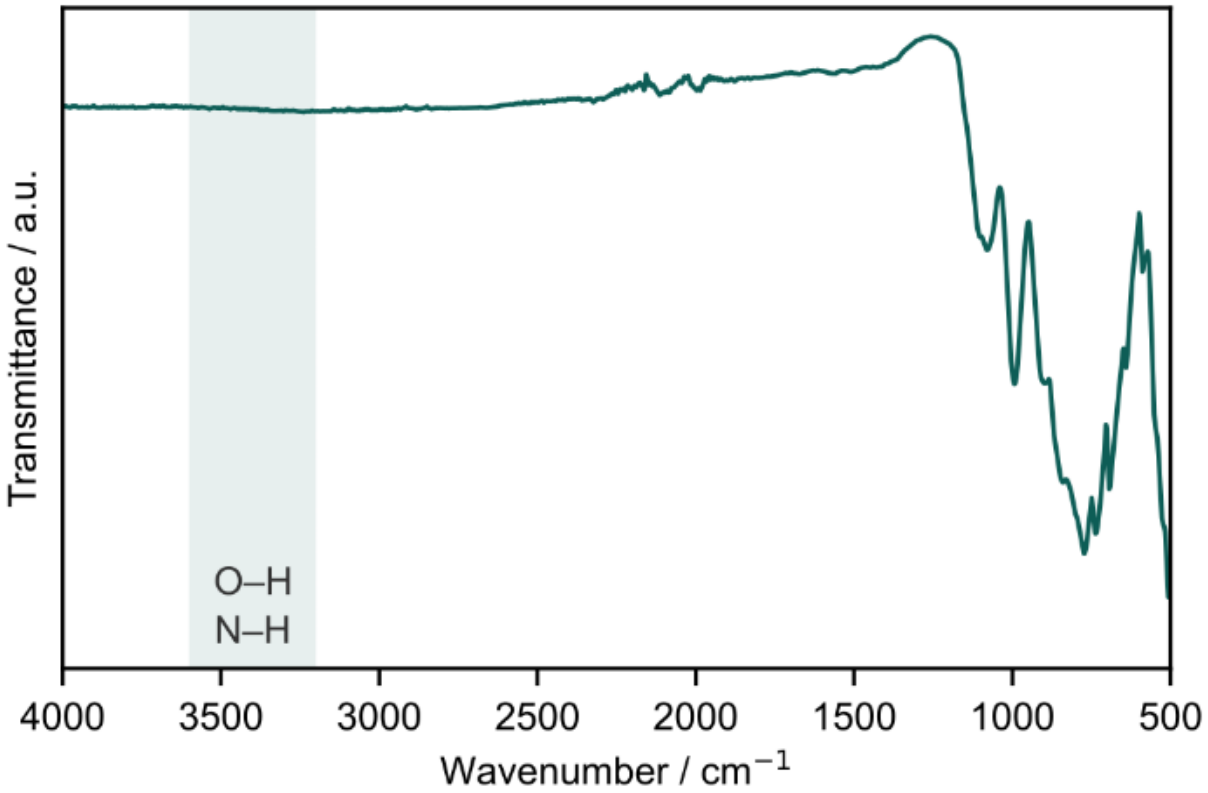

Figure 8.3 Full Fourier-transform infrared spectrum of $Sr_5Si_7P_2N_{16}$ where there are no N–H or O–H vibrations visible (expected in the region 3600–3200 cm^{-1}).

8.3.5 STEM EDX maps

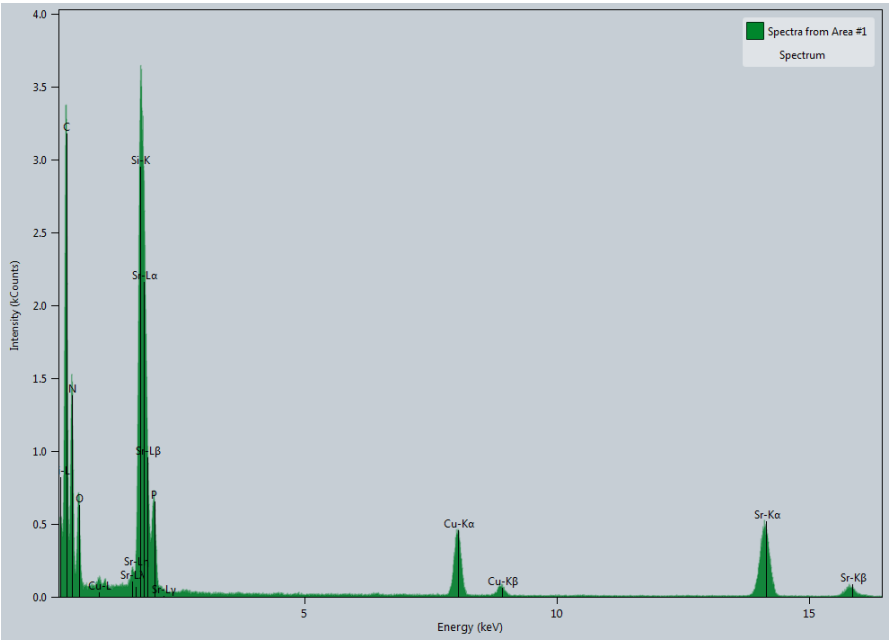

Figure 8.4 Raw EDX spectrum of the STEM EDX maps of $Sr_5Si_7P_2N_{16}$ where Cu and C originate from the TEM grid.

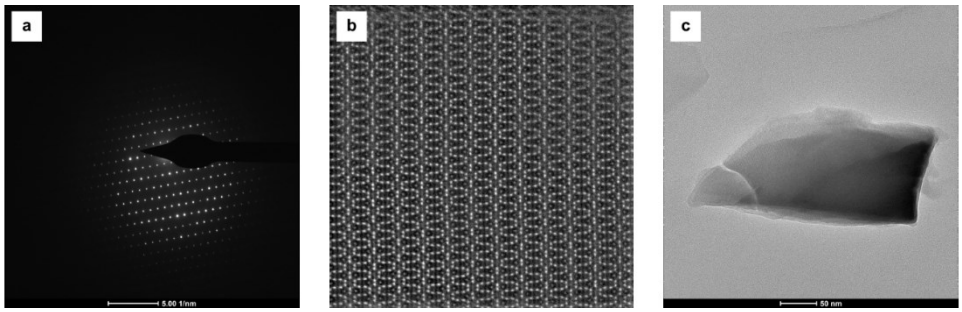

Figure 8.5 Graphical representations of (a) the zone axis, (b) the high-angle annular dark field (HAADF) image, and (c) a bright field image of the investigated crystallite of $Sr_5Si_7P_2N_{16}$.

8.3.6 Precession images

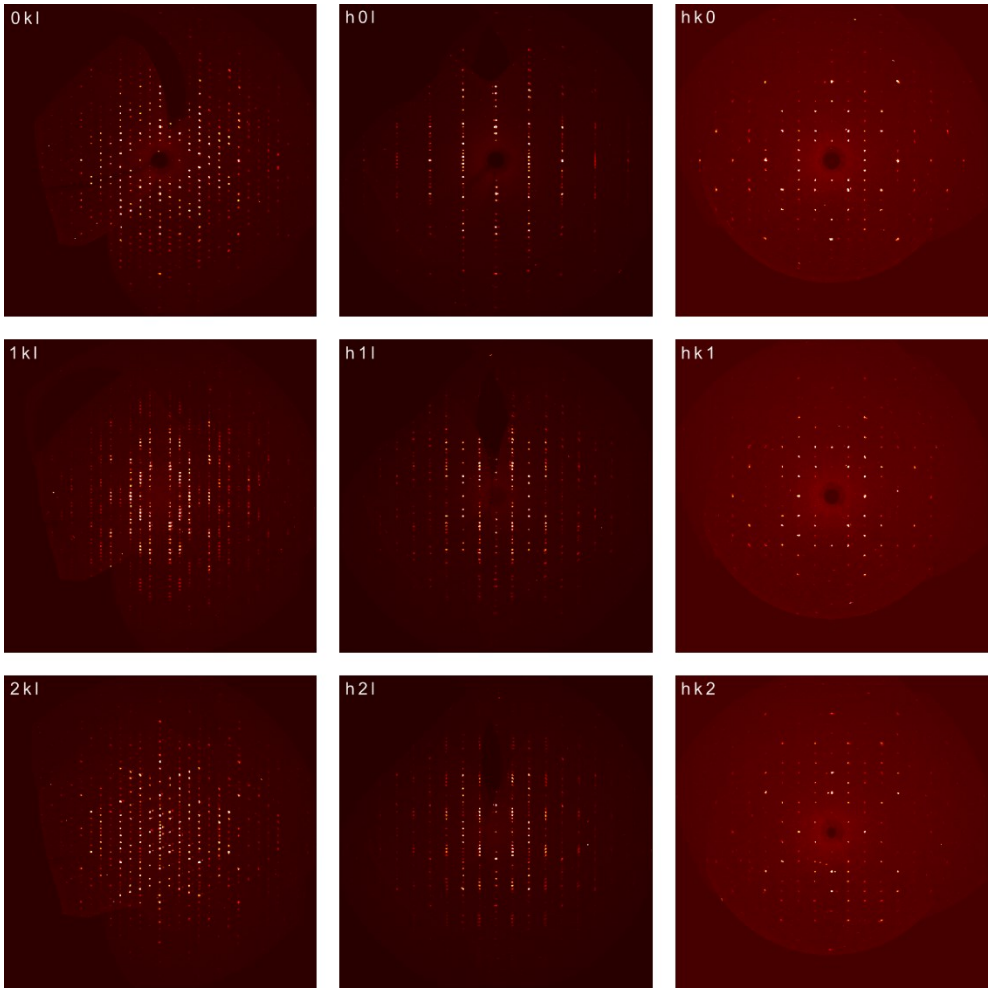

Figure 8.6 Precession images of $Sr_5Si_2P_6N_{16}$ where there are no superstructure reflections visible. However, the presence of a second domain (BASF 0.0686) that we considered during integration, absorption correction and refinement is clearly visible, best in 2*kl*.

8.3.7 ECBVD with disordered Si4 and Si5

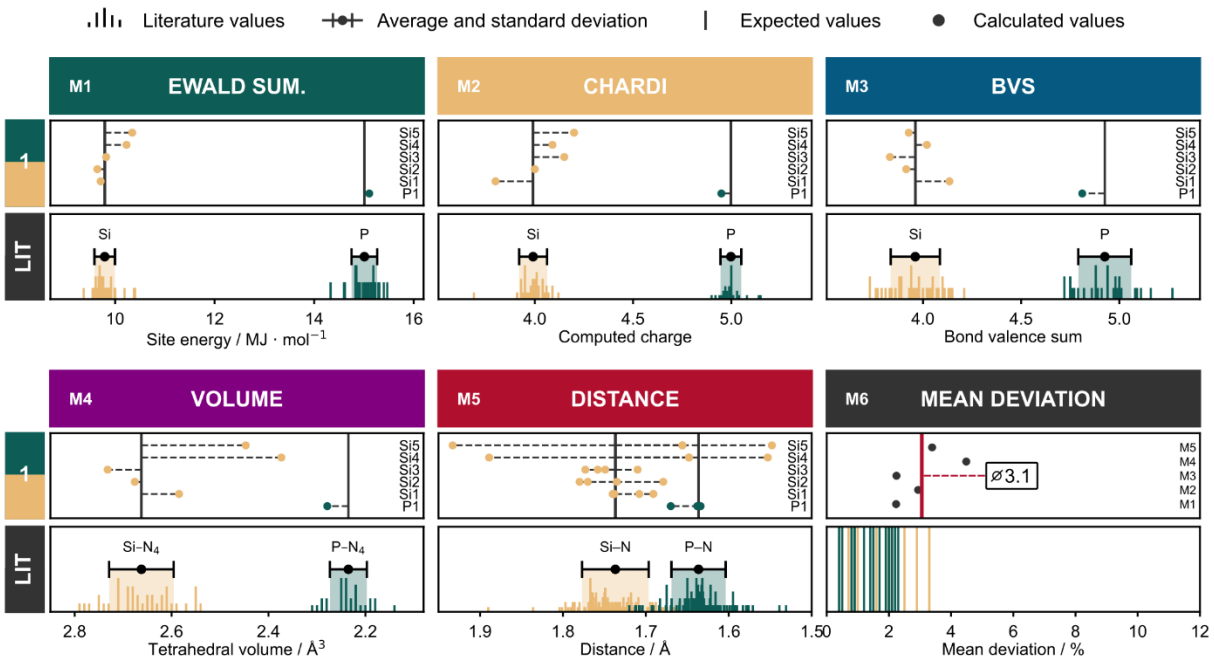

Figure 8.7 ECBVD of all tetrahedral sites in $Sr_5Si_2P_6N_{16}$ including disordered Si4 and Si5.

8.3.8 Python Script for Pekarian-type fit

In service of reproducibility, we provide a working code example (tested with Python 3.8) for a Pekarian-type fit of luminescence data on Github:

https://github.com/smarwin/LumiFit

8.4 References

(1) Stock, A.; Grüneberg, H. Über Den Phosphorstickstoff. *Ber. Dtsch. Chem. Ges.* **1907**, *40* (2), 2573–2578. https://doi.org/10.1002/cber.190704002184.

(2) Eisenburger, L.; Oeckler, O.; Schnick, W. High-Pressure High-Temperature Synthesis of Mixed Nitridosilicatephosphates and Luminescence of *AE*SiP_3N_7:Eu^{2+} (*AE*=Sr, Ba). *Chem. Eur. J.* **2021**, *27* (13), 4461–4465. https://doi.org/10.1002/chem.202005495.

(3) Suhrmann, R.; Clusius, K. Über Die Reindarstellung Der Alkalimetalle. *Z. Anorg. Allg. Chem.* **1926**, *152* (1), 52–58. https://doi.org/10.1002/zaac.19261520107.

(4) Pritzl, R. M.; Prinz, N.; Strobel, P.; Schmidt, P. J.; Johrendt, D.; Schnick, W. From Framework to Layers Driven by Pressure – The Monophyllo-Oxonitridophosphate B-$MgSrP_3N_5O_2$ and Comparison to Its A-Polymorph. *Chem. Eur. J.* **2023**, *29* (41), e202301218. https://doi.org/10.1002/chem.202301218.

(5) Walker, D.; Carpenter, M. A.; Hitch, C. M. Some Simplifications to Multianvil Devices for High Pressure Experiments. *Am. Mineral.* **1990**, *75*, 1020–1028.

(6) Rubie, D. C. Characterising the Sample Environment in Multianvil High-Pressure Experiments. *Phase Transitions* **1999**, *68* (3), 431–451. https://doi.org/10.1080/01411599908224526.

(7) Huppertz, H. Multianvil High-Pressure / High-Temperature Synthesis in Solid State Chemistry. *Z. Kristallogr. Cryst. Mater.* **2004**, *219* (6), 330–338. https://doi.org/10.1524/zkri.219.6.330.34633.

(8) Bertschler, E.; Niklaus, R.; Schnick, W. $Li_{12}P_3N_9$ with Non-Condensed $[P_3N_9]^{12-}$-Rings and Its High-Pressure Polymorph Li_4PN_3 with Infinite Chains of PN_4-Tetrahedra. *Chem. Eur. J.* **2017**, *23* (40), 9592–9599. https://doi.org/10.1002/chem.201700979.

(9) Mallmann, M.; Wendl, S.; Strobel, P.; Schmidt, P. J.; Schnick, W. $Sr_3P_3N_7$: Complementary Approach by Ammonothermal and High-Pressure Syntheses. *Chem. Eur. J.* **2020**, *26* (28), 6257–6263. https://doi.org/10.1002/chem.202000297.

(10) Marchuk, A.; Neudert, L.; Oeckler, O.; Schnick, W. $CaMg_2P_6O_3N_{10}$ – A Quinary Oxonitridophosphate with an Unprecedented Tetrahedra Network Structure Type. *Eur. J. Inorg. Chem.* **2014**, *2014* (21), 3427–3434. https://doi.org/10.1002/ejic.201402302.

(11) Rietveld, H. M. A Profile Refinement Method for Nuclear and Magnetic Structures. *J. Appl. Crystallogr.* **1969**, *2* (2), 65–71. https://doi.org/10.1107/S0021889869006558.

(12) Coelho, A. A.; TOPAS-Academic v4.1. TOPAS-Academic v4.1. **2007**.

(13) Cheary, R. W.; Coelho, A. A. A Fundamental Parameters Approach to X-Ray Line-Profile Fitting. *J. Appl. Crystallogr.* **1992**, *25* (2), 109–121. https://doi.org/10.1107/S0021889891010804.

(14) Cheary, R. W.; Coelho, A. A.; Cline, J. P. Fundamental Parameters Line Profile Fitting in Laboratory Diffractometers. *J. Res. Natl. Inst. Stand. Technol.* **2004**, *109* (1), 1. https://doi.org/10.6028/jres.109.002.

(15) Bruker-AXS. APEX4, V2021.10-0, Karlsruhe, Germany. **2021**.

(16) SAINT. SAINT, Data Integration Software, Madison, Wisconsin, USA. **1997**.

(17) Bruker-AXS. XPREP Reciprocal Space Exploration, Vers. 6.12, Karlsruhe. **2001**.

(18) Sheldrick, G. M. Crystal Structure Refinement with *SHELXL*. *Acta Crystallogr. C Struct. Chem.* **2015**, *71* (1), 3–8. https://doi.org/10.1107/S2053229614024218.

(19) Sheldrick, G. M. SHELXS-97 Program of the Solution of Crystal Structure, University of Göttingen, Göttingen. **1997**.

(20) Farrugia, L. J. *WinGX* and *ORTEP for Windows*: An Update. *J. Appl. Crystallogr.* **2012**, *45* (4), 849–854. https://doi.org/10.1107/S0021889812029111.

(21) Gatan, I. DigitalMicrograph, Version 3.6.5, Pleasanton, USA. **1999**.

(22) Lábár, J. L. Consistent Indexing of a (Set of) Single Crystal SAED Pattern(s) with the ProcessDiffraction Program. *Ultramicroscopy* **2005**, *103* (3), 237–249. https://doi.org/10.1016/j.ultramic.2004.12.004.

(23) Stadelmann, J. P. JEMS Software Package, Version 3.60907U2011, Saas-Fee, Switzerland. **2011**.

(24) Thermo Fisher Scientific. Velox, Waltham, Massachusetts, USA. **2021**.

(25) Toukmaji, A. Y.; Board, J. A. Ewald Summation Techniques in Perspective: A Survey. *Comput. Phys. Commun.* **1996**, *95*, 73–92.

(26) Ong, S. P.; Richards, W. D.; Jain, A.; Hautier, G.; Kocher, M.; Cholia, S.; Gunter, D.; Chevrier, V. L.; Persson, K. A.; Ceder, G. Python Materials Genomics (Pymatgen): A Robust, Open-Source Python Library for Materials Analysis. *Comput. Mater. Sci.* **2013**, *68*, 314–319. https://doi.org/10.1016/j.commatsci.2012.10.028.

(27) Nespolo, M. Charge Distribution as a Tool to Investigate Structural Details. IV. A New Route to Heteroligand Polyhedra. *Acta Crystallogr. Sect. B* **2016**, *72* (1), 51–66. https://doi.org/10.1107/S2052520615019472.

(28) Nespolo, M.; Guillot, B. *CHARDI2015*: Charge Distribution Analysis of Non-Molecular Structures. *J. Appl. Crystallogr.* **2016**, *49* (1), 317–321. https://doi.org/10.1107/S1600576715024814.

(29) Altomare, A.; Cuocci, C.; Giacovazzo, C.; Moliterni, A.; Rizzi, R.; Corriero, N.; Falcicchio, A. *EXPO2013*: A Kit of Tools for Phasing Crystal Structures from Powder Data. *J. Appl. Crystallogr.* **2013**, *46* (4), 1231–1235. https://doi.org/10.1107/S0021889813013113.

(30) Dialer, M.; Pointner, M. M.; Wandelt, S. L.; Strobel, P.; Schmidt, P. J.; Bayarjargal, L.; Winkler, B.; Schnick, W. Order and Disorder in Mixed (Si, P)–N Networks $Sr_2SiP_2N_6$:Eu^{2+} and $Sr_5Si_2P_6N_{16}$:Eu^{2+}. *Adv. Opt. Mater.* **2023**, 2302668. https://doi.org/10.1002/adom.202302668.

(31) Link, L.; Niewa, R. *Polynator* : A Tool to Identify and Quantitatively Evaluate Polyhedra and Other Shapes in Crystal Structures. *J. Appl. Crystallogr.* **2023**, *56* (6), 1855–1864. https://doi.org/10.1107/S1600576723008476.

(32) Momma, K.; Izumi, F. *VESTA 3* for Three-Dimensional Visualization of Crystal, Volumetric and Morphology Data. *J. Appl. Crystallogr.* **2011**, *44* (6), 1272–1276. https://doi.org/10.1107/S0021889811038970.

(33) Schmiechen, S.; Strobel, P.; Hecht, C.; Reith, T.; Siegert, M.; Schmidt, P. J.; Huppertz, P.; Wiechert, D.; Schnick, W. Nitridomagnesosilicate $Ba[Mg_3SiN_4]:Eu^{2+}$ and Structure–Property Relations of Similar Narrow-Band Red Nitride Phosphors. *Chem. Mater.* **2015**, *27* (5), 1780–1785. https://doi.org/10.1021/cm504604d.

(34) Schmiechen, S.; Schneider, H.; Wagatha, P.; Hecht, C.; Schmidt, P. J.; Schnick, W. Toward New Phosphors for Application in Illumination-Grade White Pc-LEDs: The Nitridomagnesosilicates $Ca[Mg_3SiN_4]:Ce^{3+}$, $Sr[Mg_3SiN_4]:Eu^{2+}$, and $Eu[Mg_3SiN_4]$. *Chem. Mater.* **2014**, *26* (8), 2712–2719. https://doi.org/10.1021/cm500610v.

(35) Yoshimura, F.; Yamane, H.; Yamada, T. Synthesis, Crystal Structure, and Luminescence Properties of a White-Light-Emitting Nitride Phosphor, $Ca_{0.99}Eu_{0.01}AlSi_4N_7$. *Inorg. Chem.* **2020**, *59* (1), 367–375. https://doi.org/10.1021/acs.inorgchem.9b02609.

(36) Hecht, C.; Stadler, F.; Schmidt, P. J.; auf der Günne, J. S.; Baumann, V.; Schnick, W. $SrAlSi_4N_7:Eu^{2+}$ − A Nitridoalumosilicate Phosphor for Warm White Light (Pc)LEDs with Edge-Sharing Tetrahedra. *Chem. Mater.* **2009**, *21* (8), 1595–1601. https://doi.org/10.1021/cm803231h.

(37) Zeuner, M.; Pagano, S.; Hug, S.; Pust, P.; Schmiechen, S.; Scheu, C.; Schnick, W. $Li_2CaSi_2N_4$ and $Li_2SrSi_2N_4$ – a Synthetic Approach to Three-Dimensional Lithium Nitridosilicates. *Eur. J. Inorg. Chem.* **2010**, *2010* (31), 4945–4951. https://doi.org/10.1002/ejic.201000671.

(38) Pagano, S.; Lupart, S.; Schmiechen, S.; Schnick, W. $Li_4Ca_3Si_2N_6$ and $Li_4Sr_3Si_2N_6$ – Quaternary Lithium Nitridosilicates with Isolated $[Si_2N_6]^{10-}$ Ions. *Z. Anorg. Allg. Chem.* **2010**, *636* (11), 1907–1909. https://doi.org/10.1002/zaac.201000163.

(39) Kechele, J. A.; Hecht, C.; Oeckler, O.; Schmedt auf der Günne, J.; Schmidt, P. J.; Schnick, W. $Ba_2AlSi_5N_9$ —A New Host Lattice for Eu^{2+}-Doped Luminescent Materials Comprising a Nitridoalumosilicate Framework with Corner- and Edge-Sharing Tetrahedra. *Chem. Mater.* **2009**, *21* (7), 1288–1295. https://doi.org/10.1021/cm803233d.

(40) Uheda, K.; Hirosaki, N.; Yamamoto, Y.; Naito, A.; Nakajima, T.; Yamamoto, H. Luminescence Properties of a Red Phosphor, $CaAlSiN_3:Eu^{2+}$, for White Light-Emitting Diodes. *Electrochem. Solid-State Lett.* **2006**, *9* (4), H22. https://doi.org/10.1149/1.2173192/XML.

(41) Link, L.; Niewa, R. Diversity in Nitridosilicate Chemistry: The Nitridoalumosilicate $Ca_4(AlSiN_5)$ and the Nitridosilicate Silicide $Ca_{12}Si_4[SiN_4]$. *Z. Anorg. Allg. Chem.* **2022**, *648* (10), e202200004. https://doi.org/10.1002/zaac.202200004.

(42) Ottinger, F.; Cuervo-Reyes, E.; Nesper, R. Synthesis, Crystal and Electronic Structure of the Nitridoaluminosilicate $Ca_5[Si_2Al_2N_8]$. *Z. Anorg. Allg. Chem.* **2010**, *636* (6), 1085–1089. https://doi.org/10.1002/zaac.201000046.

(43) Lupart, S.; Schnick, W. $LiCa_3Si_2N_5$ – A Lithium Nitridosilicate with a $[Si_2N_5]^{7-}$ Double-Chain. *Z. Anorg. Allg. Chem.* **2012**, *638* (12–13), 2015–2019. https://doi.org/10.1002/zaac.201200106.

(44) Strobel, P.; Weiler, V.; Schmidt, P. J.; Schnick, W. $Sr[BeSi_2N_4]:Eu^{2+}/Ce^{3+}$ and $Eu[BeSi_2N_4]$: Nontypical Luminescence in Highly Condensed Nitridoberyllosilicates. *Chem. Eur. J.* **2018**, *24* (28), 7243–7249. https://doi.org/10.1002/chem.201800912.

(45) Li, C.; Zheng, H. W.; Wei, H. W.; Su, J.; Liao, F. H.; Zhang, Z. Y.; Xu, L.; Yang, Z. P.; Wang, X. M.; Jiao, H. Narrow-Band Blue Emitting Nitridomagnesosilicate Phosphor Sr8Mg7Si9N22:Eu2+ for Phosphor-Converted LEDs. *Chem. Commun.* **2018**, *54* (82), 11598. https://doi.org/10.1039/C8CC07218C.

9 Supporting Information

Chapter 4

9.1 Experimental Part

9.1.1 Preparation of Starting Materials

We used P_4S_{10} as starting material to synthesize partially crystalline α-P_3N_5 by ammonolysis as described in literature.[1,2] $Sr(N_3)_2$ was prepared by adding aqueous HN_3 with stirring to a suspension of $SrCO_3$ as described by, and more recently by Pritzl et al.[3,4] Amorphous Si_3N_4 (UBE, SNA-00) was used as purchased. Before using amorphous SiO_2 (silica gel 60, 0.040–0.063 mm, Merck) as starting material, it was heated to 120 °C for 12 h under vacuum (<10^{-2} mbar) to remove adsorbed water. EuN was prepared from elementary Eu (smart-elements, 99.99%) in a tungsten crucible that was heated in a nitrogen atmosphere in a radiofrequency furnace (TIG 10/100; Hüttinger Elektronik Freiburg, Germany) at 1000 °C for 12 h.

9.1.2 High-Pressure High-Temperature Synthesis

The compounds $Sr_3SiP_3O_2N_7$, $Sr_5Si_2P_4ON_{12}$, and $Sr_{16}Si_9P_9O_7N_{33}$ were prepared in a multianvil press with a modified Walker-type module.[5–7] Starting materials and their ratios are given in Table S1. $Sr_{16}Si_9P_9O_7N_{33}$ was not synthesized directly but occurred as single particles next to $Sr_5Si_2P_4ON_{12}$. We handled all starting materials under strict exclusion of oxygen and water in an Ar-filled glovebox (Unilab, MBraun, Garching; O_2 <1 ppm; H_2O <1 ppm). Eu^{2+}-phosphors were synthesized by adding 1 mol% EuN with respect to Sr^{2+}. Eu^{3+} is expected to be reduced to Eu^{2+} during the synthesis due to the reducing atmosphere created by the presence of N^{3-}. After thorough mixing in an agate mortar, we transferred the starting materials to a boron nitride crucible with molybdenum inlay. Further information on the preparation and operation of the multianvil press can be found in the literature.[8–10] All reactions took place under the

same conditions, namely at 1400 °C and 3 GPa with heating, dwelling, and cooling times of each 6 h.

Table 9.1 Starting materials for the synthesis of $Sr_3SiP_3O_2N_7$ and $Sr_5Si_2P_4ON_{12}$.

	$Sr_3SiP_3O_2N_7$		$Sr_5Si_2P_4ON_{12}$	
Starting Materials	Eqivalent	m / mg	Equivalent	m / mg
$Sr(N_3)_2$	6	27.6	30	36.5
SrO	2	5.6	–	–
Si_3N_4	1	3.8	3	3.0
SiO_2	–	–	3	1.3
P_3N_5	3	13.1	8	9.2

9.1.3 Single-Crystal X-ray Diffraction (SCXRD)

SCXRD data were collected at a Bruker D8 VENTURE diffractometer with a rotating anode and Mo-Kα radiation (λ = 0.71073 Å). For the integration and absorption correction we used the APEX4 program package.[11–13] Structure solution (SHELXS) and refinement (SHELXL), were carried out using Direct methods and the least-squares method.[14–16]

9.1.4 Scanning Electron Microscopy (SEM) and Energy-Dispersive X-ray Spectroscopy (EDX)

Both SEM images and EDX spectra were collected at a FEI Helios Nanolab G3 Dual Beam UC (FEI, Hillsboro, OR, USA) with X-Max 80 SDD detector (Oxford Instruments, Abingdon, UK). To create reliable results for atomic compositions, ten separate points were measured for each individual compound.

9.1.5 Low-Cost Crystallographic Calculations (LCC)

We calculated bond lengths and tetrahedral volumes with the help of Polynator v1.3, Vesta v3.5.8, and Python Materials Genomics (pymatgen) library.[17–19] Site potentials were calculated with the Ewald Summation class of pymatgen, charge distribution (CHARDI) values using CHARDI2015 (Build 21), and bond valence sums (BVS) with EXPO2014 v1.22.11. [20–22] We used optimized BVS parameters R_0 as described in previous work ($R_0(Si^{4+}–N^{3-})$ = 1.731 and $R_0(P^{5+}–N^{3-})$ = 1.712).[23]

9.1.6 Luminescence measurements

We measured PLE and PL spectra of the Eu^{2+}-doped samples using a HORIBA Fluoromax4 spectrofluorimeter system in combination with an Olympus BX51 microscope. All measurements were performed at room temperature. To justify comparison of the spectra of the compounds, the measurements were conducted at particles of comparable size and identical settings. Excitation and emission wavelengths are given in Table S2. Due to no or very small signals in the PL spectrum, we measured no PLE for $Sr_5Si_2P_4ON_{12}$ and $Sr_{16}Si_9P_9O_7N_{33}$.

Table 9.2 Excitation and emission wavelengths of $Sr_3SiP_3O_2N_7$, $Sr_5Si_2P_6N_{16}$, $Sr_5Si_2P_4ON_{12}$, and $Sr_{16}Si_9P_9O_7N_{33}$.

	$Sr_3SiP_3O_2N_7$	$Sr_5Si_2P_6N_{16}$	$Sr_5Si_2P_4ON_{12}$	$Sr_{16}Si_9P_9O_7N_{33}$
Excitation wavelengths / nm	568	660	–	–
Emission wavelengths / nm	400	460	410	410

9.1.7 Powder X-ray Diffraction (PXRD)

PXRD data were measured on a STOE Stadi P diffractometer (STOE & Cie GmbH in Darmstadt) with a modified Debye–Scherrer configuration and Cu-$K_{\alpha1}$ radiation (λ=1.54060 Å). The detector used was of the type MYTHEN 1K stripe detector and the monochromator Ge(111). The measurement was performed on powder samples in a glass capillary with outer diameter of 0.3 mm from Hilgenberg, Malsfeld. The phase fractions were tested by Rietveld refinement using TOPAS Academic software.[24,25] Peak shapes were fitted by the fundamental parameter method. Backgrounds were fitted with a shifted Chebyshev polynomial.[26,27]

9.1.8 Inductively Coupled Plasma Optical Emission Spectroscopy

Data were collected at a Varian Vista RL with a 40 MHz RF generator and a VistaChip CCD detector.

9.1.9 Fourier-Transform Infrared Spectroscopy (FTIR)

All FTIR spectra were measured at a Bruker Alpha II FTIR device equipped with a diamond ATR component. The device was at the time of measurement in an Ar-filled glovebox.

9.1.10 Magic Angle Spinning Nuclear Magnetic Resonance Spectroscopy (MAS NMR)

All solid-state MAS-NMR data were measured on a Bruker 500 AVANCE-III spectrometer operating at a proton frequency of 500 MHz. Ground samples were filled into ZrO_2 rotors, with an outer diameter of 2.5 mm for the ^{1}H and ^{31}P, and 4 mm for the ^{29}Si measurements. For the ^{1}H, ^{31}P and $^{31}P\{^{1}H\}$ spectra, the spinning frequency was 20 kHz, and 10 kHz for the ^{29}Si measurements. All spectra were referenced indirectly to ^{1}H at −0.124 ppm in 100% TMS.

9.1.11 Density functional theory (DFT) calculations

Based on periodic density functional theory (DFT) linear first principle electronic structure calculations were performed with the Vienna *ab initio* simulation package (VASP).[28–31] VASP separates core and valence electrons using projector-augmented waves (PAW).[32,33] The exchange- and correlation-energy was calculated using the generalized gradient approximation (GGA), as described by Perdew, Burke and Ernzerhof (PBE).[34] A more detailed analysis of the band gap was achieved by using the meta-GGA functional local modified Becke-Johnson (LMBJ).[35,36] Non-spherical contributions to the gradient of the density in the PAW spheres were included when using LMBJ. Structure optimizations were performed on dense *k*-grids with a resolution of approximately 0.2/Å with an energy cutoff of 520 eV to ensure well converged structures. Band structure calculations were performed using the appropriate *k*-paths. The necessary eigenvalues were obtained from static pre-calculations. The mixed occupancies of Si/P and O/N were considered with the virtual crystal approximation.[37] The energy convergence criterion was set to 10^{-7} eV and the residual atomic forces were relaxed until the convergence criterion of 10^{-5} eV/Å was reached.

9.2 Results and Discussion

9.2.1 Powder X-ray Diffraction

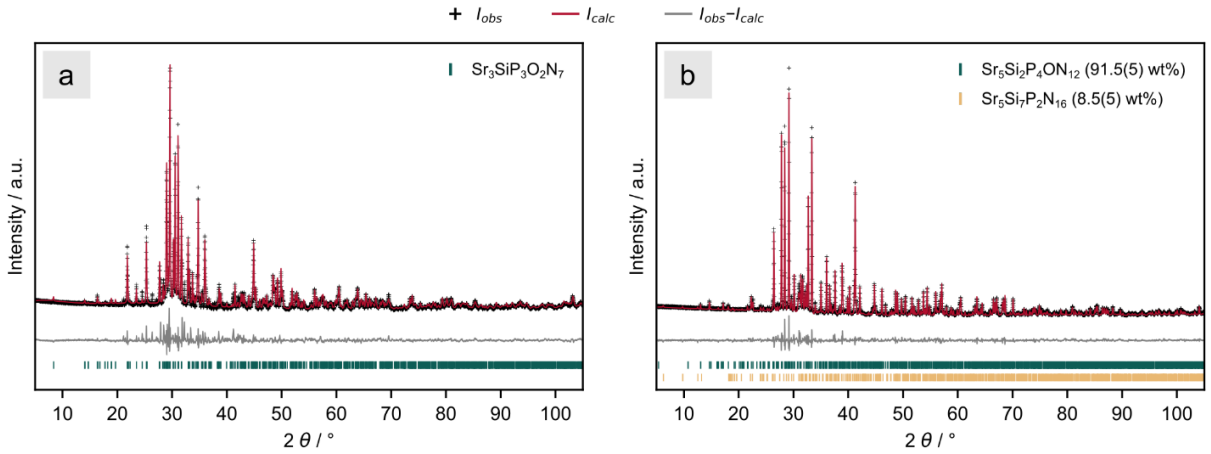

Figure 9.1 Plots of the Rietveld refinements based on powder X-ray diffraction data of the bulk sample of (a) $Sr_3SiP_3O_2N_7$ and (b) $Sr_5Si_2P_4ON_{12}$.

Table 9.3 Crystallographic data of the Rietveld refinement based on powder XRD data of $Sr_3SiP_3O_2N_7$ and $Sr_5Si_2P_4ON_{12}$. Standard deviations are given in parentheses.

Formula	$Sr_3SiP_3O_2N_7$	$Sr_5Si_2P_4ON_{12}$
Molar mass / g · mol^{-1}	513.93	802.25
Crystal system	Monoclinic	Monoclinic
Space group	$P2_1/m$ (no. 11)	$P2_1/c$ (no. 14)
Lattice parameters / Å, °	a = 6.4170(3)	a = 16.8636(1)
	b = 21.0704(1)	b = 7.4355(1)
	c = 6.4382(4)	c = 10.5819(1)
	β = 101.847(4)	β = 103.0926(1)
Cell volume / Å^3	852.0(1)	1292.38(1)
Formula units / unit cell	4	4
Diffractometer	STOE Stadi P	STOE Stadi P
Radiation	Cu-Kα_1 (λ = 1.54059 Å)	Cu-Kα_1 (λ = 1.54059 Å)
Monochromator	Ge(111)	Ge(111)
Detector	Mythen1K	Mythen1K
2ϑ range / °	5 ≤ 2ϑ ≤ 121	5 ≤ 2ϑ ≤ 121
Data points	7705	7705
Number of reflections	1329	1951
Refined parameters	126	204
Background function	Shifted Chebyshev, 18 polynomials	Shifted Chebyshev, 18 polynomials
R_p	0.0842	0.0537
R_{wp}	0.1227	0.0744
R_{exp}	0.0314	0.0297
Goodness of fit	3.91	2.50

9.2.2 Single-Crystal X-ray Diffraction

Table 9.4 Crystallographic data of $Sr_3SiP_3O_2N_7$, $Sr_5Si_2P_4ON_{12}$, and $Sr_{16}Si_9P_9O_7N_{33}$ from single-crystal refinement. Standard deviations are given in parentheses.

Formula	$Sr_3SiP_3O_2N_7$	$Sr_5Si_2P_4ON_{12}$	$Sr_{16}Si_9P_9O_7N_{33}$
Crystal system	monoclinic	monoclinic	monoclinic
Space group	$P2_1/m$ (no. 11)	$P2_1/c$ (no. 14)	$P2_1/c$ (no. 14)
Lattice parameters / Å, °	a = 6.43100(10)	a = 16.8333(6)	a = 25.7679(5)
	b = 21.0836(4)	b = 7.4456(3)	b = 7.4072(2)
	c = 6.43270(10)	c = 10.5577(4)	c = 10.6019(2)
	β = 101.9480(10)	β = 103.185(2)	β = 93.0690(10)
Cell volume / Å^3	853.31(2)	1288.36(9)	2020.66(8)
Formula units / unit cell	4	4	2
Calculated X-ray density / g · cm^{-3}	4.000	4.136	4.122
Molar mass / g · mol^{-1}	513.93	802.25	2507.79
μ / mm^{-1}	19.380	21.276	21.632
Temperature / K	297(2)	298(2)	297(2)
Absorption correction	multi-scan	multi-scan	multi-scan
Radiation	Mo-Kα	Mo-Kα	Mo-Kα
F(000)	952	1480	2312
ϑ range / °	6.474 ≤ ϑ ≤ 61.00	6.757 ≤ ϑ ≤ 64.27	5.723 ≤ ϑ ≤ 70.83
Total no. of reflections	18353	15606	16585
Independent reflections [$I \geq 2\sigma(I)$ / all]	2413 / 2669	2094 / 2737	3457 / 4282
R_{int} / R_σ	0.0431 / 0.0283	0.0583 / 0.0428	0.0361 / 0.0336
Refined parameters / restraints	151 / 0	217 / 0	335 / 0
Goodness of fit	1.074	1.030	1.065
R-values [$I \geq 2\sigma(I)$]	$R1$ = 0.0258, w$R2$ = 0.0515	$R1$ = 0.0450, w$R2$ = 0.0986	$R1$ = 0.0389, w$R2$ = 0.0835
R-values (all data)	$R1$ = 0.0317, w$R2$ = 0.0499	$R1$ = 0.0659, w$R2$ = 0.1083	$R1$ = 0.0533, w$R2$ = 0.0896
$\Delta\rho_{max}$, $\Delta\rho_{min}$ / e · Å^3	1.464, −1.362	2.929, −2.527	2.394, −2.004

Table 9.5 Wyckoff position, coordinates, equivalent thermal displacement parameters and occupancy of $Sr_3SiP_3O_2N_7$ from single-crystal refinement. Standard deviations are given in parentheses.

Atom	Wyckoff	x	y	z	U_{eq}	S.O.F.
Sr1	2e	0.75099(7)	3/4	0.90143(7)	0.01179(9)	1
Sr2	4f	0.59636(5)	0.45164(2)	0.76549(5)	0.01045(7)	1
Sr3	2e	0.19177(7)	3/4	0.45709(7)	0.01225(9)	1
Sr4	4f	0.02504(5)	0.56984(2)	-0.35411(5)	0.01404(8)	1
P1	4f	0.66691(12)	0.68033(4)	0.38173(12)	0.00583(14)	0.75
P2	4f	0.27340(12)	0.68032(4)	-0.00525(12)	0.00621(15)	0.75
P3	4f	0.53923(12)	0.60681(4)	0.74268(13)	0.00632(15)	0.75
P4	4f	-0.09109(12)	0.60292(4)	0.11818(12)	0.00701(15)	0.75
Si1	4f	0.66691(12)	0.68033(4)	0.38173(12)	0.00583(14)	0.25
Si2	4f	0.27340(12)	0.68032(4)	-0.00525(12)	0.00621(15)	0.25
Si3	4f	0.53923(12)	0.60681(4)	0.74268(13)	0.00632(15)	0.25

Si4	4*f*	-0.09109(12)	0.60292(4)	0.11818(12)	0.00701(15)	0.25
O1	4*f*	0.0056(4)	0.54510(12)	0.2685(4)	0.0149(5)	1
O2	4*f*	0.3928(4)	0.54960(11)	0.6354(4)	0.0134(5)	1
N1	2*e*	0.1539(6)	3/4	-0.0407(6)	0.0090(7)	1
N2	2*e*	0.7087(6)	3/4	0.4978(6)	0.0104(7)	1
N3	4*f*	0.4300(4)	0.67442(13)	0.2317(4)	0.0099(5)	1
N4	4*f*	0.0950(4)	0.62346(13)	-0.0134(4)	0.0091(5)	1
N5	4*f*	0.8638(4)	0.66647(13)	0.2577(4)	0.0107(5)	1
N6	4*f*	0.3947(4)	0.66811(13)	-0.2084(4)	0.0120(5)	1
N7	4*f*	0.6939(4)	0.57346(13)	0.9537(4)	0.0097(5)	1
N8	4*f*	0.6831(4)	0.62726(14)	0.5707(4)	0.0136(6)	1

Table 9.6 Wyckoff position, coordinates, equivalent thermal displacement parameters and occupancy of $Sr_5Si_2P_4ON_{12}$ from single-crystal refinement. Standard deviations are given in parentheses.

Atom	Wyckoff	*x*	*y*	*z*	U_{eq}	S.O.F.
Sr1	4*e*	0.02250(4)	-0.09943(10)	0.34332(7)	0.01143(18)	1
Sr2	4*e*	0.24491(5)	1.07268(10)	0.48780(7)	0.01312(19)	1
Sr3	4*e*	0.52893(5)	0.09260(10)	0.35214(7)	0.01490(19)	1
Sr4	4*e*	0.18974(5)	0.61073(12)	0.30150(8)	0.0189(2)	1
Sr5	4*e*	0.30962(5)	-0.10118(14)	0.16902(10)	0.0316(3)	1
P1	4*e*	0.15364(12)	0.1842(3)	0.21041(18)	0.0062(4)	0.6667
Si1	4*e*	0.15364(12)	0.1842(3)	0.21041(18)	0.0062(4)	0.3333
P2	4*e*	0.33967(12)	0.3221(3)	0.27754(18)	0.0068(4)	0.6667
Si2	4*e*	0.33967(12)	0.3221(3)	0.27754(18)	0.0068(4)	0.3333
P3	4*e*	0.06402(12)	0.3007(3)	0.43480(18)	0.0064(4)	0.6667
Si3	4*e*	0.06402(12)	0.3007(3)	0.43480(18)	0.0064(4)	0.3333
P4	4*e*	0.42516(12)	0.1788(3)	0.05238(19)	0.0082(4)	0.6667
Si4	4*e*	0.42516(12)	0.1788(3)	0.05238(19)	0.0082(4)	0.3333
P5	4*e*	0.39682(12)	-0.1618(3)	-0.09085(19)	0.0081(4)	0.6667
Si5	4*e*	0.39682(12)	-0.1618(3)	-0.09085(19)	0.0081(4)	0.3333
P6	4*e*	0.11144(11)	0.6469(3)	0.55987(18)	0.0068(4)	0.6667
Si6	4*e*	0.11144(11)	0.6469(3)	0.55987(18)	0.0068(4)	0.3333
O1	4*e*	0.3366(4)	-0.3201(10)	-0.0700(7)	0.0298(17)	0.5
O2	4*e*	0.1737(4)	0.7896(8)	0.5227(6)	0.0194(14)	0.5
N1	4*e*	0.3366(4)	-0.3201(10)	-0.0700(7)	0.0298(17)	0.5
N2	4*e*	0.1737(4)	0.7896(8)	0.5227(6)	0.0194(14)	0.5
N3	4*e*	0.3596(5)	0.2389(10)	0.1413(7)	0.0205(16)	1
N4	4*e*	0.0364(4)	0.7620(10)	0.5998(7)	0.0162(15)	1
N5	4*e*	0.5189(4)	0.2576(10)	0.1244(6)	0.0144(14)	1
N6	4*e*	0.1111(4)	0.2076(9)	0.5732(6)	0.0134(14)	1
N7	4*e*	0.4186(4)	-0.0450(9)	0.0442(6)	0.0130(14)	1
N8	4*e*	0.3489(4)	0.5493(9)	0.2762(6)	0.0144(14)	1
N9	4*e*	0.0947(4)	0.2006(10)	0.3159(6)	0.0149(15)	1
N10	4*e*	0.3998(4)	0.2260(9)	0.4071(6)	0.0147(14)	1
N11	4*e*	0.0789(4)	0.5207(9)	0.4282(6)	0.0131(14)	1
N12	4*e*	0.1646(4)	-0.0378(9)	0.1882(6)	0.0154(14)	1
N13	4*e*	0.2422(4)	0.2817(10)	0.2791(7)	0.0182(15)	1

Table 9.7 Wyckoff position, coordinates, equivalent thermal displacement parameters and occupancy of $Sr_{16}Si_9P_9O_7N_{33}$ from single-crystal refinement. Standard deviations are given in parentheses.

Atom	Wyckoff	*x*	*y*	*z*	U_{eq}	S.O.F.
Sr1	4*e*	0.48736(2)	1.10135(8)	0.33083(5)	0.01180(14)	1

Sr2	4*e*	0.15896(2)	-0.07502(8)	0.09693(6)	0.01366(14)	1
Sr3	4*e*	0.65756(2)	1.07376(9)	0.62247(6)	0.01660(15)	1
Sr4	4*e*	-0.01632(2)	0.90247(8)	-0.15956(6)	0.01502(14)	1
Sr5	4*e*	0.62297(2)	0.60839(9)	0.78194(6)	0.01899(16)	1
Sr6	4*e*	0.19799(2)	1.10418(9)	0.44279(6)	0.01986(16)	1
Sr7	4*e*	0.12435(2)	1.10168(10)	0.75310(7)	0.02168(17)	1
Sr8	4*e*	0.70108(3)	0.59871(10)	0.47341(7)	0.02464(18)	1
P1	4*e*	0.28064(6)	0.6833(2)	0.12056(14)	0.0068(3)	0.5
P2	4*e*	0.39989(6)	0.8207(2)	0.14210(14)	0.0062(3)	0.5
P3	4*e*	0.22397(6)	0.6901(2)	0.35655(14)	0.0066(3)	0.5
P4	4*e*	0.10408(6)	0.8197(2)	0.35139(14)	0.0068(3)	0.5
P5	4*e*	0.04906(6)	0.6738(2)	0.08882(14)	0.0073(3)	0.5
P6	4*e*	0.45732(6)	0.6997(2)	0.40645(14)	0.0073(3)	0.5
P7	4*e*	0.57000(6)	0.6504(2)	0.48760(15)	0.0073(3)	0.5
P8	4*e*	0.06484(6)	1.1631(2)	0.45068(14)	0.0078(3)	0.5
P9	4*e*	0.24726(6)	0.3404(2)	0.23347(15)	0.0082(3)	0.5
Si1	4*e*	0.28064(6)	0.6833(2)	0.12056(14)	0.0068(3)	0.5
Si2	4*e*	0.39989(6)	0.8207(2)	0.14210(14)	0.0062(3)	0.5
Si3	4*e*	0.22397(6)	0.6901(2)	0.35655(14)	0.0066(3)	0.5
Si4	4*e*	0.10408(6)	0.8197(2)	0.35139(14)	0.0068(3)	0.5
Si5	4*e*	0.04906(6)	0.6738(2)	0.08882(14)	0.0073(3)	0.5
Si6	4*e*	0.45732(6)	0.6997(2)	0.40645(14)	0.0073(3)	0.5
Si7	4*e*	0.57000(6)	0.6504(2)	0.48760(15)	0.0073(3)	0.5
Si8	4*e*	0.06484(6)	1.1631(2)	0.45068(14)	0.0078(3)	0.5
Si9	4*e*	0.24726(6)	0.3404(2)	0.23347(15)	0.0082(3)	0.5
O1	4*e*	0.20099(19)	0.2208(7)	0.1647(5)	0.0270(12)	0.875
O2	4*e*	0.1026(2)	1.3294(8)	0.4929(6)	0.0364(14)	0.875
O3	4*e*	0.2906(2)	0.2109(9)	0.3023(5)	0.0387(15)	0.875
O4	4*e*	0.6078(2)	0.8031(7)	0.5519(5)	0.0315(13)	0.875
N1	4*e*	0.20099(19)	0.2208(7)	0.1647(5)	0.0270(12)	0.125
N2	4*e*	0.1026(2)	1.3294(8)	0.4929(6)	0.0364(14)	0.125
N3	4*e*	0.2906(2)	0.2109(9)	0.3023(5)	0.0387(15)	0.125
N4	4*e*	0.6078(2)	0.8031(7)	0.5519(5)	0.0315(13)	0.125
N5	4*e*	0.06655(19)	0.7736(7)	-0.0425(5)	0.0121(11)	1
N6	4*e*	0.0528(2)	1.0526(7)	0.5801(5)	0.0138(11)	1
N7	4*e*	-0.0106(2)	0.7541(8)	0.1196(5)	0.0152(12)	1
N8	4*e*	0.4275(2)	0.7085(7)	0.0262(5)	0.0120(11)	1
N9	4*e*	0.2204(2)	0.4610(8)	0.3468(5)	0.0163(12)	1
N10	4*e*	0.4364(2)	0.8028(7)	0.2747(5)	0.0145(11)	1
N11	4*e*	0.0962(2)	1.0496(7)	0.3416(5)	0.0136(11)	1
N12	4*e*	0.2695(2)	0.7644(8)	-0.0263(5)	0.0175(12)	1
N13	4*e*	0.2401(2)	0.7802(7)	0.2184(5)	0.0139(11)	1
N14	4*e*	0.5524(2)	0.5237(7)	0.6079(5)	0.0130(11)	1
N15	4*e*	0.2754(2)	0.4544(7)	0.1185(5)	0.0175(12)	1
N16	4*e*	0.5210(2)	0.7598(8)	0.4128(5)	0.0159(12)	1
N17	4*e*	0.16675(19)	0.7790(8)	0.3952(5)	0.0131(11)	1
N18	4*e*	0.6070(2)	0.5449(8)	0.3869(5)	0.0156(12)	1
N19	4*e*	0.3426(2)	0.7287(8)	0.1696(5)	0.0201(13)	1
N20	4*e*	0.0907(2)	0.7286(8)	0.2098(5)	0.0191(12)	1

9.2.3 Fourier-Transform Infrared Spectroscopy

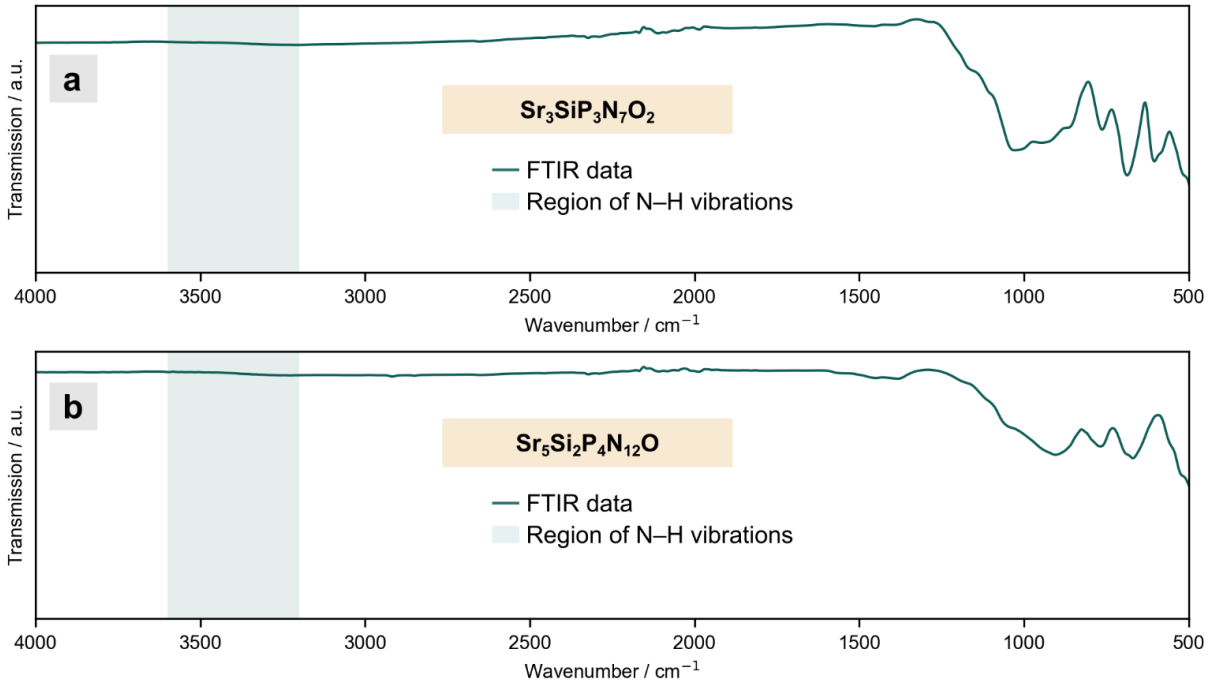

Figure 9.2 FTIR spectra of (a) $Sr_3SiP_3O_2N_7$ and (b) $Sr_5Si_2P_4ON_{12}$.

9.2.4 EDX measurements

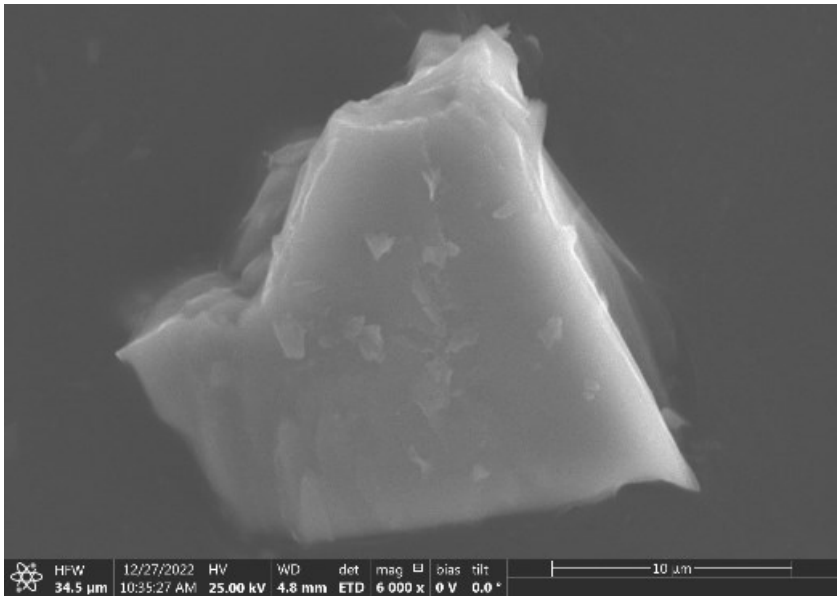

Figure 9.3 SEM image of a particle of $Sr_3SiP_3O_2N_7$ on which EDX was measured.

Table 9.8 Results of EDX measurements on a single crystal of $Sr_3SiP_3O_2N_7$.

Measurement	Sr	Si	P	N	O
1	22	10	18	32	18
2	20	9	17	35	19

3	21	10	19	34	16
4	19	9	19	37	16
5	18	8	18	38	18
6	19	9	19	37	16
7	19	9	19	37	16
8	19	8	18	36	20
9	20	9	19	36	16
10	22	10	21	33	15
Average	20(2)	9(1)	19(1)	35(2)	17(2)
Calculated	18.8	6.3	18.8	43.8	12.5

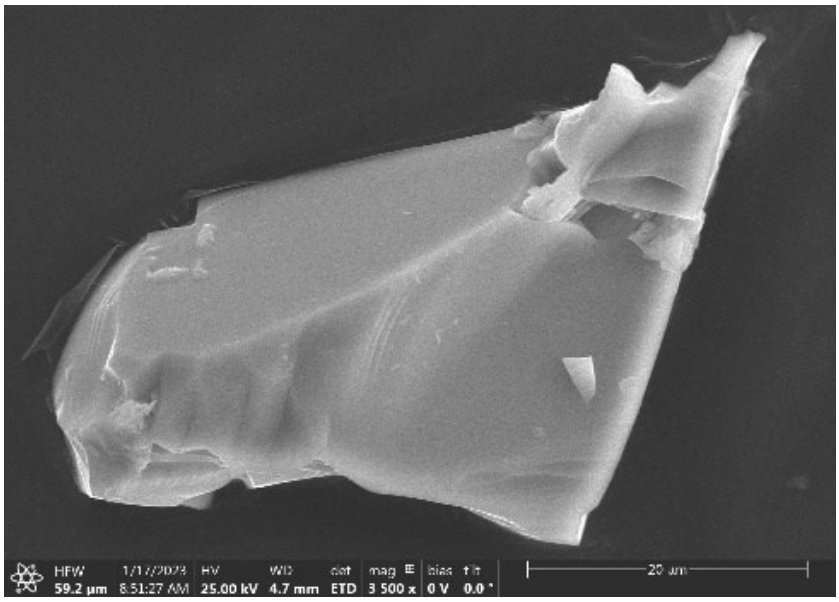

Figure 9.4 SEM image of a particle of $Sr_5Si_2P_4ON_{12}$ on which EDX was measured.

Table 9.9 Results of EDX measurements on a single crystal of $Sr_5Si_2P_4ON_{12}$.

Measurement	Sr	Si	P	N	O
1	19	10	15	47	9
2	20	10	15	47	8
3	19	10	15	49	7
4	18	9	15	50	9
5	19	9	15	47	10
6	20	10	15	47	8
7	18	9	15	51	7
8	19	9	15	50	7
9	18	9	15	50	7
10	18	9	15	50	8
Average	19(1)	9(1)	15(1)	49(2)	8(1)
Calculated	20.8	8.3	16.7	50	4.2

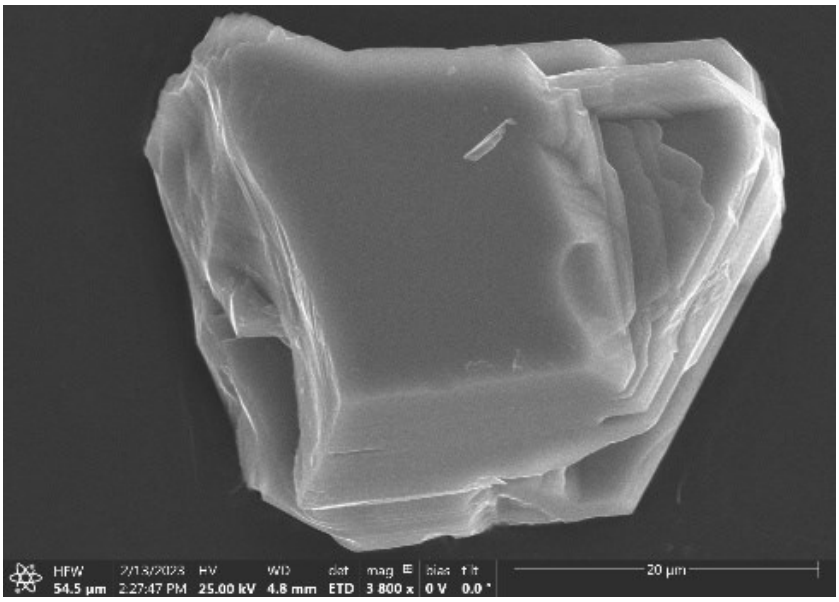

Figure 9.5 SEM image of a particle of $Sr_{16}Si_9P_9O_7N_{33}$ on which EDX was measured.

Table 9.10 Results of EDX measurements on a single crystal of $Sr_{16}Si_9P_9O_7N_{33}$.

Measurement	Sr	Si	P	N	O
1	20	12	13	45	11
2	21	12	13	43	11
3	20	12	12	44	12
4	20	12	12	44	12
5	20	12	13	44	11
6	20	12	12	43	13
7	20	12	13	43	12
8	20	12	12	44	11
9	21	12	13	43	11
10	20	12	12	45	11
Average	20(1)	12(1)	12(1)	44(1)	12(1)
Calculated	18.8	6.3	18.8	43.8	12.5

9.2.5 Magic Angle Spinning Nuclear Magnetic Resonance Spectroscopy

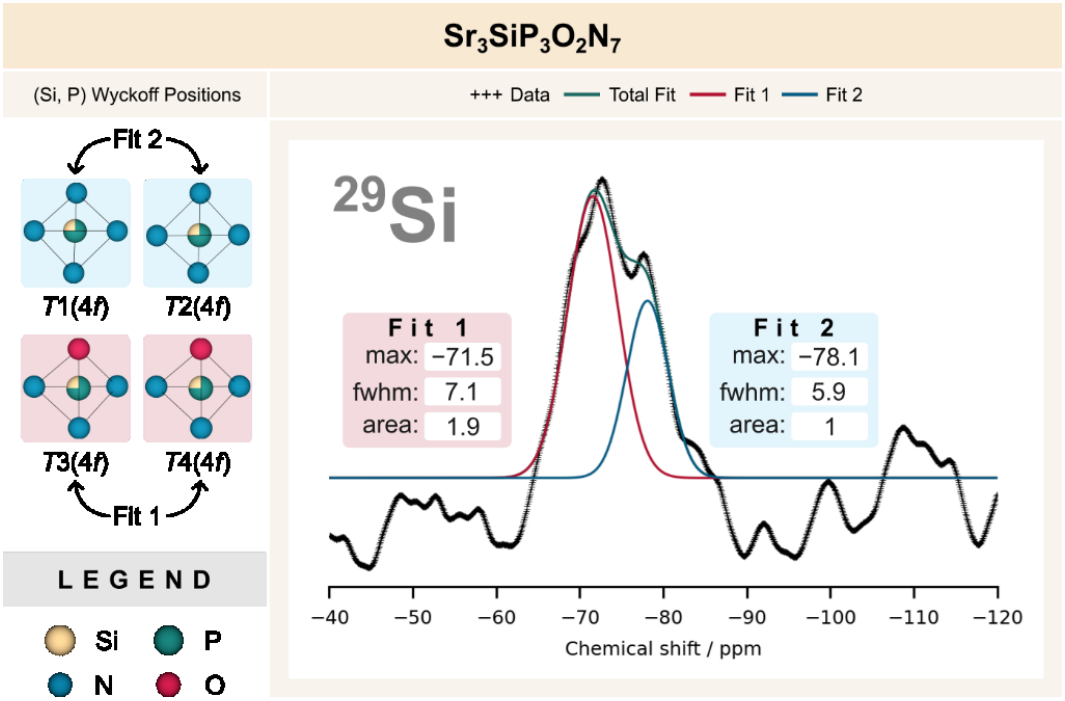

Figure 9.6 ^{29}Si NMR of $Sr_3SiP_3O_2N_7$ that was recorded at room temperature and 10 kHz. The assignment of fits to Wyckoff positions is based on the results from the ^{31}P NMR.

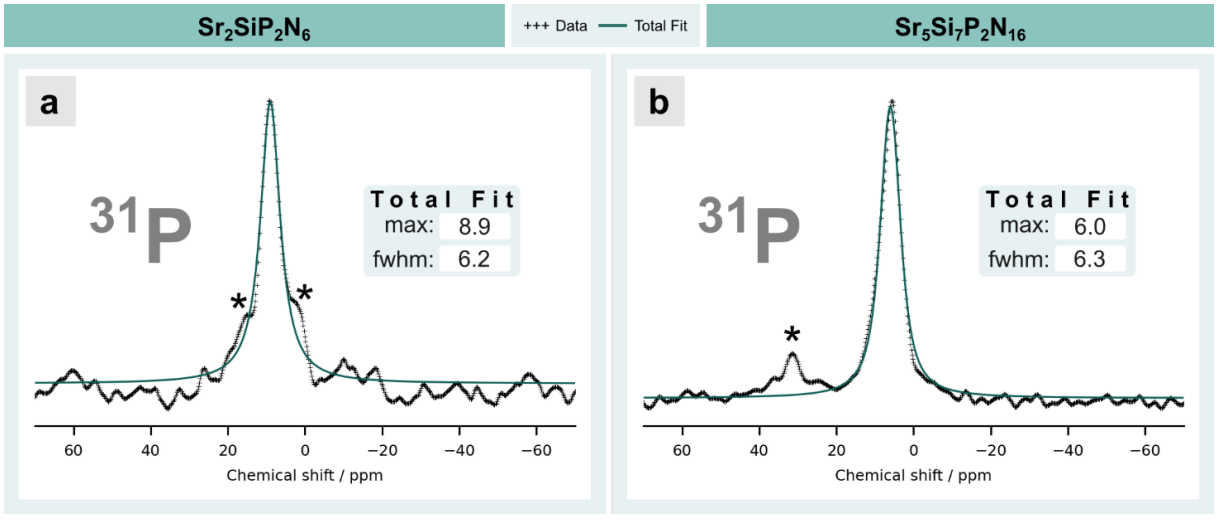

Figure 9.7 ^{31}P NMR reference spectra of ordered (a) $Sr_2SiP_2N_6$ and (b) $Sr_5Si_7P_2N_{16}$. Based on the respective structures, we expect only one signal. Side phases are marked with asterisks (*).

9.2.6 Bandstructures and Densities of States

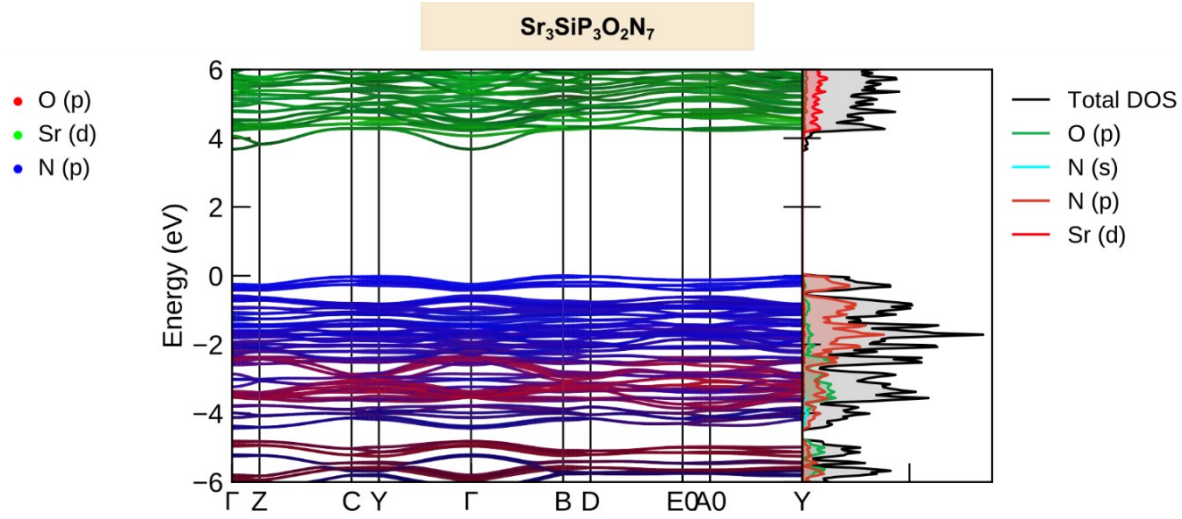

Figure 9.8 Band structure and density of states of $Sr_3SiP_3O_2N_7$.

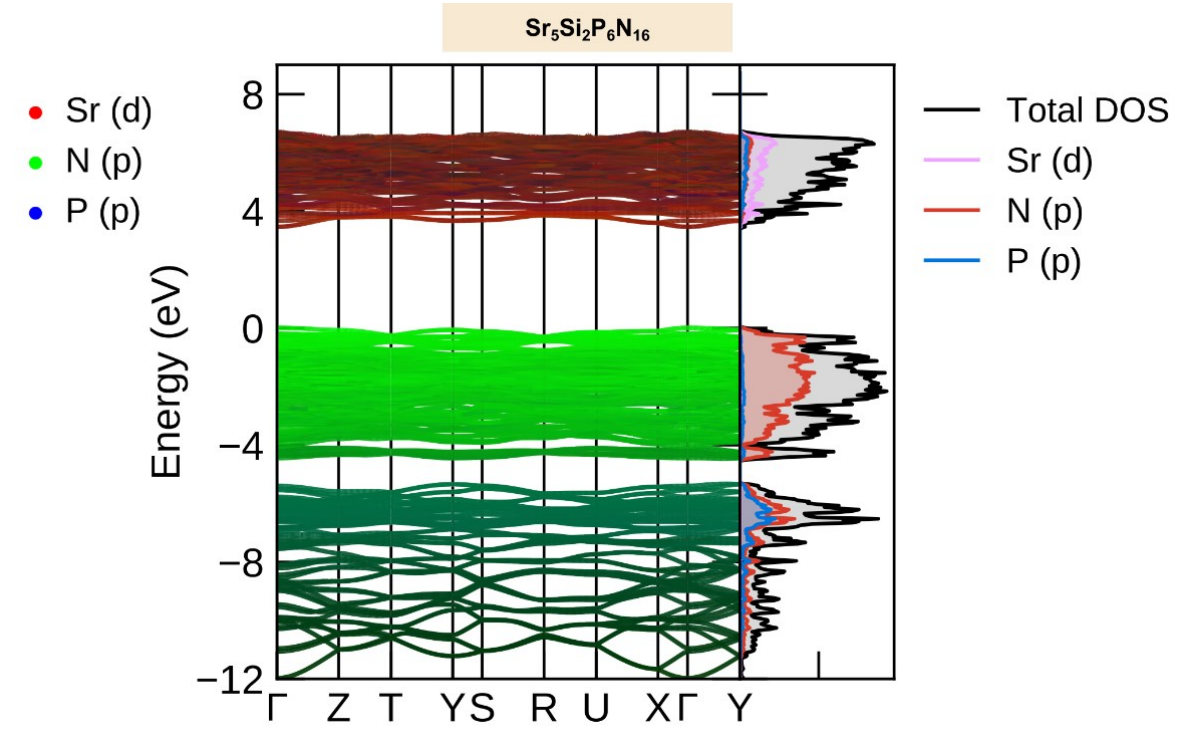

Figure 9.9 Band structure and density of states of $Sr_5Si_2P_6N_{16}$.

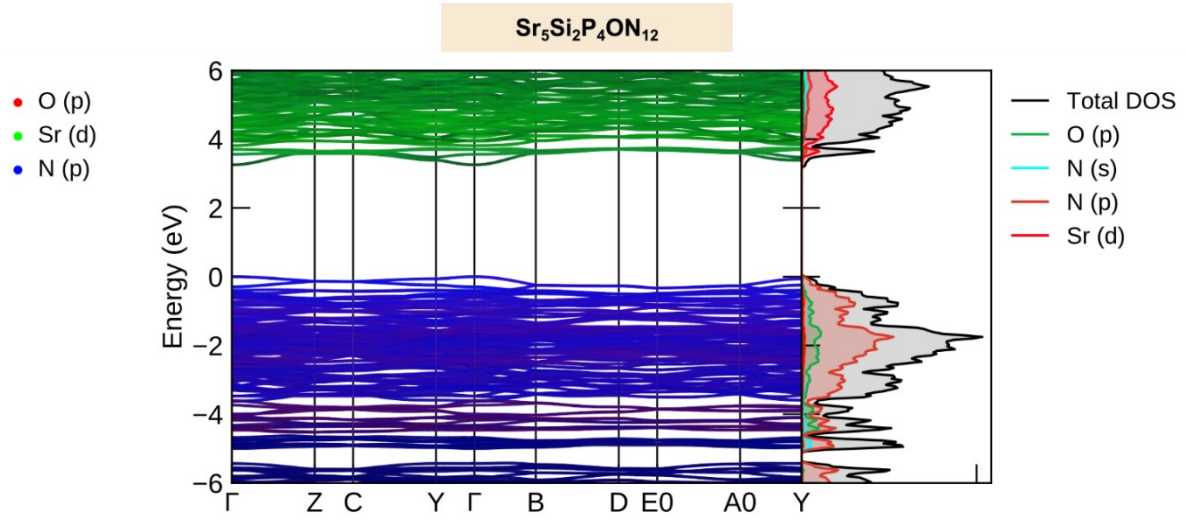

Figure 9.10 Band structure and density of states of $Sr_5Si_2P_4ON_{12}$.

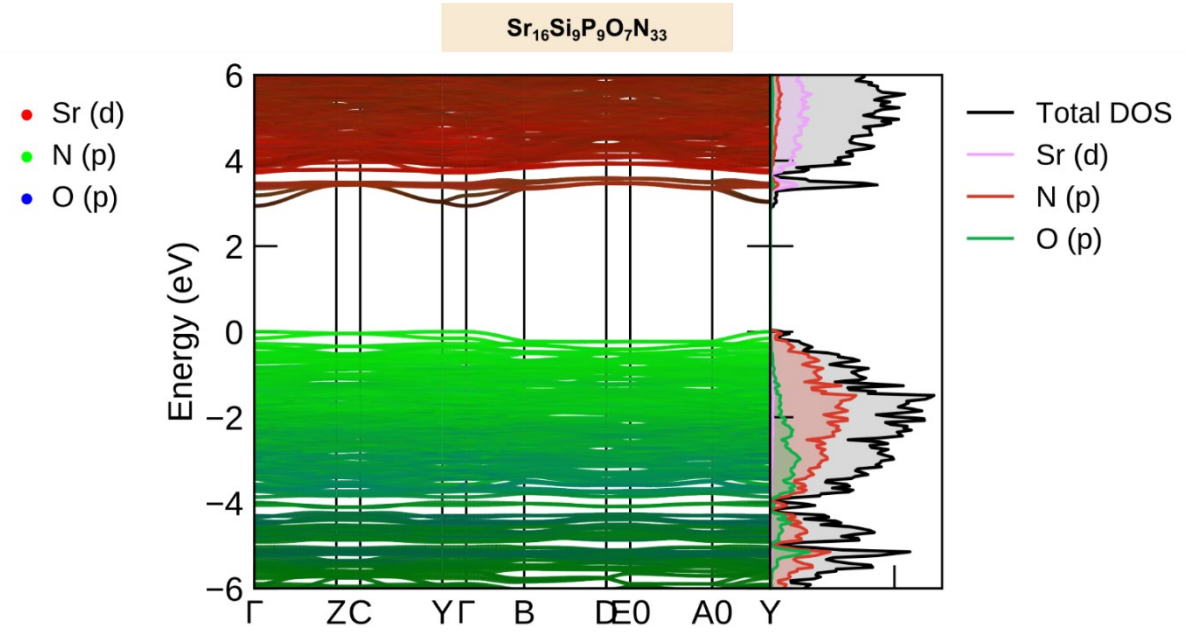

Figure 9.11 Band structure and density of states of $Sr_{16}Si_9P_9O_7N_{33}$.

9.3 References

(1) Stock, A.; Grüneberg, H. Über Den Phosphorstickstoff. *Ber. Dtsch. Chem. Ges.* **1907**, *40* (2), 2573–2578. https://doi.org/10.1002/cber.190704002184.

(2) Eisenburger, L.; Oeckler, O.; Schnick, W. High-Pressure High-Temperature Synthesis of Mixed Nitridosilicatephosphates and Luminescence of *AE*SiP_3N_7:Eu^{2+} (*AE*=Sr, Ba). *Chem. Eur. J.* **2021**, *27* (13), 4461–4465. https://doi.org/10.1002/chem.202005495.

(3) Suhrmann, R.; Clusius, K. Über Die Reindarstellung Der Alkalimetalle. *Z. Anorg. Allg. Chem.* **1926**, *152* (1), 52–58. https://doi.org/10.1002/zaac.19261520107.

(4) Pritzl, R. M.; Prinz, N.; Strobel, P.; Schmidt, P. J.; Johrendt, D.; Schnick, W. From Framework to Layers Driven by Pressure – The Monophyllo-Oxonitridophosphate B-$MgSrP_3N_5O_2$ and Comparison to Its A-Polymorph. *Chem. Eur. J.* **2023**, *29* (41), e202301218. https://doi.org/10.1002/chem.202301218.

(5) Walker, D.; Carpenter, M. A.; Hitch, C. M. Some Simplifications to Multianvil Devices for High Pressure Experiments. *Am. Mineral.* **1990**, *75*, 1020–1028.

(6) Rubie, D. C. Characterising the Sample Environment in Multianvil High-Pressure Experiments. *Phase Transitions* **1999**, *68* (3), 431–451. https://doi.org/10.1080/01411599908224526.

(7) Huppertz, H. Multianvil High-Pressure/High-Temperature Synthesis in Solid State Chemistry. *Z. Kristallogr. Cryst. Mater.* **2004**, *219* (6), 330. https://doi.org/10.1524/ZKRI.219.6.330.34633/MACHINEREADABLECITATION/RIS.

(8) Bertschler, E. M.; Niklaus, R.; Schnick, W. $Li_{12}P_3N_9$ with Non-Condensed $[P_3N_9]^{12-}$-Rings and Its High-Pressure Polymorph Li_4PN_3 with Infinite Chains of PN_4-Tetrahedra. *Chem. Eur. J.* **2017**, *23* (40), 9592. https://doi.org/10.1002/CHEM.201700979.

(9) Mallmann, M.; Wendl, S.; Strobel, P.; Schmidt, P. J.; Schnick, W. $Sr_3P_3N_7$: Complementary Approach by Ammonothermal and High-Pressure Syntheses. *Chem. Eur. J.* **2020**, *26* (28), 6257. https://doi.org/10.1002/chem.202000297.

(10) Marchuk, A.; Neudert, L.; Oeckler, O.; Schnick, W. $CaMg_2P_6O_3N_{10}$ – A Quinary Oxonitridophosphate with an Unprecedented Tetrahedra Network Structure Type. *Eur. J. Inorg. Chem.* **2014**, *2014* (21), 3427–3434. https://doi.org/10.1002/ejic.201402302.

(11) SAINT. SAINT, Data Integration Software, Madison, Wisconsin, USA. **1997**.

(12) Bruker-AXS. XPREP Reciprocal Space Exploration, Vers. 6.12, Karlsruhe. **2001**.

(13) Bruker-AXS. APEX4, V2021.10-0, Karlsruhe, Germany. **2021**.

(14) Sheldrick, G. M. SHELXS-97 Program of the Solution of Crystal Structure, University of Göttingen, Göttingen. **1997**.

(15) Sheldrick, G. M. Crystal Structure Refinement with *SHELXL*. *Acta Crystallogr. C Struct. Chem.* **2015**, *71* (1), 3–8. https://doi.org/10.1107/S2053229614024218.

(16) Farrugia, L. J. *WinGX* and *ORTEP for Windows*: An Update. *J. Appl. Crystallogr.* **2012**, *45* (4), 849–854. https://doi.org/10.1107/S0021889812029111.

(17) Link, L.; Niewa, R. *Polynator* : A Tool to Identify and Quantitatively Evaluate Polyhedra and Other Shapes in Crystal Structures. *J. Appl. Crystallogr.* **2023**, *56* (6), 1855–1864. https://doi.org/10.1107/S1600576723008476.

(18) Momma, K.; Izumi, F. *VESTA 3* for Three-Dimensional Visualization of Crystal, Volumetric and Morphology Data. *J. Appl. Crystallogr.* **2011**, *44* (6), 1272–1276. https://doi.org/10.1107/S0021889811038970.

(19) Ong, S. P.; Richards, W. D.; Jain, A.; Hautier, G.; Kocher, M.; Cholia, S.; Gunter, D.; Chevrier, V. L.; Persson, K. A.; Ceder, G. Python Materials Genomics (Pymatgen): A Robust, Open-Source Python Library for Materials Analysis. *Comput. Mater. Sci.* **2013**, *68*, 314–319. https://doi.org/10.1016/j.commatsci.2012.10.028.

(20) Nespolo, M.; Guillot, B. *CHARDI2015*: Charge Distribution Analysis of Non-Molecular Structures. *J. Appl. Crystallogr.* **2016**, *49* (1), 317–321. https://doi.org/10.1107/S1600576715024814.

(21) Nespolo, M. Charge Distribution as a Tool to Investigate Structural Details. IV. A New Route to Heteroligand Polyhedra. *Acta Crystallogr. Sect. B* **2016**, *72* (1), 51–66. https://doi.org/10.1107/S2052520615019472.

(22) Altomare, A.; Cuocci, C.; Giacovazzo, C.; Moliterni, A.; Rizzi, R.; Corriero, N.; Falcicchio, A. *EXPO2013*: A Kit of Tools for Phasing Crystal Structures from Powder Data. *J. Appl. Crystallogr.* **2013**, *46* (4), 1231–1235. https://doi.org/10.1107/S0021889813013113.

(23) Dialer, M.; Pointner, M. M.; Wandelt, S. L.; Strobel, P.; Schmidt, P. J.; Bayarjargal, L.; Winkler, B.; Schnick, W. Order and Disorder in Mixed (Si, P)–N Networks $Sr_2SiP_2N_6$:Eu^{2+} and $Sr_5Si_2P_6N_{16}$:Eu^{2+}. *Adv. Opt. Mater.* **2023**, 2302668. https://doi.org/10.1002/adom.202302668.

(24) Rietveld, H. M. A Profile Refinement Method for Nuclear and Magnetic Structures. *J. Appl. Crystallogr.* **1969**, *2* (2), 65–71. https://doi.org/10.1107/S0021889869006558.

(25) Coelho, A. A.; TOPAS-Academic v4.1. TOPAS-Academic v4.1. **2007**.

(26) Cheary, R. W.; Coelho, A. A.; Cline, J. P. Fundamental Parameters Line Profile Fitting in Laboratory Diffractometers. *J. Res. Natl. Inst. Stand. Technol.* **2004**, *109* (1), 1. https://doi.org/10.6028/jres.109.002.

(27) Cheary, R. W.; Coelho, A. A. A Fundamental Parameters Approach to X-Ray Line-Profile Fitting. *J. Appl. Crystallogr.* **1992**, *25* (2), 109–121. https://doi.org/10.1107/S0021889891010804.

(28) Kresse, G.; Hafner, J. *Ab Initio* Molecular Dynamics for Liquid Metals. *Phys. Rev. B* **1993**, *47* (1), 558. https://doi.org/10.1103/PhysRevB.47.558.

(29) Kresse, G.; Hafner, J. *Ab Initio* Molecular-Dynamics Simulation of the Liquid-Metal–Amorphous-Semiconductor Transition in Germanium. *Phys. Rev. B* **1994**, *49* (20), 14251. https://doi.org/10.1103/PhysRevB.49.14251.

(30) Kresse, G.; Furthmüller, J. Efficiency of Ab-Initio Total Energy Calculations for Metals and Semiconductors Using a Plane-Wave Basis Set. *Comput. Mater. Sci.* **1996**, *6* (1), 15–50. https://doi.org/10.1016/0927-0256(96)00008-0.

(31) Kresse, G.; Furthmüller, J. Efficient Iterative Schemes for *Ab Initio* Total-Energy Calculations Using a Plane-Wave Basis Set. *Phys. Rev. B* **1996**, *54* (16), 11169. https://doi.org/10.1103/PhysRevB.54.11169.

(32) Kresse, G.; Joubert, D. From Ultrasoft Pseudopotentials to the Projector Augmented-Wave Method. *Phys. Rev. B* **1999**, *59* (3), 1758. https://doi.org/10.1103/PhysRevB.59.1758.

(33) Blöchl, P. E. Projector Augmented-Wave Method. *Phys. Rev. B* **1994**, *50* (24), 17953. https://doi.org/10.1103/PhysRevB.50.17953.

(34) Perdew, J. P.; Burke, K.; Ernzerhof, M. Generalized Gradient Approximation Made Simple. *Phys. Rev. Lett.* **1996**, *77* (18), 3865–3868. https://doi.org/10.1103/PhysRevLett.77.3865.

(35) Rauch, T.; Marques, M. A. L.; Botti, S. Accurate Electronic Band Gaps of Two-Dimensional Materials from the Local Modified Becke-Johnson Potential. *Phys. Rev. B* **2020**, *101* (24), 245163. https://doi.org/10.1103/PhysRevB.101.245163.

(36) Monkhorst, H. J.; Pack, J. D. Special Points for Brillouin-Zone Integrations. *Phys. Rev. B* **1976**, *13* (12), 5188. https://doi.org/10.1103/PhysRevB.13.5188.

(37) Bellaiche, L.; Vanderbilt, D. Virtual Crystal Approximation Revisited: Application to Dielectric and Piezoelectric Properties of Perovskites. *Phys. Rev. B* **2000**, *61* (12), 7877. https://doi.org/10.1103/PhysRevB.61.7877.

10 Supporting Information

Chapter 5

10.1 Experimental Part

10.1.1 Preparation of Starting Materials

$Sr(N_3)_2$ was obtained from the reaction of aqueous HN_3 with $SrCO_3$, recently described by Pritzl et al..[12,13] Semi-crystalline α-P_3N_5 was synthesized from P_4S_{10} via ammonolysis as described in literature.[14] EuN was produced from elemental Eu (smart-elements, 99.99 %) in a tungsten crucible, which was heated under a nitrogen atmosphere in a radio frequency furnace (TIG 10/100; Hüttinger Elektronik Freiburg, Germany) at 1000 °C for 12 hours. The following starting materials were used as purchased: Amorphous Si_3N_4 (UBE, SNA-00), AlN (Tokuyama, 99%), Al_2O_3 (Sigma-Aldrich, 99.9 %), SiO_2 (silica gel 60, 0.040–0.063 mm, Merck), and SrH_2 (Materion, 99.9 %).

10.1.2 High-Pressure High-Temperature Synthesis

$SrSi_2PN_5$ was synthesized in a multianvil press with a modified Walker-type module.[15–17] The synthesis involved stoichiometric amounts of $Sr(N_3)_2$ (3 equivalents, 26.9 mg), amorphous Si_3N_4 (2 equivalents, 14.6 mg), and semi-crystalline α-P_3N_5 (2 equivalents, 8.5 mg). For the preparation of $SrSi_2PN_5$:Eu^{2+}, we added 1 mol% EuN with respect to Sr^{2+}. All starting materials were processed in the absence of O_2 and H_2O by working in an argon-filled glovebox (Unilab, MBraun, Garching; O_2 < 1 ppm; H_2O < 1 ppm). The starting materials were thoroughly mixed and transferred to a boron nitride crucible with additional Mo inlay. Further information on the synthesis in a multianvil press can be found in the literature.[18–20] The sample was then subjected to compression at 3 GPa and heated to 1400 °C, with each step of heating, holding, and cooling taking 6 hours.

10.1.3 Synthesis of $SrSi_2AlO_2N_3:Eu^{2+}$ and $SrSiAl_2O_3N_2:Eu^{2+}$

Both compounds were prepared in a radio-frequency furnace (TIG 10/100; Hüttinger Elektronik Freiburg, Germany) under nitrogen atmosphere at 1800°C in a short temperature program where each step of heating, dwelling, and cooling was set to 2 h. We used stoichiometric amounts of SrH_2, Al_2O_3, and amorphous Si_3N_4 for $SrSiAl_2O_3N_2$, and SrH_2, SiO_2, amorphous Si_3N_4, and AlN for $SrSi_2AlO_2N_3$. For Eu^{2+} doping, we utilized 3 mol% EuN. All syntheses were carried out in a tungsten crucible. These syntheses did not yield phase-pure products, which can be deduced from the inhomogeneous luminescence behavior of the sample. By measuring the cell dimensions of single crystals, we determined the most important minor phases as $Sr_2(Si,Al)_5(O,N)_8:Eu^{2+}$ (orange luminescence), $Sr(Si,Al)_6(O,N)_8:Eu^{2+}$ (blue luminescence) and $Sr_2SiO_4:Eu^{2+}$ (yellow luminescence).[21–23]

10.1.4 Elemental Analyses

The scanning electron microscopy (SEM) images and energy-dispersive X-ray spectroscopy (EDX) spectra were recorded on a FEI Helios Nanolab G3 Dual Beam UC (FEI, Hillsboro, OR, USA) with X-Max 80 SDD detector (Oxford Instruments, Abingdon, UK). We measured inductively coupled plasma optical emission spectroscopy (ICP-OES) on a Varian Vista RL with a 40 MHz RF generator and a VistaChip CCD detector.

10.1.5 Single-Crystal X-ray Diffraction

A single-crystal of $SrSi_2PN_5$ was measured at a Bruker D8 VENTURE diffractometer with a rotating anode and Mo-K_α radiation (λ = 0.71073 Å). The integration and absorption correction were done with the APEX4 program package.[24–26] For the structure solution and refinement, we applied Direct Methods and the least-squares method, which are implemented in SHELXS and SHELXL, respectively.[27–29]

10.1.6 Powder X-ray Diffraction

Our product was thoroughly ground and transferred to a glass capillary with outer diameter of 0.3 mm (Hilgenberg, Malsfeld). The measurement was conducted on a STOE Stadi P diffractometer (STOE & Cie GmbH in Darmstadt) with a modified Debye−Scherrer configuration and Cu-$K_{\alpha1}$ radiation (λ = 1.54060 Å). Rietveld refinements were carried out using TOPAS

Academic software, while peak shapes were fitted by the fundamental parameter method. The background fit was done with a shifted Chebyshev polynomial.[30–33]

10.1.7 Powder Neutron Diffraction

For the measurements, the powder sample was transferred into a 6 mm vanadium cylinder and sealed airtight with indium wire. Time-of-flight neutron data were acquired on the WISH diffractometer at ISIS pulsed neutron source (STFC, Rutherford Appleton Laboratory, Harwell Campus, UK).[34] The Rietveld refinement of the collected pattern was conducted using the program package FullProf, with a fundamental parameters approach and a convolution of pseudo-Voigt with back-to-back exponential functions for profile fitting.[30,35]

10.1.8 Magic Angle Spinning Nuclear Magnetic Resonance Spectroscopy

The measurements were conducted on a Bruker 500 AVANCE-III spectrometer operating at a proton frequency of 500 MHz. We used a ZrO_2 rotor with an outer diameter of 2.5 mm that was subjected to the spinning frequency of 20 kHz. We referenced the spectra indirectly to ^1H in 100% TMS at −0.124 ppm.

10.1.9 Fourier-Transform Infrared Spectroscopy (FTIR)

To secure exclusion of O_2 and H_2O, we conducted the measurement in an argon-filled glovebox on a Bruker Alpha II FTIR device equipped with a diamond ATR component. The spectra were recorded with a resolution of 2 cm^{-1} in the range of 450–4000 cm^{-1}.

10.1.10 Luminescence Measurements

Photoluminescence excitation and photoluminescence spectra of all samples were recorded on a HORIBA Fluoromax4 spectrofluorimeter system in combination with an Olympus BX51 microscope.

10.2 Results and Discussion

10.2.1 EDX measurements

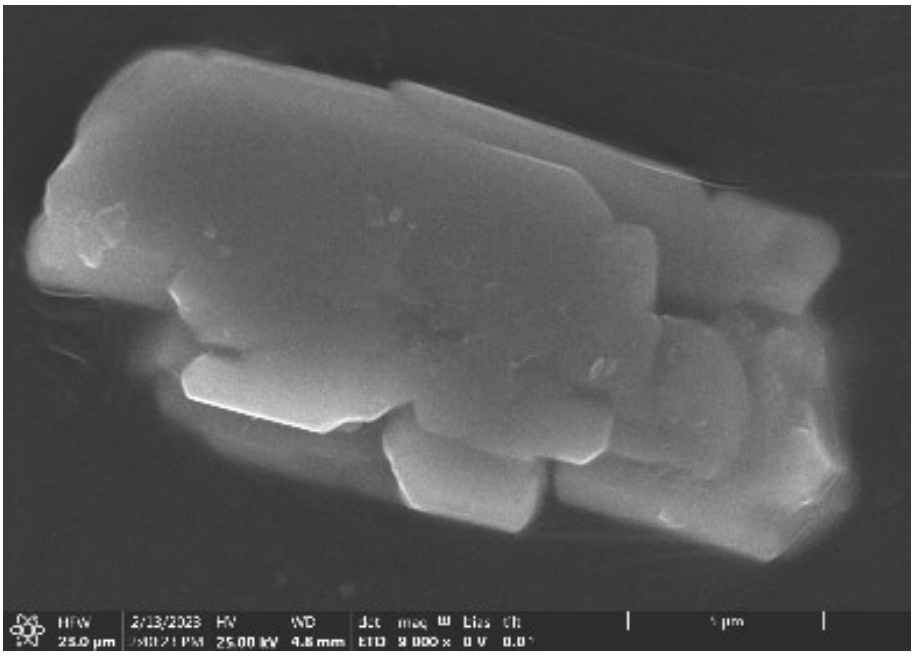

Figure 10.1 SEM image of a particle of $SrSi_2PN_5$ on which EDX was measured.

Table 10.1 Results of EDX measurements on a particle of $SrSi_2PN_5$ in at%.

Measurement	Sr	Si	P	N	O
1	11	26	9	49	5
2	10	24	8	50	8
3	9	22	8	50	11
4	11	26	9	50	4
5	11	26	9	48	5
6	11	27	9	48	5
7	9	22	9	52	8
8	11	28	9	48	5
9	11	27	9	48	5
Average	10(1)	25(2)	9(1)	49(2)	6(2)
Calculated	11.1	22.2	11.1	55.6	0

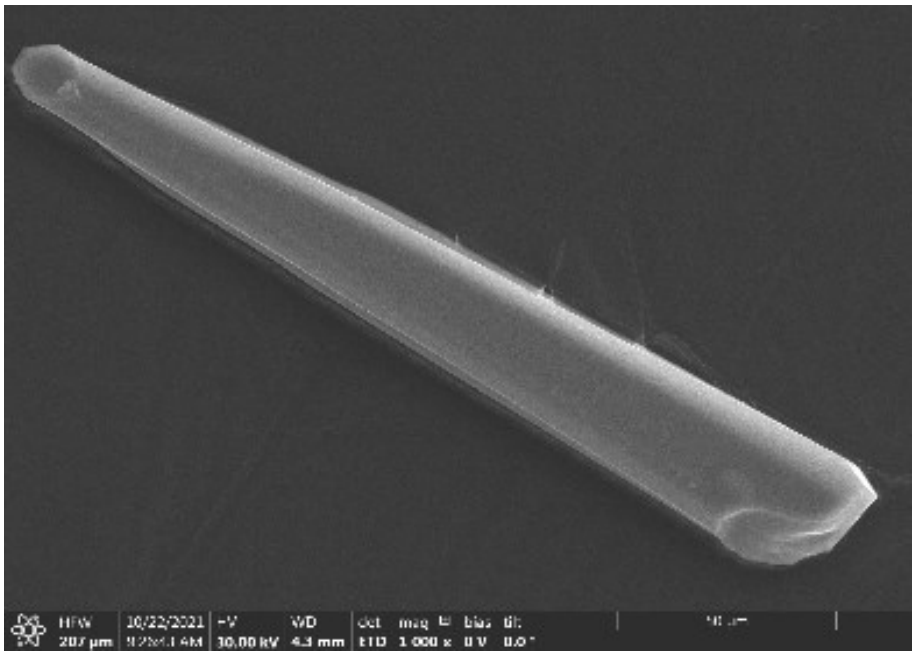

Figure 10.2 SEM image of a particle of $SrSi_2AlO_2N_3$ on which EDX was measured.

Table 10.2 Results of EDX measurements on a single crystal of $SrSi_2AlO_2N_3$ in at%.

Measurement	Sr	Si	Al	N	O
1	13	24	10	33	20
2	13	25	11	31	20
3	13	24	11	31	20
4	13	24	10	31	20
5	13	24	11	32	20
6	13	25	11	31	20
7	13	24	10	32	19
8	13	25	10	31	20
9	14	25	11	31	19
Average	13(1)	25(2)	11(1)	31(1)	20(1)
Calculated	11.1	22.2	11.1	33.4	22.2

10.2.2 Fourier-Transform Infrared Spectroscopy (FTIR)

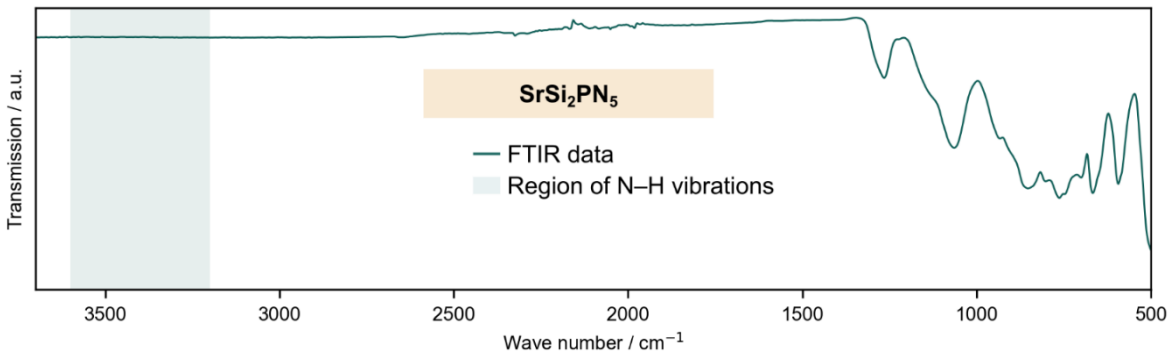

Figure 10.3 FTIR spectrum of $SrSi_2PN_5$ with no visible signals in the typical region of N–H or O–H vibrations.

10.2.3 $^{31}P\{^1H\}$ Nuclear Magnetic Resonance Spectroscopy

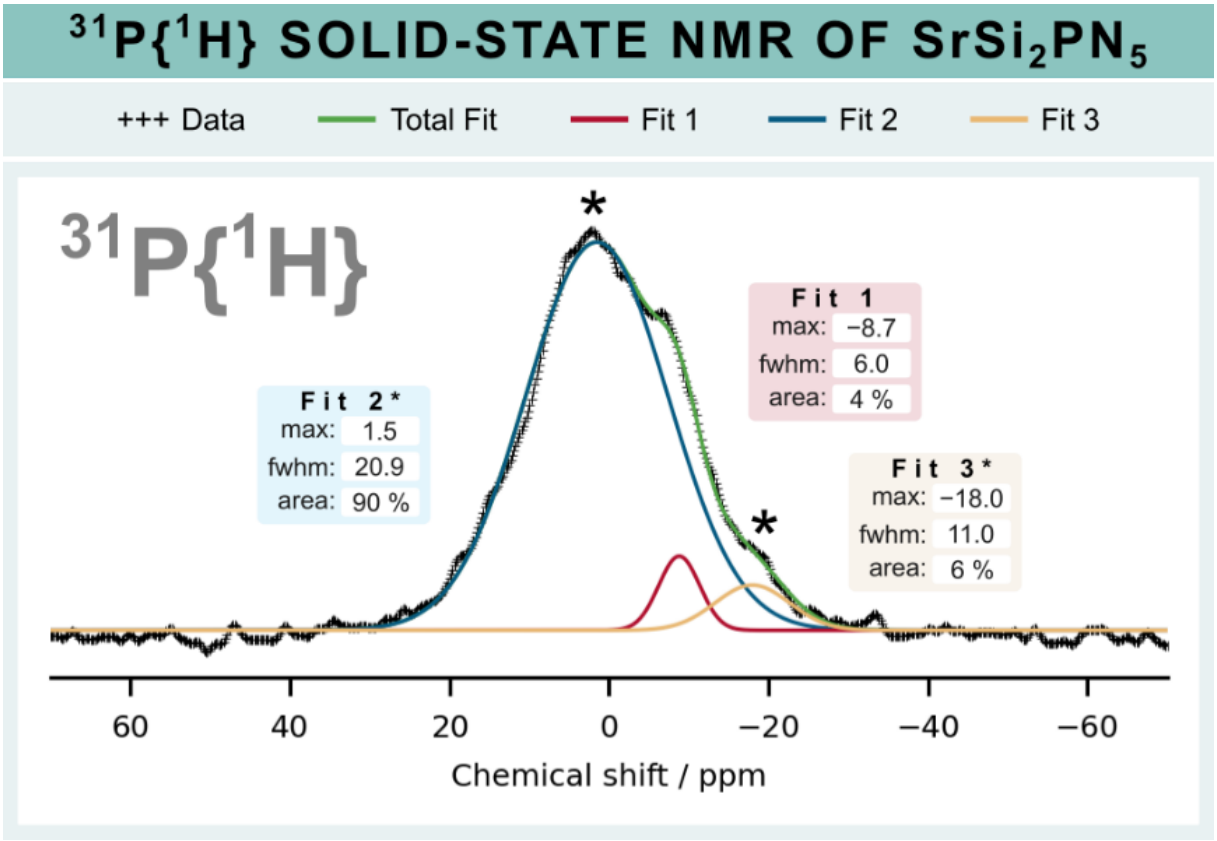

Figure 10.4 Cross-polarized $^{31}P\{^1H\}$ NMR spectrum of $SrSi_2PN_5$. The main contribution of this spectrum originates from $Sr_3SiP_3O_2N_7$:$(NH)^{2-}$ as discussed in previous work and marked by (*).[1] Considering the high number of scans for the cross-polarized experiment (>58000) compared to one scan for ^{31}P, the presence of ^1H can be neglected in the sample, more so for the title compound $SrSi_2PN_5$.

10.2.4 Single-Crystal X-ray Diffraction

Table 10.3 Crystallographic data of $SrSi2PN_5$ and $SrSi_2AlO_2N_3$ from single-crystal refinement. Standard deviations are given in parentheses.

Formula	$SrSi_2PN_5$	$SrSi_2AlO_2N_3$
Crystal system	orthorhombic	orthorhombic
Space group	$P2_12_12_1$ (no. 19)	$P2_12_12_1$ (no. 19)
Lattice parameters / Å, °	a = 4.84640(10)	a = 4.92240(10)
	b = 7.7480(3)	b = 7.91680(10)
	c = 11.4066(3)	c = 11.3469(2)
Cell volume / Å^3	428.32(2)	442.185(13)
Formula units / unit cell	4	4
Calculated X-ray density / g · cm^{-3}	3.797	3.677
Molar mass / g · mol^{-1}	244.82	244.81
Crystal sizes / µm	10 x 10 x 10	40 x 20 x 20
µ / mm^{-1}	13.381	12.821
Temperature / K	296(2)	296(2)
Absorption correction	multi-scan	multi-scan
Radiation	Mo-K_α	Mo-K_α
F(000)	464	464
ϑ range / °	$6.356 \leq 2\vartheta \leq 71.01$	$6.275 \leq 2\vartheta \leq 78.35$
Total no. of reflections	7129	2119
Independent reflections [$I \geq 2\sigma(I)$ / all]	1186 / 1297	1015 / 1044
R_{int} / R_σ	0.0363 / 0.0437	0.0342 / 0.0148
Refined parameters / restraints	83 / 0	83 / 0
Goodness of fit	1.105	1.112
R-values [$I \geq 2\sigma(I)$]	$R1$ = 0.0325, w$R2$ = 0.0577	$R1$ = 0.0179, w$R2$ = 0.0485
R-values (all data)	$R1$ = 0.0377, w$R2$ = 0.0589	$R1$ = 0.0186, w$R2$ = 0.0488
$\Delta\rho_{max}$, $\Delta\rho_{min}$ / e · Å^3	0.558, −1.048	0.424, −0,589

Table 10.4 Wyckoff position, coordinates, equivalent thermal displacement parameters and occupancy of $SrSi_2PN_5$ from single-crystal refinement. Standard deviations are given in parentheses.

Atom	Wyckoff	x	y	z	U_{eq}	S.O.F.
Sr1	4a	0.49385(18)	0.54403(7)	0.66651(4)	0.01125(13)	1
P1	4a	0.4953(5)	0.16917(16)	0.15686(12)	0.0074(2)	1
Si2	4a	0.5097(5)	0.46669(18)	-0.04274(12)	0.0054(3)	1
Si3	4a	0.5230(4)	0.29725(19)	0.41623(13)	0.0038(3)	1
N1	4a	0.5383(11)	0.3459(6)	0.0766(4)	0.0064(10)	1
N2	4a	0.6241(11)	0.2106(7)	0.2897(5)	0.0102(11)	1
N3	4a	0.1631(10)	0.1182(7)	0.1601(5)	0.0071(9)	1
N4	4a	0.1683(10)	0.5073(6)	-0.0886(5)	0.0059(10)	1
N5	4a	0.8241(11)	0.3420(7)	0.4979(5)	0.0062(9)	1

Table 10.5 Wyckoff position, coordinates, equivalent thermal displacement parameters and occupancy of $SrSi_2AlO_2N_3$ from single-crystal refinement. Standard deviations are given in parentheses.

Atom	Wyckoff	*x*	*y*	*z*	U_{eq}	S.O.F.
Sr1	4*a*	0.00992(9)	0.54177(4)	0.16569(3)	0.01344(12)	1
Al1	4*a*	0.4946(3)	0.33356(12)	0.34393(8)	0.0040(2)	1
Si2	4*a*	0.4851(3)	0.03078(13)	0.54282(9)	0.0085(2)	1
Si3	4*a*	0.4867(3)	0.20140(13)	0.08037(9)	0.0082(2)	1
O1	4*a*	0.4601(7)	0.1558(4)	0.4229(3)	0.0176(7)	0.6667
N1	4*a*	0.4601(7)	0.1558(4)	0.4229(3)	0.0176(7)	0.3333
O2	4*a*	0.3698(7)	0.2881(4)	0.2090(3)	0.0166(7)	0.6667
N2	4*a*	0.3698(7)	0.2881(4)	0.2090(3)	0.0166(7)	0.3333
O3	4*a*	0.8329(6)	0.3771(4)	0.3388(3)	0.0145(7)	0.6667
N3	4*a*	0.8329(6)	0.3771(4)	0.3388(3)	0.0145(7)	0.3333
N4	4*a*	0.8224(7)	-0.0084(5)	0.5903(3)	0.0125(8)	1
N5	4*a*	0.6915(7)	0.3470(4)	0.0027(3)	0.0102(7)	1

10.2.5 Powder X-ray Diffraction

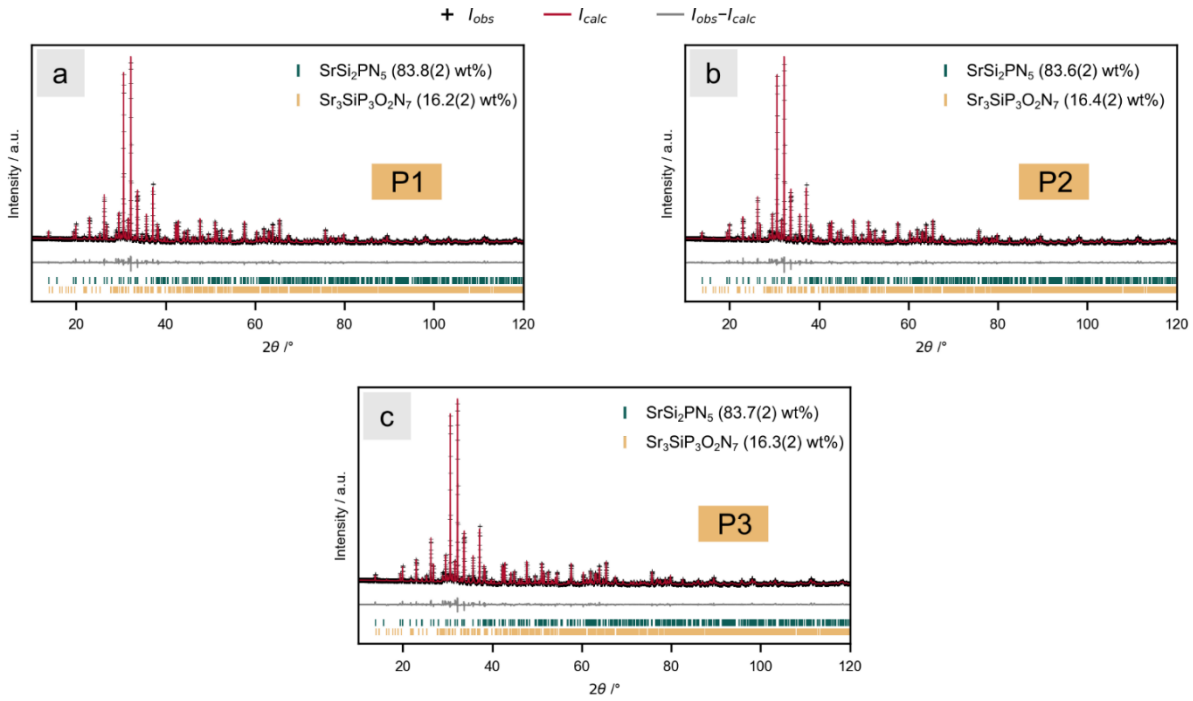

Figure 10.5 Plots of the Rietveld refinements based on powder X-ray diffraction data of the ordering variants (a) P1, (b) P2, and (c) P3 of $SrSi_2PN_5$.

Table 10.6 Crystallographic data of the Rietveld refinement based on powder XRD data of P1–P3.

Ordering Variant	P1	P2	P3
Diffractometer		STOE Stadi P	
Radiation		Cu-$K_{\alpha1}$ (λ = 1.54059 Å)	
Monochromator		Ge(111)	
Detector		Mythen1K	
2ϑ range / °		5 ≤ 2ϑ ≤ 121	
Data points		7705	
Number of reflections		406	
Refined parameters		76	
Background function		Shifted Chebyshev, 18 polynomials	
R_{Bragg}	0.0272	0.0311	0.0306
R_{wp}	0.0717	0.0737	0.0732
Goodness of fit	2.602	2.674	2.656

10.2.6 Powder Neutron Diffraction

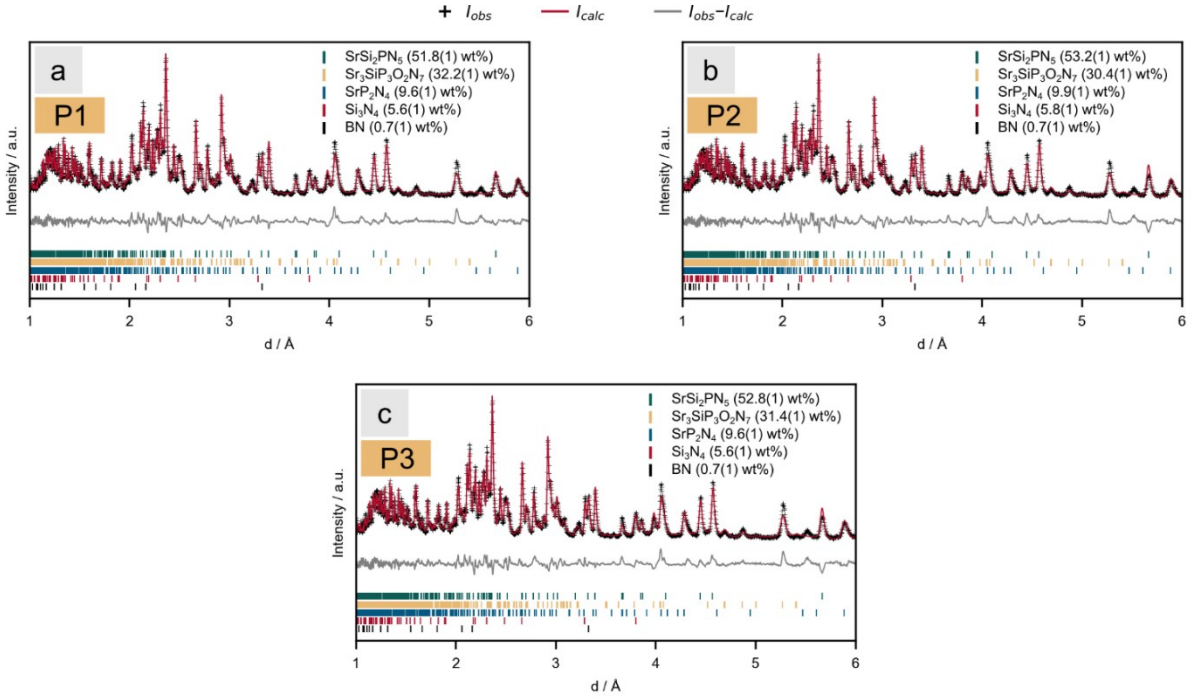

Figure 10.6 Plots of the Rietveld refinements based on powder neutron diffraction data of the ordering variants (a) P1, (b) P2, and (c) P3 of $SrSi_2PN_5$.

Table 10.7 Crystallographic data of the Rietveld refinement based on powder neutron data of P1–P3.

Ordering Variant	P1	P2	P3
Diffractometer	ISIS, WISH		
Radiation	Neutrons (*tof*)		
Data points	3974		
Number of reflections	406		
Refined parameters	97		
R_{Bragg}	0.0674	0.0767	0.0712
R_{wp}	0.124	0.130	0.126
Goodness of fit	12.42	13.42	12.76

10.3 References

(1) Dialer, M.; Witthaut, K.; Bräuniger, T.; Schmidt, P. J.; Schnick, W. The Fundamental Disorder Unit in (Si, P)–(O, N) Networks. *Angew. Chem. Int. Ed.* **2024**, e202401419. https://doi.org/10.1002/ANIE.202401419.

11 Summary

11.1 Summary of Chapter 2

Order and Disorder in Mixed (Si,P)–N Networks $Sr_2SiP_2N_6:Eu^{2+}$ and $Sr_5Si_2P_6N_{16}:Eu^{2+}$

Marwin Dialer, Monika M. Pointner, Sophia L. Wandelt, Philipp Strobel, Peter J. Schmidt, Lkhamsuren Bayarjargal, Björn Winkler, Wolfgang Schnick

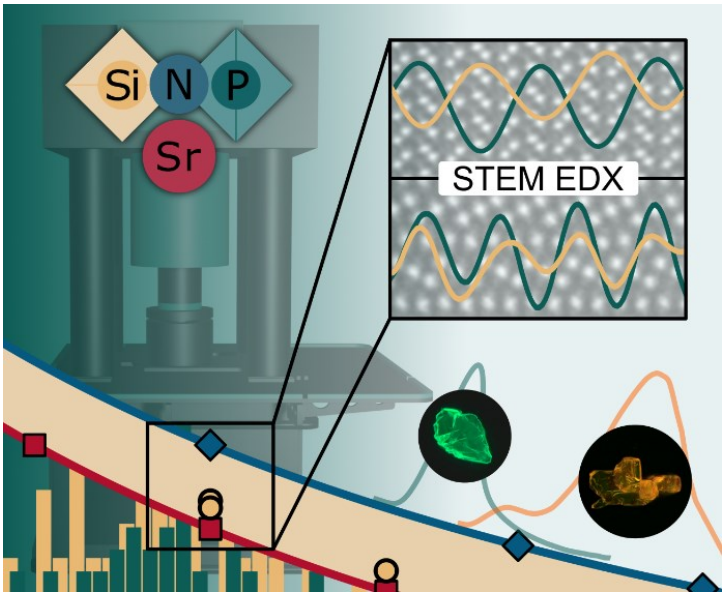

In the field of nitride phosphors, which are crucial for phosphor-converted light-emitting diodes, mixed tetrahedral networks hold a significant position. With respect to the wide range of compositions, the largely unexplored (Si,P)–N networks are investigated as potential host structures. In this work, two highly condensed structures, namely $Sr_2SiP_2N_6$ and $Sr_5Si_2P_6N_{16}$ are reported to address the challenges that arise from the similarities of the network-forming cations Si^{4+} and P^{5+} in terms of charge, ionic radius, and atomic scattering factor, a multistep workflow is employed to elucidate their structure. Using single-crystal X-ray diffraction, energy-dispersive X-ray spectroscopy (EDX), atomic-resolution scanning transmission electron microscopy (STEM)-EDX maps, and straightforward crystallographic calculations, it is found that $Sr_2SiP_2N_6$ is the first ordered, and $Sr_5Si_2P_6N_{16}$ the first disordered, anionic tetrahedral (Si,P)–N network. After doping with Eu^{2+}, $Sr_2SiP_2N_6:Eu^{2+}$ shows narrow cyan emission (λ_{max} = 506 nm, *fwhm* = 60 nm/2311 cm^{-1}), while for $Sr_5Si_2P_6N_{16}:Eu^{2+}$ a broad emission with three maxima at 534, 662, and 745 nm upon irradiation with ultraviolet light is observed. An assignment of Sr sites as probable positions for Eu^{2+} and their relation to the emission bands of $Sr_5Si_2P_6N_{16}:Eu^{2+}$ is discussed.

11.2 Summary of Chapter 3

(Dis)Order and Luminescence in Silicon-Rich (Si,P)−N Network $Sr_5Si_7P_2N_{16}:Eu^{2+}$

Marwin Dialer, Monika M. Pointner, Philipp Strobel, Peter J. Schmidt, Wolfgang Schnick

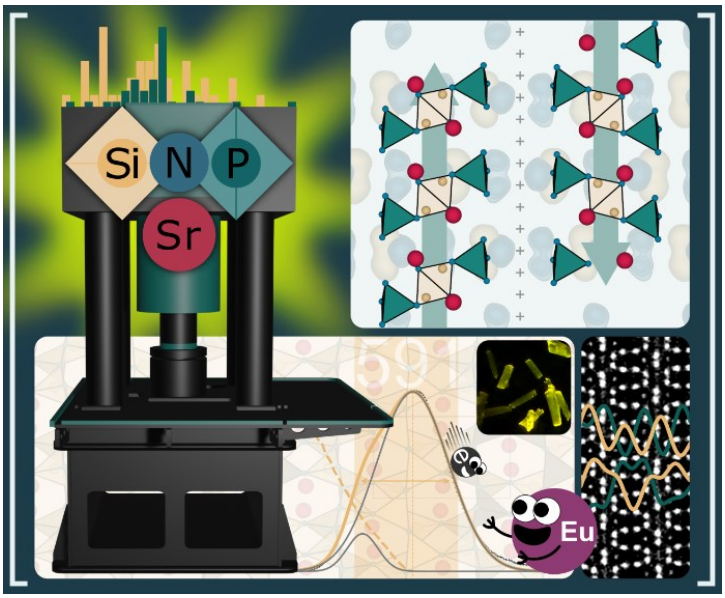

In this work, we present the synthesis, characterization, and optical properties of $Sr_5Si_7P_2N_{16}:Eu^{2+}$, the first tetrahedral (Si,P)−N network in which Si occupies more than 50% of the tetrahedra. While past studies have shown progress with anionic (Si,P)−N networks, the potential of silicon-rich compounds remains untapped. The synthesized compound $Sr_5Si_7P_2N_{16}$ exhibits a unique mixture of substitutional order and positional disorder within its network. The analytical challenges posed by the similarities between Si^{4+} and P^{5+}, along with the network's disorder, were overcome by combining single-crystal X-ray diffraction and scanning transmission electron microscopy EDX mapping. Low-cost crystallographic calculations provided additional insights into the identification of tetrahedral occupations in mixed networks. Luminescence investigations on $Sr_5Si_7P_2N_{16}:Eu^{2+}$ revealed yellow emission, adding to the known blue, green, and orange emission maxima of Sr−(Si,P)−N networks, highlighting the variability of such compounds.

11.3 Summary of Chapter 4

The Fundamental Disorder Unit in (Si,P)–(O,N) Networks

Marwin Dialer, Kristian Witthaut, Thomas Bräuniger, Peter J. Schmidt, Wolfgang Schnick

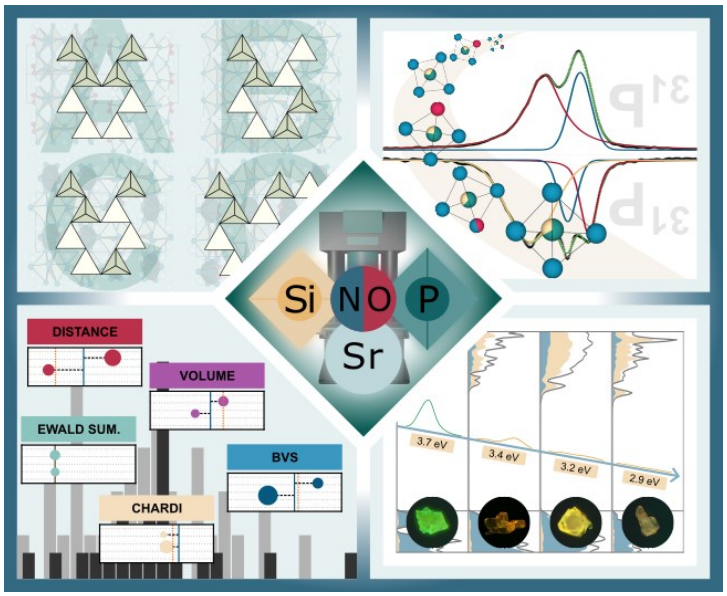

This study presents the synthesis and characterization of oxonitridosilicate phosphates $Sr_3SiP_3O_2N_7$, $Sr_5Si_2P_4ON_{12}$, and $Sr_{16}Si_9P_9O_7N_{33}$ as the first of their kind. These compounds were synthesized under high-temperature (1400 °C) and high-pressure (3 GPa) conditions. A unique structural feature is their common fundamental building unit, a *vierer* single chain of (Si, P)$(O, N)_4$ tetrahedra. All tetrahedra comprise substitutional disorder which is why we refer to it as the fundamental disorder unit (FDU). We classified four different FDU motifs, revealing systematic bonding patterns. Including literature known $Sr_5Si_2P_6N_{16}$, three of the four patterns were found in the presented compounds. Common techniques like single-crystal X-ray diffraction (SCXRD), elemental analyses, and ^{31}P nuclear magnetic resonance (NMR) spectroscopy were utilized for structural analysis. Additionally, low-cost crystallographic calculations (LCC) provided insights into the structure of $Sr_{16}Si_9P_9O_7N_{33}$ where NMR data were unavailable due to the lack of bulk samples. The optical properties of these compounds, when doped with Eu^{2+}, were investigated using photoluminescence excitation (PLE), photoluminescence (PL) measurements, and density functional theory (DFT) calculations. Factors influencing the emission properties, including thermal quenching mechanisms, were discussed. This research reveals the new class of oxonitridosilicate phosphates with unique systematic structural features that offer potential for theoretical studies of luminescence and band gap tuning in insulators.

11.4 Summary of Chapter 5

The Super-Tunable $LaSi_3N_5$ Structure Type: Insights into the Structure and Luminescence of $SrSi_2PN_5:Eu^{2+}$

Marwin Dialer, Reinhard M. Pritzl, Sophia L. Wandelt, Dmitry Khalyavin, Peter J. Schmidt, Wolfgang Schnick

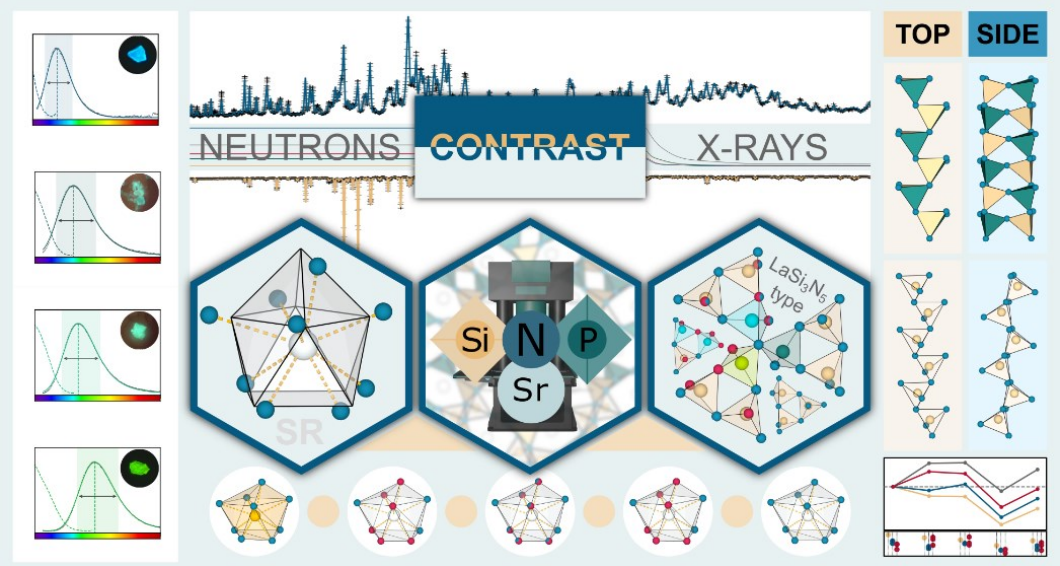

In this study, the structural and luminescence properties of $SrSi_2PN_5:Eu^{2+}$ and its analogues within the $LaSi_3N_5$ structure type are investigated using a variety of analytical techniques including X-ray diffraction (XRD), ^{31}P solid-state NMR, and powder neutron diffraction. We are exploring the challenges of chemical similarity and low X-ray contrast between the key elements to extend our analytical capabilities by powder neutron diffraction (PND) for (Si,P)–N networks. In principle, PND shows greater differences in scattering contrasts for O/N and Si/P, although it does not surpass standard powder XRD in elemental discrimination of Si/P within the network. The Eu^{2+} doping of $SrSi_2PN_5$ demonstrates the potential for tunable optical applications, within the group of $LaSi_3N_5$ analogous materials. Our results contribute to the understanding of the structural diversity and luminescence mechanisms of nitridosilicate phosphates and emphasize the importance of a comprehensive analytical approach in materials science with implications for the future development of optoelectronic devices.

12 Miscellaneous

12.1 List of Publications

The publications are listed achronologically. For all publications that are part of this dissertation, the author contributions are indicated in section 12.2.

(1) Dialer, M.; Pritzl, R. M.; Wandelt, S. L.; Khalyavin, D.; Schmidt, P. J.; Schnick, W. The Super-Tunable $LaSi_3N_5$ Structure Type: Insights into the Structure and Luminescence of $SrSi_2PN_5:Eu^{2+}$. *Chem. Mater.* **2024**, *accepted*.

(2) Dialer, M.; Witthaut, K.; Bräuniger, T.; Schmidt, P. J.; Schnick, W. The Fundamental Disorder Unit in (Si, P)–(O, N) Networks. *Angew. Chem. Int. Ed.* **2024**, e202401419. https://doi.org/10.1002/ANIE.202401419.

(3) Dialer, M.; Pointner, M. M.; Strobel, P.; Schmidt, P. J.; Schnick, W. (Dis)Order and Luminescence in Silicon-Rich (Si,P)–N Network $Sr_5Si_7P_2N_{16}:Eu^{2+}$. *Inorg. Chem.* **2024**, *63* (2), 1480–1487. https://doi.org/10.1021/acs.inorgchem.3c04109.

(4) Giftthaler, T.; Dialer, M.; Strobel, P.; Schmidt, P. J.; Schnick, W. Blue Emitting $SrBe_{1-x}Si_{2+x}O_{3-2x}N_{2+2x}:Eu^{2+}$ (x ≈0.1). *Z. Anorg. Allg. Chem.* **2024**, *650* (2), e202300208. https://doi.org/10.1002/zaac.202300208.

(5) Dialer, M.; Pointner, M. M.; Wandelt, S. L.; Strobel, P.; Schmidt, P. J.; Bayarjargal, L.; Winkler, B.; Schnick, W. Order and Disorder in Mixed (Si, P)–N Networks $Sr_2SiP_2N_6:Eu^{2+}$ and $Sr_5Si_2P_6N_{16}:Eu^{2+}$. *Adv. Opt. Mater.* **2023**, 2302668. https://doi.org/10.1002/adom.202302668.

(6) Höppe, H. A.; Jantz, S. G.; Dialer, M. Nonlinear Optical Materials and Method for Their Production. EP3366642, May 6, 2020.

(7) Jantz, S. G.; Dialer, M.; Bayarjargal, L.; Winkler, B.; van Wüllen, L.; Pielnhofer, F.; Brgoch, J.; Weihrich, R.; Höppe, H. A. $Sn[B_2O_3F_2]$—The First Tin Fluorooxoborate as Possible NLO Material. *Adv. Opt. Mater.* **2018**, *6* (17), 1800497. https://doi.org/10.1002/adom.201800497.

(8) Jantz, S. G.; Pielnhofer, F.; Dialer, M.; Höppe, H. A. On Tungstates of Divalent Cations (I) – Structural Investigation and Spectroscopic Properties of $Sr_2[WO_5]$ and $Ba_2[WO_5]$. *Z. Allg. Anorg. Chem.* **2017**, *643* (23), 2024–2030. https://doi.org/10.1002/zaac.201700334.

(9) Jantz, S. G.; Pielnhofer, F.; Dialer, M.; Höppe, H. A. On Tungstates of Divalent Cations (II) – Polymorphy of Pb_2WO_5. *Z. Allg. Anorg. Chem.* **2017**, *643* (23), 2031–2037. https://doi.org/10.1002/zaac.201700335.

12.2 Author Contributions in this Dissertation

12.2.1 The Super-Tunable $LaSi_3N_5$ Structure Type: Insights into the Structure and Luminescence of $SrSi_2PN_5:Eu^{2+}$

Marwin Dialer, Reinhard M. Pritzl, Sophia L. Wandelt, Dmitry Khalyavin, Peter J. Schmidt, Wolfgang Schnick

Chem. Mater. **2024**, *accepted*.

Marwin Dialer

Conceptualization	Lead	Formal analysis	Lead
Investigation	Lead	Validation	Lead
Visualization	Lead	Writing – original draft	Lead
Writing – review & editing	Equal		

Reinhard M Pritzl

Conceptualization	Supporting	Formal analysis	Supporting
Investigation	Supporting	Validation	Supporting
Visualization	Supporting	Writing – original draft	Supporting
Writing – review & editing	Supporting		

Sophia L. Wandelt

Conceptualization	Supporting	Formal analysis	Supporting
Investigation	Supporting	Validation	Supporting
Visualization	Supporting	Writing – original draft	Supporting
Writing – review & editing	Supporting		

Dmitry Khalyavin

Conceptualization	Supporting	Formal analysis	Supporting
Investigation	Supporting	Validation	Supporting
Visualization	Supporting	Writing – original draft	Supporting
Writing – review & editing	Supporting		

Peter J. Schmidt

Conceptualization	Supporting	Formal analysis	Supporting
Funding acquisition	Supporting	Project administration	Supporting
Resources	Supporting	Supervision	Supporting
Validation	Supporting	Writing – original draft	Supporting
Writing – review & editing	Supporting		

Wolfgang Schnick

Conceptualization	Equal	Formal analysis	Supporting
Funding acquisition	Lead	Project administration	Lead
Resources	Lead	Supervision	Lead
Validation	Equal	Writing – original draft	Supporting
Writing – review & editing	Supporting		

12.2.2
The Fundamental Disorder Unit in (Si,P)–(O,N) Networks

Marwin Dialer, Kristian Witthaut, Thomas Bräuniger, Peter J. Schmidt, Wolfgang Schnick

Angew. Chem. Int. Ed. **2024**, e202401419. 10.1002/anie.202401419.

Marwin Dialer

Conceptualization	Lead	Formal analysis	Lead
Investigation	Lead	Validation	Lead
Visualization	Lead	Writing – original draft	Lead
Writing – review & editing	Equal		

Kristian Witthaut

Conceptualization	Supporting	Formal analysis	Supporting
Investigation	Supporting	Validation	Supporting
Visualization	Supporting	Writing – original draft	Supporting
Writing – review & editing	Supporting		

Thomas Bräuniger

Conceptualization	Supporting	Formal analysis	Supporting
Investigation	Supporting	Validation	Supporting
Visualization	Supporting	Writing – original draft	Supporting
Writing – review & editing	Supporting		

Dmitry Khalyavin

Conceptualization	Supporting	Formal analysis	Supporting
Investigation	Supporting	Validation	Supporting
Visualization	Supporting	Writing – original draft	Supporting
Writing – review & editing	Supporting		

Peter J. Schmidt

Conceptualization	Supporting	Formal analysis	Supporting
Funding acquisition	Supporting	Project administration	Supporting
Resources	Supporting	Supervision	Supporting
Validation	Supporting	Writing – original draft	Supporting
Writing – review & editing	Supporting		

Wolfgang Schnick

Conceptualization	Equal	Formal analysis	Supporting
Funding acquisition	Lead	Project administration	Lead
Resources	Lead	Supervision	Lead
Validation	Equal	Writing – original draft	Supporting
Writing – review & editing	Supporting		

12.2.3
(Dis)Order and Luminescence in Silicon-Rich (Si,P)−N Network $Sr_5Si_7P_2N_{16}:Eu^{2+}$

Marwin Dialer, Monika M. Pointner, Philipp Strobel, Peter J. Schmidt, Wolfgang Schnick

Inorg. Chem. 2024, *63,* 1480−1487. https://doi.org/10.1021/acs.inorgchem.3c04109.

Marwin Dialer

Conceptualization	Lead	Formal analysis	Lead
Investigation	Lead	Validation	Lead
Visualization	Lead	Writing – original draft	Lead
Writing – review & editing	Equal		

Monika M. Pointner

Conceptualization	Supporting	Formal analysis	Supporting
Investigation	Supporting	Validation	Supporting
Visualization	Supporting	Writing – original draft	Supporting
Writing – review & editing	Supporting		

Philipp Strobel

Conceptualization	Supporting	Formal analysis	Supporting
Investigation	Supporting	Validation	Supporting
Visualization	Supporting	Writing – original draft	Supporting
Writing – review & editing	Supporting		

Peter J. Schmidt

Conceptualization	Supporting	Formal analysis	Supporting
Funding acquisition	Supporting	Project administration	Supporting
Resources	Supporting	Supervision	Supporting
Validation	Supporting	Writing – original draft	Supporting
Writing – review & editing	Supporting		

Wolfgang Schnick

Conceptualization	Equal	Formal analysis	Supporting
Funding acquisition	Lead	Project administration	Lead
Resources	Lead	Supervision	Lead
Validation	Equal	Writing – original draft	Supporting
Writing – review & editing	Supporting		

12.2.4
Order and Disorder in Mixed (Si,P)–N Networks $Sr_2SiP_2N_6:Eu^{2+}$ and $Sr_5Si_2P_6N_{16}:Eu^{2+}$

Marwin Dialer, Monika M. Pointner, Sophia L. Wandelt, Philipp Strobel, Peter J. Schmidt, Lkhamsuren Bayarjargal, Björn Winkler, Wolfgang Schnick

Adv. Opt. Mater., **2023**, 2302668. https://doi.org/10.1002/adom.202302668.

Marwin Dialer

Conceptualization	Lead	Formal analysis	Lead
Investigation	Lead	Validation	Lead
Visualization	Lead	Writing – original draft	Lead
Writing – review & editing	Equal		

Monika M. Pointner

Conceptualization	Supporting	Formal analysis	Supporting
Investigation	Supporting	Validation	Supporting
Visualization	Supporting	Writing – original draft	Supporting
Writing – review & editing	Supporting		

Sophia L. Wandelt

Conceptualization	Supporting	Formal analysis	Supporting
Investigation	Supporting	Validation	Supporting
Visualization	Supporting	Writing – original draft	Supporting
Writing – review & editing	Supporting		

Philipp Strobel

Conceptualization	Supporting	Formal analysis	Supporting
Investigation	Supporting	Validation	Supporting
Visualization	Supporting	Writing – original draft	Supporting

Peter J. Schmidt

Conceptualization	Supporting	Formal analysis	Supporting
Funding acquisition	Supporting	Project administration	Supporting
Resources	Supporting	Supervision	Supporting
Validation	Supporting	Writing – original draft	Supporting
Writing – review & editing	Supporting		

Lkhamsuren Bayarjargal

Conceptualization	Supporting	Formal analysis	Supporting
Investigation	Supporting	Validation	Supporting
Visualization	Supporting	Writing – original draft	Supporting
Writing – review & editing	Supporting		

Björn Winkler

Funding acquisition	Supporting	Project administration	Supporting
Resources	Supporting	Supervision	Supporting
Validation	Supporting	Formal Analysis	Supporting
Writing – review & editing	Supporting		

Wolfgang Schnick

Conceptualization	Equal	Formal analysis	Supporting
Funding acquisition	Lead	Project administration	Lead
Resources	Lead	Supervision	Lead
Validation	Equal	Writing – original draft	Supporting
Writing – review & editing	Supporting		

12.3 Conference Contributions and Presentations

1. Aluminum: A Difficult Patient

Marwin Dialer
Talk, Schnick Group Seminar
Munich (Germany), 29.04.2020

2. Von Holzwegen und besseren Aussichten

Marwin Dialer
Talk, Schnick Group Seminar
Munich (Germany), 07.07.2021

3. Tunable Networks: PSiAlONs

Marwin Dialer
Talk, Schnick Group Seminar
Munich (Germany), 08.06.2022

4. Cyclosilicate Analogous $[(P,Si)_3N_3O_6]^{x-}$ rings in cyan-emitting phosphor $Ba_3K_{0.67}(P,Si)_3(N,O)_9:Eu^{2+}$

Marwin Dialer, Wolfgang Schnick
Poster, 21. Vortragstagung für Anorganische Chemie der Fachgruppen Wöhler-Vereinigung und Festkörperchemie und Materialforschung
Marburg (Germany), 27.09.2022

5. (Si–N–P)LE *AE*–NOUGH

Marwin Dialer
Talk, 6. Obergurgl-Seminar Festkörperchemie
Obergurgl (Austria), 26.01.2023

6. (Si–N–P)LE *AE*–NOUGH – The Grand Finale

Marwin Dialer
Talk, Schnick Group Seminar
Munich (Germany), 26.04.2023

7. A STEM Study on Promising Phosphors $Sr_5Si_7P_2N_{16}:Eu^{2+}$ and $Sr_5Si_2P_6N_{16}:Eu^{2+}$

Marwin Dialer, Monika M. Pointner, Lucien Eisenburger, Wolfgang Schnick
Poster, 11th International Symposium on Nitrides
Saint-Malo (France), 03.05.2023

12.4 Programming Contributions

The following programs were written in Python to enhance productivity and require basic understanding in programming. All programs are distributed as GitHub repositories and should work out-of-the-box. If not you are welcome to contact me on GitHub (@smarwin).

12.4.1 IDEX – A Lean Electronic Lab Notebook

IDEX is designed for inorganic chemists who need a streamlined and efficient way to document their experiments, observations, and research findings. Built with simplicity and usability in mind, it facilitates easy entry, retrieval, and sharing of lab data. All data stays with you, and you can easily search for past experiments, balance chemical equations, and calculate molar mass and sample weigh-ins (Figure 12.1).

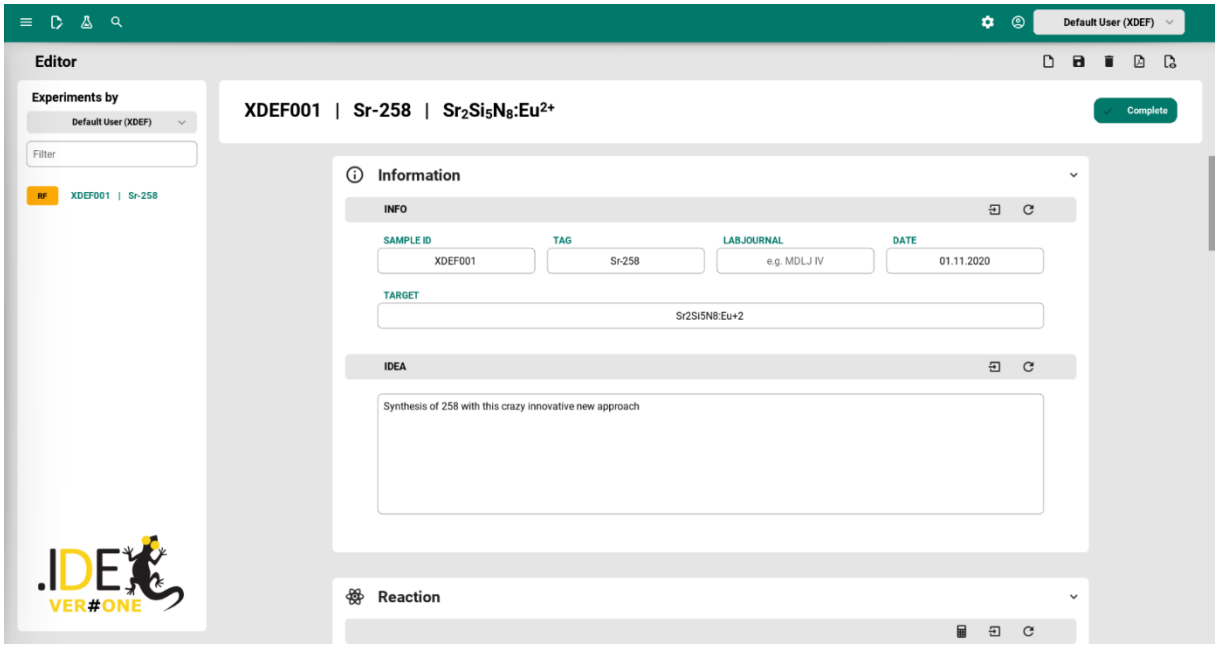

Figure 12.1 Screenshot of the graphical user interface of IDEX (Inorganic Database of Experiments).

Download: https://github.com/smarwin/idex_verone

12.4.2 LumiFit

This Python script provides a comprehensive solution for analyzing spectral data, particularly focusing on emission spectra of Eu^{2+} (Figure 12.2). It includes functionalities for importing data, smoothing spectra, performing Pekarian-type fits, and visualizing results with a focus on spectral features like peak maxima, full width at half maximum (*fwhm*), and area under the curve.

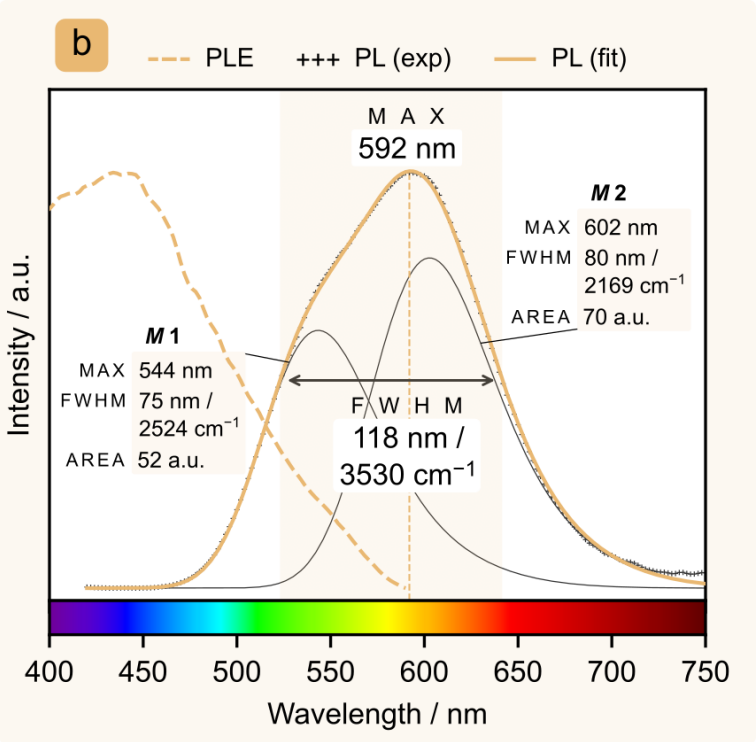

Figure 12.2 Examplary fitting results with Pekarian-type fits.[1] Text was added with Inkscape.

Download: https://github.com/smarwin/LumiFit

12.4.3 EwaldThis

This project comprises a set of Python scripts with a focus on calculating Ewald site energies for structures described in CIF files. The core of this project is the `calculate_ewald_site_potentials.py` script, which utilizes the pymatgen library to compute the electrostatic potential at atomic sites within periodic systems.[2,3]

Download: https://github.com/smarwin/EwaldThis

12.5 References

(1) Dialer, M.; Pointner, M. M.; Strobel, P.; Schmidt, P. J.; Schnick, W. (Dis)Order and Luminescence in Silicon-Rich (Si,P)–N Network $Sr_5Si_7P_2N_{16}:Eu^{2+}$. *Inorg. Chem.* **2024**, *63* (2), 1480–1487. https://doi.org/10.1021/acs.inorgchem.3c04109.

(2) Ong, S. P.; Richards, W. D.; Jain, A.; Hautier, G.; Kocher, M.; Cholia, S.; Gunter, D.; Chevrier, V. L.; Persson, K. A.; Ceder, G. Python Materials Genomics (Pymatgen): A Robust, Open-Source Python Library for Materials Analysis. *Comput. Mater. Sci.* **2013**, *68*, 314–319. https://doi.org/10.1016/j.commatsci.2012.10.028.

(3) Toukmaji, A. Y.; Board, J. A. Ewald Summation Techniques in Perspective: A Survey. *Comput. Phys. Commun.* **1996**, *95*, 73–92.